Predicting planetary rover mobility in reduced gravity using 1-g experiments

Adriana Daca

A Thesis
in
The Department
of
Electrical and Computer Engineering

Presented in Partial Fulfillment of the Requirements
For the Degree of
Doctor of Philosophy (Electrical and Computer Engineering) at
Concordia University
Montréal, Québec, Canada

November 2022

CONCORDIA UNIVERSITY
School of Graduate Studies

This is to certify that the thesis prepared

By: **Adriana Daca**

Entitled: **Predicting planetary rover mobility in reduced gravity using 1-g experiments**

and submitted in partial fulfillment of the requirements for the degree of

Doctor of Philosophy (Electrical and Computer Engineering)

complies with the regulations of this University and meets the accepted standards with respect to originality and quality.

Signed by the final examining committee:

______________________ Chair
Dr. Bruno Lee

______________________ External Examiner
Dr. Christopher Dreyer

______________________ External to Program
Dr. Brian Vermeire

______________________ Examiner
Dr. Hassan Rivaz

______________________ Examiner
Dr. Rastko Selmic

______________________ Thesis Supervisor
Dr. Krzysztof Skonieczny

Approved by ______________________
Dr. Jun Cai, Graduate Program Director

January 24, 2023 ______________________
Dr. Mourad Debbabi, Dean
Gina Cody School of Engineering and Computer Science

Abstract

Predicting planetary rover mobility in reduced gravity using 1-g experiments

Adriana Daca, Ph.D.
Concordia University, 2023

Traversing granular regolith, especially in reduced gravity environments, remains a potential challenge for wheeled rovers. Mitigating hazards for planetary rovers requires testing in representative environments, but direct Earth-based testing fails to account for the effect of reduced gravity on the soil itself. Here, experimental apparatus and techniques for reduced-gravity flight testing are used to systematically evaluate three existing Earth-based testing methods and develop guidelines for their use and interpretation: (i) reduced-weight testing, (ii) matching soil testing instrument response through soil simulant design, and (iii) granular scaling laws (GSL).

Experimentation campaigns flying reduced-gravity parabolas, with soil and wheel both in lunar-g, have shown reductions in net traction of 20% or more and increases in sinkage of up to 40% compared to Earth-based testing methods (i) and (ii). Scaled-wheel testing, according to GSL (method iii) has shown better agreement with reduced-g tests (less than 10% error) and also tends to err on the side of conservative predictions.

Limitations of GSL are investigated including a recently proposed cohesion constraint (that the wheel radius ratio must be the inverse of the gravity ratio) and the effects of wheel size and aspect ratio on GSL's accuracy. It was found that the cohesion constraint can most likely be ignored for mildly cohesive soils such as lunar regolith. Limits on wheel sizes and aspect ratio variation are also proposed.

The application of GSL to planetary rover testing is demonstrated through two studies undertaken in collaboration with NASA's Jet Propulsion Laboratory. One study compares wheel designs for a skid-steer lunar rover in single-wheel tests scaled by GSL, demonstrating that diagonal grousers improve turning performance without requiring larger wheels. The second study involves application of GSL to the design of two reconfigurable test platforms for evaluating steep-terrain mobility performance.

Another aspect of rover mobility testing—normal force control in single-wheel testbeds—is also investigated. An improved method for single-wheel testing, using a 4-bar mechanism, essentially eliminates normal force oscillations from frictional vertical sliders.

Finally, guidelines for conducting and interpreting 1-g mobility tests for lunar rovers are presented, and potential avenues for future research are outlined.

Acknowledgments

First and foremost, I would like to express my sincerest appreciation to my supervisor Dr. Krzysztof (Chris) Skonieczny for providing me the opportunity to conduct this exciting research, and for his instrumental support and encouragement throughout my PhD. He allowed me to explore ideas on my own while also providing invaluable guidance and knowledge when necessary. I would also like to thank my committee members for their helpful comments and suggestions to improve my research.

This work would not have been possible without my many collaborators in the lab: Parna Niksirat, Amir Ali Forough Nassiraei, Tyson Boer, Dominique Tremblay, George Butt, and Pierre-Lucas Aubin-Fournier. Many thanks to all the other lab members who made my PhD experience a pleasant one.

Special thanks to Canada's National Research Council Flight Research Laboratory, especially Derek "Duff" Gowanlock and Shahrukh Alavi, for facilitating the parabolic flight campaigns.

I'm also grateful to NASA's Jet Propulsion Laboratory for giving me the opportunity to participate in the JPL Visiting Student Research Program and JPL Graduate Fellowship program. I learned so much during my time at JPL and made some great friends. Thank you for being wonderful collaborators.

For financial support of my research, I am thankful to Concordia University, the Canadian Space Agency, the Natural Sciences and Engineering Research Council of Canada (NSERC), the Fonds de Recherche du Québec – Nature et Technologies (FRQNT), the donors of the J.W. McConnell Memorial Doctoral Fellowship, and NASA's Jet Propulsion Laboratory.

Thanks should also go to the many friends I made through my volunteer activities at Concordia: the Sustainability Ambassadors Program, Sustainable Concordia, Women in Engineering, and the Concordia Precious Plastic Project. Thank you for all the important work that you do. You will be missed.

I also want to thank my parents, family, and friends for always supporting me in whatever I pursue, especially my dad, Chester Daca, who encouraged me to become an engineer since I was a child, and taught me the importance of hard work.

Last but not least, I am grateful to my husband Christophe for his love, support, and encouragement throughout this journey. Thank you.

Contents

List of Figures

List of Tables

Nomenclature

δ wheel diameter

ρ bulk density of a soil

ρ_0 critical density of a soil

σ_c cohesion stress

τ shear stress

ϕ angle of internal friction

Ψ unspecified function proposed by [8]

Ω unspecified function proposed by [9]

ω angular velocity

c cohesion

D wheel thickness

D_R relative density

f wheel shape

F_{DP} drawbar pull force

F_{DP}/W drawbar pull–weight ratio (also known as drawbar pull coefficient), equal to F_{DP}/Mg

Fr Froude number

F_{turn} tangent turning force

F_{turn}/W tangent turning force coefficient, equal to F_{turn}/Mg

g gravitational acceleration

G cone index gradient

L wheel radius

M mass

P power draw

q scaling factor applied to gravitational acceleration

r scaling factor applied to wheel radius

s scaling factor applied to wheel mass

S	wheel slip
t	time
V	horizontal wheel velocity
W	wheel load
z	wheel sinkage

Chapter 1

Introduction

1.1 Motivation

Searching for signs of life beyond Earth, discovering the nature of planetary processes, and demonstrating technologies essential to human exploration are some of the major objectives of robotic space exploration missions today. Succeeding in these objectives depends on the ability to physically travel to scientifically interesting locations, which usually requires the traversal of hazardous terrain.

Of all the rocky bodies in our solar system (i.e. excluding the gas giants), Earth's gravity is the strongest. This means that wheeled planetary rovers sent anywhere in our solar system, from the milli-g environment of Mars' moon Phobos to the sandy plains of Venus [10], will need to contend with some level of gravity reduction in comparison to our home planet. The world's space agencies have designated the Moon, Mars, and asteroids as priority destinations for human and robotic exploration [11]. The terrains of the Moon, Mars, and a recently discovered class of "rubble-pile" asteroids [12, 13] primarily consist of fine granular regolith dotted with rocks, the negotiation of which has proven difficult in previous exploration missions. The Mars rovers Spirit, Opportunity, and Curiosity have all experienced mobility challenges stemming from wheel–soil interactions. Spirit had experienced high slippage when crossing loose sandy terrains and became embedded in a sulfate sand-filled crater [14], as seen in Figure 1a, ending its mission after operators were unable to free it, even with the help of many numerical and (Earth-based) experimental trials [15]. Opportunity experienced high wheel sinkage and slippage on multiple occasions when traversing sandy crater walls or wind-blown ripples. In some instances wheel slip approached 100%, leading to scenarios where the rover could not reach the desired traverse target and was forced to re-route [16]. The most significant difficulty for Opportunity was the embedding event in what was dubbed "Purgatory Dune" that lasted from Sol 446 to Sol 484. In total, Opportunity lost more than six weeks of progress while engineers focused on extrication from embedding events. Curiosity has also experienced mobility difficulties when traveling over loose, wind-deposited soil, with the most extreme slippage events occurring when the rover attempted to travel over shallow slope formations ("ripples"). More specifically, Curiosity has experienced high wheel slip events (up to 77% slip) on sols 672 and 709-711 during travel into the Hidden Valley ripple formation [17]. Similar mobility challenges were faced by the Lunar Roving Vehicle (LRV, shown in Figure 1b) on the Moon; during the Apollo 15 mission, one of its wheels became stuck, and in order to fix

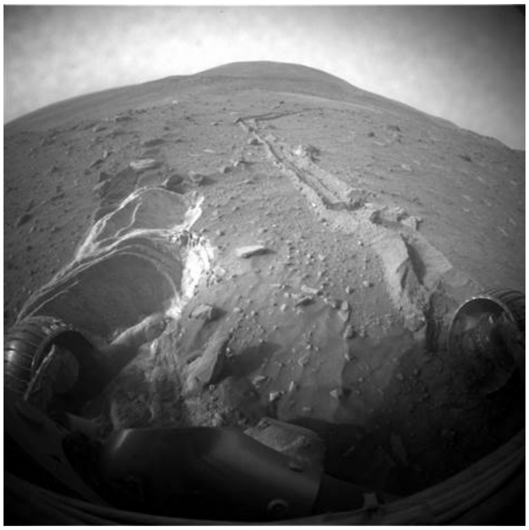

(a) Spirit rover entrenched in soft soil. Image credit: NASA/JPL-Caltech

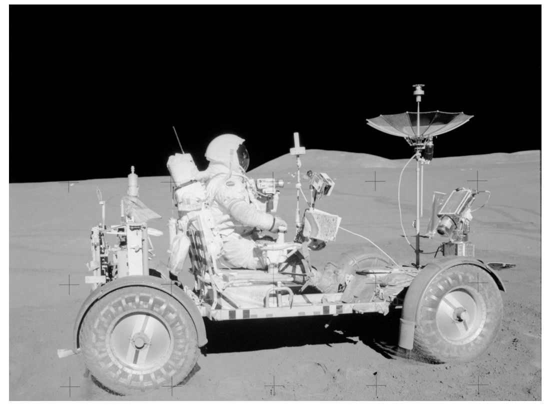

(b) Lunar Roving Vehicle (LRV). Image credit: James B. Irwin/NASA

Figure 1: Examples of previous wheeled rovers that have become entrapped in loose soil on (a) Mars and (b) the Moon.

the problem, the astronauts had to manually move the rover to a new location [18]. This would certainly not be a feasible contingency plan in a fully robotic mission.

A fundamental understanding of wheel–soil interactions and the development of accurate rover testing methods can assist rovers in traversing difficult terrain and reaching scientifically interesting locations. Current testing methods to predict rover performance are not accurate as they do not take into account the effect of reduced gravity on soil behaviour. The gravity level on Mars is about 3/8 that of Earth, and on the Moon it is about 1/6. Asteroids and other small bodies in the solar system (such as moons and dwarf planets) have even lower levels of gravity (for example, Phobos, for which an upcoming rover mission is planned [19], has a gravity level of about 1/2000-g).

SSTB-lite [20] and Scarecrow [21] (shown in Figure 2a) are 3/8 mass versions of the Mars Exploration Rovers (Opportunity and Spirit) and Mars Science Laboratory rover (Curiosity), respectively, that mimic the wheel loads experienced in martian gravity. Since lunar gravity is much lower than Earth's gravity, it is more difficult, but nonetheless possible and sometimes done, to use the same approach to test lunar rovers. Alternatively, lunar wheel loads can be achieved through gravity offload, an example of which is shown in Figure 2b [22]. Although these tests correctly capture the effect of reduced gravity (and thus weight) on wheel loads, they do not capture the effect that gravity has on the granular material itself. During efforts to extricate Spirit, this may have contributed to the fact that maneuvers that were successful in on-ground (equivalent wheel load) testing did not ultimately translate into success on Mars [23].

Testing methods that replicate as closely as possible the effects of reduced gravity on mobility are critical to the success of future rovers. Our own Moon is currently a priority destination for human and robotic exploration, as mentioned previously, and is the main focus of the work presented here. However, the concepts explored herein can be extended to the various levels of reduced gravity seen throughout the solar system.

(a) Scarecrow, a 3/8 mass version of the Mars Science Laboratory (Curiosity) rover. Image credit: NASA/JPL-Caltech.

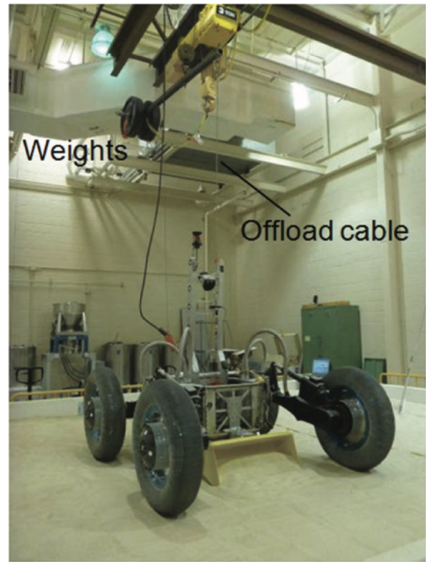

(b) Gravity offload testing to simulate excavation in lunar gravity [22].

Figure 2: Examples of a common rover testing method, reduced-weight testing, where the weight of the test rover is altered to emulate the gravitational acceleration of its destination. This type of testing method is not accurate as it does not capture the effects that gravity has on soil behaviour.

1.2 Introductory concepts

1.2.1 Wheel characteristics

Wheel characteristics referred to throughout this work are illustrated in Figure 3. V refers to horizontal wheel velocity, ω refers to angular wheel velocity, D refers to wheel thickness or width, δ refers to wheel diameter, L refers to wheel radius (i.e. characteristic length), and z refers to sinkage of the wheel below the soil surface (described in more detail in Section 1.2.2). Grousers, also known as lugs, are parts that protrude from the wheel to increase traction, and are commonly used on planetary rover wheels.

1.2.2 Mobility performance metrics

Planetary rover mobility is quantified by the following metrics: drawbar pull, sinkage, and power consumption, all as a function of wheel slip.

Slip

Slip is a ratio describing a wheel's rotational velocity relative to its horizontal motion. The amount of traction a wheel produces is related to how much it slips [24]. A key objective in enhancing the mobility of rovers operating on soft terrain is to reduce the amount of slip for a given task (with its associated required traction). Equivalently, it is desirable to be able to achieve higher net traction at any given slip. The value of slip is defined as

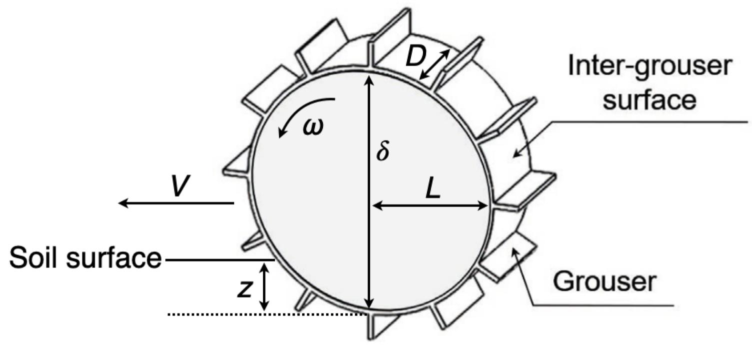

Figure 3: Diagram illustrating wheel characteristics and notation used in this document. V is the horizontal velocity of the wheel, ω is the wheel's angular velocity, D is the thickness or width, δ is the diameter, L is the radius, and z is sinkage (diagram modified from [1]).

$$S = \frac{L\omega\text{-}V}{L\omega} \times 100\% \tag{1}$$

where ω and V are the angular and horizontal wheel velocity, respectively, and L is the wheel radius.

Drawbar pull

Drawbar pull (F_{DP}) measurements are crucial for evaluating the performance of rover wheels, as F_{DP} indicates the ability of the wheel to pull/push itself in the desired direction of motion. F_{DP} is the difference between the thrust force (F_T) and the sum of resisting forces (ΣF_R) acting on the wheel, as expressed in Equation 2. A vehicle's drawbar pull is equal to the sum of the drawbar pull generated by all of its wheels and is the net external force that a vehicle can generate, which can also be related to slope climbing ability [24]. As such, F_{DP} is commonly used to predict a vehicle's slope-climbing performance [25]. However, drawbar pull tests on a flat surface do not perfectly approximate slope-climbing ability, as the normal load distribution that would be present on a full rover is not represented, and the gravity vector on the soil is not in the correct direction to represent soil behaviour on a slope.

$$F_{DP} = F_T - \sum F_R \tag{2}$$

The drawbar pull–weight ratio or drawbar pull coefficient, F_{DP}/W, is approximately constant for different loads, W, within a wheel's practical operating range, until a certain critical load where increased sinkage causes decreasing F_{DP}/W [25].

Sinkage (z)

Sinkage is the vertical displacement of a wheel beneath the undisturbed surface of the soil. It is a function of both wheel loading (static sinkage) and slip (dynamic sinkage). Wheel sinkage is a measure of the response of the terrain to a specific loading, and affects wheel performance.

At equal soil strength, higher sinkage leads to higher resistive forces. On the other hand, at equal sinkage, a soil with higher strength generates higher resistive forces. Any change in resistive forces can thus be explained by variations in sinkage and/or soil strength. These resistive forces act against the thrust, and therefore contribute to a reduction of F_{DP}.

Power consumption

Motor current measurements provide insight about the torque, and therefore the power, required to spin the wheel, or the "difficulty" with which the motor spins the wheel. Increased power is required when soil resistance is higher, which can occur as a result of increased sinkage and/or higher soil strength. It is expected that when comparing two cases with equivalent soil strength and differing sinkage, more power would be required in the case with higher sinkage. Similarly, in two cases with equal sinkage and different soil strength, power requirements would be higher in the case where stronger soil is encountered.

1.2.3 Soil characteristics

Cohesion and friction angle are important properties characterizing a soil's shear strength, τ, which can be approximated by Equation 3:

$$\tau = c + \sigma \tan \phi \tag{3}$$

where c is cohesion (electrostatic and/or interlocking forces between particles), σ is normal stress, and ϕ is the angle of internal friction. A soil's angle of internal friction, or friction angle, is defined as the angle between the normal force and the resultant force of the normal force and friction at the time of shear failure. Cohesion and angle of internal friction are both measures of a soil's ability to withstand shear stress (a higher angle of internal friction and/or higher cohesion correspond to higher soil strength).

Additionally, both friction angle and cohesion are functions of bulk density (i.e. they depend on the soil's level of compaction). A granular material can exist in a range of bulk densities, depending on its level of compaction. The relative density (D_R) of a soil represents the measured bulk density of a soil relative to its minimum bulk density (0% D_R) and maximum bulk density (100% D_R), and is calculated using Equation 4 [26]:

$$D_R = \frac{\rho_{max}}{\rho_{min}} \cdot \frac{\rho - \rho_{min}}{\rho_{max} - \rho_{min}} \cdot 100\% \tag{4}$$

where ρ is the bulk density of the soil—the weight of soil particles per unit volume, ρ_{min} is the minimum possible bulk density for that soil, and ρ_{max} is the maximum.

Soil simulants are terrestrial materials that are meant to replicate the mechanical and/or chemical properties of extraterrestrial regolith for research and testing purposes.

1.3 Problem statement

The research question being addressed is how to predict planetary rover mobility, which occurs principally on granular materials in reduced gravity, by use of novel testing methods on Earth in

1-g. Specifically, the objective of this research is to develop and implement guidelines for accurate rover mobility testing. Methods to account for the effects of reduced gravity on planetary rover mobility are evaluated experimentally, and case studies for their application to testing of future rovers are carried out. Based on these experimental evaluations, the testing method that most closely predicts actual rover mobility performance as characterized by the metrics described in Section 1.2.2 is recommended.

Investigations of three potential methods to account for reduced gravity effects were conducted. Single-wheel tests aboard parabolic flights producing effective lunar gravity were compared to equivalent on-ground experiments *for the first time* using each of the three methods. Further reduced gravity parabolic flights with a different soil simulant to confirm and expand on the findings from the recent flight campaigns are also planned. Based on the results from the first two parabolic flight campaigns and preliminary on-ground experiments with this new simulant, guidelines for mobility testing methods that most accurately reflect reduced-gravity effects are established.

The second component of this research involves application of these guidelines to mobility testing of potential future lunar rovers under development at NASA Jet Propulsion Laboratory (JPL) through the JPL Visiting Student Researcher Program (JVSRP), demonstrating that these recommendations can successfully be applied to both single-wheel and full rover testing to aid in the design of future rovers.

1.4 Literature review

1.4.1 Classical terramechanics

Terramechanics is the study of vehicle–terrain interactions. The founding modeling paradigm of this field relies on simple one-dimensional pressure–sinkage relationships to estimate compaction resistance [24] and/or empirical parameters, e.g. to estimate the location of maximum pressure beneath a wheel [27]. For rigid wheels driving on dry granular soil, which is typical for planetary rovers, the data shows more complexity than captured by these assumptions. In [28], flowing granular soil was observed, as well as pressure distributions more complex than predicted by one-dimensional compaction.

Attempts to extrapolate terramechanics models and their empirical parameters to new conditions, such as extraterrestrial regolith and gravity, have proven difficult. For example, Wong hypothesized a pressure–sinkage coefficient proportional to gravity in order to account for the results of wheel traction experiments in reduced-g flights by Kobayashi [29]. However, some pressure–sinkage coefficients, extracted from data of yet another set of reduced-g flight experiments [30], appear to in fact be constant across measurements at 1-g, 1/2-g, and 1/6-g. This inability to apply classical terramechanics theory to all available experimental data suggests that underlying assumptions need to be reevaluated, and that new models for planetary rover–soil interactions must be developed. The inadequacy of classical terramechanics models for predicting planetary rover mobility has been emphasized by several researchers today [31, 32, 33, 34].

1.4.2 Soil behaviour in reduced gravity

The problem of predicting soil behaviour in reduced gravity has been approached from multiple directions, for example: through soil simulant design [2, 35], through discrete element method (DEM) simulations [36], through semi-empirical modelling [37], and through scaling laws [8]. Limited experimental work has been completed; there is still a need for suitable reduced-gravity experimental data that can be used to validate approaches such as those taken in [2, 8, 35, 36, 37].

Aircraft flying parabolic arcs currently offer the best opportunity to achieve significant stretches of effectively reduced gravity in a controlled fashion without actually travelling to an extraterrestrial surface[1]. In [39], 1/6-g, 1-g, and 2-g cone penetrometer measurements were performed aboard parabolic flights and a positive correlation between the cone index gradient (G) and gravity was observed. Reduced-gravity flights specifically measuring soil parameters including peak friction angle, residual friction angle, and angle of repose [40, 41, 42] have yet to arrive at a comprehensive consensus on how gravity affects these parameters. Additionally, reduced-gravity flights studying excavation [43] and bearing capacity [30] have similarly produced non-trivial, non-intuitive results that provide further motivation to study rover–soil interactions in reduced gravity. In [44], experimental cone penetrometer measurements were obtained under "low gravity fields" achieved using magnetic particles subjected to magnetic fields of various strengths, and a negative correlation was found between normalized tip resistance (cone index normalized by initial vertical stress) and gravity. However, these results are not validated against any actual low-gravity experimental results (e.g. from parabolic flights).

Preliminary efforts have been made to account for the effects of gravity on granular materials, at least indirectly, through simulant design. Oravec et al. [2] designed GRC-1 to produce cone penetrometer readings comparable to those collected on the Moon (i.e. in lunar gravity) during Apollo, as seen in Figure 4. The assumption is that replicating the mechanical response of lunar soil in terms of cone penetration resistance (while ignoring other specific parameters, such as particle angularity) will also replicate the response to vehicle loading, in terms of traction for example. This assumption had not been experimentally validated and is discussed in detail in Section 2.3.2.

Another promising method for predicting wheel performance in reduced gravity is granular scaling laws (GSL), which are analogous to the scaling relations employed in the fields of aero- and hydrodynamics. These scaling relations, recently proposed by Slonaker et al. [8], can be used to predict the performance of a larger wheel based on tests with a smaller wheel, or to predict wheel performance in one gravity level based on tests in another gravity level. The use of scale models to study wheels driving in loose soil is by no means a new idea. In fact, an entire chapter in Bekker's Theory of Land Locomotion [24] is dedicated to scale model testing and dimensional analysis, and other works dating back to the 1960's and 70's studied the "similitude" of scaled agricultural vehicles and implements [45, 46, 47, 48, 49, 50, 51, 52, 53, 54]. The application of the scaling laws proposed by Slonaker et al. to tests with wheels of different sizes has been validated experimentally [8, 55, 56]. However, the gravity-variant version of the scaling laws had previously only been validated through discrete element method (DEM) simulations [8, 55, 57, 58, 59]. Thoesen et al. tested the scaling laws in different soils and with different wheel shapes using a small two-wheeled vehicle [55, 56] and expanded them for application to helically driven dynamics [57, 58].

[1]Parabolic arcs only provide up to 30 seconds of continuous reduced gravity, and NASA is going to great lengths to extend this—they recently announced a partnership with Blue Origin, where their suborbital vehicle New Shepard will act as a centrifuge while in free-fall to simulate lunar-g for over 2 minutes [38].

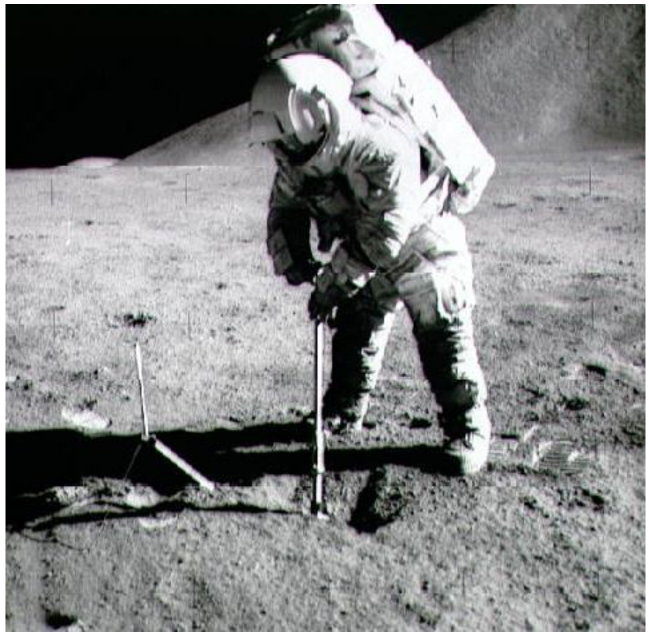

Figure 4: An Apollo astronaut takes cone penetrometer measurements on the Moon. The soil simulant GRC-1 was designed to match these measurements on Earth in 1-g. Image credit: NASA.

Recently, Zhang et al. proposed a modified version of GSL that includes a cohesion term and allows for sloped terrain [59]. GSL are discussed in more detail in Section 4.1.

It should be emphasized that similar scaling laws for predicting reduced-gravity rover mobility had previously been derived [60, 61, 62, 63, 64] and, through slightly different means, they arrived at a subset of the solutions to Slonaker's more general scaling laws. Kuroda et al. [62, 63] additionally performed experiments with scale-model rovers aboard parabolic flights to validate these scaling laws, originally proposed by Kanamori [61], in reduced gravity. In these experiments, differences were observed in front and rear wheel performance [62]. However, the overall slip ratio of each vehicle followed the scaling laws almost exactly [63]. Scale-model testing was also performed for the LRV program [65, 66] and has been revisited by NASA engineers in recent years for the Lunar Electric Vehicle (the precursor to the Space Exploration Vehicle concept) [67].

Modeling and simulation is another useful tool for predicting performance in reduced gravity, but only if built upon sound validated principles. Two state-of-the-art directions of current terrain interaction research are the discrete element method (DEM), which simulates contact mechanics for millions of individual granular particles, and the material point method (MPM), which is a combination of finite element method (FEM) and finite difference method (FDM). Both of these techniques demonstrate promise in modeling planetary rover interactions [68, 69], and are able to set the gravity acting on the soil as a parameter. Similarly, a novel technique has also been developed using elasto-plasticity theory based descriptions of the wheel–soil interaction [70]. This provides a computationally efficient representation that is fully compatible with dynamic models of rovers. Efforts are underway to incorporate the effects of gravity into such models [71]. As with any new modeling and simulation techniques, or with the application of existing techniques to new problems (in this case, simulating the effects of gravity on wheel–soil interactions), the predictions made will need to be validated against new experimental data.

Few datasets have been described in the literature for wheels driving in soil during reduced-g flights. In a 1971 NASA report [72], a lunar roving vehicle (LRV) wheel drove along a circular path in Lunar Soil Simulant 4 (LSS-4) inside a vacuum chamber mounted inside an aircraft flying parabolic arcs, with the goal of testing fenders for dust mitigation. While the objective of these experiments was to determine the amount of dust churned up by the wheels, as well as dust settling behaviour in vacuum, low-gravity conditions, some additional interesting observations were made. Increased soil build-up was observed in front of the wheel, which meant that more power was required to drive in lunar-g. It was also observed that vacuum conditions may have increased the apparent cohesion of the soil[2].

In [29], experiments by Kobayashi et al. consisted of a self-propelled wheel driving in FJS-1 lunar soil simulant and in Toyoura sand in a broad range of gravity conditions: 1/6-g, 1/2-g, 3/4-g, 1-g, and 2-g. The experimental data included horizontal travel distance, vertical sinkage, and wheel torque. This dataset was compared to corresponding data collected in 1-g with varying vertical wheel load, W (e.g. 1/6 W, 1/2 W, etc.), such that the effect of gravity on the soil particles was isolated. Kobayashi observed that wheel travel was impaired when both the wheel and the soil were subjected to reduced gravity. However, when only the wheel load was reduced, wheel mobility improved. These experiments provide some evidence that only adjusting the wheel load while the soil remains in 1-g does not capture mobility performance in reduced gravity. This motivated our group's work in more comprehensively studying the effects of gravity on wheel performance, as will be presented throughout the remainder of this document.

1.4.3 Single-wheel testbeds

Single-wheel testbeds (SWTBs) are widely used to evaluate wheel performance and to study wheel–soil interactions with application to terrestrial off-road vehicles as well as planetary exploration rovers.

To study wheel–soil interactions, many different SWTBs have been utilized around the world. One aspect of SWTBs that often seems to be overlooked is the actual measured normal force resulting from wheel load application and testbed dynamics. Normal force oscillation has been reported in several SWTBs and has usually been attributed to grousers. However, normal force fluctuations have also been observed when testing wheels without grousers in some systems. Moreover, the amplitude of these normal force variations cannot be explained by accelerations related to vertical displacements of the wheel alone. Below, the characteristics of SWTBs at different institutions are outlined and, where time-series data are reported, their dynamic behaviour is described. A summary of the key information discussed below can also be found in Table 1.

[2] Research comparing a wheel driving in vacuum and atmospheric conditions in three different simulants (including mildly cohesive martian simulant MMS-1 with cohesion of 0.81 kPa [73]) found that driving in vacuum did not significantly affect drawbar pull [74], although previous work found conflicting evidence (improved [75, 76] or hindered [77, 78] wheel performance in vacuum) that Sutoh [74] attributed to the difficulty of controlling vacuum conditions.

Table 1: Characteristics of SWTBs at different institutions (continued on next page).

Institution/ SWTB #	Mode of motion control	Mode of normal force application	Normal force behaviour	Reference(s)
Massachusetts Institute of Technology (MIT) #1	Slip-controlled	Deadweight	N/A	[79, 80, 81, 82]
MIT #2	Slip-controlled	Deadweight	N/A	[83]
MIT #3	Free-slip or slip-controlled	Deadweight	N/A	[84, 85, 86]
Tohoku University #1	Slip-controlled	Counterweight	N/A	[87, 88, 89, 90]
Tohoku University #2	Free-slip	Not reported	N/A	[91]
Kyushu University	Free-slip	Counterweight	N/A	[29]
German Aerospace Center (DLR) Bremen/ RUAG	Slip-controlled	Counterweight and deadweight with 4-bar mechanism	N/A	[92, 93, 94, 95]
Japan Aerospace Exploration Agency (JAXA)	Free-slip	Counterweight	N/A	[96, 97]
Virginia Polytechnic Institute and State University	Slip-controlled	Pneumatic system with active control	Oscillating normal force without active control, normal force stays within $\pm 3\%$ of setpoint with active control	[98, 99, 100, 101, 102]
Harbin Institute of Technology	Slip-controlled	Counterweight	N/A	[103, 104, 105, 106, 107]
Carnegie Mellon University (CMU) #1	Slip-controlled	Deadweight	Oscillating normal force	[108, 109]
CMU #2	Free-slip	Deadweight	N/A	[110]
Tianjin University	Slip-controlled	Not reported	N/A	[111]
Politecnico di Torino	Slip-controlled	Deadweight	N/A	[112]
Dalhousie University	Slip-controlled	Counterweight	Oscillating normal force	[33, 113, 114]
Technical University of Munich	Free-slip	Counterweight and 4-bar mechanism	Oscillating normal force	[115]

Table 1 Continued: Characteristics of SWTBs at different institutions.

Institution/ SWTB #	Mode of motion control	Mode of normal force application	Normal force behaviour	Reference(s)
University of Oklahoma	Slip-controlled	Not reported	N/A	[116]
Indian Space Research Organisation (ISRO) #1	Free-slip	Counterweight	N/A	[117]
ISRO #2	Slip-controlled	Counterweight and 4-bar mechanism	Small normal force oscillations (approx. $\pm$ 1 N)	[118]
Beijing University of Aeronautics and Astronautics	Slip-controlled	Unknown	N/A	[119]
Jilin University	Slip-controlled	Counterweight	N/A	[120, 121]
Federal University of Technology, Akure	Free-slip	Deadweight	N/A	[122]
Concordia University #1	Slip-controlled	Deadweight and counterweight	Oscillating normal force without 4-bar mechanism, steady with 4-bar mechanism	[123]
Concordia University #2	Slip-controlled	Pneumatic system	Oscillating normal force	[124, 5]

Most SWTBs employ a driven wheel mounted on a driven horizontal carriage (i.e. the wheel slip is controlled). Such is the case in the SWTB at the Field and Space Robotics Laboratory at the Massachusetts Institute of Technology (MIT) [79, 80, 81, 82], which applies the wheel load through a deadweight system while also allowing free vertical motion of the wheel. Iagnemma et al. [79] reported fluctuating drawbar pull data with a smooth rigid wheel, Shibly et al. [80] reported fluctuating drawbar pull and wheel torque, also with a smooth rigid wheel, and Bauer et al. [82] reported oscillating wheel torque data when using a rigid wheel with grousers. No normal force data were reported in any of these studies. A second SWTB of the same design was later constructed by the Robotic Mobility Group at MIT [83]. These two MIT SWTBs also have glass sidewalls, a feature that has been used by Senatore and Iagnemma [83] to visualize wheel–soil interactions using PIV analysis. A third SWTB was constructed by the Robotic Mobility Group at MIT of a similar design but much larger in scale [84, 85, 86]. This testbed can also perform "free-slip" tests in addition to slip-controlled tests, and has a glass sidewall as well. Oscillating motor torque and vertical acceleration were reported by Bouguelia et al. [86] in free-slip tests.

Tohoku University's SWTB is also slip-controlled, with a free vertical axis, and normal load applied via a counterweight mechanism [87, 88, 89, 90]. It also has the ability to simulate steering (i.e. the wheel can have a nonzero yaw angle—it can be rotated around the vertical axis). Yoshida et al. [87] reported oscillating sinkage with a grouser wheel; no normal force data were reported. This SWTB also has a glass sidewall. In response to many space agencies' and private companies' interest in developing rovers capable of traveling at higher velocities, a new SWTB was recently developed at Tohoku University that is capable of conducting experiments at speeds up to 0.5 m/s. This new SWTB performs free-slip experiments while measuring forces and torques on the wheel in addition to slip and sinkage [91].

At Kyushu University, an SWTB was developed for use on reduced-gravity parabolic flights [29]. In this SWTB, the rotation of the wheel is controlled, but not its horizontal velocity (i.e. slip is measured, not controlled). It has a free vertical axis and the normal load can be varied via counterweight (this was only done in the on-ground experiments). Kobayashi et al. [29] reported noisy/oscillating sinkage and wheel torque data for experiments using a smooth rigid wheel. No normal force data were reported.

At the German Aerospace Center (DLR) Bremen/ RUAG [92, 93, 94, 95] is another slip-controlled SWTB that uses a combination counterweight/deadweight system to apply a vertical load to the wheel. It also has a free vertical axis and a 4-bar mechanism to balance vertical loads. Fluctuating drawbar pull and wheel torque were reported by Michaud et al. [95] using a flexible wheel with grousers.

JAXA's SWTB [96, 97] controls the wheel rotation only (not the wheel's horizontal motion), and slip is measured. It employs a counterweight system to apply the wheel load, and has a free vertical axis as well as tilting capability (for tests on sloped terrain). It also utilizes a parallel link mechanism (similar to a 4-bar mechanism) to balance vertical loads. Small oscillations/fluctuations are seen in the slip ratio data [96, 97] as well as sinkage data [97] for wheels with grousers and other surface features.

The SWTB at the Virginia Polytechnic Institute and State University, or Virginia Tech, is slip-controlled and the vertical load is applied using a pneumatic system [98, 99, 100, 101, 102]. The pressure in two pneumatic air springs is controlled with an electro-pneumatic control valve based on feedback from a force sensor measuring the normal force on the wheel [101]. Naranjo [100] reported an oscillating normal force before the active control system was developed, and then reported $\pm 3\%$ variation in normal force after implementing the active control system. This testbed is also capable of turning simulation.

The Harbin Institute of Technology has a slip-controlled SWTB with a counterweight load application system and a free vertical axis [103, 104, 105, 106, 107]. This SWTB also has a glass sidewall and the ability to simulate steering. Ding et al. [106] reported oscillating drawbar pull and wheel torque for wheels with and without grousers, and oscillating sinkage for a wheel with grousers.

At Carnegie Mellon University (CMU) a slip-controlled SWTB has been used with a deadweight system to apply the wheel load [108, 109]. This SWTB also has a free vertical axis in addition to a glass wall for visualization of soil motion beneath the wheel. Time-series data were not published by Skonieczny et al. [108], but the first author has confirmed that oscillation was observed in the normal force data. Moreland et al. [109] reported fluctuating drawbar pull for wheels with and without grousers. Another SWTB was developed at CMU to test a large inflatable wheel. This testbed has a free vertical axis and deadweight load application method [110]. In this testbed, wheel angular velocity is controlled and slip is measured.

Tianjin University [111] also has a slip-controlled SWTB. No normal load application method was mentioned, and the vertical axis is not free (i.e. sinkage is held constant). Fluctuating drawbar pull versus angular position of the wheel was reported for wheels with and without grousers, with higher amplitude fluctuations seen in the wheels with grousers.

There is also an SWTB at Politecnico di Torino [112] which is slip-controlled with a dead-weight system for applying the wheel load. It has a free vertical axis and side-slip and camber angle control. Noisy lateral force data were reported, but no other time-series data were provided.

At Dalhousie University there is a slip-controlled SWTB which employs a counterweight mechanism to control the wheel load and has a free vertical axis [33, 113, 114]. In this SWTB, the wheel is stationary and the soil moves underneath of it (the SWTB was designed as a modified creep feed grinding machine). Irani reported oscillating normal force, drawbar pull, and sinkage for wheels with grousers [33], as well as oscillating drawbar pull [113, 114] and normal force [114] for wheels without grousers.

The SWTB at the Technical University of Munich controls wheel rotation while slip is measured [115]. It employs a counterweight system to apply the wheel load, and has a free vertical axis. It also has a uniquely large 4-bar mechanism. Oscillating normal force and drawbar pull were reported for wheels with grousers.

A novel SWTB was also developed at the University of Oklahoma where the wheel spins above a table that is able to translate and rotate in order to simulate turns and other scenarios. The vertical load is applied via a counterweight mechanism [116]. No time-series data were reported.

The Indian Space Research Organisation (ISRO) has a SWTB in which the wheel rotation is controlled and slip is measured [117]. This SWTB employs a counterweight system to apply the wheel load, and it has a free vertical axis. No time series data have been reported. The ISRO's second SWTB is slip-controlled with the wheel load applied via counterweight and a 4-bar mechanism [118]. Small normal force oscillations observed in this SWTB were attributed to friction in the 4-bar mechanism's hinges.

Tongji University's SWTB is slip-controlled with the wheel load being applied via counter-weight [125]. The wheel is allowed to move freely in the vertical axis. No method for controlling vertical load on the wheel is mentioned. Oscillating sinkage and torque were reported when testing a wheel with grousers.

At the Beijing University of Aeronautics and Astronautics is a slip-controlled SWTB with a free vertical axis [119]. It also has transparent sidewalls. No time-series data were reported.

Jilin University also has a slip-controlled SWTB that uses a counterweight mechanism to apply the wheel load [120, 121].

At the Federal University of Technology, Akure, a free-slip SWTB was recently developed for agricultural studies [122].

Rotary testbeds have also been developed where the wheel travels around a circular track [126, 127], but the details of these testbeds are not considered here.

Concordia University has two SWTBs. One is a larger, stationary SWTB—dubbed the laboratory SWTB. The second is a smaller, mobile SWTB that was designed to meet the requirements imposed by reduced-gravity parabolic flights [124]. Thus, it is referred to as the parabolic flight SWTB. These SWTBs are described in detail in Sections 2.1.1 and 2.1.2, respectively. The laboratory SWTB is slip-controlled and uses a counterweight system to apply the vertical load. It has a free vertical axis and a glass wall for visualization of soil motion beneath the wheel. It also has the ability to simulate steering by changing the orientation of the wheel around the vertical axis. Additionally, it can be tilted for experiments on sloped terrain. Normal force oscillation has been observed in this SWTB. Detailed experimental results showing the dynamic behaviour of this SWTB are shown in Sections 2.5.1 and 2.5.2. The parabolic flight SWTB is also slip-controlled, and uses a pneumatic system to apply the wheel load. It also has a free vertical axis and a glass sidewall. Additionally, it has automated soil preparation capabilities. Normal force oscillation has been observed for wheels with [5] and without [128] grousers in this SWTB. Time-series data from this SWTB are shown in Section 2.5.2.

This is not an exhaustive list. Many other SWTBs have been used; for example: [129, 130, 131, 132, 133]. Furthermore, Ani et al. [134] published a comprehensive review of SWTBs from 1914 to 2015.

In summary, normal force data have only been published from Dalhousie University, the Technical University of Munich, the Indian Space Research Organization, the Virginia Polytechnic Institute and State University, and Concordia University SWTBs, to the best of the author's knowledge. Normal force oscillations are observed for any system that incorporates a frictional vertical axis assembly.

1.4.4 From single-wheel testbeds to full rovers

When contemplating the utility of single-wheel experiments for predicting planetary rover mobility, a question that might arise is that of the applicability of experimental results obtained from single-wheel tests to full 4- or 6-wheeled rovers. Considerations might include whether the distribution of the rover's load amongst its wheels affects its mobility, or if results from single-wheel tests can be considered equal to an average wheel on a full vehicle. The "multi-pass" effect is a phenomenon that complicates the study of full rovers. This effect arises from the fact that the front wheels drive on untouched soil, whereas the rear wheels drive over soil that has been disturbed and/or compacted by the front wheels. Another confounding observation is that of normal force oscillation in single-wheel testbeds (SWTBs), as discussed in Section 1.4.3.

Limited work has been done to resolve these questions. Irani et al. [33, 114] observed normal force oscillations in their SWTB, and subsequently built a mini 4-wheeled rover to investigate if such oscillations are present in a full vehicle. In the single-wheel tests, ripples were observed in the soil behind the wheel, and since the frequency of those ripples matched that of the normal force oscillations, they concluded that if ripples are present, then normal force oscillation must be present as well. Such ripples were observed in the mini rover tests, so they concluded that normal force oscillations must have been present in the mini rover. However, they did not actually measure the normal forces on the mini rover's wheels.

Thoesen et al. [56] attempted to validate the granular scaling laws (GSL) proposed by Slonaker et al. [8] (described above) using a 2-wheeled mini-rover, and observed differences in power consumption in the front and rear wheels in some experiments, suggesting that the multi-pass effect may have an impact on GSL prediction error. Kuroda et al. [62, 63] performed experiments with scale model rovers (one 4-wheeled rover and one 5-wheeled rover) to validate the scaling laws proposed by Kanamori [61] in reduced gravity and similarly observed differences in front and rear wheel performance. However, the overall slip ratio of each vehicle followed the scaling laws quite well.

Turnage and Banks [135] compared multi-pass single-wheel tests and one pass of a 4- and 6-wheeled vehicle at 20% slip, and concluded that the differences observed in measured drawbar pull were insignificant. However, the wheel loads were not exactly the same, there were few data points, and no statistical analysis was completed.

Flippo et al. attempted to predict performance of a skid steer rover using single-wheel tests to perform skid-steering maneuvers [136, 116]. They were able to predict turning efficiency within 10%. Then, they devised a mapping function to predict the full rover power consumption based on the single-wheel power consumption.

Fiset et al. [137] used both a skid-steered 4-wheeled robot and a single-wheel testbed to study power consumption of skid-steer rovers. Similar trends were observed in each dataset, but the results were not directly comparable, as different soils were used in the single-wheel and full rover tests.

Ishigami et al. [89] extended their single wheel setup to a full rover simulation with four steerable and controlled wheels. They first developed a wheel–soil mechanics model and validated it using their SWTB. Then, they simply incorporated the wheel–soil model into an articulated multibody model that described the motion of the vehicle's body and chassis. Their work focused on steering maneuvers.

Senatore et al. [85] compared three different methods of estimating a 6-wheeled rover's slope-climbing ability: i) simulations of the full rover, ii) simulations of single-wheel tests, and iii) simulations of single-wheel tests considering weight transfer (i.e. uneven normal load distribution on the rover's wheels when driving uphill). These methods were evaluated by comparison to field tests using the full rover. They used SWTB simulations for comparison to the field tests because they could not obtain sand from the field test site for SWTB experiments (they validated their SWTB model using a different soil, then matched the soil properties in their model to those of the field test site). They concluded that it is possible to use single-wheel experiments to estimate full vehicle performance without the need to know the vertical load distribution among the axles, at least for the rover configuration, soil, and test conditions considered in their work.

In a series of single-wheel and full rover experiments and simulations, Ghotbi et al. [138], however, showed that the normal load distribution on a 6-wheeled rover's wheels does affect its slope climbing ability. Therefore, knowing the vertical load distribution among the wheels should provide a more accurate prediction of full rover mobility, in contrast to the conclusion of Senatore et al. [85]. Ghotbi et al. found that that the multi-pass effect influences the optimal normal load distribution as well, with an even load distribution being optimal when the multi-pass effect was not considered, and the optimal solution requiring the load to be shifted towards the rear wheels when accounting for the multi-pass effect. In order to measure the normal force distribution among the rover's wheels, the rover had force/torque sensors mounted above each wheel. Normal force oscillations can be seen in the data, but as no soil preparation procedures were described, it is impossible to know if these oscillations were due to uneven terrain, friction in the vertical axis, or other dynamics.

1.4.5 Rover suspension design

In past and present planetary exploration missions, many areas have been out of reach due to vehicle limitations in terms of the types of terrain that can be traversed. For example, the six-wheeled passive rocker-bogie suspension [139] used on all of NASA's Mars rovers offers a simple and reliable design that can negotiate uneven terrain, but is unable to overcome steep slopes covered with loose regolith. The ability to overcome steeper terrain would allow rovers to take shorter paths through previously inaccessible areas, reducing their overall traverse length and thus the time required to travel to regions of scientific interest. Furthermore, the ability to traverse steeper terrain would enable further progress towards many objectives relevant to planetary science and human exploration where the steep areas are themselves the regions of interest. For example, mapping and characterization of near-surface volatiles on the Moon and Mars has been highlighted as an objective in the 2023 Planetary Decadal Survey [140]. Achieving this objective would require exploration of steep slopes covered in loose regolith such as permanently shadowed regions (PSRs) in craters near the Moon's south pole.

Many research and development studies have been conducted towards improving mobility on steeper terrain and weaker soils, having arrived at solutions to this problem that involve active suspension systems capable of "wheel-walking" or "push-pull" locomotion, such as the Scarab rover [141], SRR rover [142] and limbed locomotion systems such as the All-Terrain Hex-Limbed Extra-Terrestrial Explorer (ATHLETE) [143] and RoboSimian [144, 145]. What most of these concept rovers have in common is a highly complex design with many actuators and degrees of freedom. This is undesirable for most planetary rover missions as it increases cost and risk. Despite this, NASA's upcoming VIPER lunar rover [146] and ESA's forthcoming Rosalind Franklin Mars rover [147] both have highly complex designs intended to leverage the benefits of wheel-walking type locomotion over loose soils. However, for future exploration, reducing complexity and cost while still enabling mobility over steep terrain would allow more concept rovers to be transitioned to actual flight missions. The tethered 2-wheeled Axel rover [148] is a good example of a simple concept that can enable mobility on extremely steep terrain, however, its traverse distance is limited by the tether length. Despite all of this prior research, no systematic study has been undertaken to compare the many possible configurations for overcoming steep terrain in order to converge on a solution that maximizes benefits while minimizing complexity.

1.4.6 Skid-steer rover sinkage and rover wheel design

Skid steer rovers' wheels do not turn explicitly; vehicle turning is achieved by rotating the left and right wheels at different velocities. In order to achieve a turn, the wheels must inherently experience a high amount of slip, which can lead to high sinkage. Despite this shortcoming, skid steering is a popular choice for planetary rover missions due to its simplicity, low cost, and low mass in comparison to explicit steering systems.

Sinkage can be reduced with changes to wheel design such as wider wheels, larger diameter wheels, or flexible wheels[3], all of which reduce sinkage by increase the size of the contact patch, thereby decreasing the contact pressure of the wheel. Regarding the effects of wheel design on sinkage, only straight-driving tests have been published (e.g. [152, 153, 154]). For application to skid-steer rovers, there are no experiments reported in the literature looking at wheel designs to reduce sinkage during skid-steer turning maneuvers.

[3]Examples of flexible rover wheels include the Lunar Roving Vehicle wheels [149], the Rosalind Franklin rover wheels [150], and new shape-memory alloy wheels developed at NASA's Glenn Research Center [151]. These types of wheels are usually cost prohibitive, thus, most missions opt for rigid wheels with grousers.

1.5 Contributions

The contributions of this work fall into two categories: the data collected and the new implications that can be derived from the analysis of that data, including recommendations for 1-g testing that will improve the prediction of rover mobility in reduced gravity. The contributions presented in this thesis are summarized below:

1. Assessed the accuracy of three 1-g rover testing methods that aim to account for reduced-gravity effects: (i) reduced-weight testing, (ii) matching soil testing instrument response through soil simulant design (the "equal G (cone index gradient)" method) and (iii) granular scaling laws (GSL)

   1.1 Reduced-gravity flight experiments were compared to on-ground experiments at equal wheel load to reveal that method (i), reduced-weight testing, does not accurately represent wheel–soil interactions in reduced gravity, and in fact overestimates wheel performance, since it does not capture the effects of reduced gravity on the soil itself. Since this testing method is extremely common, this finding has major implications on the future of planetary rover mobility testing, and indicates that improved testing methods must be implemented to boost future rovers' chances of success.

   1.2 In a second parabolic flight campaign, the relationship between gravity and cone penetration resistance was characterized for the lunar terramechanics soil simulant GRC-1 to reveal that shear strength decreases significantly in reduced gravity, further highlighting the need to account for reduced-gravity effects on soil behaviour when testing planetary rovers. Wheel performance in reduced gravity was compared to wheel performance predicted by tests using method (ii), the equal G method, and method (iii), GSL, demonstrating that the equal G method also overestimates wheel performance, whereas GSL both more accurately and conservatively predicts reduced-g wheel performance. These results imply that caution should be exercised when interpreting tests completed in the soil simulant GRC-1 (i.e. following the equal G method). Beyond that, GSL was identified as the recommended testing method for accurate representation of the effects of reduced gravity on wheel–soil interactions.

   1.3 Further 1-g tests improved our understanding of the limitations of GSL, demonstrating that a recently proposed cohesion constraint (that the radius ratio must be the inverse of the gravity ratio, e.g. tests in 1-g aiming to represent performance in lunar-g must be done with a 1/6-scaled wheel) can be neglected for mildly cohesive lunar regolith without decreasing the method's accuracy, and illustrating that errors introduced by testing with extremely small wheels and/or significantly differing wheel aspect ratios dwarfs any errors due to neglecting the cohesion constraint.

2. Demonstrated the application of GSL to rover test campaigns as part of the JPL Visiting Student Research Program (JVSRP) at NASA's Jet Propulsion Laboratory

   2.1 GSL was successfully applied to the design of sub-scale prototypes devised to improve our understanding of different locomotion modes for enhanced steep-terrain mobility, and to tests resulting in the identification of an improved wheel design to enhance turning performance of a skid-steer lunar rover.

3. Characterized two common normal force application methods in single-wheel testbeds (SWTBs)

    3.1 The origin of normal force oscillations in vertical-slider SWTBs was isolated to be slider friction. Such oscillations, and their negative transient dynamics impacts, can be avoided with a 4-bar mechanism to balance loads and ensure a constant (not oscillating) normal load. If adopted widely, these improved experimental procedures will improve the quality of experiments across the field of terramechanics.

1.6 Publications and conferences

Included in this thesis is research which has been or will be published or presented in the following:

- Journal papers
    1. Niksirat, P., **Daca, A.**, and Skonieczny, K. The effects of reduced-gravity on planetary rover mobility. *The International Journal of Robotics Research*, 39(7), 797-811, 2020.
    2. **Daca, A.**, Tremblay, D., and Skonieczny, K. Experimental evaluation of cone index gradient as a metric for the prediction of wheel performance in reduced gravity. *Journal of Terramechanics*, 99, 1-16, 2022.
    3. **Daca, A.**, Nassiraei, A. A. F., and Skonieczny. Comparison of wheel load application methods in single-wheel testbeds. *Journal of Terramechanics*, 99, 35-55, 2022.
    4. **Daca, A.**, Tremblay, D., and Skonieczny, K. Expansion and experimental evaluation of scaling relations for the prediction of wheel performance in reduced gravity. *Microgravity Science and Technology*. Submitted 2022.
- Conferences (* indicates presenting author)
    - Oral presentations
        1. **Daca, A.*** and Skonieczny, K. Towards improved prediction of lunar rover mobility in reduced gravity. *Canadian Space Agency (CSA) Canadian Lunar Workshop*, Online, June 2021.
        2. **Daca, A.*** and Skonieczny, K. Predicting wheel performance in lunar gravity on cohesionless and cohesive soils. *Canadian Aeronautics and Space Institute (CASI), 21st Astronautics Conference*, Online, November 2021.
        3. Butt, G.*, **Daca, A.**, Aubin-Fournier, P.L., Skonieczny, K. Parabolic Flights with a Single-Wheel Testbed to Study Rover Wheel–Soil Interactions in Lunar Gravity and LMS-1. *Canadian Aeronautics and Space Institute (CASI), 21st Astronautics Conference*, Montreal, Quebec, November 2022.
    - Oral presentations with peer-reviewed papers
        1. **Daca, A.***, Tremblay, D., and Skonieczny, K. The relationship between cone penetration resistance and wheel–soil interactions in lunar gravity. *IEEE Aerospace Conference Proceedings*, Online, March 2021.

2. **Daca, A.***, Nassiraei, A. A. F., and Skonieczny, K. Design and characterization of a 4-bar mechanism to balance normal loads in a single-wheel testbed. *International Society for Terrain-Vehicle Systems (ISTVS) 20th International Conference*, Online, September 27-29, 2021.
3. **Daca, A.*** and Skonieczny, K. Towards improved prediction of planetary rover mobility in reduced gravity. *International Society for Terrain-Vehicle Systems (ISTVS) 20th International Conference*, Online, September 27-29, 2021.
4. **Daca, A.*** and Skonieczny, K. Experimentally evaluating granular scaling laws for predicting lunar-gravity wheel performance in cohesive regolith. *American Society of Civil Engineers (ASCE), Earth and Space 18th Biennial International Conference*, Denver, Colorado, April 2022.
5. Bouton, A.*, Reid, W., Brown, T., **Daca, A.**, Sabzehi, M. and Nayar, H. A Comparative Study of Alternative Rover Configurations and Mobility Modes for Planetary Exploration. *IEEE Aerospace Conference Proceedings*, Big Sky, Montana, United States, March 2023.

– Oral presentations with non peer-reviewed papers

1. **Daca, A.** and Skonieczny, K.* Evaluating 1-g testing methods for predicting planetary rover mobility in reduced gravity. *16th Symposium on Advanced Space Technologies in Robotics and Automation (ASTRA) 2022*, Noordwijk, The Netherlands, June 2022.
2. **Daca, A.***, Skonieczny, K., and Moreland, S. Diagonal grousers improve turning performance in skid-steer rovers. *International Society for Terrain-Vehicle Systems (ISTVS) Americas Symposium*, Montreal, Quebec, Canada, October 2022.

1.7 Outline

The remainder of this thesis is organized as follows: experimental apparatus, along with an investigation into normal force application methods in single-wheel testbeds, are described in Chapter 2. The next three chapters present experimental results evaluating the three rover testing methods described in Section 1.5. Experimental results from a parabolic flight campaign evaluating the method of reduced-weight testing are presented in Chapter 3. In Chapter 4, results from a second parabolic flight campaign evaluating two further rover testing methods (the equal-G method and GSL) are presented. Recent work evaluating the proposed cohesion constraint for GSL, along with plans for an upcoming parabolic flight campaign, can be found in Chapter 5. Then, Chapter 6 presents results from the application of the GSL method to rover test campaigns as part of the JPL Visiting Student Research Program (JVSRP) at NASA's Jet Propulsion Laboratory. Finally, conclusions, future work, and recommendations for 1-g rover testing are presented in Chapter 7. The work in this thesis can be divided into sub-topics as shown in Figure 5, where the major topics studied are highlighted in green.

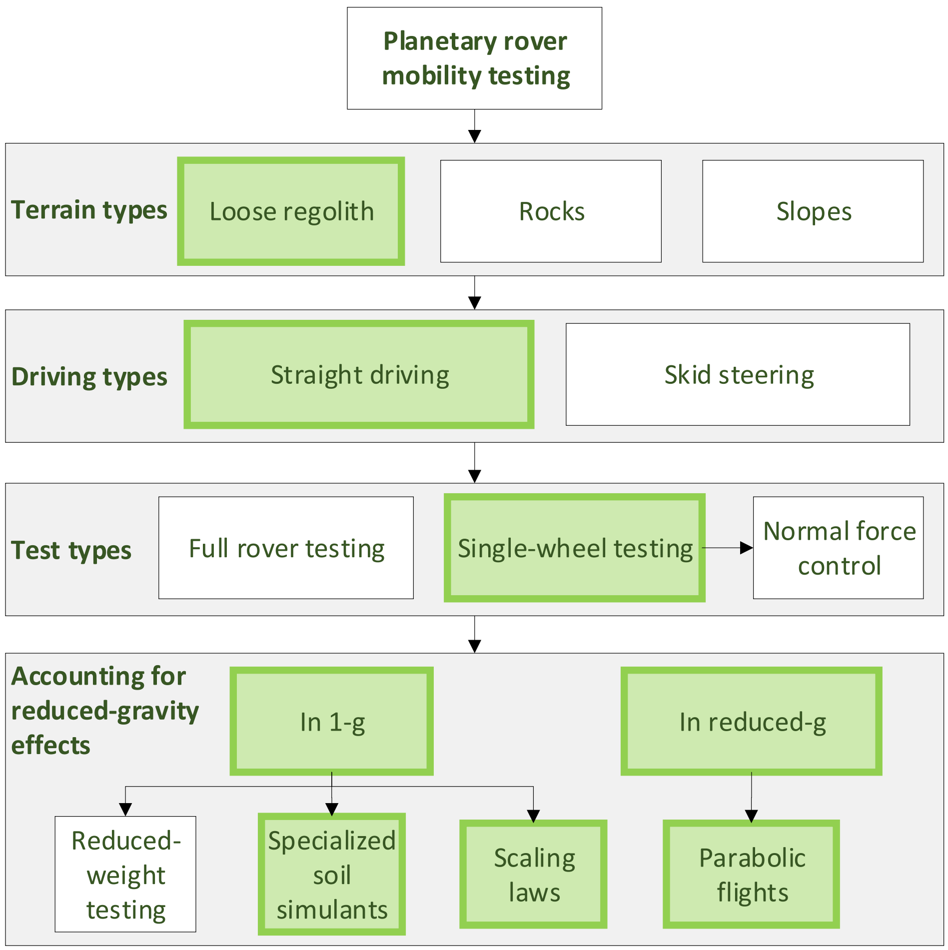

Figure 5: Diagram depicting the topics studied herein, with major topics highlighted in green.

Chapter 2

Experimental Apparatus

Experimentation is central to this thesis, both in reduced gravity and in 1-g. This chapter details the experimental apparatus and key experimental techniques used throughout this work. Section 2.5 also presents a detailed characterization of normal force application methods in wheel–soil experiments, published by the author in [128] and listed in Section 1.5 as contribution 3.

2.1 Single-wheel testbeds

Concordia University has two single-wheel testbeds (SWTBs). One is a larger, stationary SWTB—dubbed the laboratory SWTB. The second is a smaller, portable SWTB that was designed to meet the requirements imposed by reduced-gravity parabolic flights [124]. Thus, it is referred to as the parabolic flight SWTB. These SWTBs are described in detail below.

2.1.1 Laboratory SWTB

The laboratory SWTB, shown in Figure 6, consists of a 2.2m$\times$2.2m sandbox and a Macron Dynamics MCS-UC2-XYZ robotic gantry that can control the position of the wheel unit along the X and Y axes shown in the figure, along with its orientation around the Z axis. The wheel unit is free to move along the Z axis which is an assembly of extrusions guided by linear bearing rails (see Figure 7). The wheel axis is driven by a Maxon RE35 motor and MaxPos 50/5 driver, and the vertical load is controlled by a counterweight system with pulleys. Sinkage is measured using a TE Connectivity SP2-25 string potentiometer. Drawbar pull and normal force data are measured using an ATI Delta IP60 6-axis force/torque sensor with National Instruments USB-6210 data acquisition system. The laboratory SWTB also has a glass sidewall through which subsurface wheel–soil interactions could be filmed.

For experiments comparing the parabolic flight SWTB to the laboratory SWTB (presented in Section 2.5), a small box, shown in Figure 8, was placed in the bigger sandbox to replicate the dimensions of the parabolic flight SWTB (see Section 2.1.2). For these experiments, the wheel was driven through the smaller box, against the glass wall, in order to replicate the conditions of the parabolic flight SWTB experiments as closely as possible. The dimensions of this box (298 mm $\times$ 914 mm) are very close to those of the parabolic flight SWTB (200 mm $\times$ 900 mm). However, this box had to be slightly larger in order to accommodate the tamper used for soil preparation

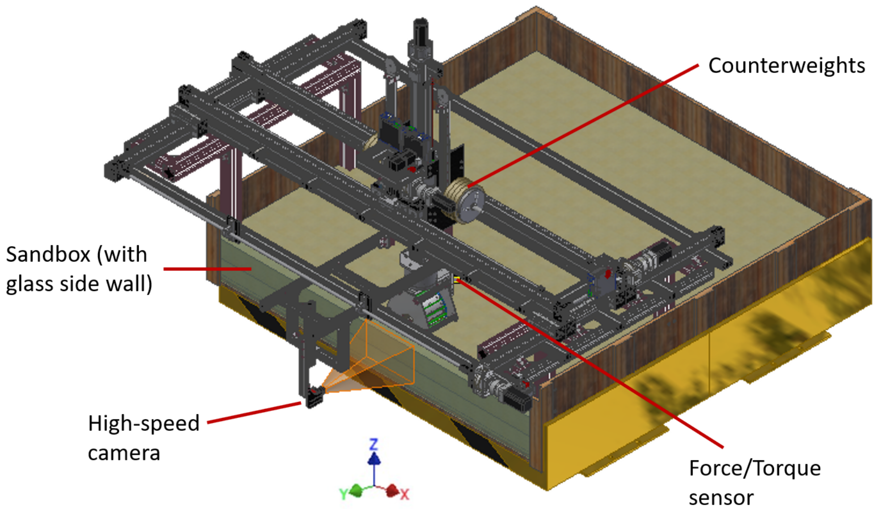

Figure 6: Design of laboratory SWTB with key functional elements identified.

(also shown in Figure 8). Additionally, the sand depth was between 290 mm and 340 mm, which is deeper than the 240 mm found to be sufficient to minimize boundary effects in the soil used, GRC-1, which is described in Section 2.3.2 [2].

4-Bar Mechanism

A 4-bar linkage, shown in Figure 9, was designed to reduce friction in the vertical axis by employing hinges that rotate freely, with the goal of balancing loads to ensure that a constant normal force is applied to the wheel. It consists of an inner frame and an outer frame that are connected by hinges. The force/torque sensor is connected to the wheel on one side and the inner frame of the 4-bar linkage on the other. The outer frame is connected to the robotic gantry by another set of hinges. As the wheel sinks, the angle of the outer frame increases with respect to the horizontal, whereas the inner frame remains level, as shown in Figure 10. This allows the wheel to translate in the vertical direction independently of the testbed's vertical axis. For the experiments utilizing the 4-bar mechanism and the rigid wheel, one of the counterweights was relocated and used as a deadweight on top of the wheel (also shown in Figure 9) in order to achieve the desired load.

Figure 11 illustrates how the laboratory SWTB can mimic skid-steer maneuvers by fixing the wheel at an angle relative to its forward trajectory. Figure 11a shows that in a point turn, each wheel moves at an angle β relative to its forward/aft axis (tangent to the circle tracing the rover wheels' trajectory). This angle will remain constant throughout the point turn. In single wheel tests, the wheel is fixed at angle β while it is moved forward in a straight path at a constant velocity while simultaneously rotating at a constant angular velocity. This represents skid-steer turns at fixed slip ratios. Also seen in Figure 11b is a modified 4-bar mechanism that operates similarly to the one shown in Figure 9, but allows for lower wheel loads by virtue of a counterweight system attached to the 4-bar mechanism.

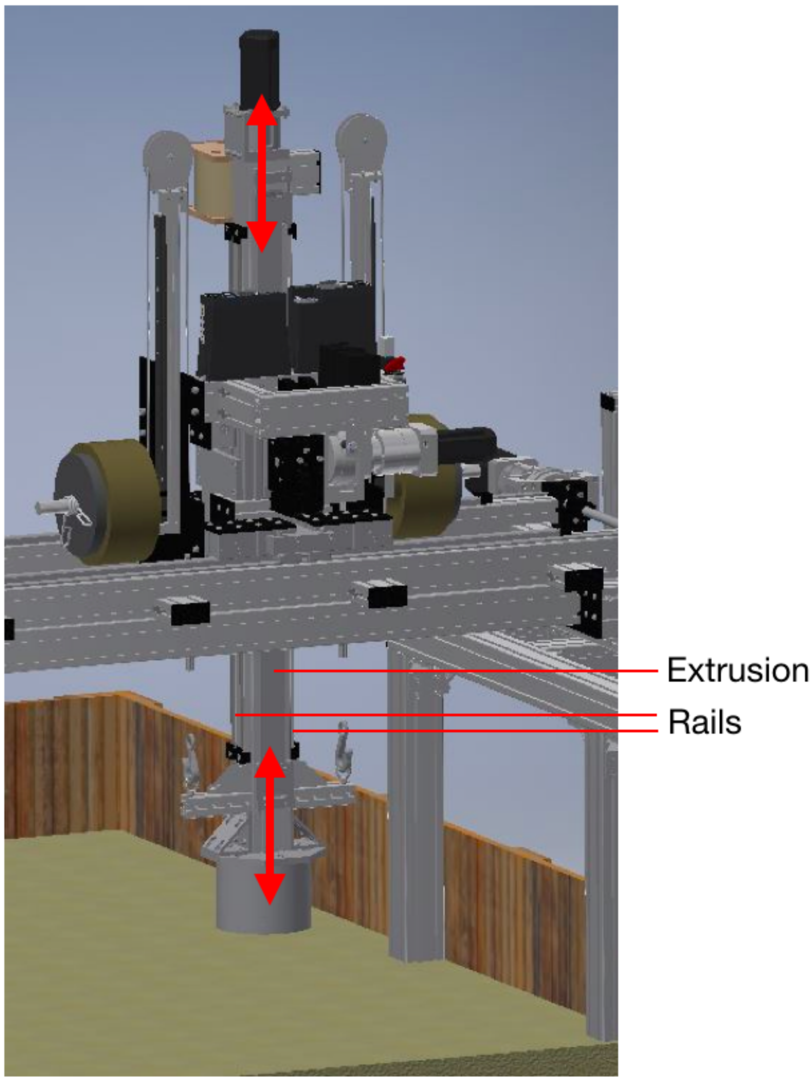

Figure 7: Illustration of the motion of the laboratory SWTB's vertical axis. The entire extrusion assembly moves up and down, kept neutrally balanced by the counter weights located on each side of the vertical axis.

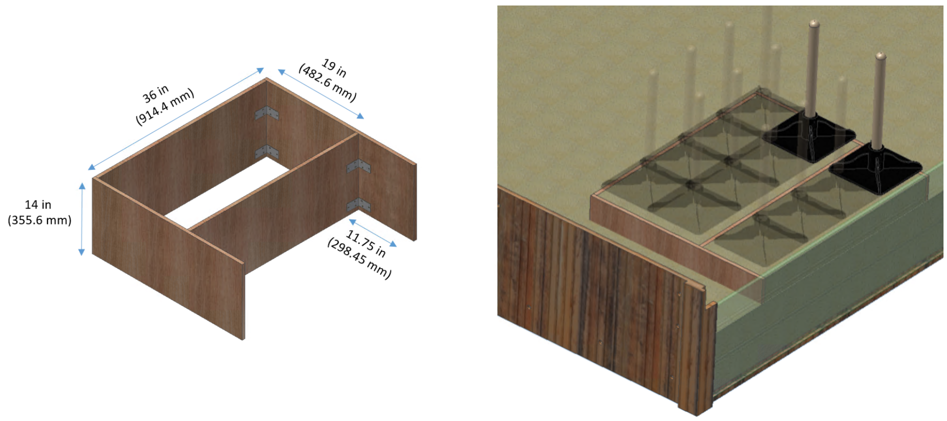

Figure 8: Small box that was placed in the large sandbox to replicate the dimensions of the parabolic flight SWTB. Terramechanics experiments were completed with the wheel against the glass sidewall (in the smaller part of the wooden box). The tamper used for soil preparation is also shown to illustrate its dimensions.

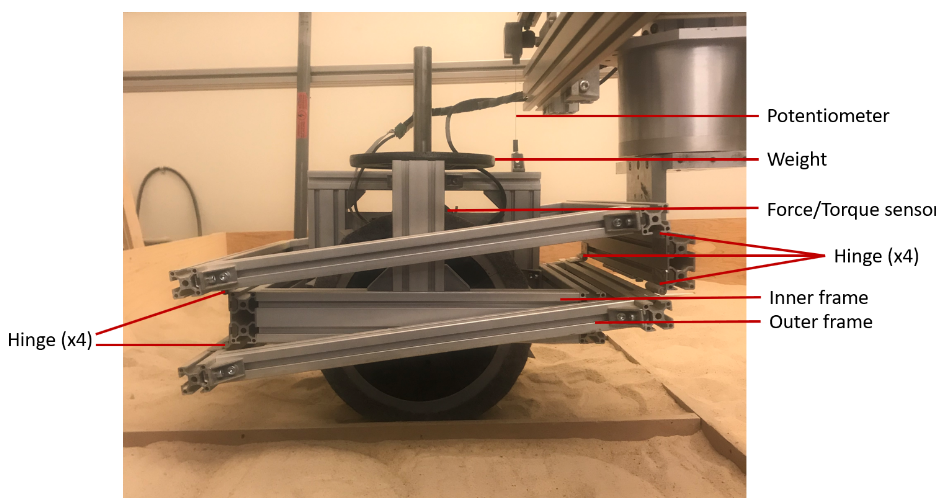

Figure 9: 4-bar mechanism mounted on the robotic gantry in the laboratory SWTB. Note that only the hinges visible in the image are labelled.

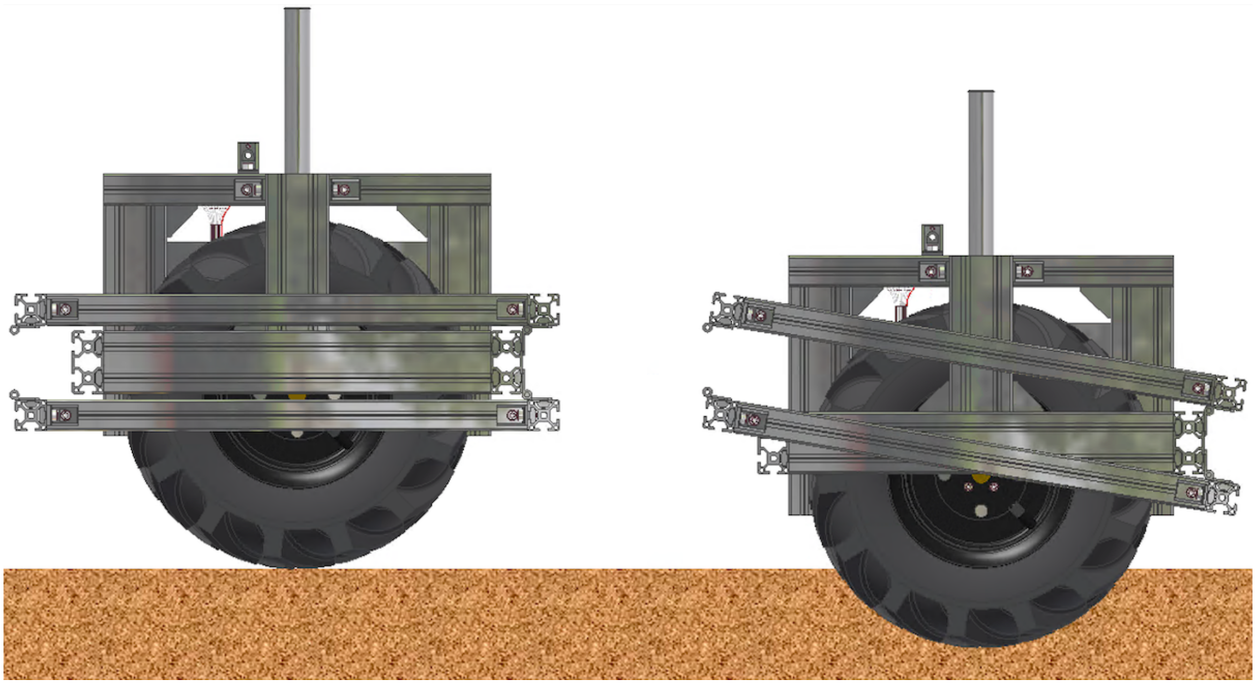

Figure 10: Diagram illustrating how the 4-bar mechanism's hinges rotate as the wheel translates vertically, allowing the wheel to translate in the vertical direction independently of the testbed's vertical axis.

2.1.2 Parabolic flight SWTB

A specialized robotic test apparatus was previously developed to meet the constraints imposed by reduced-gravity parabolic flights [124]. Accordingly, this apparatus is referred to as the "parabolic flight SWTB". In the parabolic flight SWTB, a wheel is driven through a 900 mm (L) $\times$ 200 mm (W) $\times$ 290 mm (approximate soil depth) instrumented sandbox that collects data including drawbar pull, vertical wheel displacement (i.e. sinkage), normal force, and motor current. The wheel slip is controlled via synchronized control of a horizontal linear actuator and a wheel motor. The wheel is allowed to move freely in the vertical direction, via a Misumi SSELBWZ16-230-MC linear guide, while a vertical load is applied. The parabolic flight SWTB also has the capability to record video of subsurface wheel–soil interactions through a transparent window that the wheel is driven against. Additionally, the parabolic flight SWTB performs automated soil preparation, which consists of loosening and compacting the soil to a repeatable state. Loosening is performed by blowing air through manifolds at the bottom of the sandbox, and compaction is achieved with a Martin NTS 50/04 non-impacting pneumatic vibrator. This system is also robust to in-flight vibrations. Skonieczny et al. [155] presented a detailed analysis of the repeatability of this soil preparation system including a comparison of cone penetrometer measurements taken in flight and on the ground.

The automated soil preparation subsystem was upgraded relative to previous experiments [5, 155]. One recent improvement was the addition of a porous plastic sheet (Porex) to the bottom of the sandbox (as opposed to individual valves used initially), as described in [156]. This allows for more uniform airflow distribution during the loosening stage of soil preparation (which is achieved

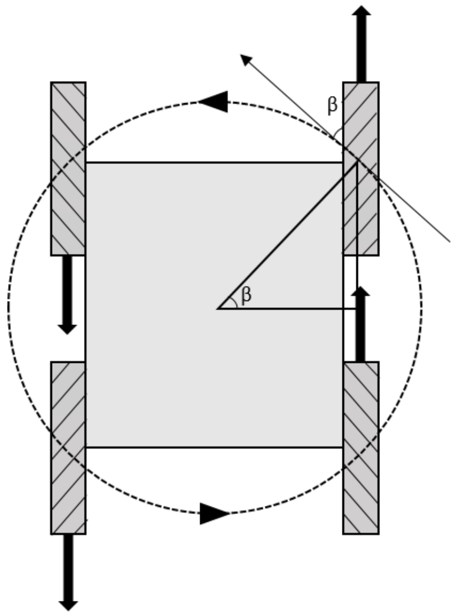

(a) Skid-steer rover viewed from below. In a point turn, each wheel moves at an angle β relative to its forward/aft axis.

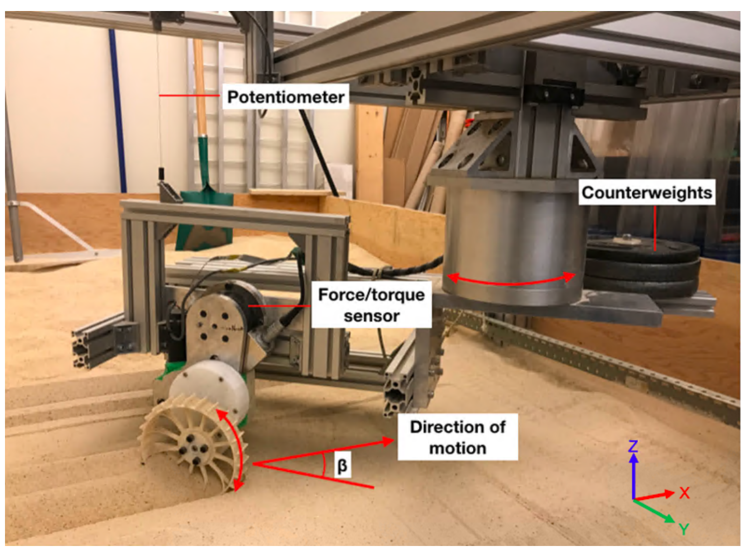

(b) Modified 4-bar mechanism with counterweights attached to the 4-bar allowing lower wheel loads to be achieved.

Figure 11: The laboratory SWTB can be used to mimic skid steer maneuvers by fixing the wheel at an angle relative to its forward trajectory.

by blowing compressed air through manifolds in the bottom of the sandbox), further refining the uniformity and consistency of the soil preparation.

The parabolic flight SWTB is shown in Figure 12 with key elements identified. The wheel axis is driven by a Maxon RE35 motor and MaxPos 50/5 driver, and horizontal motion (along X as defined in the figure) is achieved by a Macron Dynamics R6S linear actuator driven by a Kollmorgen AKM23C motor and AKD-P00306 driver. The motions of the two axes are coordinated using a Trio MC4N ECAT. Vertical (Z) wheel loading is controlled by a pair of SMC Pneumatics MQQLB25-100D pneumatic cylinders, which allows for system compactness as well as the ability to automatically set the wheel load. The pressure in the pneumatic cylinders is controlled by an Equilibar QB4 digital pressure regulator with a time constant on the order of 100 ms. Force/torque data are collected using an ATI Delta IP60 with a National Instruments USB-6210 data acquisition system, and the vertical (Z) wheel displacement is measured using a 100 mm ALPS 10 kOhm slide potentiometer.

Images are captured using an IO Industries Flare 4MP monochrome camera with 16 mm EFL f/1.4 lens and Core2 digital video recorder. The camera observes soil motion through a glass sidewall in the sandbox via a mirror tilted at 45 degrees, for the sake of system compactness and vibration reduction. The images are captured, processed, and analyzed using the Soil Optical Flow Technique (SOFT) [157].

For testing a 1/6-scaled wheel (see Chapter 5), a modified apparatus was needed. The 1/6-scaled wheel is driven by a Nema 17 stepper motor with a TB6600 driver. Force/torque data are collected using an ATI Nano25 IP65 with a National Instruments USB-6210 data acquisition system. Vertical (Z) wheel displacement is measured using a TE Connectivity SP2-25 string potentiometer, and the vertical loading is achieved with system self-weight. A 4-bar mechanism similar to the one in the laboratory SWTB only much smaller, shown in Figure 13, allows vertical motion for the 1/6-scaled wheel along with its motor and F/T sensor.

Cone Penetrometer

A cone penetrometer is an instrument used to measure a soil's compaction and shear strength versus depth, and is widely used in the field of geotechnical engineering. This instrument has particular relevance to the study of soil properties in reduced gravity because in situ cone penetrometer measurements were taken during the Apollo missions to the Moon; thus, cone penetrometer measurements are usually incorporated into reduced-gravity soil studies due to the availability of this reference data. Additionally, it has been widely used by the U.S. Army to provide a "go/no-go" assessment of terrains for off-road vehicle travel [158].

A cone penetrometer consists of a cone on a long shaft that is inserted into the ground. The pressure required for insertion (denoted cone index, CI) at a constant speed (typically about 30 mm/s) is measured versus depth.

Previously, a Rimik CP40ii cone penetrometer was mounted to the test apparatus, but due to difficulties automating the device as well as interference of test apparatus components with the ultrasonic depth sensor, the author opted to use an ATI Delta IP60 force/torque sensor attached to the cone shaft, as seen in Figure 12b, to measure cone index (measured in kPa—calculated as force divided by cone base area—in this case a 323 mm^2 cone was used) and motor encoder data to obtain depth information. A standard 30° cone with 323 mm^2 surface area (the same design used for characterization of GRC-1 [159]), and 30 mm/s penetration rate were used in all tests.

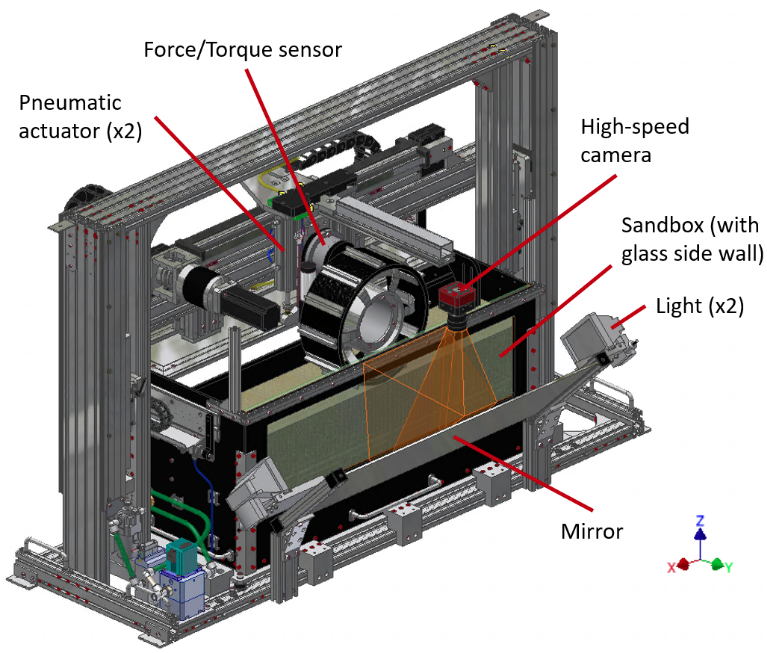

(a) Automated test apparatus configured for wheel testing.

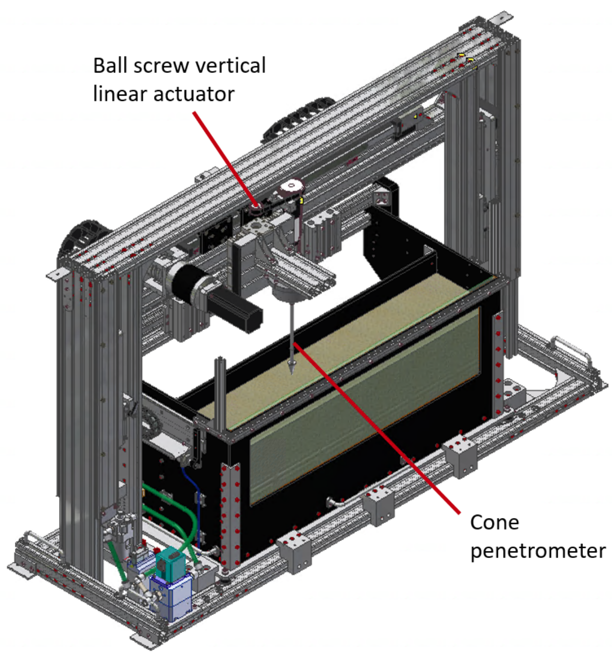

(b) Automated test apparatus configured for cone penetrometer testing.

Figure 12: Design of specialized SWTB for parabolic flights with key functional elements identified.

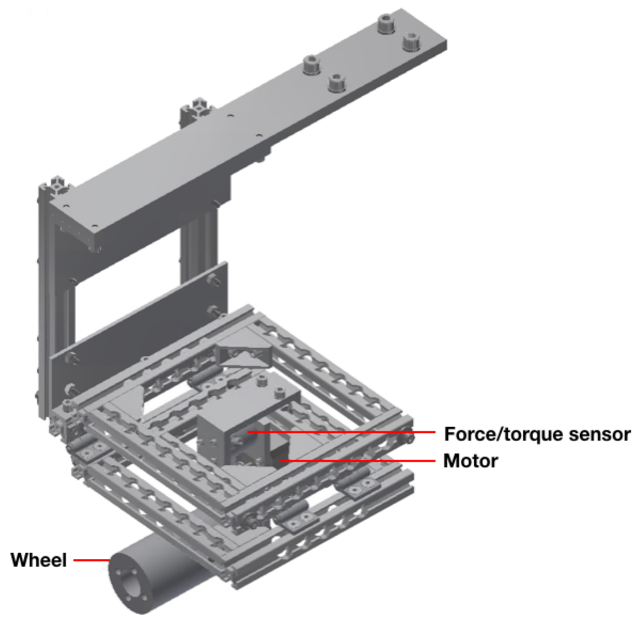

Figure 13: Lightweight apparatus for 1/6-wheel testing. A 4-bar mechanism allows vertical motion for the scaled wheel, motor, and F/T sensor.

2.2 Wheels

2.2.1 Clearpath Husky A200 wheel

A wheel from a Clearpath Husky A200 robot was used for the first set of experiments described in Section 2.5 (evaluation of the laboratory SWTB with and without the 4-bar mechanism). This wheel, a 330 mm lug tread pneumatic tire, was previously used for experiments in the laboratory SWTB for comparison to field tests using the Husky [160], and is shown in Figure 14.

2.2.2 Rigid wheels

A simple rigid wheel, shown in Figure 15, was used in the second set of experiments described in Section 2.5 (comparison of the laboratory SWTB with the 4-bar mechanism to the parabolic flight SWTB). This wheel was 3D printed out of PLA in four separate parts (due to printer size limitations) and has 12 removable grousers. A simple rigid wheel was desired for these experiments in order to facilitate analysis of time-series data (i.e. to avoid data complexities due to wheel flexibility). The wheel is 300 mm in diameter and 125 mm wide.

During initial testing of this wheel in the parabolic flight SWTB, some of the larger soil particles became lodged between the wheel and the glass, causing significant scratching of the glass. To prevent this from recurring, a ring of felt with adhesive backing was affixed to the side of the wheel, as seen in Figure 16.

To experimentally evaluate granular scaling laws (GSL) in GRC-1 (see Chapter 4), the rigid wheel shown in Figure 15 was used (without grousers, in order to simplify future numerical modeling) in effective lunar gravity, and a second, smaller rigid wheel was printed for use in 1-g experiments, shown in Figure 16. The smaller wheel has 1/2 the radius and 2/3 of the width of the

Figure 14: Husky wheel used in the evaluation of the 4-bar mechanism in the laboratory SWTB (see Section 2.5).

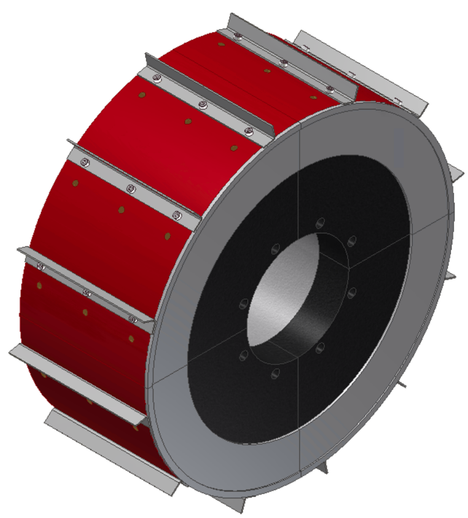

Figure 15: Rigid wheel with removable grousers (shown here with grousers attached) used in the comparison of the laboratory SWTB with the 4-bar mechanism to the parabolic flight SWTB (see Section 2.5).

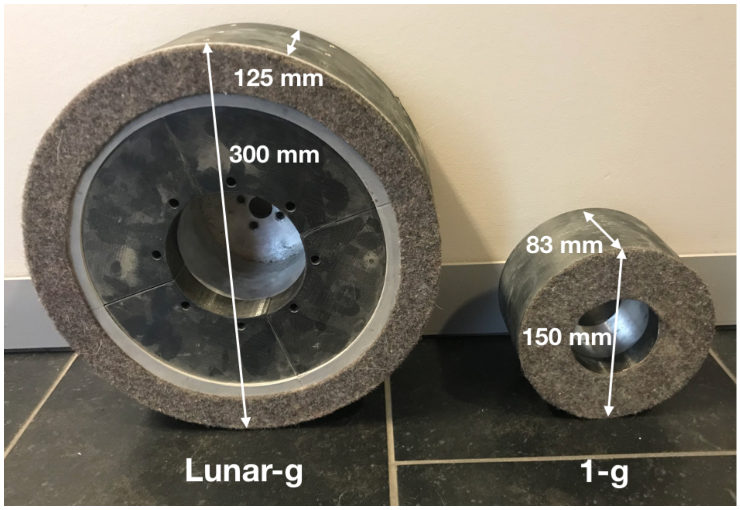

Figure 16: Smaller wheel used in 1-g (right) to predict performance of a larger wheel in lunar-g (left).

original wheel. The selection of these dimensions is discussed further in Section 4.1.2.

Next, to test a proposed cohesion constraint for GSL (see Chapter 5), sleeves with grousers were printed for the two wheels in Figure 16, and a smaller wheel with 1/6 the radius of the large wheel was printed, shown in Figure 17. There are 24 grousers on each wheel. The grousers on the large wheel are 21 mm long and 9 mm wide. The grousers on the 1/2-scaled wheel are 10.5 mm long and 4.5 mm wide, and the on the 1/6-scaled wheel they are 3.5 mm long and 1.5 mm wide. For these tests, grousers were used in order to increase the signal-to-noise ratio of the drawbar pull measurements for the 1/6-scaled wheel.

The surfaces of these PLA-printed wheels are not perfectly smooth, as seen in Figure 18, which shows a close-up of the wheel surface texture as printed. In Figures A.4, A.5, and 50 to 53, it can be seen that the surface roughness was sufficient to cause significant soil motion beneath the wheel, and the velocity of soil close to the wheel was equal to the speed of the wheel rim, as expected.

2.2.3 Rosalind Franklin rover wheel

The experiments reported in Chapter 3 studied the performance of a prototype wheel, designed and developed by MDA, for the European Space Agency (ESA) Rosalind Franklin rover (part of the ExoMars mission). The Rosalind Franklin wheel has a unique flexible design consisting of a high-strength stainless steel sheet metal rim with two sets of leaf-springs for impact energy absorption. This wheel is 285 mm in diameter and 120.8 mm in width, with 12 grousers (Figure 19).

2.2.4 Skid-steer rover experimental wheels

To evaluate wheel design changes to reduce sinkage and improve skid-steer performance for a potential future NASA JPL lunar rover (see Chapter 6), seven different wheel designs were 3D-printed (ABS), shown in Figure 20. Wheel #1 is the current baseline for the rover, which is a rigid 150 mm diameter, 30 mm wide wheel with 27 grousers that are 8 mm long. The remaining wheel designs were intended to reduce sinkage. Wheel #2 is the same as the baseline wheel but with

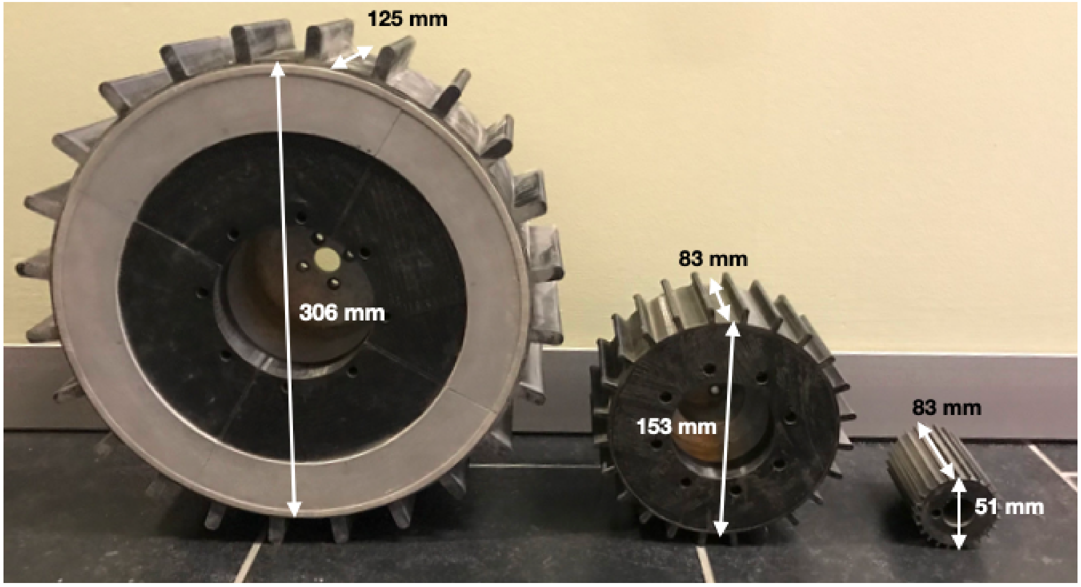

Figure 17: Scaled wheels used in 1-g to test a cohesion constraint for GSL.

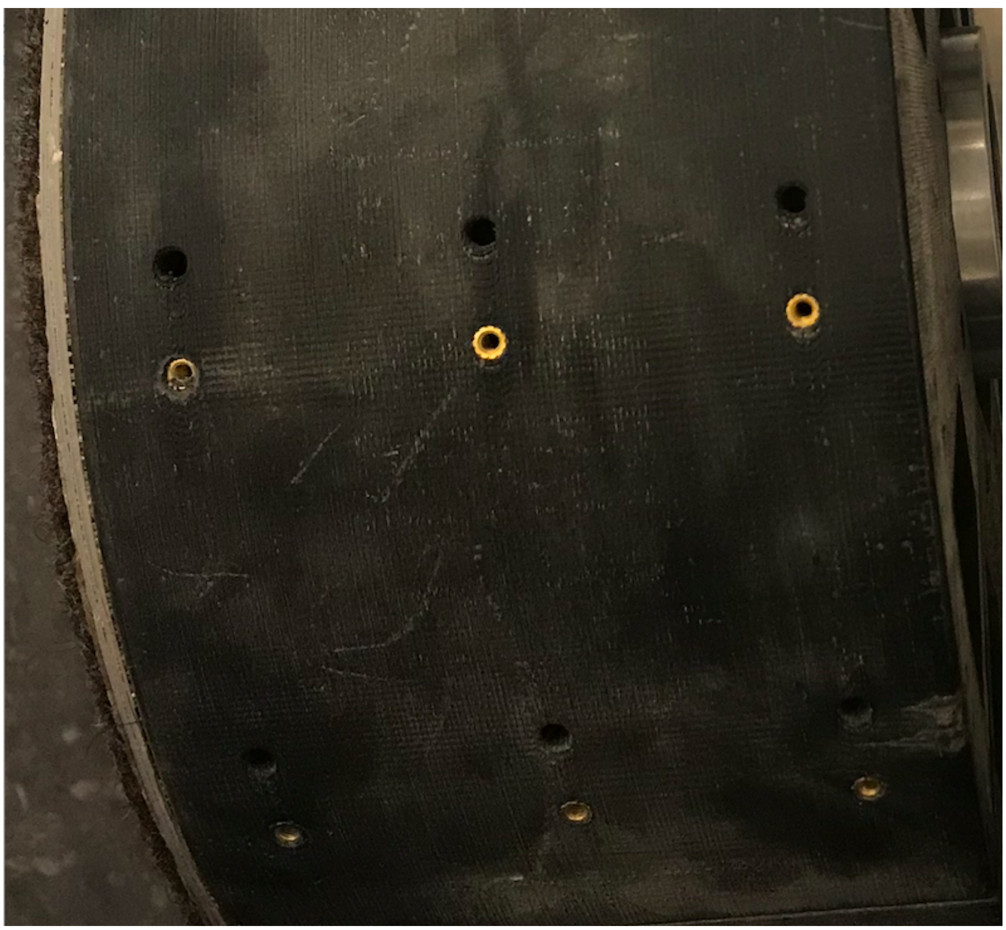

Figure 18: Close-up of the wheel surface texture as printed.

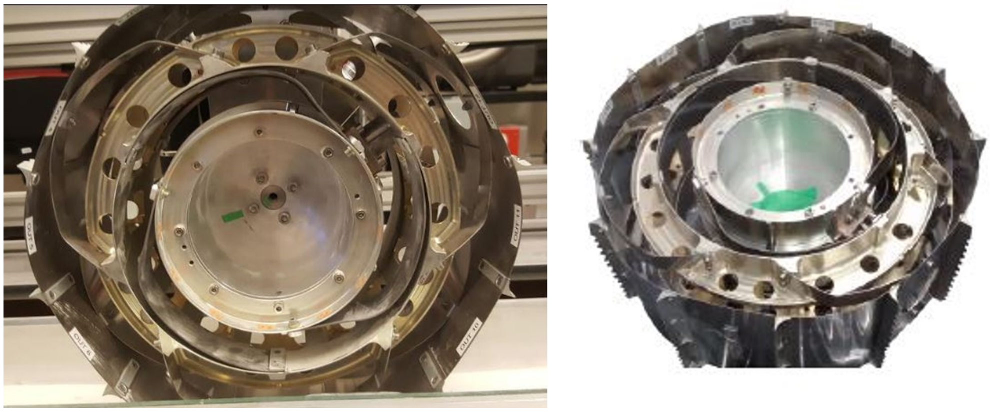

Figure 19: A prototype of the Rosalind Franklin rover flexible wheel.

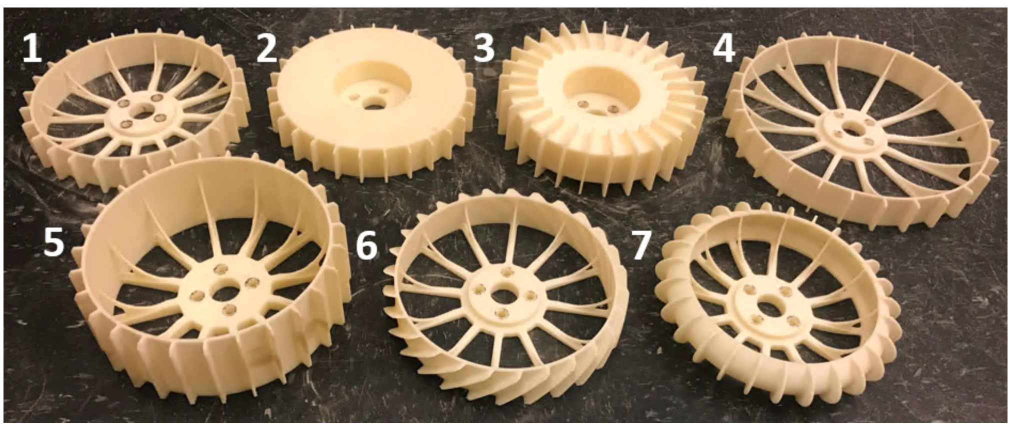

Figure 20: Photo of the seven 3D-printed wheel designs that were tested for a potential future lunar rover.

closed sides; it was theorized that this may reduce sinkage by preventing soil from passing through the wheel. Wheel #3 is the same as wheel #2 but with side grousers; this design was meant to prevent soil from passing through the wheel while also providing additional traction with the side features. Wheels #4 and #5 are the same as wheel #1 but larger in diameter (200 mm) and in width (60 mm), respectively; these designs are meant to decrease sinkage by increasing the size of the contact patch, thereby decreasing the contact pressure of the wheel. Wheel #6 is the same as wheel #1 but with the grousers angled at 45°; this wheel design is meant to increase turning efficiency by positioning the grousers perpendicular to the wheel's direction of motion in a point turn, as shown in Figure 11a. The angle of 45° was chosen based on the geometry of the rover as shown in the diagram. A similar design had previously been used on JPL's cancelled Nanorover [161]. Wheel #7 is the same as wheel #1 but with a rounded profile; similar to wheels #2 and #3, this design is meant to prevent soil from passing through the wheel. It should be noted that the grouser height and count had already been optimized using previously established methods [162].

2.3 Soil simulants

Soil simulants are terrestrial materials that are meant to replicate the mechanical and/or chemical properties of extraterrestrial regolith. In this section, the various soil simulants used throughout this research are described along with their properties relevant to terramechanics. See Section 1.2.3 for an introduction of relevant soil properties of simulants.

Note that in our experiments, the soil is prepared such that its density is approximately constant with depth. In contrast, on the Moon and Mars, density tends to increase with depth [163, 164, 165]. The soil is approximately 30 cm deep in our experiments; thus, our tests can be considered to be representative of driving over a 30 cm layer of regolith on top of bedrock (represented by the hard surface at the bottom of the testbed).

2.3.1 ES-2

ES-2 is a martian soil simulant developed by the European Space Agency (ESA). It is a very fine sand with particle sizes between 30 and 125 microns, designed to be representative of loose soils found in many locations on Mars (e.g. between sand dunes) [166]. Characterization of ES-2 via direct shear tests showed that the friction angle was similar in all densities tested (37° to 42°). The soil was also found to have low cohesion [166], which is difficult to measure precisely [167]. For planetary rover testing, ESA recommends a bulk density of 1.45 ± 0.025 g/cm^3 to represent an average soil strength occurring on Mars.

2.3.2 GRC-1

Glenn Research Center lunar soil simulant #1 (GRC-1) was developed to match the in-situ cone penetrometer measurements obtained during the Apollo missions [2]. The main assumption in the design of GRC-1 was that rover performance correlates with cone penetrometer measurements. The idea was that by preparing GRC-1 to different densities, and matching the cone penetrometer measurements to those taken during Apollo, then rovers can be more accurately tested on Earth using this new simulant.

GRC-1 was designed as a frictional, cohesionless mixture of readily available manufactured sand that is prepared to a particle size distribution that is similar to the coarse fraction of lunar soil (particles $< 75\mu$m were excluded in order to prevent dust generation). By varying the relative density (see Section 2.4.2) of this simulant, different cone index profiles (see Section 2.4.3) can be achieved. By preparing GRC-1 to different densities, different cone index gradient (G) values can be achieved that match various Apollo measurement locations.

Two assumptions were made in the design of GRC-1:

1. Cone index gradient (G) values derived from cone penetrometer measurements from the lunar surface are relatively insensitive to cohesion, and highly sensitive to the frictional component of terrain strength.

2. If a dry, granular terrain is designed to match G values from the lunar surface, then the material will also respond similarly to vehicle loading in terms of compaction and shear resistance, which control vehicle mobility.

Table 2: Variation in the friction angle of GRC-1 with density (adapted from [2]).

Average density, ρ (g/cm^3)	Relative density, D_R (%)	Friction angle, ϕ (°)
1.60	0.00	29.8
1.64	15.90	33.3
1.71	41.92	33.8
1.76	59.25	38.4
1.82	78.78	44.4

The first assumption has been shown to be true, at least in Earth gravity, by measurements in dry desert sand showing that small changes in the friction angle produce large changes in the cone index [168], and measurements in clay indicating that small changes in cohesion forces in the range that may exist on the lunar surface (0.1–1 kPa [163]) do not significantly affect cone index measurements [169].

The second assumption is based on the experimental and theoretical work of Bekker [170, 171] as well as a US Army Waterways Experiment Station report [25]. Bekker argued that vehicle mobility on any planet should be determined by the terrain's stress–strain relationships in compaction and shear. He posited that two terrains that have the same measured response to compaction and shear loading would have analogous wheel sinkage (which he related to compaction strength) and wheel slip (which he related to shear strength). Although a cone penetrometer cannot independently determine compaction and shear strength, the cone index gradient (G) was chosen as the indicator of these terrain properties in the development of GRC-1, since the only terrain property measurements available from the Apollo missions are those obtained from a cone penetrometer. In the US Army Waterways Experiment Station (WES) report [25] cited in [2], a slight increase in drawbar pull coefficient is seen for a 4×4 vehicle driving on wet sand with a higher cone index gradient versus loose, dry sand with a lower cone index gradient. However, there are only two data points, and the comparison was done between wet sand and dry sand (rather than dry sand with two different cone index gradients, which would be more applicable to GRC-1). In another WES report [172], a weak correlation between drawbar pull and G is shown, however, there are not enough data points for this to be considered conclusive. The work in [2] relies heavily on these WES reports as evidence for the relationship between G and drawbar pull, despite the fact that the evidence they provide is not very substantial. Additionally, there was no investigation into sinkage behaviour versus G, and even if G is a good indicator of vehicle mobility on Earth, there is still no evidence that gravity does not have additional effects on wheel–soil interactions that would go undetected using only a cone penetrometer.

Nevertheless, due to its relatively low cost and availability in large quantities, GRC-1 is commonly used as a lunar terramechanics simulant. As mentioned previously, GRC-1 is essentially cohesionless, and its friction angle depends on its bulk density as shown in Table 2.

2.3.3 LMS-1

Particle shape is another important factor in determining a soil's shear strength. As seen in Figure 21, lunar regolith is more angular than GRC-1, thus it has more interlocking forces between particles, and therefore higher shear strength [163]. Exolith Lab's Lunar Mare Simulant #1 (LMS-1)

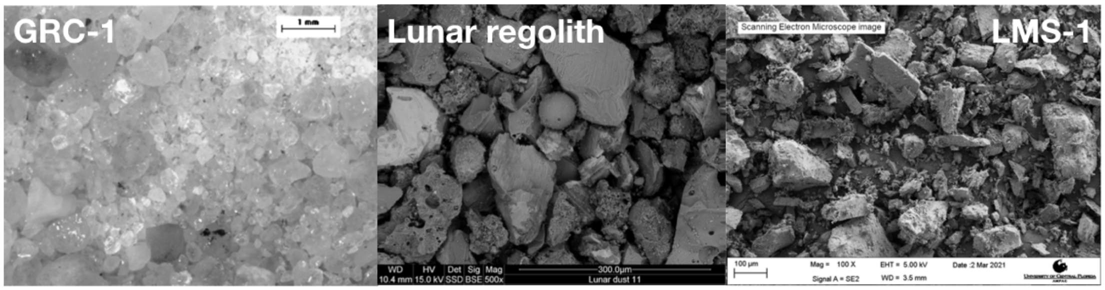

Figure 21: Left: GRC-1 grain geometry and particle size [2], middle: Scanning electron microscope (SEM) image of Apollo 12 sample [3], right: SEM image of Lunar Mare Simulant #1 (LMS-1) [4].

is a lunar soil simulant that was designed to match the texture of lunar regolith by combining mineral and rock fragments in accurate proportions, as well as to match the particle size distribution of returned lunar samples [4]. Thus, it also has higher shear strength in comparison to GRC-1. LMS-1 is a mineral-based simulant meant to replicate the mechanical and chemical properties of an average mare location on the Moon. The minimum bulk density of LMS-1 is estimated to be between 1.37 g/cm^3 [173] and 1.56 g/cm^3 [174]. The cohesion and friction angle of loose LMS-1 (measured via direct shear testing) are 0.341 ± 0.022 kPa and $49.63 \pm 3.89°$, respectively [173]. The current best estimates of the cohesion and friction angle of lunar regolith are 0.1–1 kPa and 30°–50°, respectively [163]. Measurements of the friction angle and cohesion of LMS-1 at higher densities are not yet available in the literature. However, since cohesion is expected to increase with density, and tests performed in this research were at a higher density than that used for the cohesion measurements in [173], it is estimated that the cohesion of LMS-1 is between 0.341 and 1 kPa at the density used in this research.

2.4 Experimental parameters

This section introduces experimental inputs and outputs relevant to the experiments described throughout this thesis, starting with inputs that apply to both cone penetrometer and wheel experiments, namely effective gravity and soil density. Then, inputs and outputs specific to each type of experiment are described.

2.4.1 Input: Effective gravity (g)

The experimental apparatus described in Section 2.1.2 was flown aboard Canada's National Research Council's (NRC) Falcon 20 aircraft. To achieve effective partial gravity, the aircraft performs ascent and descent flight maneuvers as shown in Figure 22c. A partial gravity environment is maintained for approximately 20–30 seconds during each parabola, which occurs between two 2-g maneuvers. Longitudinal (A_x), lateral (A_y), and vertical (A_z) acceleration were measured with an inertial measurement unit (IMU) during the flights. In Figure 22, it can be seen that lateral and longitudinal accelerations are almost zero during the partial gravity parabola, indicating that it is not necessary to account for accelerations in directions other than A_z.

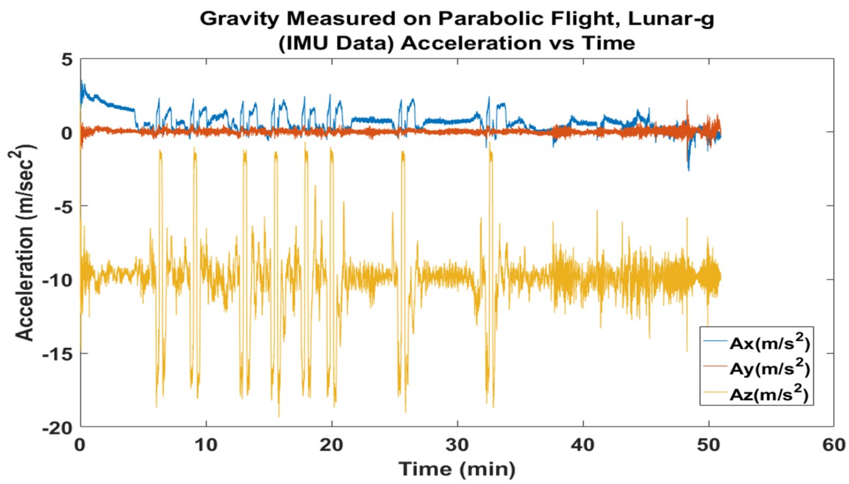

(a) Effective lunar-g

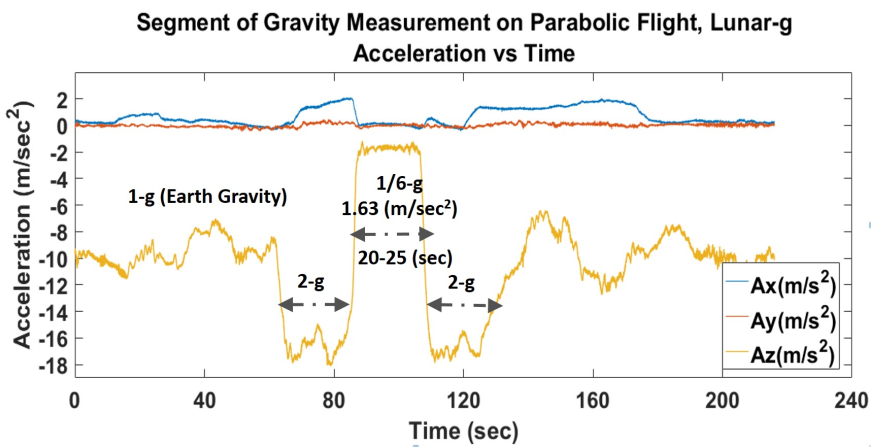

(b) A segment of effective lunar-g

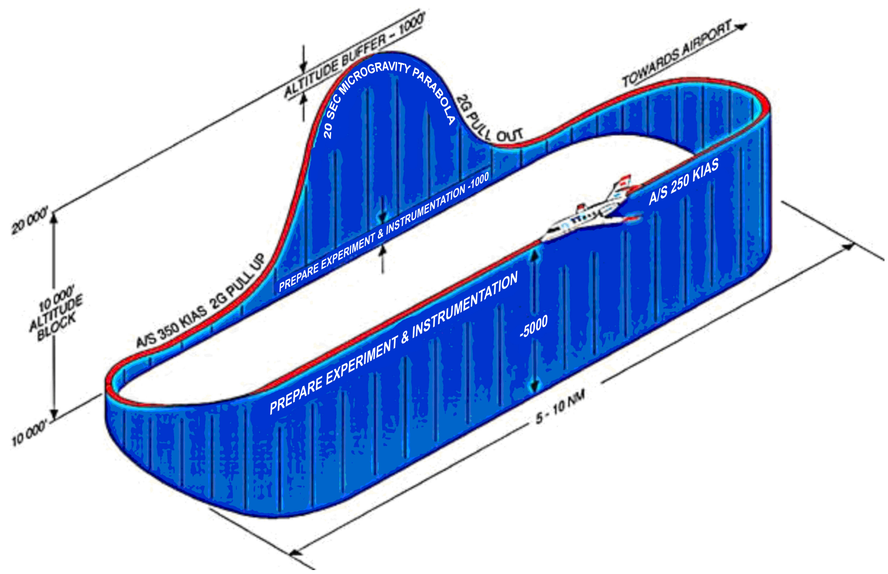

(c) A parabolic maneuver

Figure 22: Parabolic flights: (a) lunar-g flight with zoom-in (b) on one parabola; (c) partial gravity flight trajectory including a reduced-g parabola as well as an experiment and instrumentation preparation phase between parabolas [5].

2.4.2 Input: Soil density (ρ)

Soil density is another important input to wheel–terrain interaction studies. As discussed in Section 1.2.3, a soil's density affects its shear strength, and thus its response to vehicle loading. In order to ensure consistency between tests, the soil must be prepared to a repeatable state between each experiment. In the laboratory SWTB, this is done manually by loosening with a shovel, compacting with a tamper, and then leveling with a blade. This procedure had previously been used with GRC-1 and is described in detail by Creager et al. [175] and Woodward [176].

The parabolic flight SWTB has an automated soil preparation system, described in Section 2.1.2. Soil preparation settings for each set of experiments are described in their respective chapters.

2.4.3 Cone penetrometer experiments

Output: Cone index gradient (G)

The output of the cone penetrometer experiments is the cone index gradient, G, derived from cone index (CI) versus depth. G is calculated using Equation 5 [158]:

$$\mathrm{G} = \frac{\sum_{i=1}^{n}(d_i - \overline{d})(CI_i - \overline{CI})}{\sum_{i=1}^{n}(d_i - \overline{d})^2} \tag{5}$$

where n is the number of measurements in an insertion, i is the measurement number, d_i and CI_i are the depth and cone index at point i, respectively, and $\overline{d}$ and $\overline{CI}$ are the mean of all the depth and cone index values measured in the insertion, respectively.

2.4.4 Wheel experiments

For wheel experiments, the outputs of the system include the measured drawbar pull (F_{DP}), measured sinkage (z), and high speed images of the wheel–soil interactions. Motor velocities and currents are also collected. The wheel motor current is used to calculate the power, P, required to spin the wheel. The velocity from both the linear actuator motor and wheel motor can be examined together to verify the commanded slip.

Input: Wheel load (W)

Wheel load is another parameter that affects traction, and thus rover mobility. The wheel load, W, is the sum of the wheel unit weight and applied force on the wheel unit. In the laboratory SWTB (Section 2.1.1), the wheel load is controlled via a counterweight system while a 4-bar mechanism allows the wheel to move freely in the vertical direction. When testing larger wheels in the parabolic flight SWTB (Section 2.1.2), the wheel load is applied using a set of pneumatic cylinders and a digital pressure regulator. When testing smaller wheels in the parabolic flight SWTB, the wheel load is achieved using system self-weight, and a 4-bar mechanism allows vertical motion of the wheel. An investigation into wheel load application methods in SWTBs and resulting effects on measured normal forces can be found in Section 2.5.

In partial gravity experiments, the weight of the wheel unit is lower than on Earth, so for directly comparable tests (i.e. at equal total wheel load) this reduction in weight is compensated by an equal and opposite increase in applied pneumatic force (using the pneumatic cylinders and digital pressure regulator described earlier) during the reduced-gravity flights.

Output: Drawbar pull (F_{DP})

Drawbar pull (F_{DP}) is defined in Section 1.2.2.

In the single-wheel experiments reported herein, a force/torque sensor connected to the wheel unit gives a measurement of F_{DP} during slip-controlled traverses.

Additionally, for tests completed with the rigid wheels (Figures 15 and 16), it was observed that the forces in the Y direction (perpendicular to the glass, as shown in Figure 12) could not be neglected because the experiments were conducted with the wheel pressed against the glass. As such, the coefficient of friction between the glass and the felt covering the wheels was estimated using an inclined plane test, and a friction correction was applied to the drawbar pull data using the measured force between the wheel and the glass. The coefficient of friction between the felt and the glass was determined to be approximately 0.25. Accordingly, the following correction was applied at each time step: $F_{DP} = F_X + 0.25F_Y$.

Output: Sinkage (z)

Sinkage (z) is defined in Section 1.2.2. In the single-wheel experiments reported here, sinkage is estimated from the vertical hub displacement of the wheel as measured by a potentiometer attached to the wheel unit. The raw z measurements, when converted to units of millimeters, represent the distance between the wheel hub and the potentiometer. In order to obtain measurements that represent sinkage relative to the top of the soil (i.e. such that a value of 0 mm corresponds to the top of the soil), the initial sinkage measurement (representing the distance between the wheel hub and the potentiometer) was subtracted from each data point, and then the initial static sinkage, if any was present (which was measured from the videos), was added to each data point.

Output: Power (P)

The power required by the wheel, P, is calculated as follows:

$$P = \tau\omega \tag{6}$$

where ω is the angular velocity of the wheel and τ is the torque at the wheel, calculated using Equation 7:

$$\tau = k_T I \tag{7}$$

where I is the measured motor current, k_T is the net torque constant at the wheel, calculated by multiplying the motor's torque constant by the gear ratios and the gearbox efficiencies.

This torque calculation method was verified by an alternate calculation method shown in Equation 8.

$$\tau = \tau_Y - F_{DP}\Delta Z \tag{8}$$

Table 3: Parameter settings used for SOFT.

Regularization parameter, λ	0.1
Pyramid levels	3
Spacing of pyramid levels	2
Maximum number of iterations	10

where τ_Y is the torque measured by the force/torque sensor about the Y axis shown in Figure 1, F_{DP} is the measured drawbar pull, and ΔZ is the vertical distance between the centre of the force/torque sensor and the centre of the wheel.

Output: Normal Force (F_N)

Normal force is an important parameter to consider as it affects traction and thus vehicle mobility. However, the actual normal force on the wheel resulting from the applied load and SWTB dynamics is often overlooked in the literature. It is important to consider the effects of time-varying normal force on experimental results, especially when comparing results from different SWTBs and/or different wheel load application methods. Here, the vertical force on the wheel unit is measured using a force/torque sensor, and the resulting normal force is calculated as the sum of the wheel unit weight and the measured force. See Section 2.5 for a study comparing wheel load application methods in SWTBs and resulting effects on measured normal forces.

Output: Images

Observing how the soil responds to being acted upon by a wheel can provide insight into phenomena governing wheel performance [108, 157]. A high-speed camera is used to image the soil in the region where it interfaces with the wheel. The camera is attached to the horizontal axis and moves alongside the wheel capturing the high-resolution image frames of the wheel–soil interaction from the mirror reflection of the testbed's window. In Figure 12, the camera's angle of view and glass sidewall view field are shown in orange.

Two external LED floodlights are placed approximately 1000 mm apart at both ends of the mirror at an angle pointing towards the window, to avoid direct reflection into the camera, providing illumination, high contrast, and reduced shadows along the mirror.

Videos from wheel–soil interaction experiments are collected in grayscale at 37 frames per second. The videos are subsequently converted to images where each pixel represents an area of approximately 0.4 $\times$0.4 mm.

To analyze soil motion observed through the glass sidewall of the sandbox, a dense motion estimation technique called the soil optical flow technique (SOFT) is used, discussed in detail by [157]. This technique calculates motion at each pixel of the image between consecutive images. Two displacement fields are produced, one for horizontal and one for vertical motion, in units of pixels. The parameter settings used in this work, which were previously found to be suitable for similar applications [157, 177] are shown in Table 3.

Using this technique, velocity vectors are obtained for each pair of successive frames. Then, these vectors are averaged over periods of several seconds. This is done to eliminate noise and transients caused by minor variations in soil state. Averaging boosts the signal-to-noise ratio and

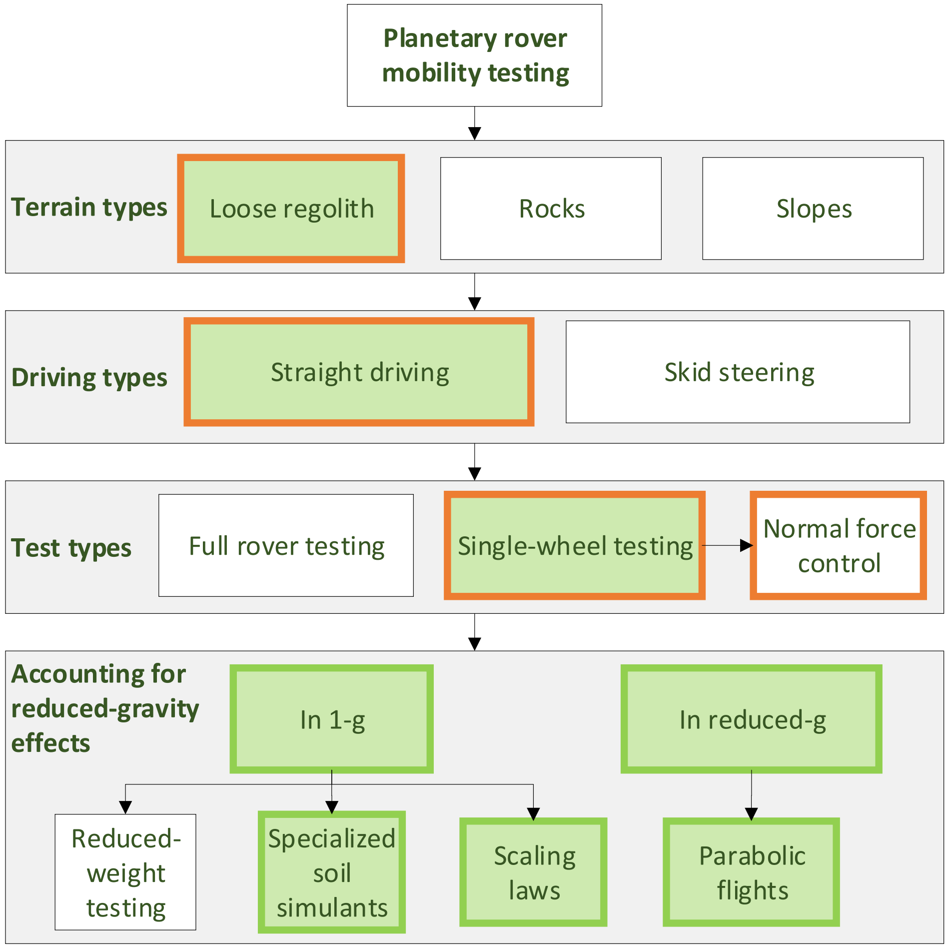

Figure 23: Diagram depicting the topics studied in this thesis, with major topics highlighted in green. The specific topics studied in this section are highlighted in orange.

thus depicts smoother flow patterns, portraying more meaningful results in comparison to a single frame pair.

Finally, for the purpose of comparing the average estimated flow fields, the velocity magnitudes at each slip are all normalized with respect to the rim speed. Rim speed is computed as the tangential rim velocity relative to the wheel hub ($L\omega$, which is constant across all tests) minus horizontal wheel (and thus hub) velocity (which decreases with increasing slip, but is constant and equal for all tests at a particular slip).

2.5 Comparison of wheel load application methods in single wheel testbeds

As highlighted previously in Section 1.4.3, single-wheel testbeds (SWTBs) are widley used in terramechanics experiments. Time-series normal force data are not always reported, but a few different authors have reported normal force oscillation in their SWTBs [5, 33, 114, 115, 128]. This has usually been attributed to grousers, but is also visible for wheels without grousers [114, 128] suggesting other system dynamics (e.g. friction in the vertical axis) are the cause.

The 4-bar linkage shown in Figure 9 was developed to ensure that a constant (not oscillating) normal load is achieved throughout terramechanics experiments by allowing the wheel to move freely in the vertical direction, independent of the frictional vertical axis of the testbed. Here, a summary of previously published work [128] evaluating the 4-bar mechanism, comparing it to the pneumatic system in the parabolic flight SWTB, and measuring friction in the vertical axis of each testbed, is presented. Figure 23 illustrates the context of the work summarized in this section relative to the thesis topics.

2.5.1 Evaluation of 4-bar mechanism

System behaviour with and without the 4-bar mechanism was assessed, highlighting the importance of characterizing normal force time-behaviour in SWTBs and using a 4-bar mechanism or other method of balancing normal loads if a constant normal force is desired.

Normal force data for 50% slip experiments using the Husky wheel (described in Section 2.2.1) in the laboratory SWTB with and without the 4-bar mechanism are shown in Figure 24a. It can be seen that use of the 4-bar mechanism ensures a more constant normal force, whereas without the 4-bar mechanism, the normal force oscillates. Additionally, the measured normal force is lower when not using the 4-bar mechanism. Note that these experiments both had the same target load (1/4 of the Husky weight). The decreased normal force without the 4-bar mechanism is most likely due to friction in the vertical axis assembly. Using the 4-bar mechanism, this friction is essentially eliminated, and the measured normal force is much closer to the target load of 150 N.

Drawbar pull and sinkage data for 50% slip experiments using the Husky wheel are shown in Figures 24b and 24c, respectively. No significant differences were observed in drawbar pull or sinkage with and without the 4-bar mechanism.

2.5.2 Comparison of 4-bar mechanism to pneumatic system

The effects of normal force oscillation on experimental results were assessed by comparing the laboratory SWTB with the 4-bar mechanism to the pneumatic system in the parabolic flight SWTB. Examples of time-series normal force data at 20% and 70% slip are shown in Figure 25. It can be seen that the normal force is much more constant in the laboratory SWTB with the 4-bar mechanism in comparison to the pneumatic system in the parabolic flight SWTB.

An initial thought was that the fluctuations in normal force in the parabolic flight SWTB were caused by cycles of expansion and compression of air in the pneumatic cylinders leading to pressure oscillations as the wheel moved up and down. To test this theory, the pressure in the pneumatic cylinder was measured, and this measurement was used to calculate the vertical force applied by the pneumatic system. Example data from one of the 40% slip tests is shown in Figure 26. It can be seen that the force from the pneumatic system does fluctuate slightly, but the pressure regulator is able to control it to a relatively constant value. Therefore, the magnitude of oscillations seen in the force sensor data cannot be explained by pressure in the pneumatic system.

Furthermore, the magnitude of the oscillations cannot be explained by accelerations related to vertical displacements of the wheel (whether caused by grousers or otherwise), which were

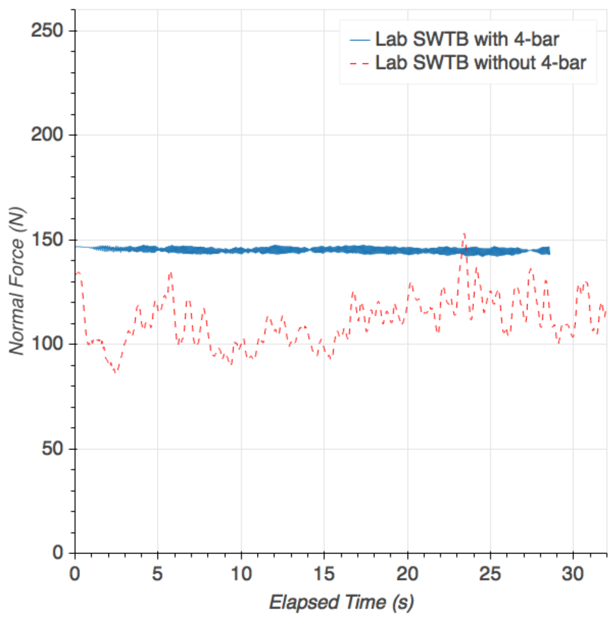

(a) Normal force

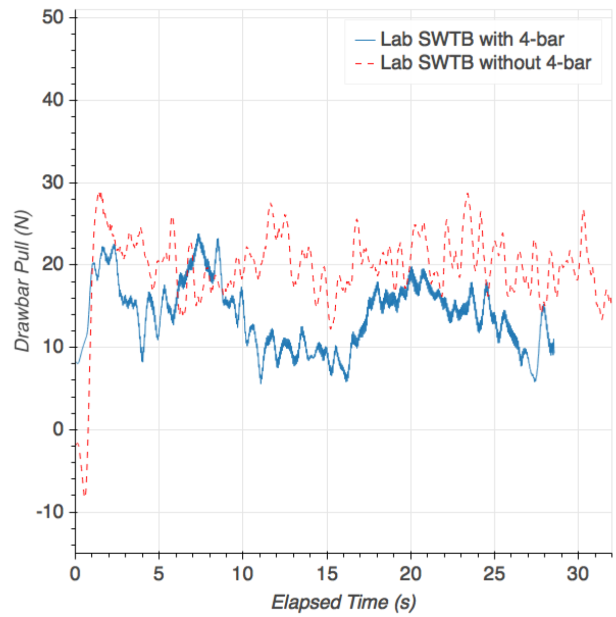

(b) Drawbar pull

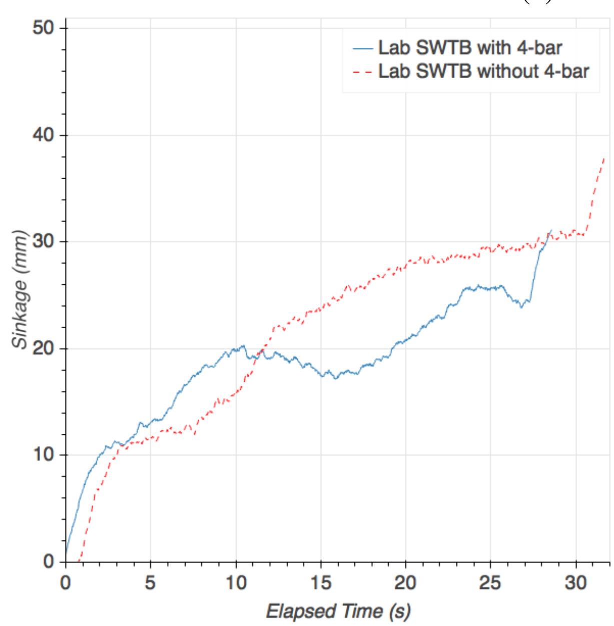

(c) Sinkage

Figure 24: Time-series data for 50% slip experiments with (blue) and without (red) the 4-bar mechanism using the Husky wheel in the laboratory SWTB. GRC-1 density was approximately 1.72 ± 0.02 g/cm^3.

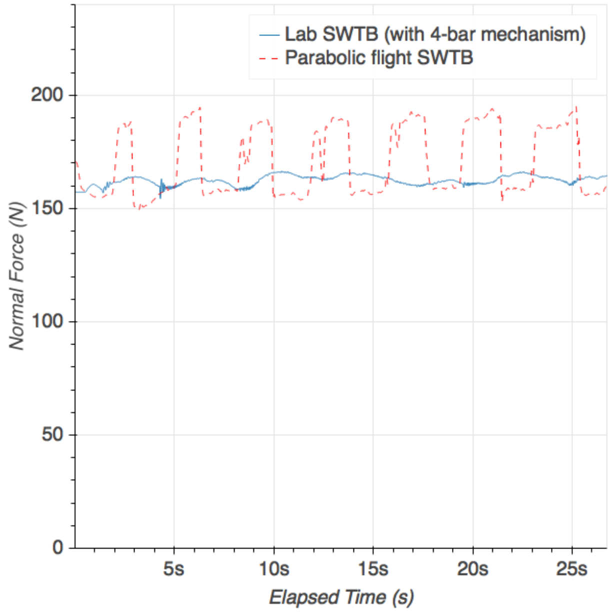

(a) Rigid wheel with grousers, 20% slip

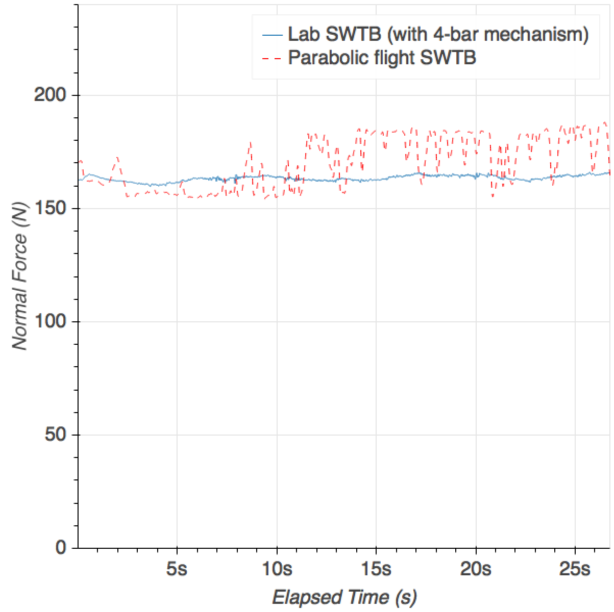

(b) Rigid wheel without grousers, 20% slip

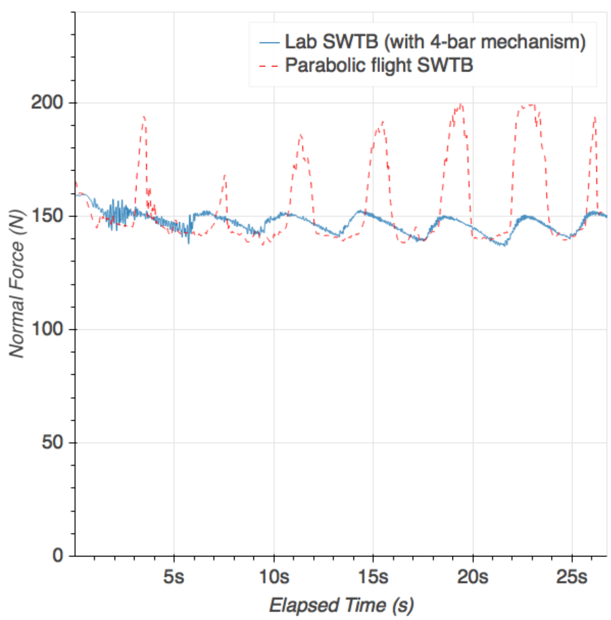

(c) Rigid wheel with grousers, 70% slip

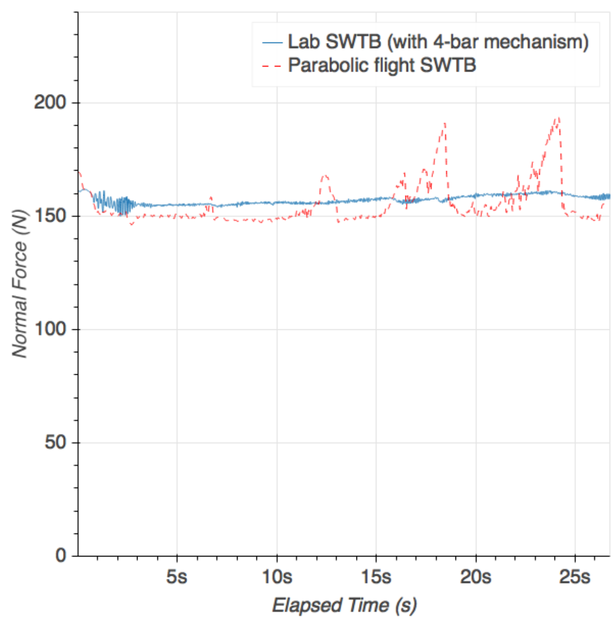

(d) Rigid wheel without grousers, 70% slip

Figure 25: Time-series normal force data from 20% slip tests using the rigid wheel (a) with and (b) without grousers, and 70% slip tests (c) with and (d) without grousers. GRC-1 density was approximately 1.72 ± 0.02 g/cm^3.

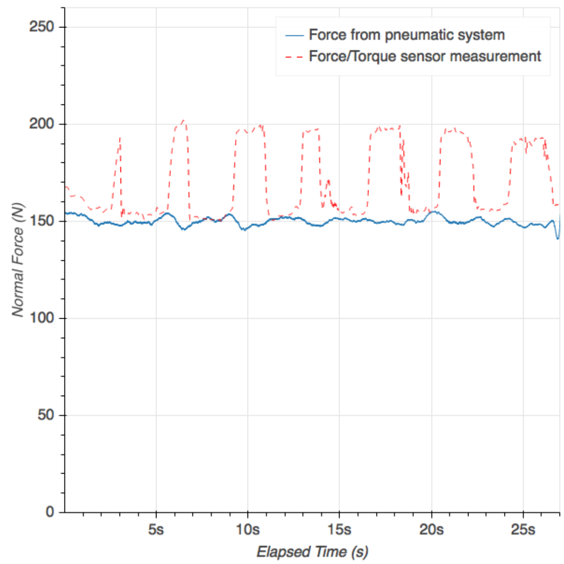

Figure 26: Normal force measured by the force/torque sensor and normal force calculated from measured pressure in the pneumatic cylinder from a 40% slip test using the rigid wheel with grousers.

estimated to account for only $\pm$ 6 N at most by direct calculation of vertical acceleration from the sinkage data. This leads to the conclusion that the force oscillations are mainly due to friction in the vertical axis.

Examples of time-series drawbar pull data for tests with grousers at 20% and 70% slip are shown in Figure 27. The corresponding normal force data are also shown, along with the drawbar pull coefficient or drawbar pull–weight ratio (F_{DP}/W), calculated by dividing F_{DP} by F_N at each time step. It can be seen in Figures 27a and 27c that there are drops in F_{DP} that coincide with the drops in normal force in the parabolic flight SWTB, whereas in the laboratory SWTB with the 4-bar mechanism (Figures 27b and 27d), these secondary drops in F_{DP} are not seen. At 70% slip in the laboratory SWTB (Figure 27d), the drawbar pull exhibits a very clear sawtooth pattern. At 70% slip in the parabolic flight SWTB (Figure 27c), when the normal force is divided out to calculate F_{DP}/W, the secondary dips in F_{DP} are cancelled and a similar sawtooth pattern can be seen. However, at 20% slip (Figure 27a), the F_{DP}/W calculation does not fully cancel out the effects of the normal force fluctuation, and the secondary dips are still seen in the F_{DP}/W data.

Overall, normal force oscillation did not have a significant effect on average drawbar pull measurements, but it added artifacts to the time-series data. The use of a 4-bar mechanism eliminates such artifacts by ensuring that a more constant normal force is applied, thus simplifying the analysis of time-series data.

Examples of time-series sinkage data at 20% and 70% slip are shown in Figure 28. The corresponding normal force and drawbar pull data are also shown. It can be seen that the normal force is lower when the sinkage is increasing (i.e. when the wheel is moving downwards), and the normal force is higher when the sinkage is constant or decreasing (i.e. when the wheel is moving upwards). This is due to friction in the vertical axis. As illustrated in Figure 29, friction resisting upwards motion would cause an increase in the measured normal force, as the frictional force would be in the same direction as the applied wheel load, and friction resisting downwards motion

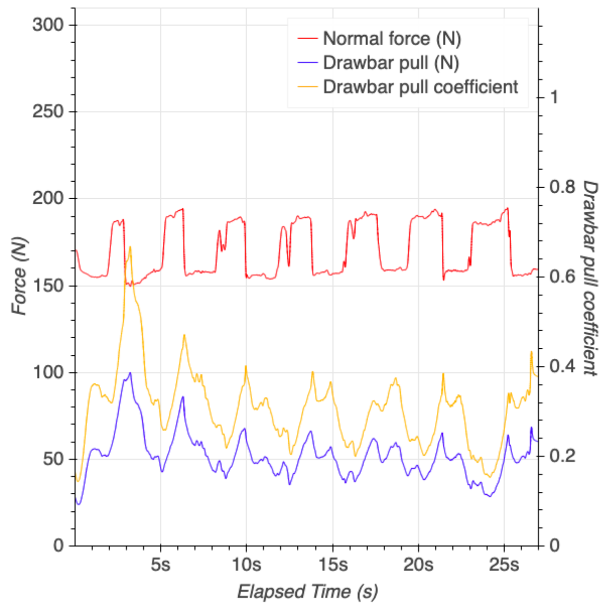

(a) 20% slip, parabolic flight SWTB

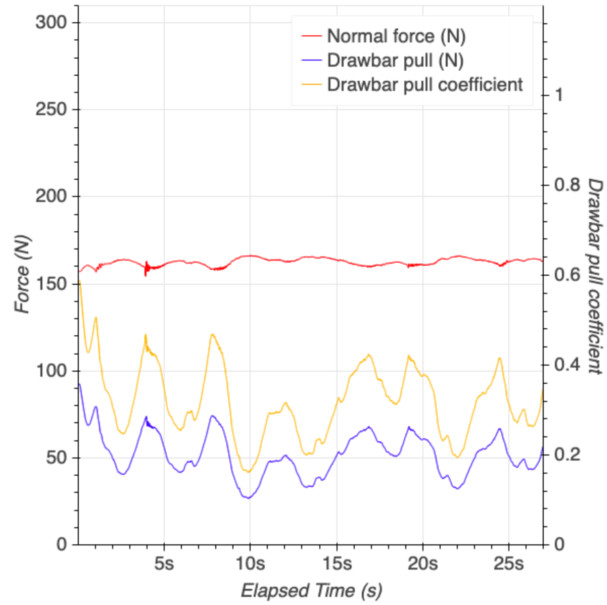

(b) 20% slip, laboratory SWTB (with 4-bar mechanism)

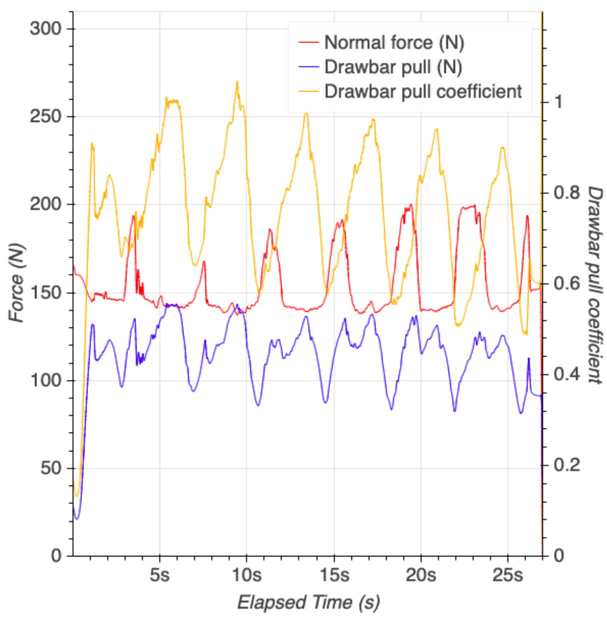

(c) 70% slip, parabolic flight SWTB

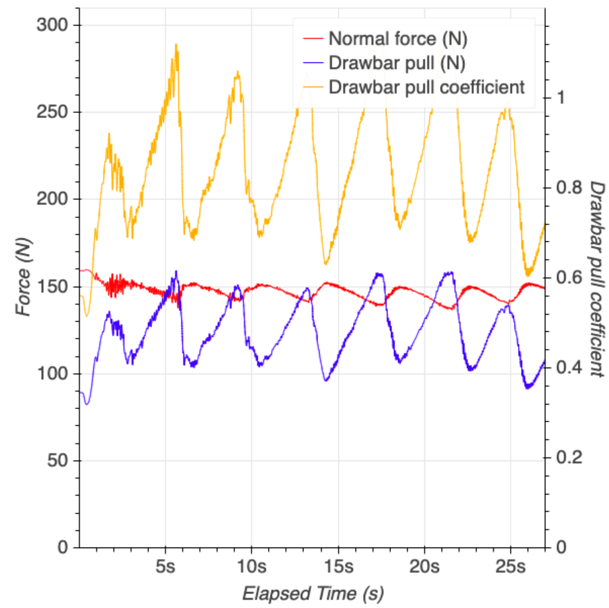

(d) 70% slip, laboratory SWTB (with 4-bar mechanism)

Figure 27: Time-series drawbar pull (F_{DP}), normal force (F_N), and drawbar pull coefficient (F_{DP}/W) data at 20% slip in the (a) parabolic flight SWTB, and (b) laboratory SWTB with the 4-bar mechanism, and at 70% slip in the (c) parabolic flight SWTB, and (d) laboratory SWTB with the 4-bar mechanism, using the rigid wheel with grousers. GRC-1 density was approximately 1.72 $\pm$ 0.02 g/cm^3.

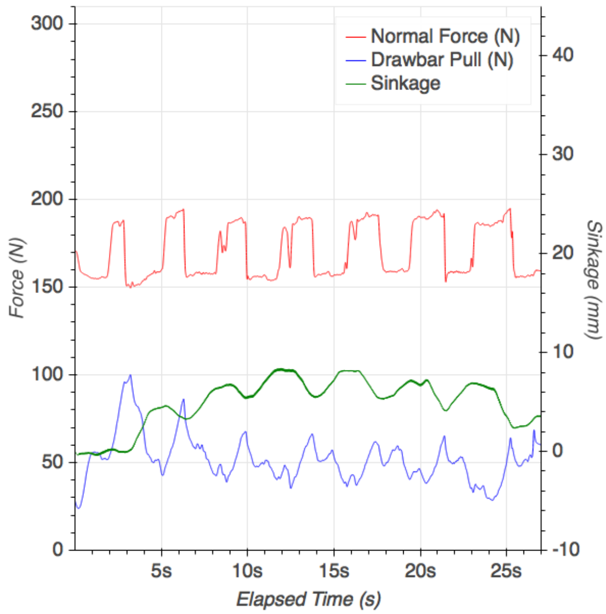

(a) 20% slip, parabolic flight SWTB

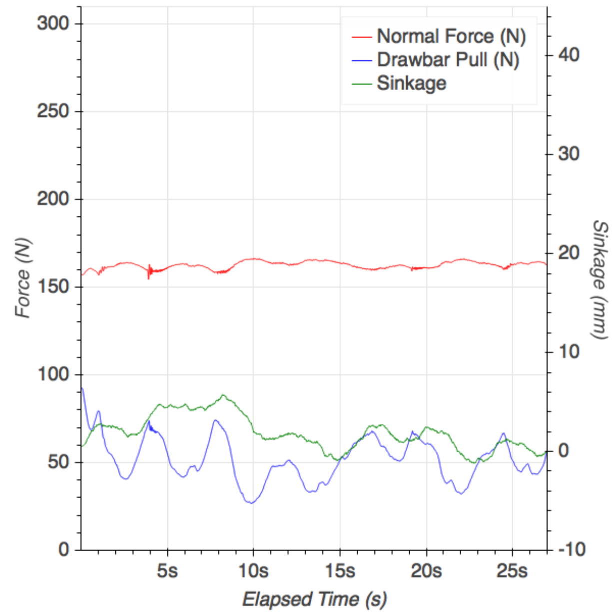

(b) 20% slip, laboratory SWTB (with 4-bar mechanism)

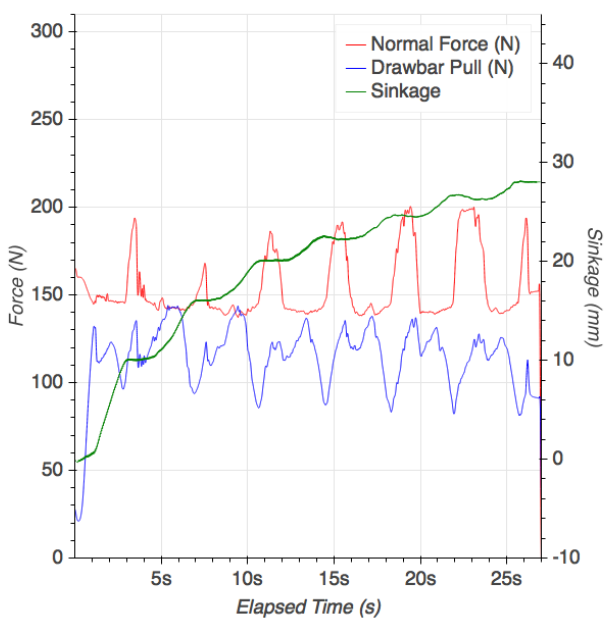

(c) 70% slip, parabolic flight SWTB

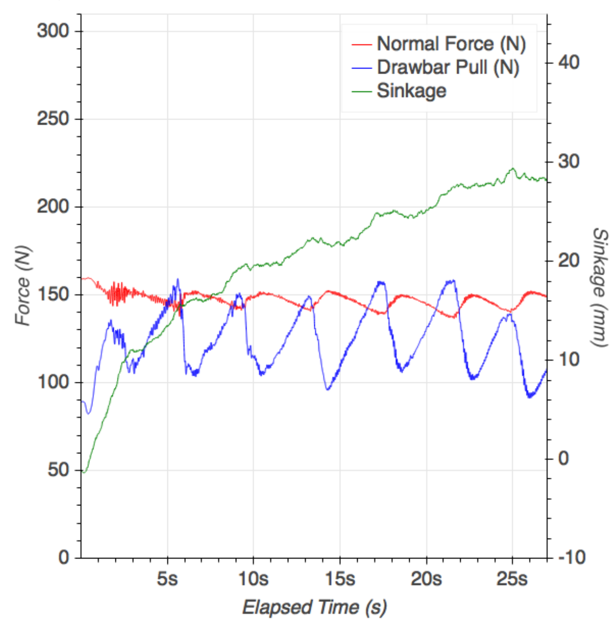

(d) 70% slip, laboratory SWTB (with 4-bar mechanism)

Figure 28: Time-series sinkage, normal force, and drawbar pull data at 20% slip in the (a) parabolic flight SWTB and (b) laboratory SWTB with the 4-bar mechanism and at 70% slip in the (c) parabolic flight SWTB and (d) laboratory SWTB with the 4-bar mechanism, using the rigid wheel with grousers. GRC-1 density was approximately 1.72 ± 0.02 g/cm^3.

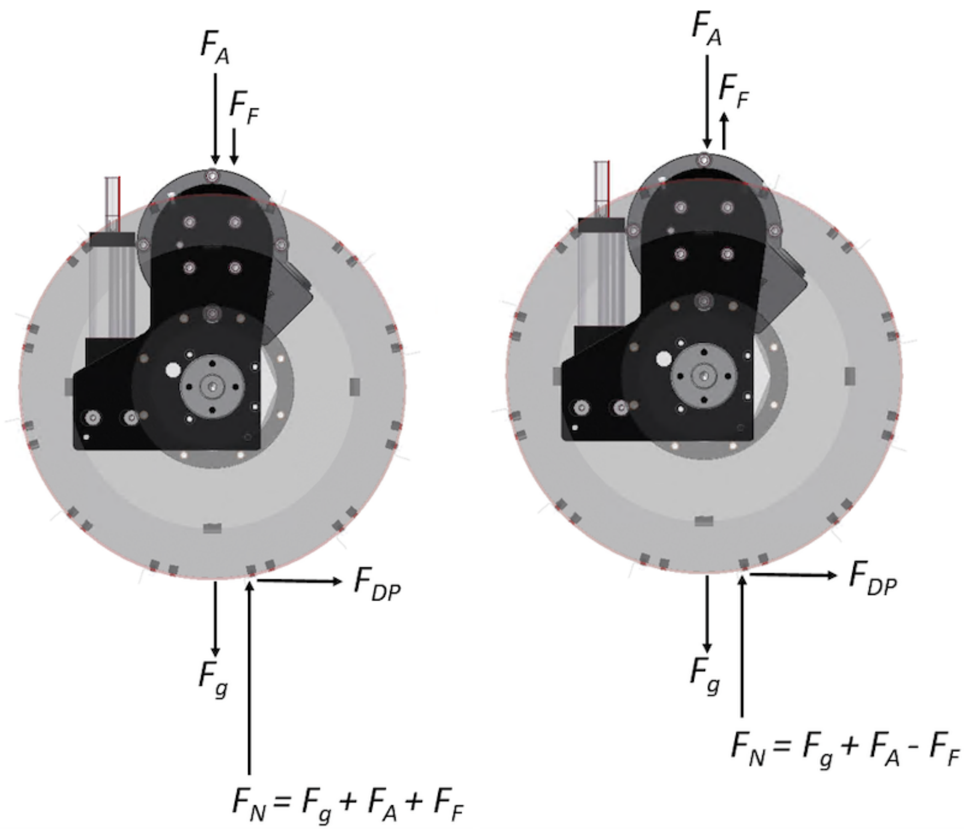

(a) Wheel recovers vertically (b) Wheel sinks

Figure 29: The effect of friction in the vertical axis when the wheel a) recovers vertically and b) sinks, where F_A is the applied wheel load, F_g is the force due to gravity, F_F is the force of friction, F_N is the normal force, and F_{DP} is the drawbar pull force.

would cause a decrease in the measured normal force.

2.5.3 Friction characterization

Laboratory SWTB

To characterize the friction in the Z axis of the laboratory SWTB (without the 4-bar mechanism), the force/torque sensor (FTS) was held underneath the Z axis slider and both were manually pushed up until the Z axis slider began to move up. Following that, the FTS was moved to a different location and the FTS and Z axis slider were pushed down, as illustrated in Figure 30.

The vertical position of the slider was also recorded using the potentiometer in order to determine the applied force when the slider started moving up or down. This allowed for characterization of the static friction force acting on the slider.

An example of FTS and potentiometer data are shown in Figure 31. The difference between the force required to push the slider up, $F_{FTS,up}$, and the force required to push the slider down $F_{FTS,down}$ is twice the force of friction F_F, as shown in Equation 9, which corresponds to the forces labeled in Figure 30. Note that the FTS was rotated between pushing the slider up and pushing the

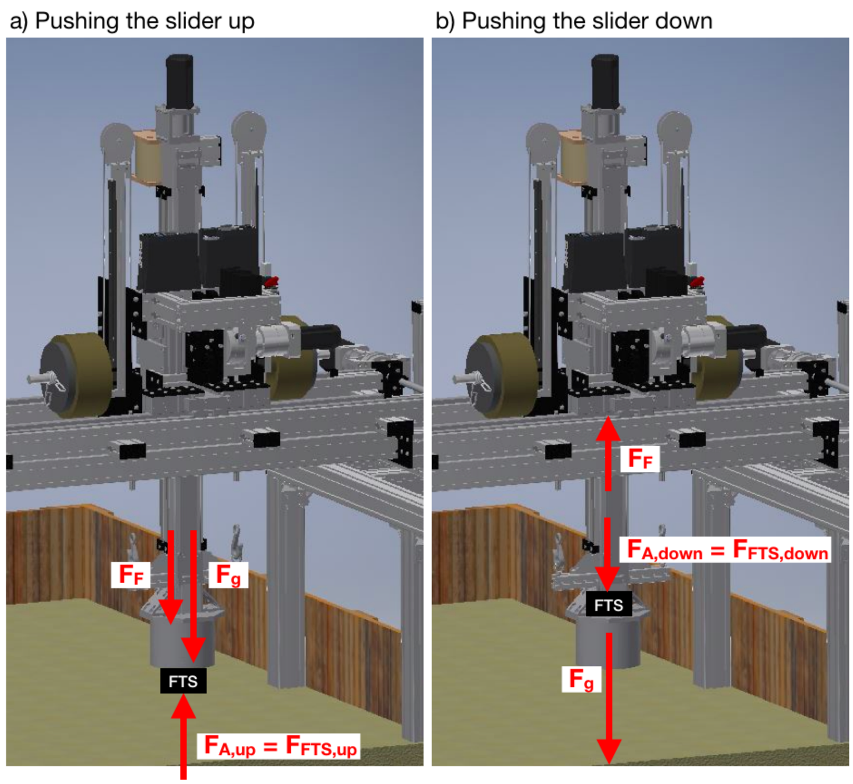

Figure 30: Diagram illustrating friction characterization experiments performed in the laboratory SWTB. F_F represents the force of friction, F_A represents the applied force, F_g represents the force of gravity, $F_{FTS,up}$ represents the force measured by the FTS when pushing the slider up, and $F_{FTS,down}$ represents the force measured by the FTS when pushing the slider down.

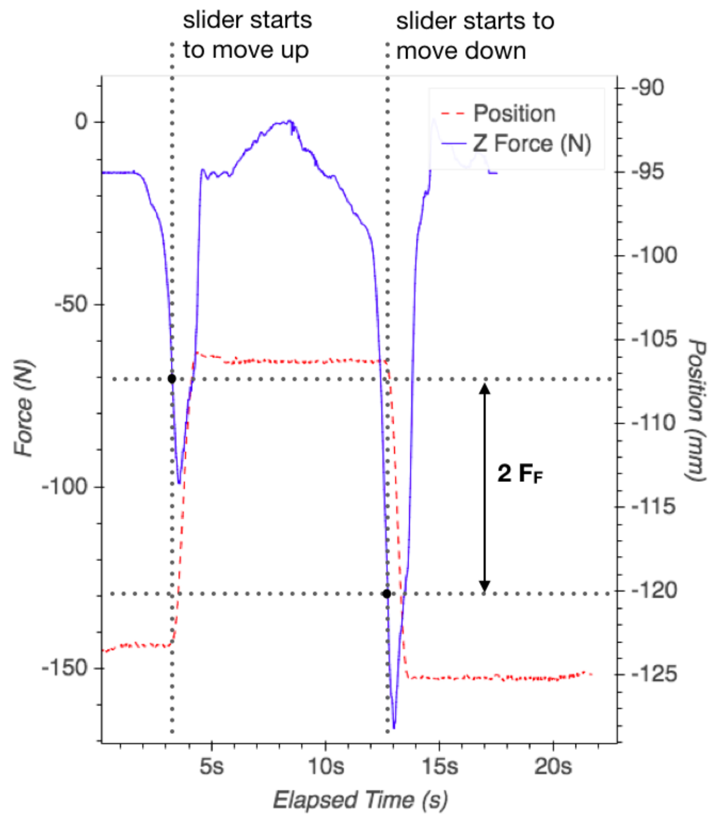

Figure 31: An example of FTS and potentiometer data measured during the friction characterization experiments in the laboratory SWTB slider (i.e. when the 4-bar mechanism is not used). The force readings at the moments when the slider starts to move up and when it starts to move down can be used to calculate the force of friction in the slider.

slider down, so a negative sign was placed in front of $F_{FTS,down}$.

$$\begin{aligned} F_{FTS,up} &= F_g + F_F \\ -F_{FTS,down} &= F_F - F_g \\ F_{FTS,up} - F_{FTS,down} &= (F_g + F_F) + (F_F - F_g) \\ F_{FTS,up} - F_{FTS,down} &= 2F_F \end{aligned} \tag{9}$$

Four repeats of this experiment were performed, and the average difference between the force required to push the slider up and the force required to push the slider down was found to be 60 $\pm$ 11 N. This result is similar to the fluctuations of approximately $\pm$ 60 N observed in Figure 24a (the amplitude of the fluctuations from peak to peak in a wheel experiment would include friction in the upwards direction as well as friction in the downwards direction, i.e. $2F_F$).

It is noteworthy that the laboratory SWTB setup is particularly high-friction. However, the parabolic flight SWTB setup is more typical and there is still a significant amount of friction, as described below.

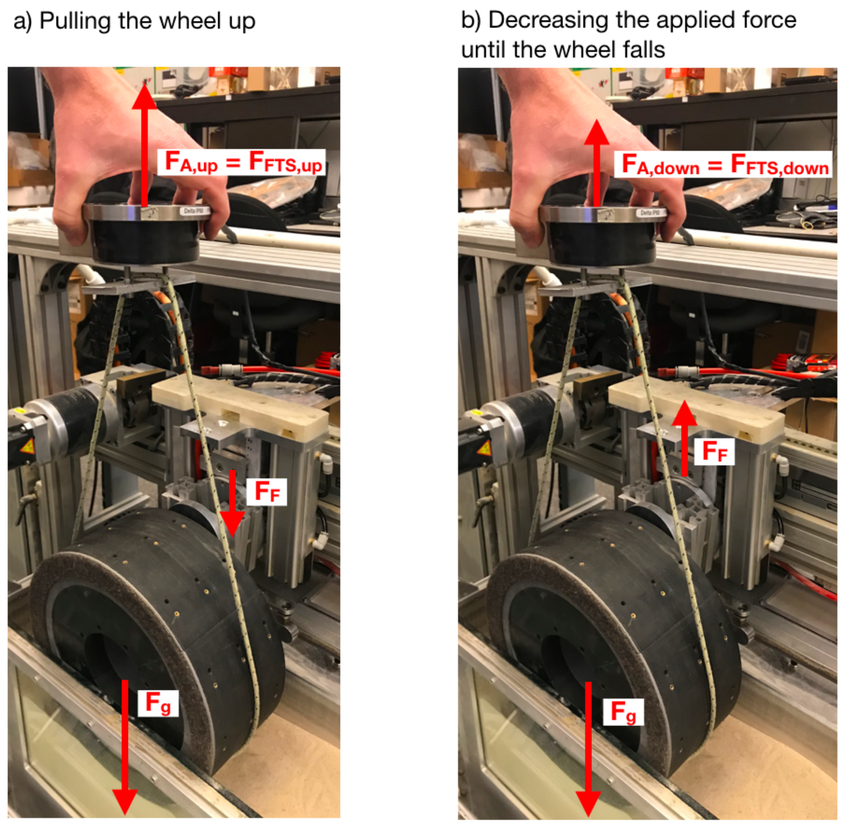

Figure 32: Photo depicting friction characterization experiments performed in the parabolic flight SWTB. F_F represents the force of friction, F_A represents the applied force, F_g represents the force of gravity, $F_{FTS,up}$ represents the force measured by the FTS when pulling the wheel up, and $F_{FTS,down}$ represents the force measured by the FTS when allowing the wheel to fall.

Parabolic Flight SWTB

Using a similar method, the static friction in the parabolic flight SWTB was also characterized. In this case, the FTS was attached to a rope placed around the wheel, and then the wheel was lifted manually, held up briefly, and then lowered. In this way, the force required to lift up the wheel was measured along with the decrease in force required lower the wheel. This is illustrated in Figure 32.

Again, potentiometer data were simultaneously recorded in order to determine the force when the wheel started to move up or down. Also note that the pneumatic pistons were not attached, so only the friction of the slider, potentiometer, and friction between the wheel and the glass were measured. As before, the difference in the force at the time the wheel started to move up, $F_{FTS,up}$, and at the time the wheel started to move down, $F_{FTS,down}$, was twice the force of friction, F_F, (see Equation 10 and corresponding forces labeled in Figure 32).

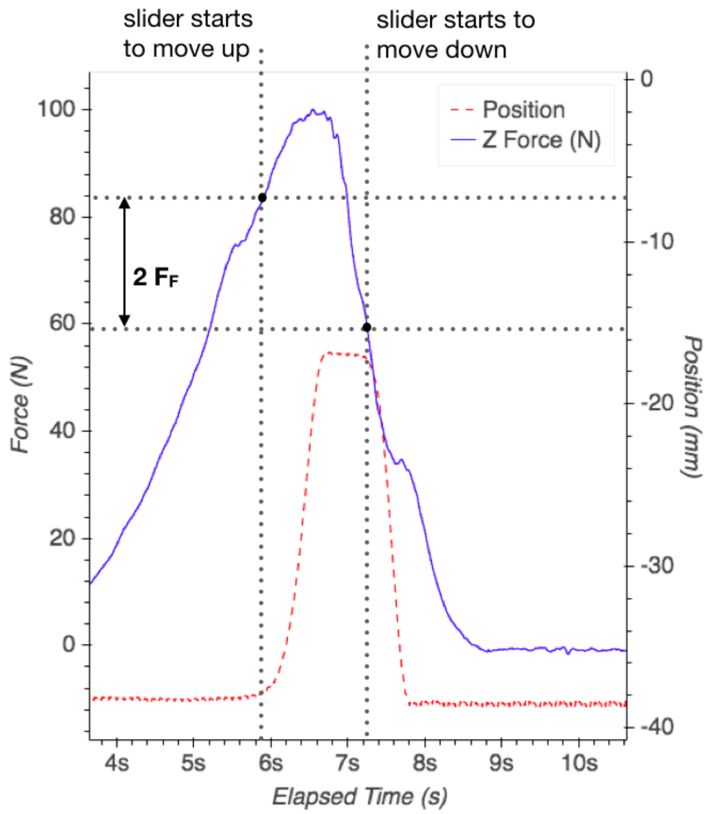

Figure 33: An example of FTS and potentiometer data from the friction characterization experiments in the parabolic flight SWTB. The force readings at the moments when the wheel starts to move up and when it starts to move down can be used to calculate the force of friction in the vertical axis.

$$\begin{aligned} F_{FTS,up} &= F_g + F_F \\ F_{FTS,down} &= F_g - F_F \\ F_{FTS,up} - F_{FTS,down} &= (F_g + F_F) - (F_g - F_F) \\ F_{FTS,up} - F_{FTS,down} &= 2F_F \end{aligned} \tag{10}$$

Six repeats of this experiment were performed, and the average difference between the force required to lift up the wheel and force required to lower the wheel was found to be 26 $\pm$ 9 N. An example is shown in Figure 33. This result is similar to the magnitude of the oscillations observed in Figure 25. Even though the slider and pistons are supposed to be low friction individually, when all the parts are added together, the constraints of the setup seem to make the vertical axis relatively high friction as a whole.

2.5.4 Conclusion regarding SWTB normal force application

The 4-bar mechanism greatly reduced normal force oscillation, and should be used when a constant normal force is desired. Insight was also gained into the causes of normal force oscillation in the two different SWTBs—in both cases it is primarily caused by friction in the vertical axis assemblies. The pressure in the pneumatic system in the parabolic flight SWTB was measured and it was concluded that the changes in measured normal force could not be explained by changes in pressure. Furthermore, it was shown that vertical accelerations of the wheel mass could not account for more than a small fraction of the normal force oscillations.

Experiments characterizing the friction in each SWTB's vertical axis were completed, and the estimated amounts of friction aligned well with the magnitude of normal force oscillations observed in the wheel experiments. Of course, each SWTB setup is unique, but if normal force oscillations are present in a SWTB they may be due to friction in the vertical axis, and this is something that should be characterized. These results motivate a recommendation that vertical friction be routinely characterized, and normal force data be routinely reported, in SWTB publications, which is not currently the norm. If a steady normal force is desired, a 4-bar mechanism that allows the wheel to move freely up and down, independent of the vertical axis, can be used to greatly reduce those oscillations.

These conclusions do not necessarily imply that data collected without a load-balancing mechanism are not useful. Comparisons between data collected using the same SWTB with the same normal force behaviour are valid, and comparisons of *average* data collected using different SWTBs and different wheel load application methods appear to be valid as well. No significant effect on average measurements was observed due to normal force oscillation, but it adds artifacts to time-series measurements of data such as drawbar pull, which may complicate the analysis of dynamic behaviour. Thus, if time-series data are to be analyzed, or if a constant normal force is desired for any other reason, the use of a 4-bar mechanism will ensure that a constant normal force is applied by substantially eliminating friction in the vertical axis.

Chapter 3

Reduced-weight testing

The first parabolic flight campaign with the single-wheel testbed (SWTB) described in Section 2.1.2 was completed with the goal of evaluating the method of reduced-weight testing. Figure 34 illustrates how this work fits into the topics covered in this thesis. Niksirat et al. [5] compared reduced-gravity flights with on-ground experiments (performed by the author, listed as contribution 1.1 in Section 1.5) to evaluate the effect of reduced gravity on wheel–soil interactions of a Rosalind Franklin rover wheel prototype (described in Section 2.2.3) driving in martian soil simulant ES-2 (see Section 2.3.1). Results from martian and lunar gravity were compared with on-ground experiments with all parameters equal, including wheel load, such that the only difference between the experiments was the effect of gravity on the soil itself (i.e. the difference between the experiments was equivalent to the difference between actually driving a rover on the Moon or Mars and testing a reduced-mass version of the rover—with equal normal wheel load—in similar soil on Earth). These experiments were the first to collect wheel–soil interaction imagery and force/torque sensor data alongside wheel sinkage data in reduced gravity. In lunar gravity, a statistically significant average reduction in traction of 20% was observed compared with 1-g, and in martian gravity an average traction reduction of 5–10% was observed. Subsurface soil imaging showed that soil mobilization increases as gravity decreases, suggesting a deterioration in soil strength, which could be the cause of the reduction in traction. Statistically significant increases in wheel sinkage in both martian and lunar gravity provided additional evidence for decreased soil strength. Thus, these experiments showed that reduced-weight mobility testing on Earth overestimates wheel performance: it overestimates drawbar pull and underestimates sinkage.

This chapter presents the main content of the journal article [5]. Although the reduced-gravity flights themselves were carried out by Niksirat before the start of my program, I conducted the on-ground experiments, performed the statistical analyses, and wrote the article.

3.1 Experimental parameters

In these experiments, the inputs to the system were slip (S), wheel load (W), soil density, and the effective gravitational acceleration (g). The outputs of the system included the measured drawbar pull or net traction (F_{DP}), normal force (F_N), measured vertical hub displacement (z, distinguished from sinkage here due to the wheel's flexibility), and high speed images of the wheel–soil interactions. These inputs and outputs are described in Sections 1.2.2 and 2.4.

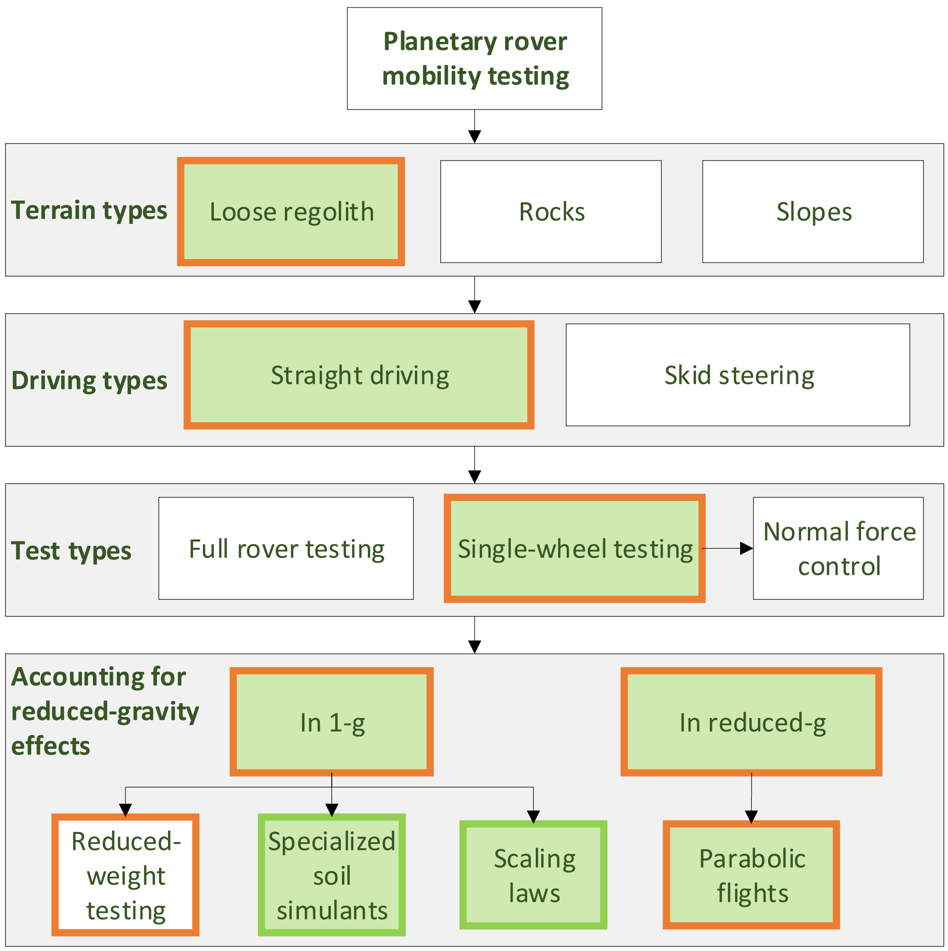

Figure 34: Diagram depicting the topics studied in this thesis, with major topics highlighted in green. The specific topics studied in this chapter are highlighted in orange.

Table 4: Number of experiments completed at each combination of parameter settings. All tests conducted in ES-2 (density of 1.450 $\pm$ 0.025 g/cm^3), with ω = 0.15 rad/s.

		Number of Tests		
Slip (%)	Wheel Load (N)	1-g	Martian-g	Lunar-g
10	164	1	1	1
20	164	3	3	2
30	164	1	1	1
40	164	1	1	1
70	164	1	1	1
10	225	1	1	0
20	225	1	1	0
30	225	1	1	0

Additionally, motor currents and velocities were collected; the latter were used to verify the commanded slip. The angular velocity of the wheel was kept constant at 0.15 rad/s (for a constant $L\omega$ value of 21 mm/s) in all operations. This corresponds to a travel distance of approximately 15 to 50 cm, depending on the slip value (since the wheel rotation speed and the test length were held constant, the distance travelled changed based on the slip value). Considering the low speed, it is assumed these experiments correspond to a quasi-static condition. The motor current was used to validate the motor performance and to confirm the F/T sensor data.

Table 4 summarizes the tests conducted in this experimentation campaign.

3.1.1 Soil preparation

Low-density regolith is the most challenging for rovers to traverse. It was loose, low-density regolith that trapped NASA's Spirit rover. Accordingly, for these experiments, ES-2 was prepared in concordance with ESA's recommended density range, aiming for the lower end of the range.

Requirements from ESA were used to select the depth of the soil, ultimately set at 31 cm. There has been (unpublished) research performed by ESA-contracted researchers to find the depth at which the floor of the sandbox no longer influences terramechanics experiments for the Rosalind Franklin rover wheel driving in ES-2 simulant (i.e. with wheel loads and wheel design similar to those used in our experiments). These studies concluded that soil depth greater than 30 cm does not detectably affect the performance while, on the other hand, soil depths less than 25 cm may affect performance.

In order to ensure repeatable soil conditions, soil preparation procedures including loosening and then compacting and leveling the soil were conducted between each wheel experiment. In recent years, efforts had been made to automate soil preparation [178, 179]. To achieve automation despite tight in-flight time and space constraints (as seen in Figure 35), a novel rapid automated procedure using pneumatics was developed. The testing and soil preparation were fully automated so that the apparatus could be enclosed to avoid any dust entering the aircraft's ventilation system. The design and verification of this sub-system is presented in [124]. ES-2's very fine particles make it a challenging soil to prepare and work with. Nonetheless, soil height after soil preparation was consistently 31 cm $\pm$ 0.7 cm; soil density consistency was shown by the fact that over 80% of cone penetrometer readings within the central 28 cm of the sandbox (covering 100% of the length of the 40% slip and 70% slip tests, and 90% of the length of the 20% slip tests) fell within the 95% confidence bounds determined from a set of reference measurements. Repeatability of soil preparation in flight was demonstrated by the excellent congruence of sinkage and traction data between the three repeats of the 20% slip martian-g test [124]. It should be noted that soil preparation was always conducted during a 1-g preparation phase of flight (between parabolas as shown in Figure 22) for consistency. Further, there was no change in the soil level viewed by the high-speed camera throughout any portion of the flights, suggesting the soil density, once prepared, did not change in reduced gravity.

3.1.2 Processing of drawbar pull data

F_{DP} measurements were averaged for each slip test and divided by average wheel load (W). The drawbar pull–weight ratio (F_{DP}/W) is a commonly used metric in the field of terramechanics that refers to the load a vehicle can tow relative to its own weight, or vertical load, and can also be related to its slope-climbing ability as discussed in Section 1.2.2. In these experiments, due to the wheel's grousers and suspension springs (and other system dynamics, see Section 2.5), the drawbar pull and wheel load data exhibit a periodic pattern, which has previously been observed in wheels with and without grousers [180]. Consequently, the data used for averaging had to be selected systematically in order to facilitate meaningful comparisons between the tests. The approach was to analyze exactly two periods of data, and always at the same stage of the test. This was done by first identifying the start of motion, t_0, in each test. Then t_1, the length of time between the start of motion and the beginning of the averaging window, was selected such that the transients at the beginning and end of the test were not included in the average calculation (i.e. such that the quasi-steady state condition was achieved, as determined by qualitatively observing the data). Finally t_2, the length of the averaging window, was defined to encompass two periods of oscillation, which is 14 s out of the 20–25 s of wheel motion (since the periodicity of the data was found to correspond to the geometry of the wheel, and the rotational speed was constant for all tests, the period is the same for each test). Only t_0 differed between tests; t_1 and t_2 were the same for all tests. These time segments are demarcated in Figure 36, which shows two examples of F_{DP} and W data from 10% and 20% slip tests in martian-g with wheel load setpoints of 225 N. At low slip values a true quasi-steady state is achieved; as can be seen in Figure 36, the maximum and minimum values of drawbar pull are similar for each period. At higher slip values a true steady-state cannot be achieved in under 20 s, but nonetheless relative comparisons of F_{DP} (and sinkage) between different gravity levels are still valid because using the same t_1 and t_2 ensures the data is from equivalent phases of the motion.

3.1.3 Processing of sinkage data

Sinkage was estimated from the vertical hub displacement of the wheel as measured by a potentiometer attached to the wheel unit. The wheel hub displaces vertically due to sinkage but also due to wheel deflection. Average wheel deflection is assumed to stay constant throughout any given test with constant wheel loading.

As described in Section 2.4.4, the raw sinkage measurements represent the distance between the wheel hub and the potentiometer. To obtain measurements that represent sinkage relative to the top of the soil, the distance between the wheel hub and the potentiometer (i.e. the initial sinkage

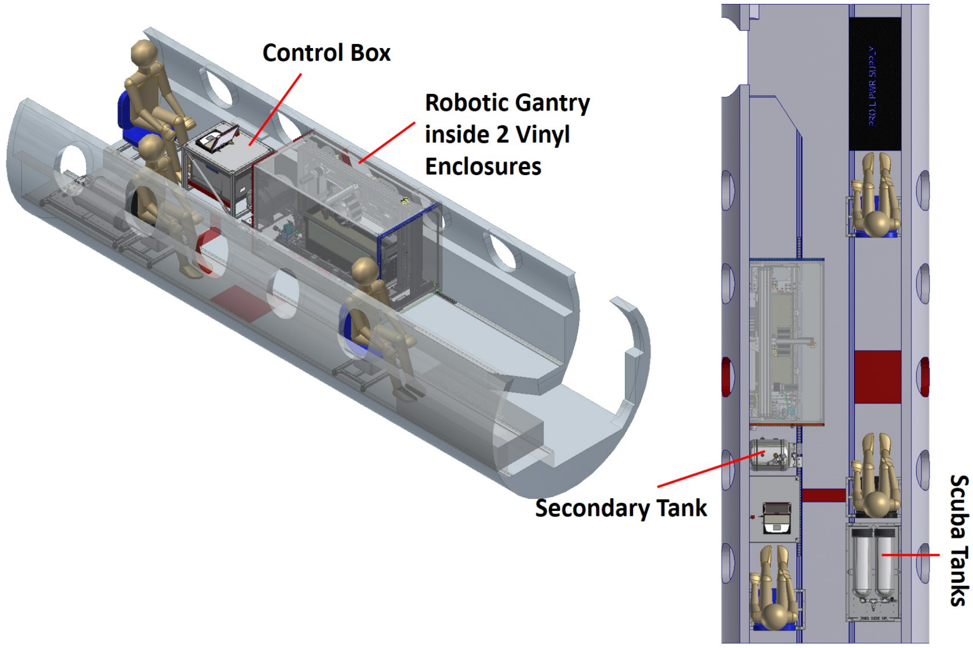

(a) Design of the cabin layout for reduced gravity flights.

(b) Inside Falcon 20 cabin.

Figure 35: Detailed instrument installation inside the cabin; (a) shows the positioning of the system components within the aircraft cabin and (b) shows the automated terramechanics testing system inside a 2-stage vinyl enclosure (centre-left) during reduced-gravity flights [5].

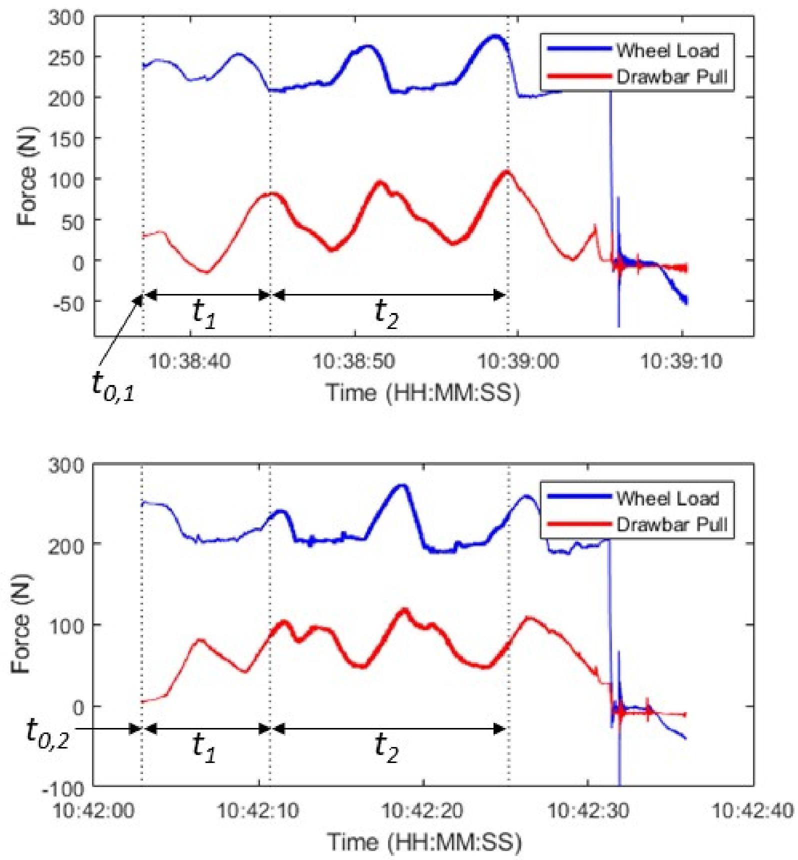

Figure 36: Examples of periodic drawbar pull and wheel load data from the 10% (top) and 20% (bottom) slip tests in martian-g with wheel load setpoints of 225 N. t_0 marks the start of motion (data prior to t_0 are not shown here), t_1 is the time between t_0 and the beginning of the averaging window, and t_2 is the length of the averaging window (two periods of oscillation). Bold lines show segments of data used for averaging.

measurement) must be subtracted from each measured data point, and then any initial sinkage of the wheel below the soil surface (as measured from the videos) must be added to each data point. However, in this parabolic flight campaign, one video was lost (one of the tests in lunar-g at 20% slip), so for this case, the average initial sinkage measurement was used.

Example sinkage data is shown in Figure 37. It can be seen that sinkage continues to increase throughout the tests. Although a quasi-steady state is not achieved in terms of sinkage, relative comparisons of sinkage between different gravity levels are made by comparing the maximum sinkage achieved throughout the test, rather than an average sinkage value.

3.1.4 Image processing

Using the Soil Optical Flow Technique (SOFT) described in Section 2.4.4, videos from the tests were processed to obtain vectors estimating the horizontal and vertical soil velocity at each pixel between frame pairs. Then, these vectors were averaged over time ranges identified from patterns observed in the corresponding sinkage data. This was done to eliminate noise and transients caused by the response to passing grousers or minor variations in soil state. Averaging boosts the signal-to-noise ratio for compliant wheels that induce small soil motion and thus depicts smoother flow patterns, portraying more meaningful results in comparison to a single frame pair. Additionally, it was hypothesized that soil motion would be consistent in sections with relatively constant rates of change in sinkage. Examples of sinkage data are shown in Figure 37, with arrows indicating the sections selected for averaging. In Figure 37a, sections 1, 3, and 5 are called "rises", as the sinkage is rising during these segments. Similarly, sections 2, 4, and 6 are called "plateaus". In the lower slip ratio tests, sinkage "falls" (e.g. sections 1, 5, and 9 in Figure 37b) and "valleys" (e.g. sections 2, 6, and 10 in Figure 37b) are also observed.

In order to directly compare tests exhibiting only two distinct types of sinkage behaviour (rises and plateaus, as seen in Figure 37a) to tests where four types of sinkage behaviour were seen (rises, plateaus, falls, and valleys, as seen in Figure 37b), the sinkage plateaus in the former were divided into three segments. The phenomenon observed in 37b is concurrent with the varying of the wheel's stiffness (depending on leaf-spring positions), and demonstrates the wheel hub recovering vertically when stiffer sections of the wheel interact with the soil at low slip. Sinkage behaviour similar to that shown in Figure 37a tended to occur during higher-slip conditions. At higher slip, the stiffer sections of the wheel dig into and excavate soil (slip-sinkage), overwhelming any possible vertical recovery.

Finally, for the purpose of comparing the average estimated flow fields, the velocity magnitudes at each slip are all normalized with respect to the rim speed. Rim speed is computed as the tangential rim velocity relative to the wheel hub ($L\omega$, which is constant across all tests) minus horizontal wheel (and thus hub) velocity (which decreases with increasing slip, but is constant and equal for all tests at a particular slip).

SOFT output is shown in Figure 43.

3.1.5 Motor current data

As discussed in Section 1.2.2, motor current measurements provide insight about the torque and therefore the power required to spin the wheel. As shown in Section 2.4.4, the power required by the wheel is equal to $P = k_T \omega I$, where k_T is the net torque constant at the wheel and I is

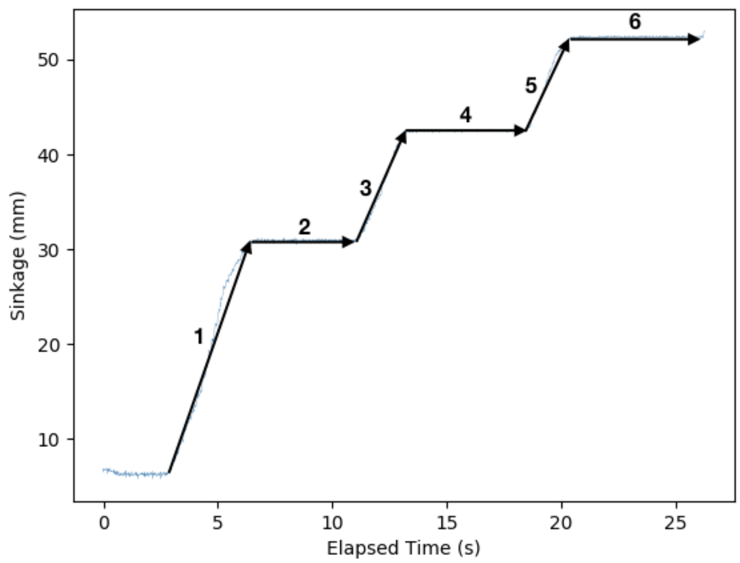

(a) Sinkage data for test in martian-g at 70% slip and 164 N wheel load.

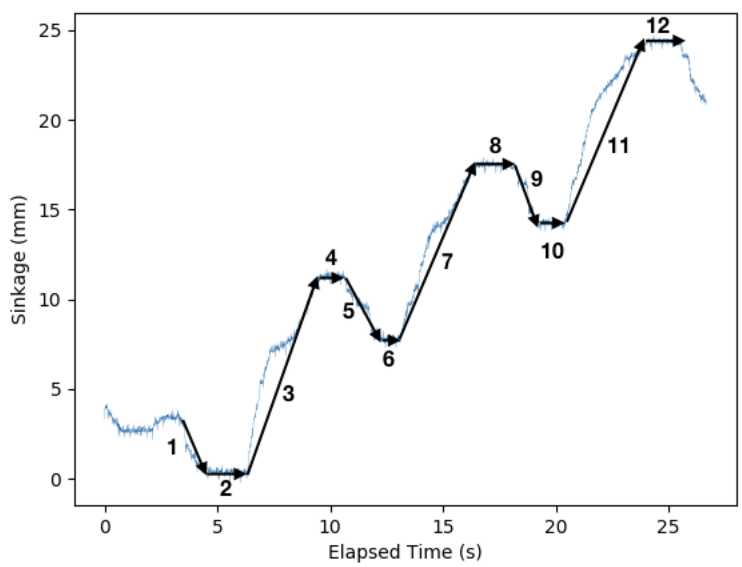

(b) Sinkage data for test in martian-g at 20% slip and 164 N wheel load (Repeat A).

Figure 37: Examples of sinkage data with numbered arrows indicating segments used for averaging of the SOFT results.

the measured motor current. Since in these experiments, k_T and ω are constant between tests, comparing motor currents is akin to comparing power consumption.

3.2 Results and discussion

3.2.1 Experimental uncertainty

One source of error in these experiments is the variance remaining after soil preparation. The properties of the soil simulant used, ES-2, are sensitive to soil conditions [124], and each time the soil preparation procedure is performed, some error is introduced with a zero mean and a nonzero variance (i.e. this error is random, not systematic). Another possible source of error is the variability in gravity level during the flights. Looking at the IMU data from the flights, the gravity levels were not perfectly constant and consistent, as can be seen in the examples shown in Figure 22, but the variations within and between tests are much smaller than between lunar-g, martian-g, and 1-g. Finally, there is also the further difference between reduced-g experiments done in flight and 1-g experiments done in a stable laboratory environment (with a more rigid substrate and less vibration). However, the differences observed between lunar-g and martian-g results are themselves substantial and consistent with an interpretation that the 1-g tests are valid for comparison (i.e. the differences observed between lunar-g and 1-g are larger than those between martian-g and 1-g, with both differences in the same direction).

3.2.2 Drawbar pull

Average F_{DP}/W versus slip ratio can be seen in Figures 38 and 39 for (i) 164 N wheel load tests in 1-g and lunar-g, and (ii) 164 N and 225 N tests in 1-g and martian-g, respectively. The average ratio of F_{DP}/W in reduced-g to 1-g was computed for each case, and a paired, two-tailed t-test was used to determine statistical significance ($p < 0.05$).

Effect of gravity on drawbar pull

F_{DP}/W was 20% lower on average in lunar-g compared to 1-g, and the difference between these two datasets was statistically significant (p = 0.02). In martian-g, a decrease in F_{DP}/W was also detected (6% with 164 N wheel load, 14% with 225 N wheel load, and 8% if the 164 N and 225 N datasets are combined), but it was not statistically significant (p = 0.30, 0.24, and 0.09 respectively). This can be explained by the fact that

(i) the statistical degrees of freedom (*n*-1), where *n* is the number of data points in the sample, are relatively low in these datasets, resulting in low statistical power of the hypothesis tests; consequently, only relatively large differences are detected as significant,

(ii) there is some nonzero experimental error, as described above, and

(iii) the difference between martian-g and 1-g is not as large as the difference between lunar-g and 1-g (since there is a smaller difference in the input signal, gravity, the difference in the output signal, drawbar pull, is also smaller, and thus there is a lower signal-to-noise ratio, resulting in the difference not being statistically significant in this case).

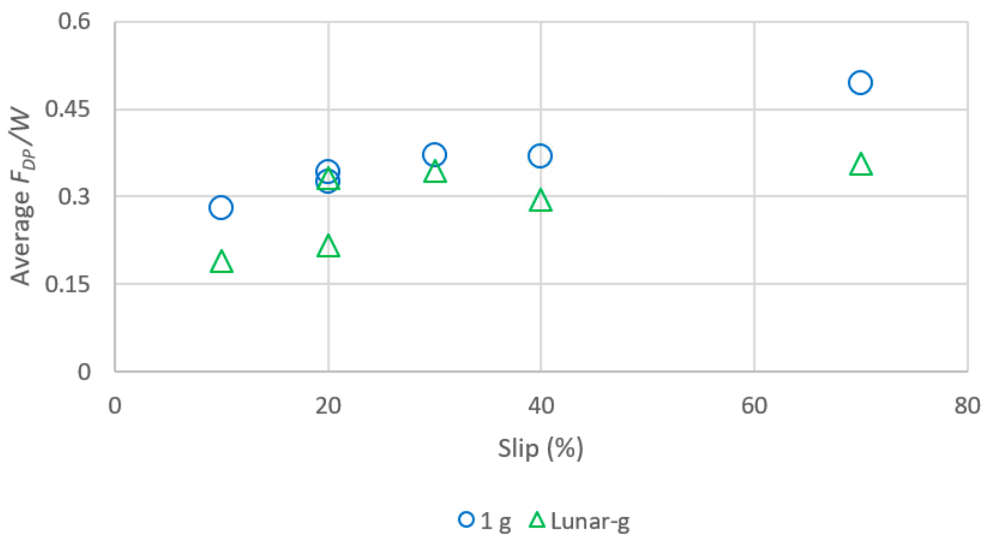

Figure 38: Average drawbar pull-wheel load ratio versus slip ratio for tests in 1-g and lunar-g with wheel load setpoint of 164 N and ES-2 density 1.45 g/cm^3.

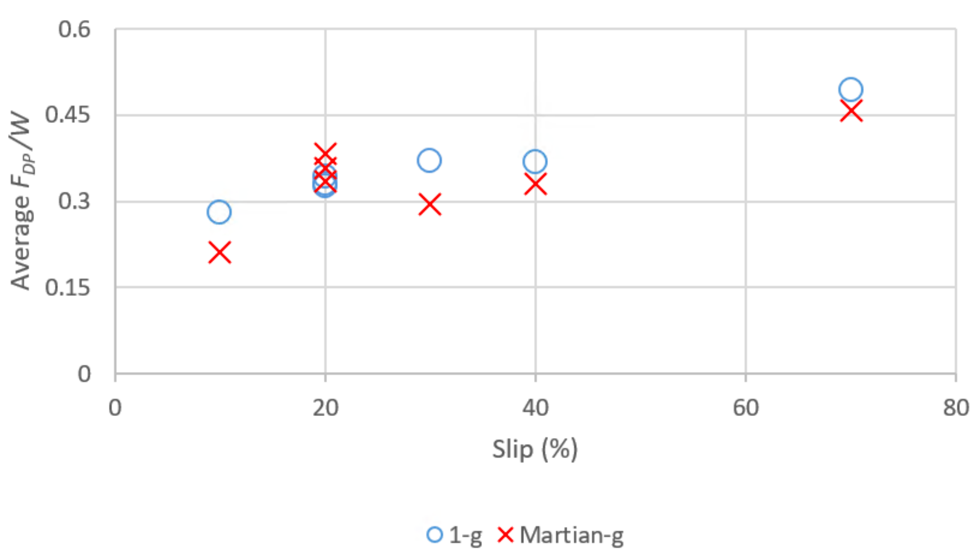

Figure 39: Average drawbar pull–weight ratio versus slip ratio for tests in 1-g and martian-g with wheel load setpoints of 164 N and 225 N and ES-2 density 1.45 g/cm^3.

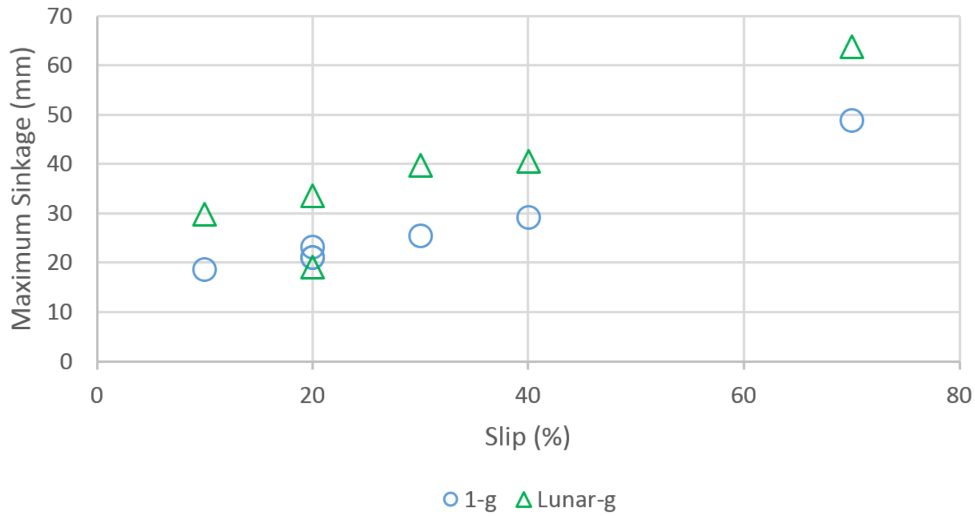

Figure 40: Maximum sinkage versus slip ratio for tests in 1-g and lunar-g with wheel load setpoint of 164 N and ES-2 density 1.45 g/cm^3.

Nevertheless, a decrease in drawbar pull was detected in martian-g, and coupled with the statistically significant decrease observed in lunar-g, this leads to the conclusion that drawbar pull is monotonically related to gravity.

A reduction in drawbar pull is consistent with lower soil strength in reduced gravity.

3.2.3 Sinkage

Figures 40 and 41 show the maximum sinkage reached during each test (irrespective of number/types of segments observed, see Figure 37) versus slip ratio for tests with, respectively, (i) 164 N wheel load in 1-g and lunar-g and (ii) 164 N and 225 N wheel loads in 1-g and martian-g. Again, paired, two-tailed t-tests were used to determine the statistical significance of the differences observed between the reduced-g and 1-g results.

Effect of gravity on sinkage

Maximum sinkage was 38% higher on average in lunar-g compared to 1-g, and this difference was statistically significant ($p = 0.01$). In martian-g, with wheel loads of 164 N and 225 N, maximum sinkage was 27% and 47% higher than in 1-g, respectively. Both of these differences were found to be statistically significant ($p = 0.001$ and 0.02, respectively). These results lead to the conclusion that sinkage increases in reduced gravity. Increased sinkage in reduced-g is consistent with reduced soil strength, as bearing capacity (a soil's ability to withstand vertical load without failing) is directly related to soil strength.

Effect of gravity on sensitivity to wheel loading

When the wheel load was increased from 164 N to 225 N (an increase of 37%), maximum sinkage increased by an average of 14% in the 1-g experiments, and in martian-g, maximum sinkage

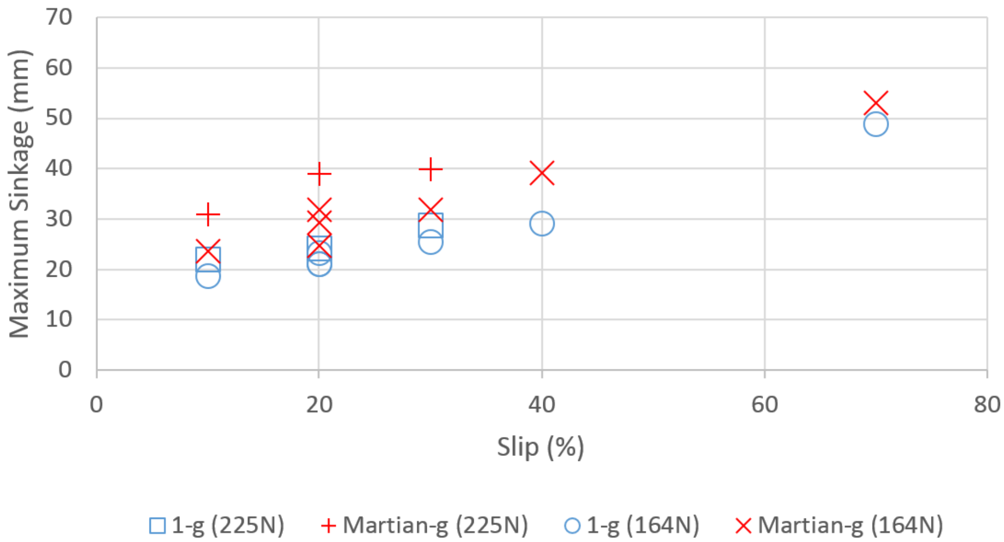

Figure 41: Maximum sinkage versus slip ratio for tests in 1-g and martian-g with wheel load setpoints of 164 N and 225 N and ES-2 density 1.45 g/cm^3.

increased by an average of 31%. This difference can be observed visually in Figure 41. This result indicates that sensitivity to wheel loading may also be increased in reduced gravity. This is again consistent with reduced soil strength and thus reduced bearing capacity. In martian-g, sinkage increases almost proportionally to the increase in load, whereas in 1-g the additional sinkage is much less than proportional. In terramechanics, such an effect may suggest a gravity dependent (static and/or dynamic) pressure–sinkage exponent.

3.2.4 Image processing

A raw image can be seen in Figure 42 with indicators illustrating that the rolling wheel is driving counterclockwise and traveling from right to left in the image.

Figures 43a, 43b, and 43c show visualizations of the magnitude of soil flow velocity for 1-g, martian-g, and lunar-g tests at 70%, 40%, and 20% slip, respectively, and Figure 43d shows the effect of wheel load setpoint on the magnitude of soil flow velocity in 1-g and martian-g. The velocities are normalized with respect to the commanded rim speed such that the color map indicates dark blue as static and dark red as maximum motion (i.e. commanded rim speed or higher). Also note that the illumination (by floodlights at both ends of the mirror) sometimes introduces artifacts in the lower corners of the images, so they have been cropped accordingly. Additionally note that the optical flow technique [157] used in this work can have the tendency to smooth over discontinuities (e.g. at the soil shear plane beneath the wheel).

Vector fields for the 70% slip tests are shown in Figure 44. Here, both the magnitude and the direction of soil flow velocity are represented, and the magnitude of the commanded rim speed is indicated by a reference arrow in the upper right of each plot.

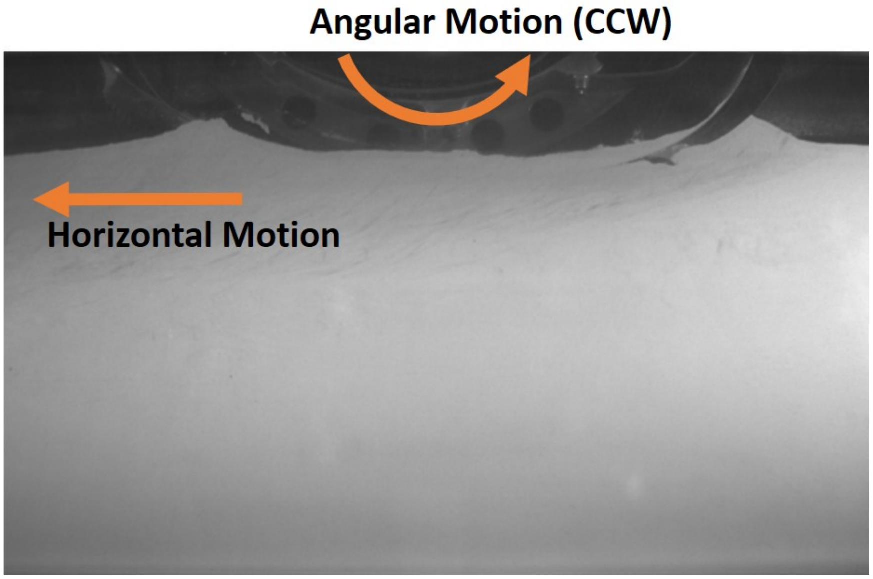

Figure 42: Image illustrating the direction of wheel motion as captured through the glass window [5]; camera field of view is shown in Figure 12a.

Effect of gravity observed in image analysis

In Figures 43a, 43b, and 43c, looking down a column shows the changes in soil motion with respect to time (averaged according to the sections identified in the sinkage data). Looking across a row compares soil motion in different gravities for a particular section of time in a test.

It is clear that at any time, and at any slip rate, there is more soil motion in partial gravity (martian and/or lunar) than in 1-g. Furthermore, there is notably more soil motion in lunar gravity than in martian gravity. In reduced gravity, shearing forces generated during wheel–soil interaction produce more soil mobilization at any slip rate at equal loading.

In lower gravity, as the wheel traverses forward in time, the regions of mobilized soil become larger and the magnitude of velocity fields increases. On the other hand, the results suggest that in 1-g, the region and magnitude of mobilized soil do not increase over time. In Figures 43a and 44, comparing the column of lunar results with the corresponding column of 1-g results illustrates the time-dependent mobility deterioration in low gravity.

Another observation is that in both 1-g and martian-g, increasing the wheel loading from 164 N to 225 N does not impact the soil mobilization significantly. Figure 43d illustrates the effect of these variations at 30% slip. From the illustrations, it is clear that the influence of gravity on the soil mobilization is much more prominent than the influence of the normal load.

Furthermore, it was observed that in all 1-g tests, there was significantly more soil motion in the sinkage valleys (i.e. just before an increase in sinkage). It appears that shear failure of the soil occurs during the valley segments, which leads to the subsequent rise in sinkage. It was also noted that in all tests, the cyclical sinkage behaviour corresponded to the position of the wheel's leaf-springs. In reduced gravity, the experiments at lower slip ratios (e.g. 20% slip, as seen in Figure 43c) exhibit a similar pattern with the highest amount of soil motion occurring in the valleys, but at higher slip ratios (e.g. at 30% and 40% slip, as seen in Figures 43d and 43b, respectively), there is more motion earlier in the cycle (during the sinkage falls), indicating that soil failure occurs

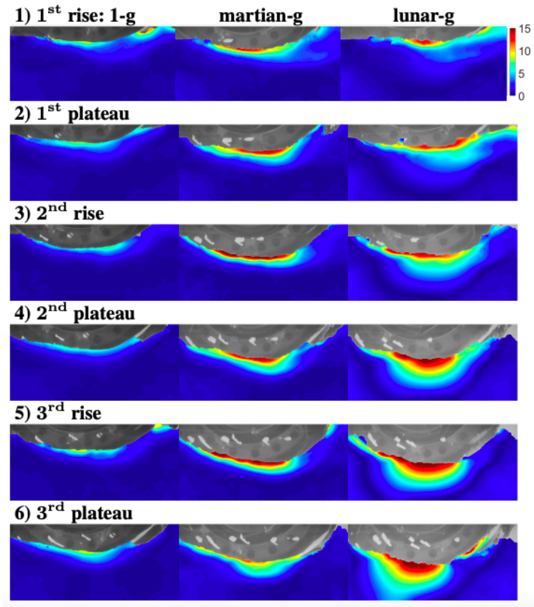

(a) From left to right, tests in 1-g, martian-g, and lunar-g at 70% slip and 164 N wheel load, averaged over sinkage rise and plateau segments as demonstrated in Figure 37a.

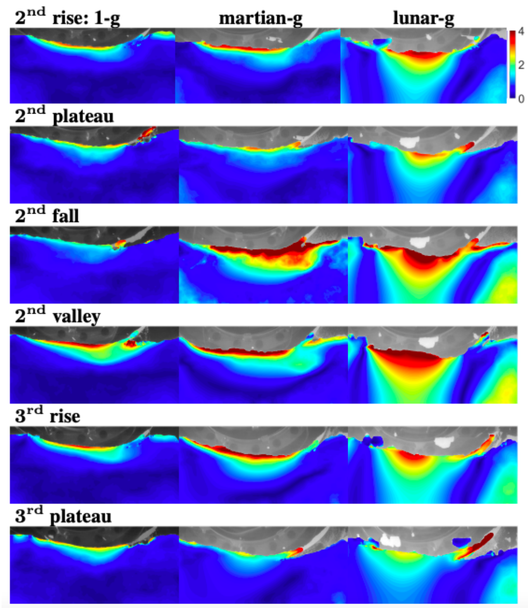

(b) From left to right, tests in 1-g, martian-g, and lunar-g at 40% slip and 164 N wheel load, averaged over sinkage plateau, fall, valley, and rise segments as demonstrated in Figure 37b.

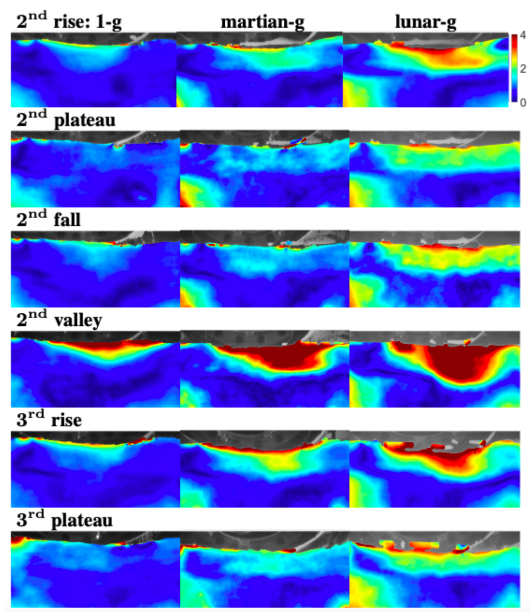

(c) From left to right, tests in 1-g, martian-g, and lunar-g at 20% slip and 164 N wheel load, averaged over sinkage plateau, fall, valley, and rise segments as demonstrated in Figure 37b.

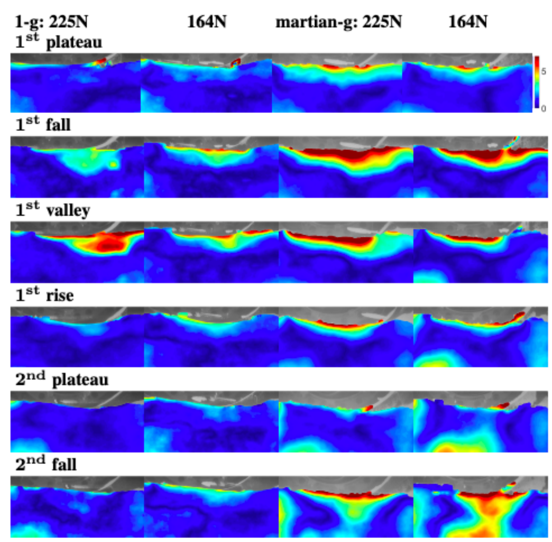

(d) Tests with wheel load setpoints of 164 N and 225 N in 1-g and martian-g, at 30% slip. Results are averaged over sinkage plateau, fall, valley, and rise segments as demonstrated in Figure 37b.

Figure 43: Visualizations of magnitude of soil flow velocity. The colorbars indicate velocity in mm/s (with the maximum being commanded rim speed). ES-2 density setpoint was 1.45 g/cm^3 for all tests.

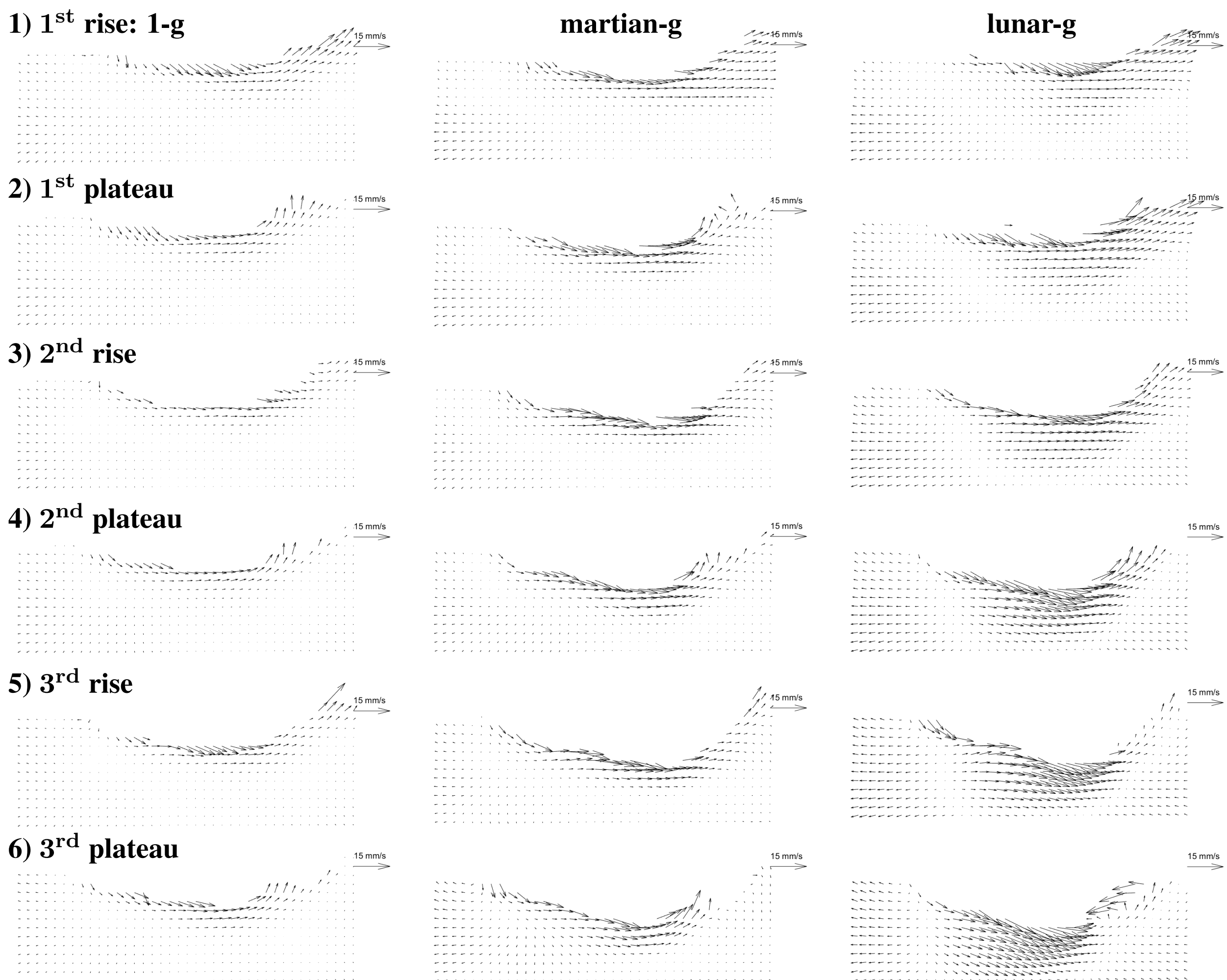

Figure 44: Velocity fields for, from left to right, tests in 1-g, martian-g, and lunar-g, at 70% slip and 164 N wheel load, averaged over sinkage rise and plateau segments as demonstrated in Figure 37a. Arrows labelled 15 mm/s indicate magnitude of commanded rim speed. ES-2 density setpoint was 1.45 g/cm^3 for all tests.

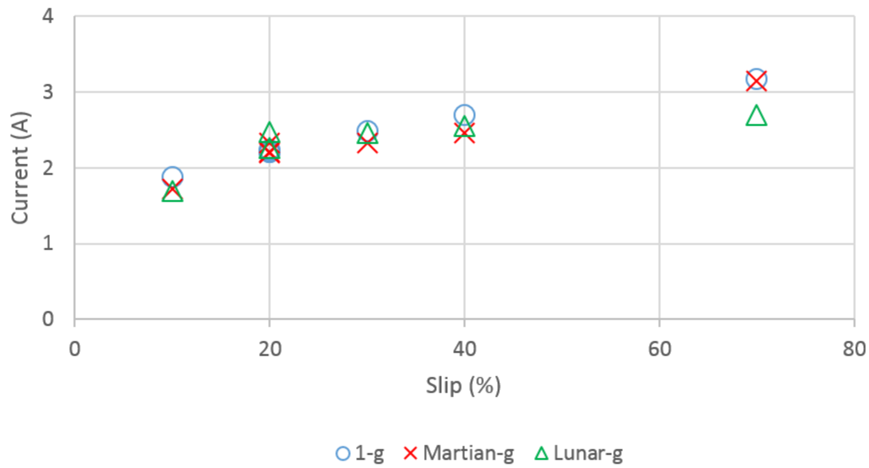

Figure 45: Average drive motor current versus slip ratio for tests in 1-g, martian-g, and lunar-g with wheel load setpoints of 164 N and ES-2 density of 1.45 g/cm^3.

more readily in reduced gravity. There is also more soil motion during the sinkage rise segments in reduced gravity, which reveals that increased soil motion continues for a longer period of time after failure.

In summary, gravity has a significant effect on the wheel–soil interaction at equal slip and wheel loading. Moreover, under the influence of lower gravity, these interactions are more variable in time than in 1-g. The greater soil mobilization observed in reduced-g is consistent with reduced soil strength, as more soil motion demonstrates a greater propensity for the soil to fail.

3.2.5 Drive motor current

Figure 45 shows average drive motor current versus slip for tests in 1-g, martian-g, and lunar-g with 164 N wheel load setpoints, and Figure 46 shows average drive motor current versus slip for tests in 1-g and martian-g with 225 N wheel load setpoints.

Effect of gravity on drive motor current

There is no significant difference observed in drive motor current between the effective gravity levels. In the 225 N wheel load tests, the average current was slightly lower in martian-g than in 1-g, but this difference was not statistically significant ($p = 0.097$). The lack of difference in motor current is, however, consistent with the differences observed in the corresponding sinkage measurements. Normally, it is expected that more motor current is required when more sinkage is encountered under equivalent soil strength. However, in the reduced-gravity experiments, sinkage increased significantly, but motor current did not. This discrepancy can be attributed to decreased soil strength in lower gravity.

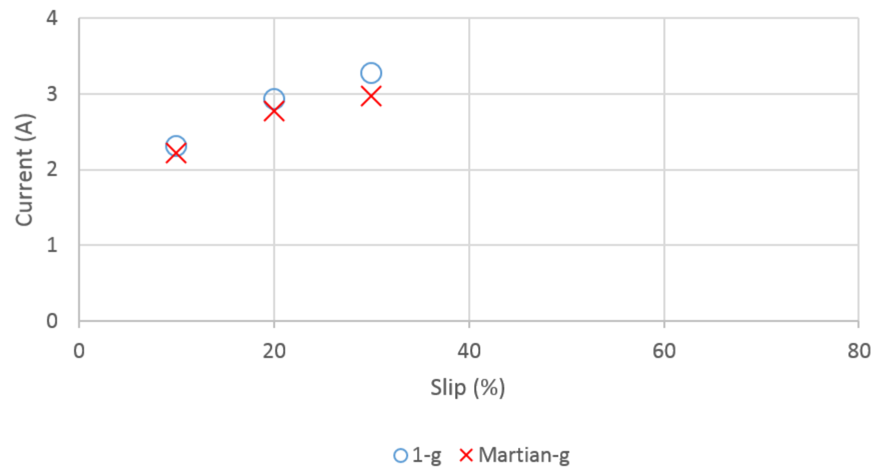

Figure 46: Average drive motor current versus slip ratio for tests in 1-g and martian-g with wheel load setpoints of 225 N and ES-2 density of 1.45 g/cm^3.

3.3 Chapter summary and conclusion

This work was the first to directly observe rover wheel–soil interactions in reduced gravity, aboard parabolic flights achieving martian and lunar gravitational accelerations. A Rosalind Franklin rover wheel prototype was operated against a glass window along the side of a sandbox, and the wheel–soil interactions were visualized using a previously established computer vision technique. Results are compared to experiments conducted in Earth gravity.

Controlling the wheel slip and wheel load ensures that the only difference between experiments is the effect of gravity on the soil particles themselves. It is important to consider that these differences between experiments are equivalent to the difference between actually driving a rover on Mars and testing a reduced-mass or gravity-offloaded version of the rover (i.e. with equal wheel normal load) in similar soil on Earth.

Optical flow–based visualization of the soil motion (imaged with a high-speed camera) shows that more soil is mobilized by the wheel in reduced gravity. More soil motion is observed in martian-g than in 1-g and, especially at high slip, even more is observed in lunar-g. More variation in soil motion with respect to time is also observed in reduced-g than at 1-g. Analysis of the force data from the instrumented wheel experiments shows monotonically decreasing drawbar pull as gravity is reduced. F_{DP} (at equal normal load and slip) is 8% lower on average in martian-g than in 1-g, and F_{DP} in lunar-g shows a statistically significant 20% reduction compared to 1-g. Sinkage is statistically significantly higher in reduced-g than in 1-g. All of these results are consistent with a weakening of soil strength in reduced gravity.

All of the above observations hinder a rover's ability to drive, and must be taken into consideration when interpreting results from mobility tests on Earth where only wheel load is reduced proportionally to the target reduction in gravity. The quantitative results suggest a starting point for factors of safety that could be applied when designing planetary rover wheels to meet minimum traction and/or maximum sinkage requirements. Further, this work demonstrates the need for new models and test methods that take into account the effect of reduced gravity on soil behaviour.

Chapter 4

The equal G method and granular scaling laws (GSL)

As demonstrated in Chapter 3, new test methods for planetary rovers that take into account the effect of reduced gravity on soil behaviour are required. Two methods that aim to do so were introduced in Section 1.4.2: matching the soil's cone penetrometer response (cone index gradient, G, thus called the equal G method), and granular scaling laws (GSL).

The soil simulant GRC-1 is designed to produce cone penetrometer readings comparable to those collected on the Moon (i.e. in lunar gravity) during Apollo. The underlying assumption is that replicating the mechanical properties of lunar soil in terms of cone penetration resistance will also replicate the response to vehicle loading in terms of traction. See Section 2.3.2 for more information about this simulant.

Granular scaling laws (GSL) have recently been proposed in the literature that are analogous to scaling relations employed in the fields of aero- and hydrodynamics. These granular scaling relations were developed in order to predict experiments with a larger wheel based on tests with a smaller wheel, or to predict experiments in one gravity level based on tests in another gravity level.

Prior to the work presented here, neither of these methods had been experimentally validated in reduced gravity. Experiments were conducted with the testbed described in Section 2.1.2 to assess the accuracy of these methods by measuring performance of a single wheel (see Section 2.2.2, Figure 16) driving in GRC-1 aboard parabolic flights that reproduce the effects of reduced gravity, and comparing those results to data collected on the ground using each method. Based on these tests, the granular scaling laws show greater promise. The method of matching the soil's cone penetrometer response, however, did not prove to be as successful.

This work is listed as contribution 1.2 in Section 1.5, and the topics explored in this chapter are highlighted in Figure 47. This chapter includes a summary of work on the equal G method published previously [181] and on the GSL method, submitted for publication in *Microgravity Science and Technology*.

4.1 Granular scaling laws (GSL)

As described in Section 1.4.2, granular scaling laws (GSL) are analogous to scaling relations employed in the fields of aero- and hydrodynamics that use dimensionless numbers such as the

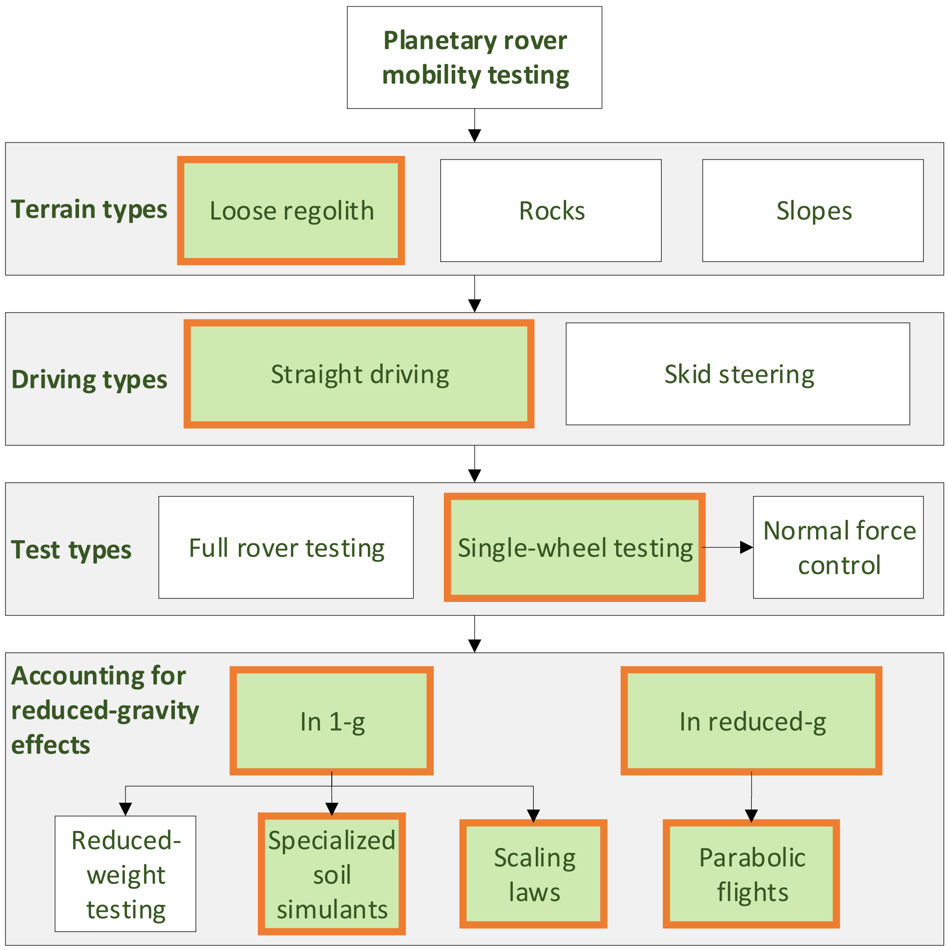

Figure 47: Diagram depicting the topics studied in this thesis, with major topics highlighted in green. The specific topics studied in this chapter are highlighted in orange.

Reynold's number. These scaling relations, recently proposed by [8], can be used to predict wheel performance in one gravity level based on tests in another gravity level.

4.1.1 Derivation of granular scaling laws

Granular scaling laws have been derived from several different starting points. Slonaker et al. [8] derived their scaling laws starting from Resistive Force Theory (RFT), which is an empirical force model for bodies moving freely in granular media [182], and with the help of some assumptions, they also arrived at the same scaling relations when commencing their derivation from Coulomb plasticity theory [183]. Then, Zhang et al. [59] derived similar scaling relations accounting for cohesion and sloped terrain starting from a simple continuum model and an assumed constitutive relation for cohesion.

Previous to the derivations of Slonaker and Zhang, Kanamori [61] derived very similar scaling laws with a classical mechanics approach. Using approaches involving classical terramechanics, Schuring [184] and later Li et al. [64] derived similar scaling laws that were independent of cohesion (whereas Kanamori's laws inherently included the same cohesion constraint that Zhang later derived). The work here focuses on the version derived by Slonaker et al. [8] as it is more general than the previously derived versions.

The granular scaling relation that Slonaker et al. derived (starting from both RFT and Coulomb plasticity) can be seen in Equation 11 [8]. This form of the equation assumes that the wheel surface texture and the granular media are fixed for a pair of scaled tests. Then, with a standard nondimensionalization, the wheel's steady driving limit cycle is assumed to follow the form:

$$\left[\frac{P}{Mg\sqrt{Lg}}, \frac{V}{\sqrt{Lg}}\right] = \Psi\left(\sqrt{\frac{g}{L}}t, f, \frac{g}{L\omega^2}, \frac{\rho D L^2}{M}\right) \tag{11}$$

where Ψ is some unspecified 4-input, 2-output function, P is the power expended, M is the wheel mass, g is the gravitational acceleration, L is the characteristic length (in the case of a wheel, its radius), V is the horizontal velocity of the wheel, t is time, f is a set of points defining the wheel shape, ω is the wheel's angular velocity, ρ is the bulk density of the soil, and D is the wheel width. Each term in Equation 11 is dimensionless. The Froude number, $\mathrm{Fr} = V/\sqrt{Lg}$, is the ratio of inertial forces to gravitational forces. GSL is based on a steady-state, quasi-rate-independent/ quasi-static assumption [8] (i.e. $\mathrm{Fr} < 1$)[1]. Note that the term $g/L\omega^2$ is another Froude-like number in the GSL formulation. V and ω are related to each other by the slip ratio (Equation 1).

Assuming the tests have the same wheel shape, f, and bulk density, ρ, with one test having inputs (g, L, M, D, ω), and a second test having inputs (g', L', M', D', ω') = (qg, rL, sM, $sr^{-2}D$, $q^{1/2}r^{-1/2}\omega$) for any positive scalars q, r, and s, each test has the same non-dimensional inputs to the function Ψ (except non-dimensional time). Then, the corresponding driving cycles are assumed to follow $< P' >= q^{3/2}r^{1/2}s < P >$ and $< V' >= q^{1/2}r^{1/2} < V >$.

One further modification proposed by Slonaker et al. is the addition of a constant drawbar pull force, F_{DP}, as an input, shown in Equation 12 [8]. This additional term was not validated experimentally or numerically.

[1]True rate-independence would be achieved at $\mathrm{Fr} \leq 10^{-3}$ [185].

$$\left[\frac{P}{Mg\sqrt{Lg}}, \frac{V}{\sqrt{Lg}}\right] = \Psi\left(\sqrt{\frac{g}{L}}t, f, \frac{g}{L\omega^2}, \frac{\rho D L^2}{M}, \frac{F_{DP}}{Mg}\right) \tag{12}$$

4.1.2 Expansion of granular scaling laws

Starting from Equation 12, the nondimensional drawbar pull term (F_{DP}/Mg) proposed by Slonaker et al. [8] was moved to the left side of the equation, as in our experiments F_{DP} is a measured output, not a constant input. Note that there are two methods of conducting single-wheel terramechanics experiments: controlled slip (where a constant slip ratio is imposed) and controlled pull (where a constant drawbar pull force is applied to the wheel). While controlled pull tests more closely resemble the conditions that an actual wheel would experience, it has been shown that controlled slip tests are preferable (in terms of ease of measurement and control) for obtaining drawbar pull vs. slip curves (a standard method for characterizing wheel performance), while still generating equivalent final results [186]. This work represents the first time the nondimensional F_{DP} term (F_{DP}/Mg) in GSL is validated experimentally; the validation by experiment or simulation had been left as suggested future work in the literature [8].

Similarly, the Froude number (i.e. the nondimensional velocity term), $V/\sqrt{Lg}$, was moved to the right side of the equation, as in our experiments, the horizontal velocity is controlled in order to achieve a constant slip ratio. Furthermore, a new output term was added: nondimensional sinkage, z/L, as sinkage is an important output measured in these experiments (see Section 1.2.2). The modified function (Equation 13) is called Ω.

$$\left[\frac{F_{DP}}{Mg}, \frac{z}{L}, \frac{P}{Mg\sqrt{Lg}}\right] = \Omega\left(\sqrt{\frac{g}{L}}t, f, \frac{g}{L\omega^2}, \frac{\rho D L^2}{M}, \frac{V}{\sqrt{Lg}}\right) \tag{13}$$

Utilizing the framework outlined in Section 4.1.1, assuming f and ρ are the same between test pairs, with one test having inputs (g, L, M, D, ω, V), and a second test having inputs (g', L', M', D', ω', V') = (qg, rL, sM, $sr^{-2}D$, $q^{1/2}r^{-1/2}\omega$, $q^{1/2}r^{1/2}V$), the scalars q, r, and s (which scale the gravity, wheel radius, and mass, respectively) can be chosen arbitrarily, and the inputs to the unspecified function Ω will remain the same for each case. For example, looking at the term $\frac{V}{\sqrt{Lg}}$ and applying the scaling factors for horizontal velocity ($V' = q^{1/2}r^{1/2}V$), gravity ($g' = qg$), and radius ($L' = rL$), the term becomes $\frac{q^{1/2}r^{1/2}V}{\sqrt{rL \cdot qg}}$, which simplifies to $\frac{V}{\sqrt{Lg}}$. In other words, $\frac{V'}{\sqrt{L'g'}} = \frac{V}{\sqrt{Lg}}$. Also note that the slip ratio between any set of tests will be equal, as shown in Equation 14. Correspondingly, the outputs F_{DP}, z, and P scale such that (F'_{DP}, z', P') = (qsF_{DP}, rz, $q^{3/2}r^{1/2}sP$).

$$
\begin{aligned}
S &= \frac{L\omega - V}{L\omega} \times 100\% \\
S' &= \frac{L'\omega' - V'}{L'\omega'} \times 100\% \\
S' &= \frac{rL \cdot q^{1/2} r^{-1/2} \omega - q^{1/2} r^{1/2} V}{rL \cdot q^{1/2} r^{-1/2} \omega} \times 100\% \\
S' &= \frac{q^{1/2} r^{1/2} L\omega - q^{1/2} r^{1/2} V}{q^{1/2} r^{1/2} L\omega} \times 100\% \\
S' &= \frac{L\omega - V}{L\omega} \times 100\% \\
S' &= S
\end{aligned}
\tag{14}
$$

4.2 Experimental parameters

Experiments were performed to evaluate the GSL and equal G methods. Cone penetrometer experiments were performed to determine soil parameters in reduced-g and 1-g, while wheel experiments measured mobility metrics. The number of cone penetrometer and wheel experiments performed at each combination of input parameter settings is shown in Table 5. Note that all wheel experiments were performed with the larger (300 mm diameter/ 150 mm radius) wheel shown in Figure 16 except for the GSL experiments, which were performed with the smaller (150 mm diameter/ 75 mm radius) wheel.

To evaluate GSL experimentally, with q fixed by the relative gravity levels investigated (q = 6 since the gravity on Earth is 6$\times$ higher than lunar gravity), r, and s were chosen such that the inputs and outputs fit within the operating limits of the testbed. The chosen inputs for GSL tests in 1-g that are meant to predict tests in lunar-g, and their corresponding outputs, can be seen in Table 6. Note that the Froude number in these experiments was $\sim$0.01, thus the quasi-static assumption applies.

In all experiments, the wheel load was set to 164 N in order to match previous experiments using this apparatus (Chapter 3). In those experiments, the wheel load was based on ESA's Rosalind Franklin rover (for the ExoMars mission). However, it should be noted that this wheel load may be somewhat high for lunar rovers with the same wheel size. For example, NASA's upcoming VIPER rover will have a load of approximately 200 N per wheel, but its wheels are larger (500 mm diameter) [187]. In contrast, CNSA's Yutu rovers have wheel loads of approximately 40 N, and wheel diameters of 300 mm [188].

4.2.1 Soil preparation

Each soil preparation procedure begins with blowing air through the manifolds in the bottom of the sandbox for 2000 ms. To prepare the soil to a relative density of 0%, no vibration is performed after the "puffing" step. To prepare to soil to 6% D_R, vibration at 32 Hz for 500 ms is performed. To prepare the soil to relative densities of 46%, 63%, or 69%, vibration is performed for 2000 ms one, two, or three times, respectively, with breaks of 650 ms between vibrations. Relative density (D_R) was calculated from the 1-g data based on the correlation between cone index gradient (G, defined

Table 5: Number of experiments performed at each combination of parameter settings. All tests conducted in GRC-1. Wheel experiments all had a vertical load setpoint of 164 N and angular velocity of 0.13 rad/s, except for the GSL experiments which had an angular velocity of 0.45 rad/s. Each cone penetrometer experiment consists of readings from two locations in the sandbox.

				Wheel experiments	
Gravity	ρ (g/cm^3)	D_R	Cone penetrometer experiments	20% slip	70% slip
1-g	1.79 ± 0.02	$69 \pm 4\%$	3	3 (GSL)	3 (GSL)
1-g	1.78 ± 0.03	$63 \pm 6\%$	2	-	-
1-g	1.72 ± 0.01	$46 \pm 4\%$	3	-	-
1-g	1.61 ± 0.003	$6 \pm 1\%$	3	3 (equal G)	3 (equal G)
1-g	1.60 ± 0.002	$0 \pm 1\%$	3	3	3
1/6-g	1.79 ± 0.02	$69 \pm 4\%$	3	4	3
1/6-g	1.78 ± 0.03	$63 \pm 6\%$	2	-	-
1/6-g	1.72 ± 0.01	$46 \pm 4\%$	2	-	-

Table 6: Inputs and outputs for the GSL experiments relative to the lunar-g experiments with q = 6, $r = 1/2$, and $s = 1/6$.

	Inputs					Outputs			
Lunar-g	g	L	M	D	ω	V	F_{DP}	z	P
1-g	$6g$	$1/2\,L$	$1/6\,M$	$2/3\,D$	$2\sqrt{3}\,\omega$	$\sqrt{3}\,V$	F_{DP}	$1/2\,z$	$\sqrt{3}\,P$

Table 7: Average measured cone index gradient, G, and corresponding derived relative density, D_R, and bulk density, ρ, achieved by each soil preparation procedure in 1-g.

Vibration (ms)	Average G (kPa/mm)	Average D_R	Average ρ (g/cm^3)
0	0.8 ± 0.1	0 ± 1%	1.60 ± 0.002
1 × 500	2.0 ± 0.1	6 ± 1%	1.61 ± 0.003
1 × 2000	5.4 ± 0.4	46 ± 4%	1.72 ± 0.01
2 × 2000	6.8 ± 0.5	63 ± 6%	1.78 ± 0.03
3 × 2000	7.4 ± 0.4	69 ± 4%	1.79 ± 0.02

in Section 2.4.3) and D_R presented by [2]. Average G values and relative densities achieved by each soil preparation procedure can be seen in Table 7.

4.3 Experimental uncertainty

As discussed in Section 3.2.1, the soil preparation procedure introduces some random error, in addition to the variability in gravity level during the flights. However, IMU data from the flights (e.g. Figure 22) shows that although the gravity levels were not perfectly constant and consistent, the variations within and between tests are much smaller than between 1/6-g and 1-g.

Additionally, as mentioned in Section 2.4.4, a correction was applied to the F_{DP} data based on the estimated coefficient of friction between the felt covering the wheels and the glass sidewall of the sandbox. Any error in the estimated friction coefficient would contribute to experimental error in the drawbar pull results.

Furthermore, despite the aircraft's pitch attitude being maintained at 0° during soil preparation, the soil level became sloped after vibration. The slope angle was estimated from each video (an average slope of 6° was observed) and corrections were applied to the F_{DP} and sinkage data. The derivation and validation of these corrections are discussed in Appendix A.

Finally, there is also the further difference between reduced-g experiments done in flight and 1-g experiments performed in a stable laboratory environment (with a more rigid substrate and less vibration). However, the goal of the wheel experiments was to compare wheel performance at different densities in different gravity levels, and the effect of gravity is certainly much larger than any effect of being in flight vs. on the ground, as observed previously in Chapter 3. Previous publications [181, 155] provide a more detailed discussion of experimental uncertainty in the parabolic flight experiments.

4.4 Results and discussion

4.4.1 Cone penetrometer results

Figure 48 shows cone index gradient (G) values from the three different soil preparation procedures performed in flight (46%, 63%, and 69% D_R). Since two cone penetrometer insertions were performed for each soil preparation, the number of data points for each combination of parameter settings is twice the number of experiments shown in Table 4. On average, G values measured after the same soil preparation were 4× lower in 1/6-g than in 1-g. Since cone penetrometer measurements are an indication of both compaction and shear strength, and the compaction (density) did not change (as soil preparation was performed in the 1-g phase of flight, and no change to the soil level was observed upon entering 1/6-g), this indicates a considerable decrease in soil strength in reduced gravity. This reduction in soil strength was also suggested by the earlier observations discussed in Chapter 3. Figure 48 also includes the G values of the lower-density (6% D_R) soil that was found to produce an average G value in 1-g equal to that measured at the highest density (69% D_R) tested in 1/6-g; G = 2.0 kPa/mm in both cases. Additionally, the G values measured at the lowest achievable density (0% D_R) are shown, G = 0.8 kPa/mm. Wheel experiments testing the equal G method were conducted at 6% relative density in 1-g and 69% relative density in 1/6-g, as highlighted in the figure. Recall that the wheel experiments at 6% in 1-g and 69% in 1/6-g, producing equal average G, are of particular interest to test the hypothesis that equal G (even across varying gravity) will produce equivalent wheel response. Supplementary wheel experiments were also conducted at 0% D_R in 1-g, discussed further in Section 4.4.2. Finally, wheel experiments testing the GSL method were conducted with a smaller wheel in 1-g at 69% D_R (i.e. the same density as the lunar-g experiments).

4.4.2 Wheel experiment results

Comparison of the lunar-g results to the predicted drawbar pull–weight ratio (F_{DP}/W, equivalent to F_{DP}/Mg in Equation 13), sinkage, and power using each method (equal G and GSL) can be seen in Figure 49. Note that the outputs from the 1-g tests with the small wheel were divided by the scaling factors shown in Table 6 in order to compute the predicted lunar-g outputs. Additionally, the time scale for the 1-g experiments was divided by $2\sqrt{3}$, since the dimensionless time term is $\sqrt{\frac{g}{L}}t$, and time is therefore scaled by $\sqrt{\frac{g}{r}}$ or $\sqrt{\frac{6}{(1/2)}} = 2\sqrt{3}$. Furthermore, to compute F_{DP}/W over time, the measured (and corrected) drawbar pull was divided by the measured normal force at each time step (the normal force fluctuates in this testbed due to friction in the vertical axis, as discussed previously in Section 2.5). Each line in the figures represents the average of three to four experimental repeats. The mean and 95% confidence interval of the repeats were computed at each time step, and the 95% confidence intervals are shown in the figures as light-coloured bars around the average lines.

Comparing Figures 49a and 49b, F_{DP}/W was higher at 70% slip than at 20% slip, as expected based on previous experiments with this wheel and soil [128]. At 20% slip (Figure 49a), the GSL prediction and lunar-g results were very similar throughout the experiment, with slightly lower F_{DP}/W predicted by the GSL experiment as the tests approached a steady state. On the other hand, the equal G method predicted higher F_{DP}/W throughout the experiment. At 70% slip (Figure 49b), F_{DP}/W predicted with the GSL method was initially much lower than F_{DP}/W measured in 1/6-g, but as the experiments approached steady-state, the predicted F_{DP}/W began to approach the lunar-g values. Since GSL development is based on a steady-state assumption [8] (the assumed start of GSL validity for our analysis is marked on the figures), lower initial accuracy at 70% slip may be due to the fact that the 70% slip case was further away from steady-state (i.e. F_{DP} was changing more rapidly). At higher slip, the wheel rim is spinning faster relative to the soil, thus the strain rate is higher and the scenario moves further away from the quasi-static assumption.

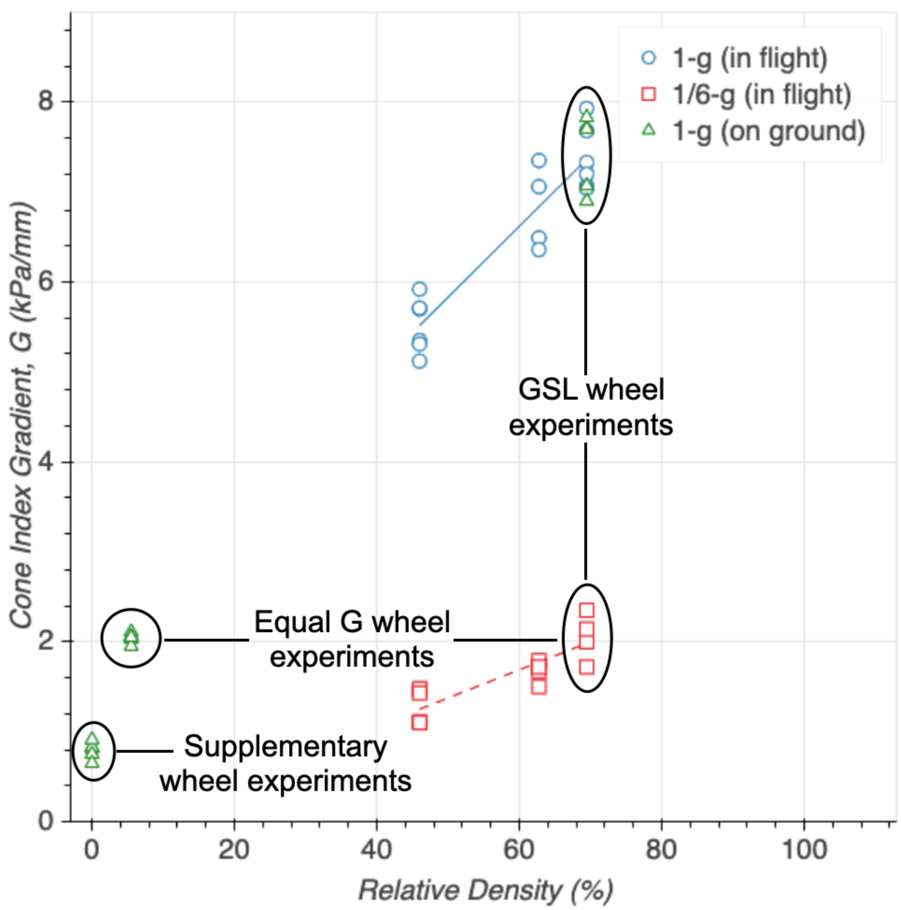

Figure 48: Cone index gradient (G) values obtained in flight in 1-g and 1/6-g at relative densities of 46% (1.72 g/cm^3), 63% (1.78 g/cm^3), and 69% (1.79 g/cm^3), and later on the ground at relative densities of 6% (1.61 g/cm^3) and 0% (1.60 g/cm^3).

The rim speed ($L\omega - V$) could be used instead of only the horizontal velocity V in the numerator of the Froude number to capture this. In the equal G test, the predicted F_{DP}/W was initially lower than the lunar-g results, but as the experiments approached steady-state, F_{DP}/W was higher in the 1-g equal G tests than in 1/6-g.

Comparing Figures 49c and 49d, sinkage was higher at 70% slip than at 20% slip, as expected, due to slip-sinkage. At both 20% and 70% slip, sinkage predicted by the GSL tests was lower during the first few seconds of the experiments. However, as the experiments reached a quasi steady-state (after about 5 seconds), the sinkage prediction was almost perfect at 20% slip, and sinkage was overestimated at 70% slip (again, higher error at 70% slip may be due to further deviation from the steady-state assumption in comparison to the 20% slip case). At both slip values tested, sinkage predicted by the equal G method was lower than what was seen in the lunar-g tests, although at 70% slip the two experiments had very similar sinkage for the first few seconds.

Looking at Figures 49e and 49f, more power was required at 70% slip than at 20% slip, as expected, due to higher sinkage and therefore more resistance. At 20% slip, the power requirements predicted by the GSL tests were very close to the lunar-g results during the first few seconds of the experiments, and then slightly higher when the tests reached a steady state. Conversely, at 70% slip, the power requirements were underestimated for the first few seconds of the tests, and as the experiments reached steady state, the prediction was much more accurate. In both cases, the equal G method slightly overestimated the power requirements. This could be due to increased soil resistance as a result of higher soil strength in 1-g. Even though the sinkage was lower in 1-g (at G = 2 kPa/mm) than in 1/6-g, slightly more power was required, again suggesting that the soil was significantly stronger in 1-g.

Mean squared percent error (MSPE) values comparing the GSL and equal G predictions to the lunar-g results can be found in Table 8. The MSPE was calculated from 5–20 s, when the experiments were in a quasi-steady state (i.e. after the initial transients at the start of the experiment had passed). Looking at the MSPE of the equal G experiments in 1-g, which tested the assumption that wheel performance would be equivalent in different gravity levels if the cone penetrometer response is equivalent, the predicted wheel performance was less accurate at 20% slip than at 70% slip; note that 20% slip is a more common case for planetary rovers than 70% slip. Also recall that F_{DP}/W was overestimated (Figures 49a and 49b) and sinkage was underestimated at both 20% and 70% slip (Figures 49c and 49d). Thus, wheel performance was overestimated at both slips tested. On the other hand, power requirements were slightly overestimated, by 4.5% on average. All MSPEs for GSL were less than 10%, demonstrating that this method can provide accurate predictions of F_{DP}/W, sinkage, and power requirements. Furthermore, recall that F_{DP}/W was underestimated at both 20% and 70% slip, sinkage was overestimated at 70% slip, and power requirements were overestimated at 20% slip, indicating that this prediction method is not only accurate, but also conservative (lower F_{DP}, higher sinkage, and higher power requirements correspond to poorer wheel performance). Of course, the observed differences may also be attributed to any of the sources of experimental error discussed in Section 4.3.

Cone penetrometer measurements (G values) are influenced by both density and shear strength. Shear strength itself is affected by both density and gravity. The cone penetrometer results in Figure 48 demonstrated a significant dependency of shear strength on gravity when density was equal. In the equal G (G = 2.0 kPa/mm) wheel experiments, the density in the 1-g experiments was modified to match the average G value measured in 1/6-g. Thus, the density in the 1-g experiments was lower, but in order to have the same G value, shear strength must have been much higher. Drawbar

Table 8: Mean squared percentage error (MSPE) from 5–20 s. All tests performed in GRC-1. Lunar-g and GSL tests performed at 69% D_R (1.79 g/cm^3); equal G method tests performed at 6% D_R (1.61 g/cm^3).

	Method 1: Equal cone index gradient (G)			Method 2: Granular scaling laws (GSL)		
	20% slip	70% slip	Average	20% slip	70% slip	Average
F_{DP}/W	76%	12%	44%	9%	8%	8.5%
Sinkage	21%	6%	13.5%	0.4%	5%	2.7%
Power	8%	1%	4.5%	7%	0.6%	3.8%

pull and sinkage are also influenced by density and shear strength. Drawbar pull is expected to increase with increasing density, and to increase with increasing shear strength. On the other hand, sinkage is expected to decrease with increasing density and/or shear strength. Comparing the lunar-g experiments to the equal G experiments in 1-g, relative density and shear strength both changed, but in opposite directions, so it would be difficult to intuitively predict how this would affect F_{DP} and sinkage. Looking at the experimental results, it appears that F_{DP} and sinkage were influenced more by the change in shear strength (and therefore by the change in gravity) than they were by the change in density. Specifically, in lunar-g, shear strength was lower, leading to lower F_{DP} and higher sinkage, even though the density was much higher, and in the G = 2.0 kPa/mm experiments in 1-g, shear strength was higher, which resulted in higher F_{DP} and lower sinkage, despite the density being much lower. If F_{DP} and sinkage were more affected by density than by the effect of gravity on shear strength, the opposite trend would have been observed. Thus, these results indicate that gravity's effect on shear strength has a greater influence on F_{DP} and sinkage than density does, and that wheel performance in a lower shear strength condition (i.e. low gravity) cannot be replicated by simply reducing density. In summary, the assumption made during the creation of GRC-1 is not quite accurate, and equivalent G values did not result in equivalent wheel performance.

Soil flow visualizations

Figures 50 and 51 show visualizations of the magnitude of soil flow velocity at 20% and 70% slip, respectively, for the lunar-g tests with the large wheel, the 1-g tests with the small wheel (GSL), and the 1-g tests with the large wheel (equal G), averaged over 5 second periods. Note that the time scale for the GSL experiments was converted to "lunar time" (i.e. divided by $2\sqrt{3}$, since the dimensionless time term is $\sqrt{\frac{g}{L}}t$, and time is therefore scaled by $\sqrt{\frac{g}{r}}$). Additionally, the velocities are normalized with respect to the commanded rim speed such that the colormap indicates black as static and light yellow as maximum motion (i.e. commanded rim speed or higher). Note that the wheels are traveling from right to left in these images. Additionally note that the optical flow technique [157] used in this work can have the tendency to smooth over discontinuities (e.g. at the soil shear plane beneath the wheel). The geometry of the soil motion regions is similar between the 1/6-g and GSL tests in both Figures 50 and 51, demonstrating that the soil behaviour is analogous between the pair of scaled tests. Of course, the region of soil motion is smaller in tests with the small wheel. Comparing the size of the regions of soil motion in the lunar-g and

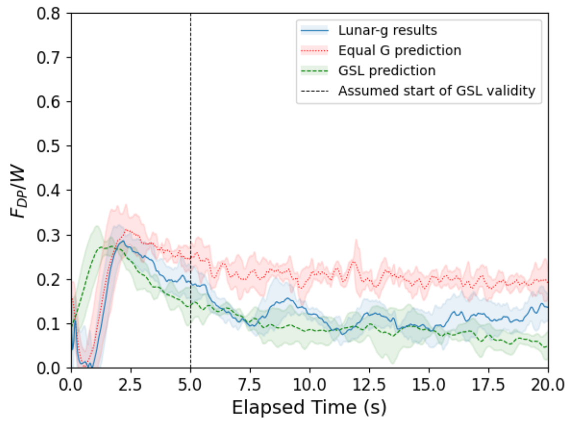

(a) F_{DP}/W, 20% slip

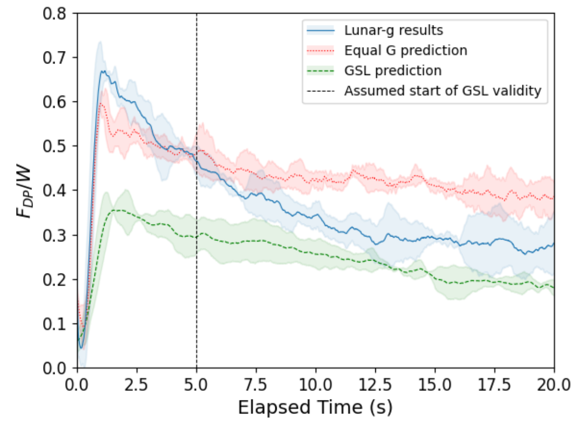

(b) F_{DP}/W, 70% slip

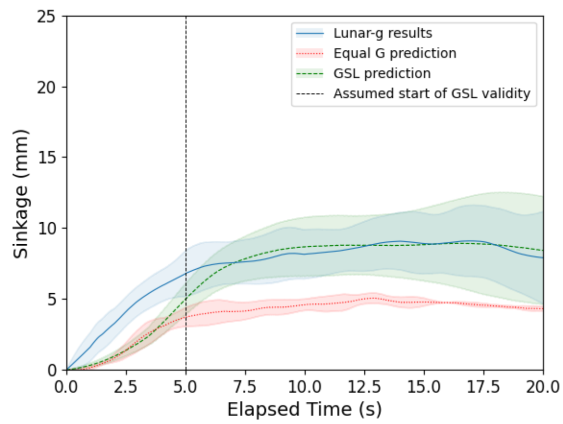

(c) Sinkage, 20% slip

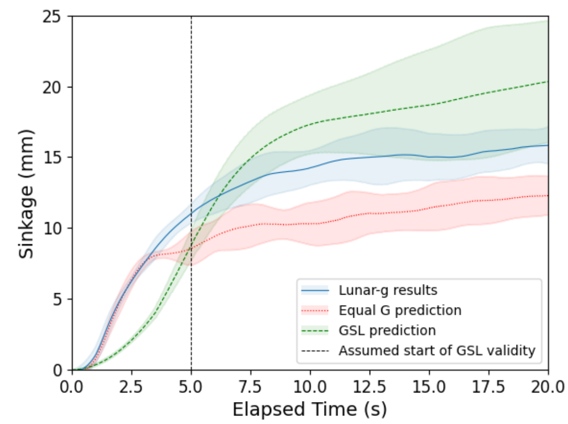

(d) Sinkage, 70% slip

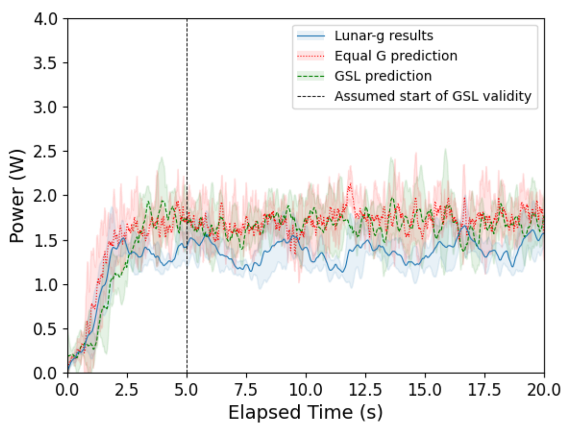

(e) Power, 20% slip

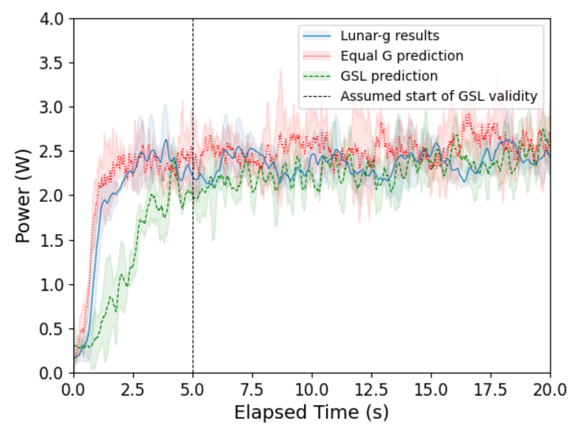

(f) Power, 70% slip

Figure 49: Drawbar pull–weight ratio (F_{DP}/W), sinkage, and power measured in lunar-g compared to equal G and GSL predictions, all performed in GRC-1. Each line consists of an average of three to four experimental repeats. Light-coloured regions represent 95% confidence intervals. Lunar-g and GSL tests performed at 69% D_R (1.79 g/cm^3); equal G method tests performed at 6% D_R (1.61 g/cm^3). The assumed start of quasi-steady state (i.e. GSL validity) is additionally marked.

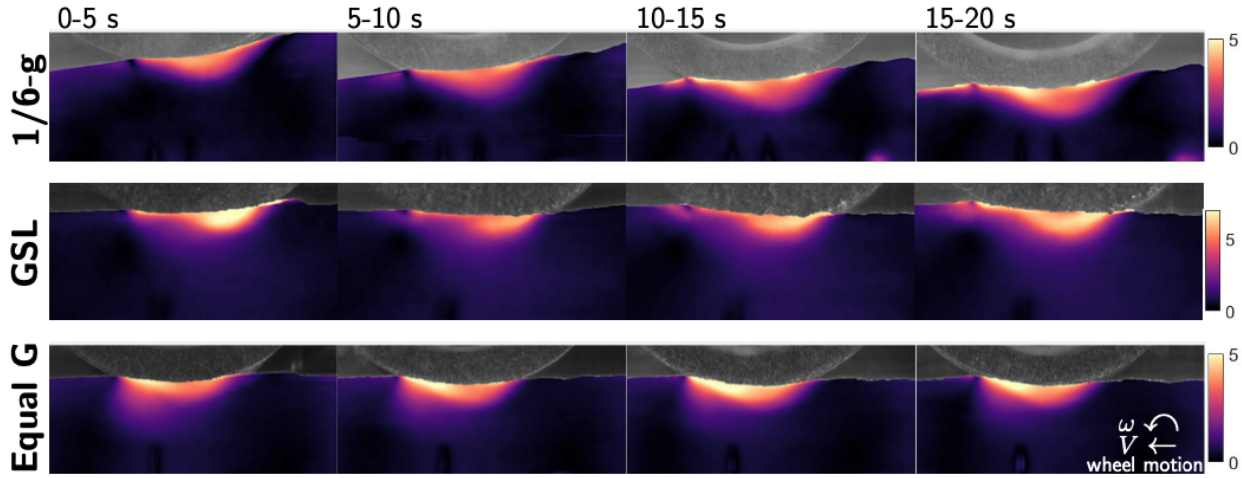

Figure 50: Visualizations of magnitude of soil flow velocity at 20% slip, averaged over 5-second periods. Note that GSL images are zoomed in 2× for ease of comparison (since the wheel radius was scaled by 1/2). The colorbars indicate velocity in mm/s with the maximum being commanded rim speed. Colormap developed by [6]. All tests performed in GRC-1. Lunar-g and GSL tests performed at 69% D_R (1.79 g/cm^3); equal G method tests performed at 6% D_R (1.61 g/cm^3).

equal G tests in Figure 50 (i.e. the top and bottom rows), there is more soil motion in lunar-g (the region of soil motion identified by kmeans clustering is 30% larger on average), especially later in the experiment, where regions of soil motion in front of the wheel are observed as well as more motion deeper into the soil[2]. The shape of the regions of soil motion also look different between these two experiments. In Figure 51 at 70% slip, more soil motion is again seen in the lunar-g experiments than the equal G experiments; the region of soil motion is 80% larger on average. The observed contact patch is also larger in 1/6-g compared to the equal G experiments in 1-g (due to higher sinkage). The vector fields in Figures 52 and 53 provide more insight into the soil behaviour beneath the wheel.

Figures 52 and 53 show the soil flow directions for the 15–20 second period (again, in lunar time) at 20% and 70% slip, respectively (corresponding to the 4th columns in Figures 50 and 51). The soil velocity around the rim is higher in the small-wheel (GSL) experiments in 1-g due to the higher angular velocity of the small wheel (see Table 6). Additionally, forward-flowing soil in front of the wheel is observed the lunar-g and GSL tests, which can cause a reduction in drawbar pull by increasing resistance. The force causing this forward soil displacement must have an opposite reaction force (according to Newton's 3rd law), which acts on the wheel opposite to its direction of motion [123]. This is sometimes called bulldozing resistance. This phenomenon is accurately captured in the GSL experiments. Conversely, in the equal G experiments, this effect is not observed, and the soil near the front of the wheel moves downwards. This forward flowing soil could have contributed to the lower drawbar pull observed in the lunar-g and GSL experiments[3]. Overall, the soil flow visualizations demonstrate that the general soil behaviour is captured by the

[2]Also, there may have been even more soil motion beneath the wheel at 20% slip if the lunar-g experiments had been conducted on perfectly flat soil (refer to Appendix A and Figure A.4).

[3]Note that this forward-flowing soil was not observed in the sloped terrain experiments in 1-g (see Appendix A, Figure A.5), meaning that this phenomenon is related to the gravity level and not to the slope of the terrain.

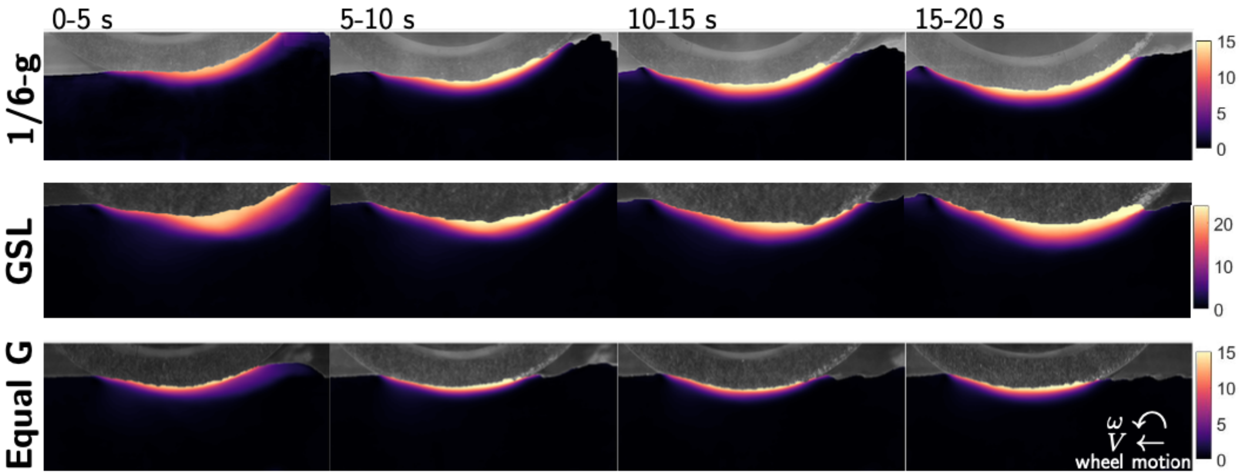

Figure 51: Visualizations of magnitude of soil flow velocity at 70% slip, averaged over 5-second periods. Note that GSL images are zoomed in 2× for ease of comparison (since the wheel radius was scaled by 1/2). The colorbars indicate velocity in mm/s with the maximum being commanded rim speed. All tests performed in GRC-1. Lunar-g and GSL tests performed at 69% D_R (1.79 g/cm^3); equal G method tests performed at 6% D_R (1.61 g/cm^3).

GSL experiments, albeit on a smaller scale.

To further demonstrate the geometric similarity between the GSL and 1/6-g experiments, the soil flow velocity was plotted with respect to distance from the wheel rim (d) normalized by the wheel radius (L) and the wheel angle relative to the surface normal, ϕ (i.e. projected to normalized polar coordinates). Figure 54 shows some examples of this normalized flow velocity versus d/L and ϕ at 20% slip in the lunar-g experiments, GSL experiments, and equal G experiments. In Figure 54, similarities are observed between the experiments that followed GSL (seen in the top two rows) that are not present in the equal G experiments (bottom row). For example, higher soil velocity is observed in front of the wheel ($\phi < -0.5$) in the top two rows, but not in the bottom row. Additionally, there is more soil motion beneath the front half of the wheel ($0 < \phi < -0.5$) in the equal G experiments (bottom row) than in the scaled experiments (top two rows). This again indicates that the soil behaviour observed in the 1-g tests following the GSL method is more similar to the lunar-g experiments than the 1-g tests following the equal G method.

Additional experiments with looser soil

We were interested to see if reducing the density of GRC-1 to its lowest limit could reduce mobility prediction to the point where it matches lunar-g results. Performing tests in the loosest possible state (G = 0.8 kPa/mm) did provide a more accurate prediction of F_{DP}/W, although it was still overestimated. MSPE values comparing the G = 0.8 kPa/mm experiments in 1-g to the G = 2.0 kPa/mm experiments in 1/6-g can be found in Table 9. Again, the MSPE was calculated from 5–20 s, when the experiments were in a quasi-steady state. In 1-g with GRC-1 in its loosest possible state (D_R = 0%, G = 0.8 kPa/mm), F_{DP}/W was slightly lower than at 6% D_R in 1-g, but still higher than at 69% D_R in 1/6-g by 5%–45%.

In the 0% D_R soil in 1-g (G = 0.8 kPa/mm), approximately 15 mm of static sinkage was

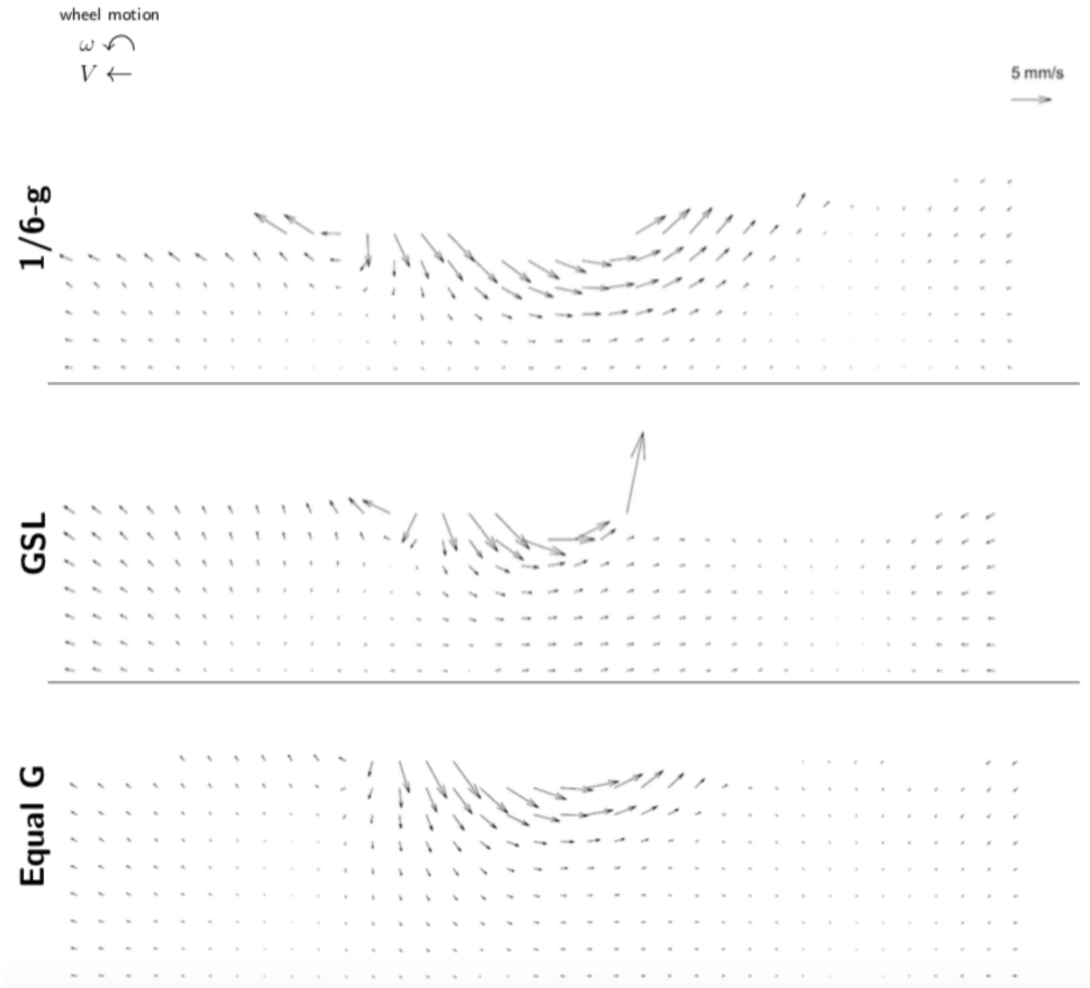

Figure 52: Visualizations of the direction of soil motion at 20% slip with the large wheel in 1/6-g (top), the GSL method in 1-g (middle, note: not zoomed in here), and the equal G method in 1-g (bottom), averaged over 5 second period (from 15–20 s). The arrows represent velocity in mm/s, with the rim speed indicated in the upper right corner of each plot. Note the forward soil flow observed at the front of the wheel in the top two rows, but not the bottom row. All tests performed in GRC-1. Lunar-g and GSL tests performed at 69% D_R (1.79 g/cm^3); equal G method tests performed at 6% D_R (1.61 g/cm^3).

Table 9: Mean squared percentage error (MSPE) of 1-g results at G = 0.8 kPa/mm (GRC-1 at 1.6 g/cm^3 or 0% D_R) compared to lunar-g results at G = 2.0 kPa/mm (GRC-1 at 1.79 g/cm^3 or 69% D_R), calculated from 5–20 s.

	20% slip	70% slip	Average
F_{DP}/W	45%	5%	25%
Sinkage	117%	34%	76%
Power	17%	2%	9.5%

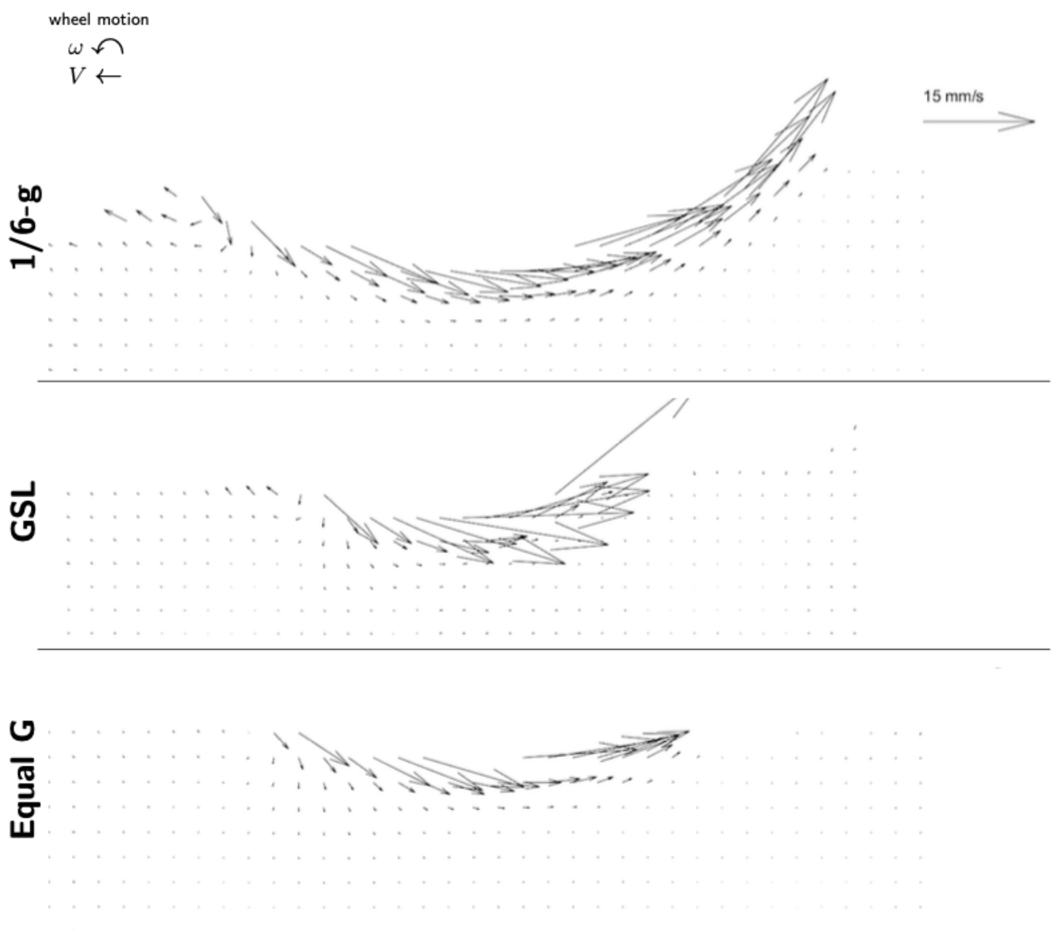

Figure 53: Visualizations of the direction of soil motion at 70% slip with the large wheel in 1/6-g (top), the GSL method in 1-g (middle, note: not zoomed in here), and the equal G method in 1-g (bottom), averaged over 5 second period (from 15–20 s). The arrows represent velocity in mm/s, with the rim speed indicated in the upper right corner of each plot. Note the forward soil flow observed at the front of the wheel in the top two rows, but not the bottom row. All tests performed in GRC-1. Lunar-g and GSL tests performed at 69% D_R (1.79 g/cm^3); equal G method tests performed at 6% D_R (1.61 g/cm^3).

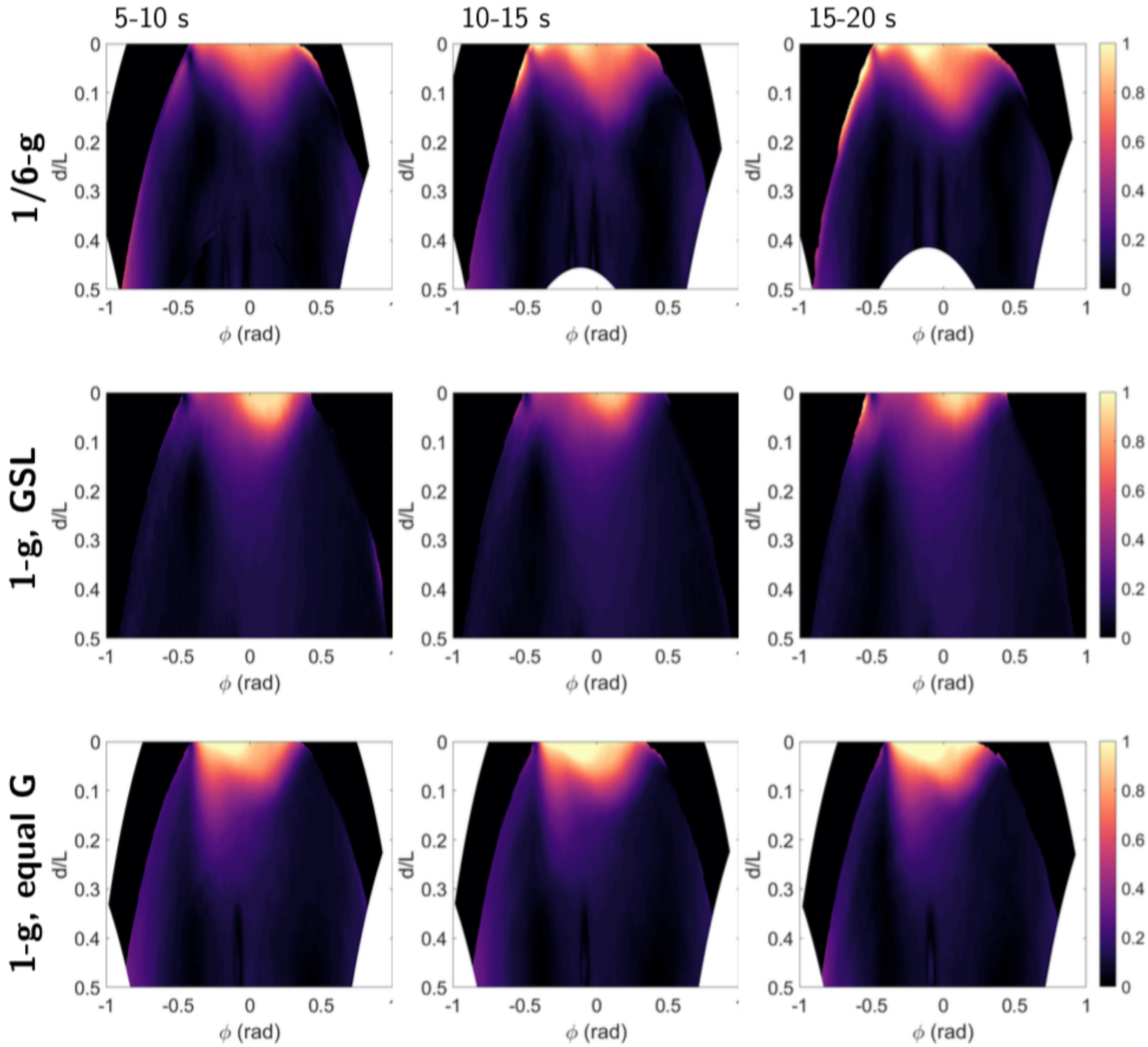

Figure 54: Visualizations of the magnitude of soil flow velocity normalized by rim speed and plotted against distance from the wheel rim (d) normalized by wheel radius (L) and angle relative to the surface normal (ϕ), from tests at 20% slip with the large wheel in 1/6-g (top), the GSL-scaled wheel in 1-g (middle), and the large wheel in 1-g (bottom), averaged over 5 second periods. Note the similarities observed between the scaled experiments (top two rows), such as higher soil velocity in front of the wheel ($\phi < -0.5$) and relatively low velocity beneath the front of the wheel ($0 < \phi < -0.5$), that are not observed in the non-scaled experiment (bottom). All tests performed in GRC-1. Lunar-g and GSL tests performed at 69% D_R (1.79 g/cm^3); equal G method tests performed at 6% D_R (1.61 g/cm^3).

observed at the start of the experiments, leading to the highest total sinkage of all the experiments, even though these tests exhibited the least dynamic sinkage.

Looking at the sinkage MSPE, on average, sinkage was 76% higher in the 1-g tests at G = 0.8 than in the lunar-g tests at G = 2.0 kPa/mm, due to much higher static sinkage (as seen at t = 0 in Figure 55). These tests also overestimated the power required by the wheel by an average of 9.5%, due to increased soil resistance caused by both higher sinkage and higher soil strength in 1-g. Thus, wheel experiments in very loose GRC-1 in 1-g overestimated the F_{DP} (and thus slope climbing ability), sinkage, and power in comparison to 69% D_R GRC-1 in lunar-g. Clearly, static sinkage is highly sensitive to density at this extreme end of the range of achievable density values.

The shape of the soil motion in the soil flow visualization for the loosest soil (G = 0.8 kPa/mm in 1-g) was similar to that observed in the equal G tests (at G = 2.0 kPa/mm in 1-g), although the region of soil motion was slightly larger. There is a small amount of forward-moving soil in front of the wheel at 20% slip in the 0% D_R soil in 1-g (G = 0.8 kPa/mm, seen in Figure 56), but the ratio of soil moving downwards near the front of the wheel to soil moving forwards in front of the wheel is much larger than that observed at G = 2.0 kPa/mm in lunar-g. Bulldozing resistance also perhaps aided in the slight reduction of F_{DP}/W observed when reducing the soil density to 0% D_R in 1-g, at least at 20% slip, when a small amount of forward-flowing soil was observed (Figure 56).

4.5 Chapter summary, conclusion and future work

Wheel experiments were completed aboard parabolic flights generating effective lunar gravity (1/6-g) and compared to experiments using each of these methods in 1-g, to experimentally evaluate two different 1-g testing methods that endeavor to account for the effects of reduced gravity on wheel–soil interactions. Three output metrics were compared between tests: the drawbar pull–weight ratio (F_{DP}/W), wheel sinkage, and power draw.

Cone penetrometer tests were also performed in 1-g and 1/6-g aboard NRC's Falcon 20 aircraft after preparing GRC-1 to three different densities. It was found that the cone index gradient (G) values measured in 1/6-g after equivalent soil preparations were $4\times$ lower on average than those measured in 1-g. Soil preparation was performed in 1-g for all tests, and no change in density (as indicated by soil level) was observed upon entering 1/6-g. Since cone penetrometer measurements are influenced by both compaction and shear strength, and compaction (density) did not change, this indicates a decrease in shear strength in reduced gravity.

Next, wheel experiments were conducted at 20% and 70% slip in 1/6-g in a single-wheel testbed aboard the Falcon 20. Then, to test the underlying assumption of the equal G method (that rover mobility is equivalent across gravity levels as long as the cone index gradient (G) values are equal), corresponding wheel experiments were performed in 1-g at a looser soil density that generated an equivalent cone index gradient to the higher-density soil in 1/6-g. It was observed that wheel performance was overestimated using this method—drawbar pull was overestimated by 44%, sinkage was underestimated by 13.5%, and less soil motion was observed. Forward-flowing soil (which causes bulldozing resistance) was seen in front of the wheel in 1/6-g but not in 1-g, which could be the cause for lower F_{DP} observed in 1/6-g. On the other hand, the power required by the wheel was slightly overestimated (4.5%). The overestimation of drawbar pull, underestimation of sinkage, and overestimation of power were more pronounced at 20% slip, which is a

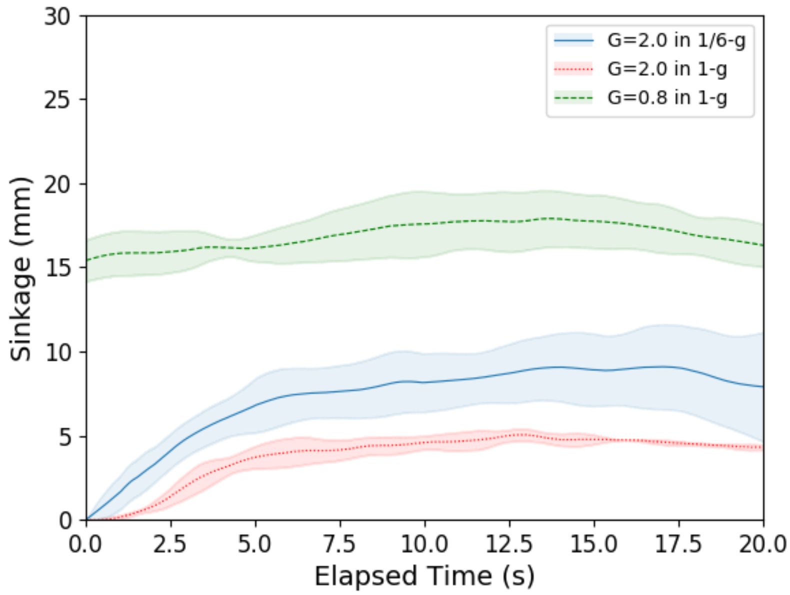

(a) 20% slip

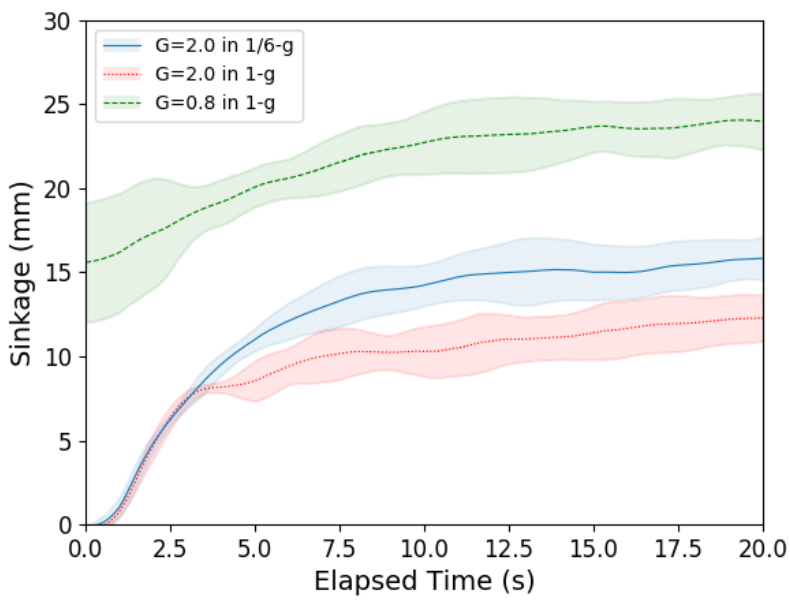

(b) 70% slip

Figure 55: Sinkage measured in 1/6-g in soil producing a cone index gradient of G = 2.0 kPa/mm (1.79 g/cm^3 or 69% D_R), compared to sinkage measured in 1-g in looser soil (1.61 g/cm^3 or 6% D_R) producing an equivalent cone index gradient as well as soil at the loosest achievable state (1.60 g/cm^3, 0% D_R, G = 0.8 kPa/mm). Each line consists of an average of three to four experimental repeats, and light-colored regions represent the 95% confidence intervals.

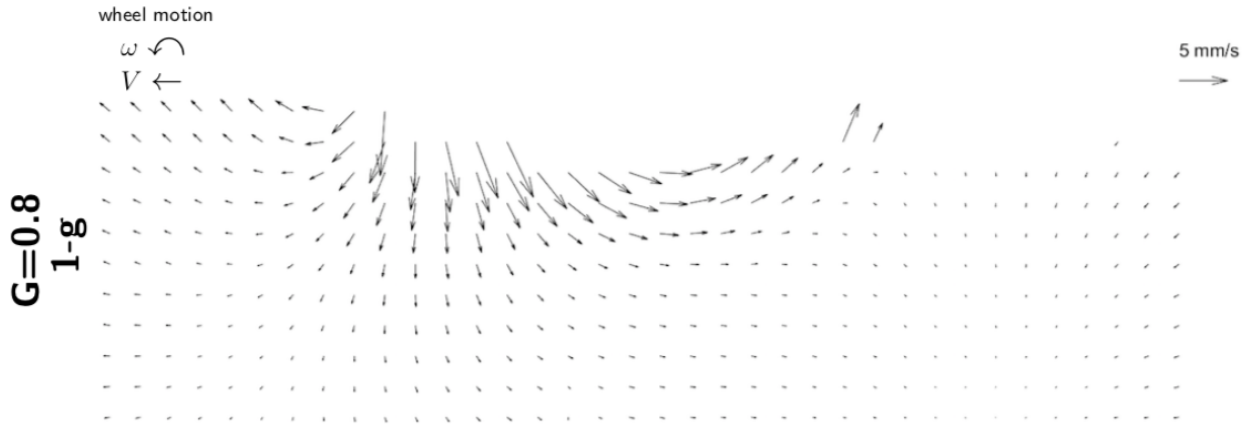

Figure 56: Visualizations of the direction of soil motion at 20% slip in 1.60 g/cm^3 (0% D_R) soil producing a cone index gradient of G = 0.8 kPa/mm in 1-g, averaged over 5 second period (from 15–20 s). The arrows represent velocity in mm/s.

more likely case than 70% slip for planetary rovers. Further wheel experiments were then performed at the lowest possible density in 1-g to determine if a more accurate prediction could be achieved. These 0% relative density experiments again overestimated drawbar pull, although to a lesser extent (25%). They overestimated sinkage by 76%. They additionally overestimated the required power by 9.5% on average. Based on these results, it appears that the main assumption made during the creation of GRC-1 was not quite correct, and that care needs to be taken when interpreting results obtained from tests with GRC-1. Performing experiments in soil prepared to a density that produced an equivalent cone index gradient (G value) in 1-g as that measured in 1/6-g did not result in equal wheel performance. In particular, drawbar pull was significantly overestimated. Predicting drawbar pull, and by extension slope climbing, in reduced-g based on GRC-1 tests in 1-g should be considered with a safety factor to account for the potential overestimation.

Tests were then completed with a scaled wheel in 1-g to evaluate the GSL method. A new output term for sinkage was added to the existing GSL, and further modifications were implemented to make the scaling laws applicable to the type of experiments that were performed. For all metrics, less than 10% mean squared percent error (MSPE) was achieved by the scaled 1-g tests compared to the lunar-g tests. Furthermore, these errors were conservative (i.e. predicted wheel performance was worse than actual wheel performance, with lower F_{DP}/W, higher sinkage, and more power required). Sources of experimental error that could have contributed to these differences were also discussed. Subsurface soil imaging showed similar soil behaviour between the pair of scaled tests, e.g. bulldozing, indicating that low-gravity soil behaviour was successfully replicated by the scaled tests in 1-g. These results indicate that granular scaling laws, previously experimentally validated only in gravity-invariant tests and in DEM simulations, are also valid in different gravity levels, at least in cohesionless soils.

Thus, based on these results, the recommended method is GSL. However, since the equal G method provides optimistic predictions and the GSL method provides pessimistic predictions, it could also be useful to use both testing methods and treat them as estimates of bounds on a rover's performance in lunar-g.

The intention of the equal G experiments reported here was to test the assumption that wheel performance correlates with G values, and conducting the 1-g and 1/6-g tests in the same soil allowed for the elimination of any other soil-specific variables. However, it was observed that the effect of gravity on shear strength played a major role in determining wheel performance in terms of traction, sinkage, and the behaviour of soil beneath the wheel, and that this effect could not be replicated by simply reducing the soil's compaction. Interestingly, the in-situ cone index gradient values measured during the Apollo missions were higher (approximately G = 3 to 10 kPa/mm [2]) than those seen in 1/6-g in the present research (approximately G = 1 to 2 kPa/mm). This is due to the high strength of lunar soil—owing to its angularity and wide particle size distribution [163]—in comparison to GRC-1. Thus, to further evaluate the efficacy of GRC-1 as a lunar terramechanics simulant, planned future work includes experiments comparing wheel performance in lunar-g in a stronger simulant—one that more accurately represents the cohesion and angularity of lunar regolith—to wheel performance in GRC-1 in 1-g at densities producing equivalent G values.

These future lunar-g tests in a stronger soil simulant will also be used to further characterize the performance of GSL. 1-g experiments characterizing the performance of GSL in a soil simulant with cohesion similar to the estimated cohesion of lunar regolith are presented in Chapter 5.

Chapter 5

Limitations of GSL

The investigations in Chapter 4 utilized the cohesionless soil simulant GRC-1. However, lunar regolith is estimated to be mildly cohesive, and for cohesive soils, an additional constraint for GSL has been proposed in the literature. This newly proposed cohesion constraint states that the radius ratio must be the inverse of the gravity ratio. For example, to predict wheel performance in lunar-g based on 1-g tests, the wheel radius in 1-g must be 1/6 of the wheel radius in lunar-g (given than the gravity on Earth is 6× higher than lunar gravity). As testing a 1/6-scaled lunar rover may not be practical or desirable, it is useful to quantify the error introduced by ignoring this cohesion constraint. To evaluate this cohesion constraint, experiments have been performed measuring performance of single wheels of different radii (described in Section 2.2.2) driving through the lunar soil simulant LMS-1 (described in Section 2.3.3), which has cohesion similar to the estimated cohesion of lunar regolith, in the testbed described in Section 2.1.2. These experiments indicate that the cohesion constraint can likely be ignored for mildly cohesive soils such as lunar regolith, at least at low slip. These experiments also led to the discovery of other possible limitations of GSL regarding wheel size relative to soil particle size and/or limitations concerning changes to the wheel aspect ratio between scaled tests. Figure 57 illustrates the topics covered in this chapter. This work is listed as contribution 1.3 in Section 1.5.

5.1 Background

Recently, Zhang et al. [59] proposed a modified version of GSL that accounts for cohesion and allows for sloped terrain:

$$\left[\frac{P}{Mg\sqrt{Lg}}, \frac{V}{\sqrt{Lg}}\right] = \Psi_c\left(\sqrt{\frac{g}{L}}t, f, \frac{g}{L\omega^2}, \frac{\rho_0 DL^2}{M}, \theta, \frac{\rho_0 Lg}{\sigma_c}\right) \tag{15}$$

where θ is the terrain slope angle, σ_c is cohesion stress and ρ_0 is a critical density of the granular material (below ρ_0, the material is disconnected and thus stress free, and above ρ_0, a frictional and cohesive rheology is assumed). Since the soil properties ρ_0 and σ_c would be difficult (though possible [189]) to control, this leaves only the radius L as a parameter that can be readily changed to obtain a scaled test pair between two different gravity levels.

When considering cohesive soils, the cohesion term $\frac{\rho_0 Lg}{\sigma_c}$ proposed by Zhang et al. [59] (seen in Equation 15) can be added to Equation 13. Furthermore, assuming the soil is the same between

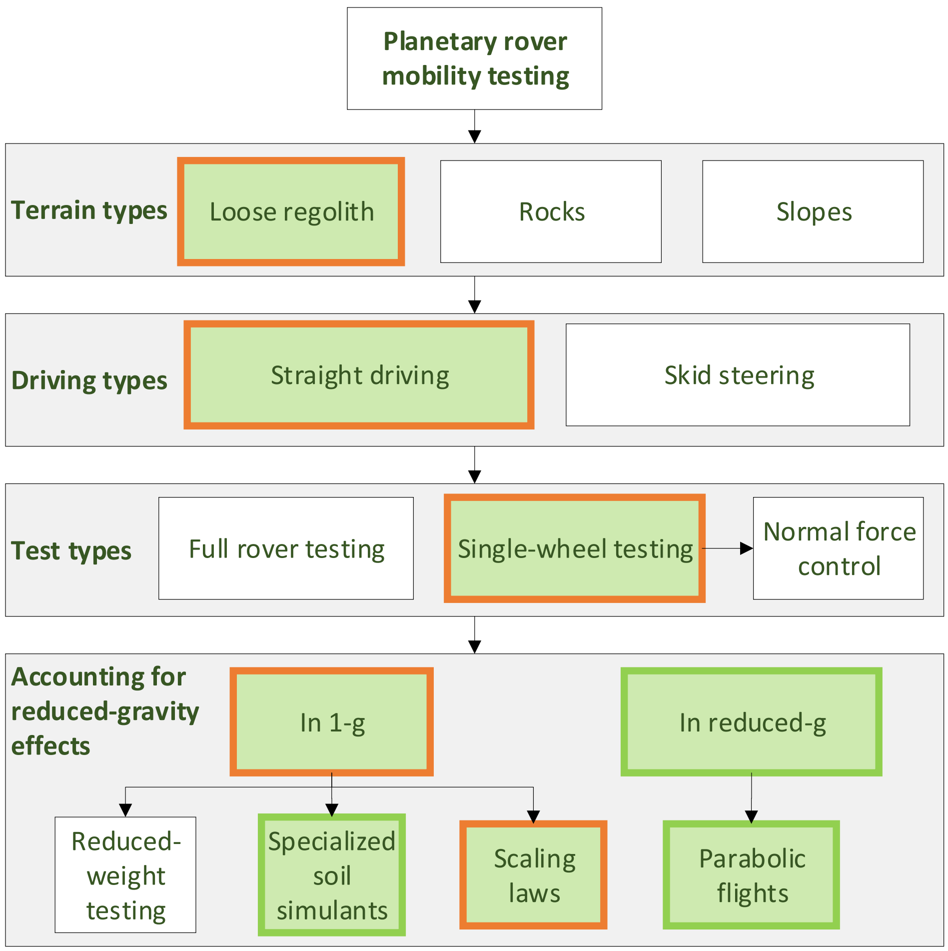

Figure 57: Diagram depicting the topics studied in this thesis, with major topics highlighted in green. The specific topics studied in this chapter are highlighted in orange.

a pair of scaled tests, the soil parameters ρ_0 and σ_c can be absorbed into the function to yield:

$$\left[\frac{F_{DP}}{Mg}, \frac{z}{L}, \frac{P}{Mg\sqrt{Lg}}\right] = \Omega_c \left(\sqrt{\frac{g}{L}}t, f, \frac{g}{L\omega^2}, \frac{DL^2}{M}, \frac{V}{\sqrt{Lg}}, Lg\right) \tag{16}$$

Now, for cohesive soils, in order for scaling pairs to be valid (i.e. in order for the new nondimensional term Lg to be equal for a pair of scaled tests), an additional constraint is added to the parameter space: $r = 1/q$. As described previously, this implies that lunar rovers must be tested at 1/6 scale. To date, this has only been validated using numerical simulations[1] [59]. Here, we consider this proposed GSL cohesion constraint for lunar regolith, which is estimated to be mildly cohesive (0.1–1 kPa [163]). To quantify the error introduced by ignoring this cohesion constraint, experiments have been performed in the lunar soil simulant LMS-1, which has cohesion similar to the estimated cohesion of lunar regolith. Figure 21 shows particles of GRC-1, lunar regolith, and LMS-1. It can be seen that the particles of lunar regolith and LMS-1 are both more angular than the particles of GRC-1, meaning there are more interlocking forces between particles and therefore more cohesion.

5.2 Soil preparation

5.2.1 GRC-1

For tests reported in this chapter, GRC-1 (described in Section 2.3.2) was prepared to a relative density of approximately 10% (approximately 1.62 g/cm^3 bulk density). After blowing air through the manifolds in the bottom of the sandbox for 2000 ms at a pressure of 0.15 MPa, the soil was compacted by vibrating at 32 Hz for 1000 ms.

5.2.2 LMS-1

To prepare the soil simulant LMS-1 (described in Section 2.3.3) to a repeatable state between tests, the automated soil preparation procedure described in Section 2.1.2 was used, with some adjustments from previous experiments [5, 181, 155]. Since LMS-1 is more difficult to fluidize than GRC-1 due to its cohesion and smaller particle sizes [190], a higher pressure was required for the loosening stage in addition to an extra "bubbling" step, which involves simultaneous vibration and aeration. First, air is blown through the manifolds in the bottom of the sandbox for 10 pulses of 250 ms with pauses of 250 ms, at a pressure of 0.25 MPa. Then, bubbling (simultaneous aeration and vibration) is performed for 2500 ms at a pressure of 0.09 MPa and a vibration frequency of 29 Hz. Finally, the soil is compacted by vibrating 7 times at 32 Hz for 1000 ms, with breaks of 400 ms between vibrations, achieving a density of approximately 2.0 g/cm^3. It is estimated that the cohesion of LMS-1 is between 0.3 and 1 kPa at the density used in these experiments.

[1] Li et al. [64] proposed a similar idea: under the assumption that lunar soil's low cohesion can be ignored, they modified Kanamori's scaling laws [61] (which inherently included the cohesion constraint proposed by Zhang et al.) to allow utilization of the same wheel in 1-g and lunar-g. However, to the author's knowledge, this idea had not been validated.

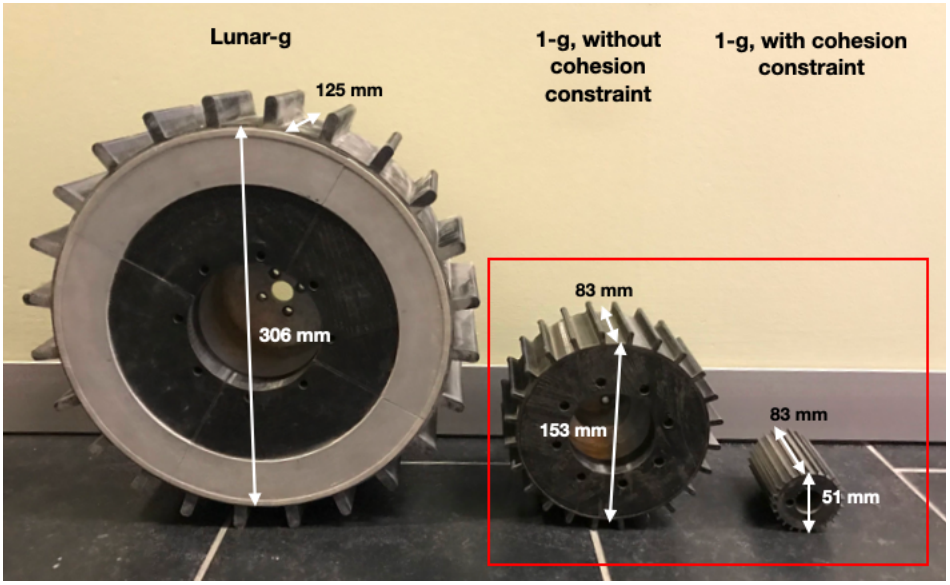

Figure 58: Smaller wheels used in 1-g (middle, right) to predict performance of a larger wheel in lunar-g (left) in order to test a cohesion constraint proposed for GSL. Grouser height and thickness scaled proportionally to wheel radius.

5.3 Initial tests with smaller wheels

5.3.1 Experimental parameters

The first set of experiments completed in this investigation was performed with a 25.5 mm radius wheel and a 76.5 mm radius wheel, with the intent of comparing the results to experiments with a larger 153 mm radius wheel on parabolic flights producing effective lunar gravity. These wheels are shown in Figure 58 and are described in more detail in Section 2.2.2. The two smaller wheels have radii equal to 1/6 and 1/2 of the radius of the wheel that will be flown in lunar-g. As tests with the 1/6-radius wheel followed the cohesion constraint and tests with the 1/2-radius wheel did not, the intent of these experiments was to estimate the error introduced by ignoring the cohesion constraint based on the difference between the dimensionless results from tests with each wheel.

The scaling factor q was fixed by the relative gravity levels investigated (q = 6 since the gravity on Earth is 6$\times$ higher than lunar gravity). The scalars r and s were chosen such that the inputs and outputs fit within the operating limits of the SWTB. The chosen inputs for tests in 1-g that are meant to replicate tests in lunar-g, and their corresponding outputs, can be seen in Table 10. The number of experiments completed at each combination of parameter settings can be seen in Table 11.

5.3.2 Results and discussion

First, experiments were completed with the two smaller wheels in LMS-1. Average[2] dimensionless drawbar pull (F_{DP}/W) vs. slip and maximum dimensionless sinkage (z/L) vs. slip are shown in

[2] Averaging was performed following the procedure outlined in Section 3.1.2.

Table 10: Scaling parameters for tests completed with the smaller (25.5 mm radius and 76.5 mm radius) wheels.

153 mm radius wheel in lunar-g	1/2-radius (76.5 mm) wheel in 1-g with q = 6, r = 1/2, s = 1/6 (ignoring cohesion constraint)	1/6-radius (25.5 mm) wheel in 1-g with q = 6, r = 1/6, s = 1/54 (considering cohesion constraint)
g_L	6 g_L	6 g_L
L_L	1/2 L_L	1/6 L_L
M_L	1/6 M_L	1/54 M_L
W_L	W_L	1/9 W_L
D_L	2/3 D_L	2/3 D_L
ω_L	$2\sqrt{3}\,\omega_L$	6 ω_L
V_L	$\sqrt{3}\,V_L$	V_L
$F_{DP,L}$	$F_{DP,L}$	1/9 $F_{DP,L}$
P_L	$\sqrt{3}\,P_L$	1/9 P_L
z_L	1/2 z_L	1/6 z_L
t_L	$1/(2\sqrt{3})\,t_L$	1/6 t_L

Table 11: Number of experiments performed at each combination of parameter settings with the two smaller wheels. Wheel radii, angular velocities, and loads are scaled according to Table 10.

				Number of tests at each slip				
Wheel radius (mm)	Soil	Angular velocity (rad/s)	Load (N)	10%	20%	30%	40%	70%
76.5	LMS-1	0.45	108	3	3	3	3	3
25.5	LMS-1	0.78	12	3	3	3	3	3
76.5	GRC-1	0.45	108	3	3	3	3	3
25.5	GRC-1	0.78	12	3	3	3	3	3

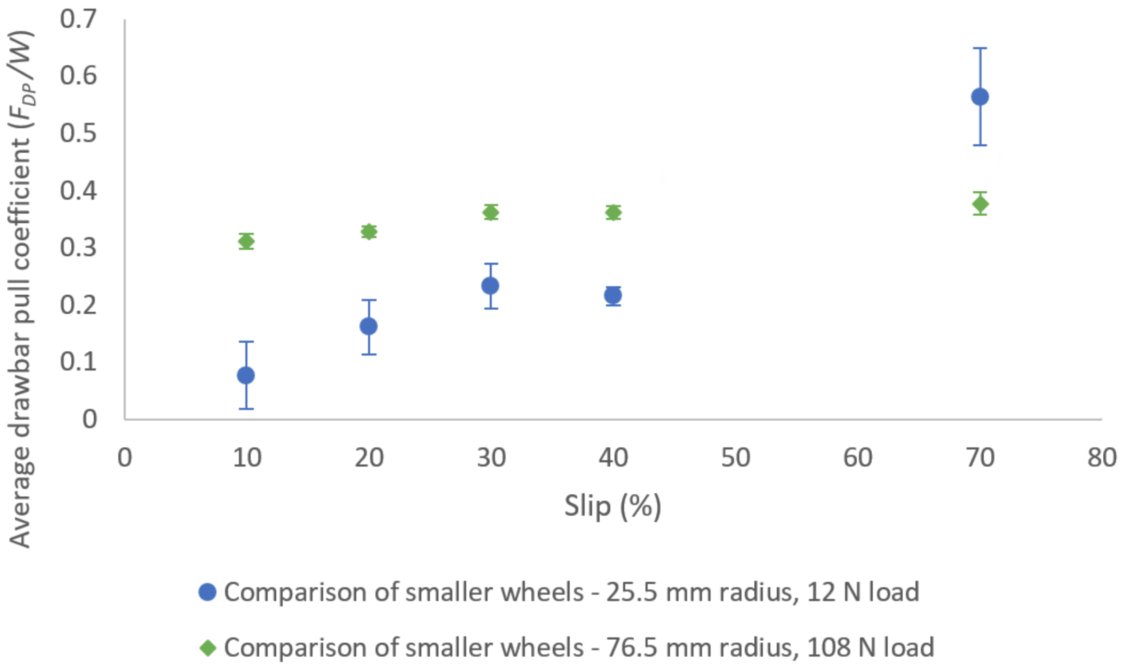

Figure 59: Average dimensionless drawbar pull vs. slip for tests with the 2 smaller wheels in LMS-1 (mildly cohesive) prepared to 2.0 g/cm^3. Error bars represent standard deviation across 3 experimental repeats.

Figures 59 and 60, respectively. It can be seen that the dimensionless results do not match between the 1/6- and 1/2-scaled wheels, which would seem to suggest that the cohesion constraint cannot be ignored. On average, F_{DP}/W of the smaller wheel varied by 50% compared to the larger wheel, and maximum z/L of the smaller wheel was 65% lower than that of the larger wheel.

However, since lunar-g data is not yet available to compare against, from these tests alone it cannot be confirmed if the differences are due to the cohesion of the soil, or something else. Thus, the same tests were performed in GRC-1—since GRC-1 is cohesionless, the cohesion constraint does not apply, and the dimensionless outputs from these tests should match. If the results in GRC-1 match, this would confirm that the differences seen in the tests with LMS-1 are due to cohesion and not due to another problem with the application of the scaling laws.

Average F_{DP}/W vs. slip and maximum dimensionless z/L vs. slip for tests with the two smaller wheels in GRC-1 are shown in Figures 61 and 62, respectively. A similar pattern is seen where the dimensionless outputs are not matching. F_{DP}/W of the smaller wheel differed from that of the larger wheel by nearly 130% on average, and maximum z/L of the smaller wheel was almost 45% lower than that of the larger wheel.

There are two potential reasons for this discrepancy: (1) the radius of the 25.5 mm wheel may be too small relative to the soil particles, and (2) the aspect ratio of the 25.5 mm radius wheel may be too large relative to that of the 76.5 mm radius wheel for the scaling laws to be valid. It should be noted that the aspect ratio of the 25.5 mm wheel was chosen such that a higher load could be applied to the wheel according to the scaling relations (according to the dimensionless number $\rho DL^2/M$). It is difficult to accurately apply extremely low loads in single-wheel tests (if the wheel width were scaled by 1/6 in addition to the radius, the load would need to be 3 N). However, this

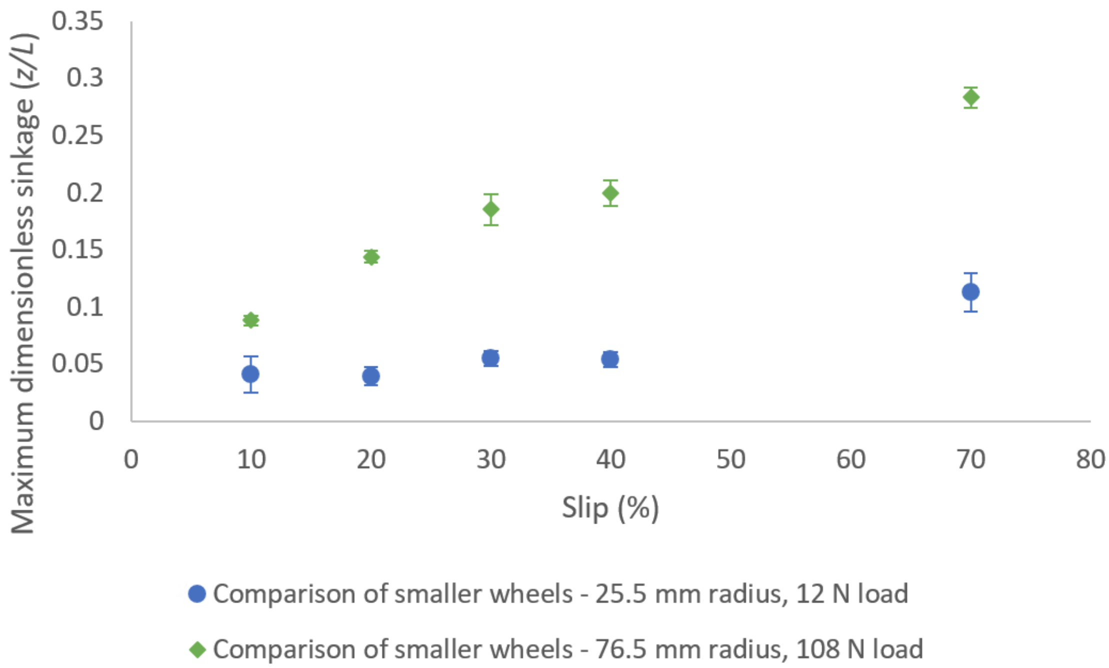

Figure 60: Maximum dimensionless sinkage vs. slip for tests with the 2 smaller wheels in LMS-1 (mildly cohesive) prepared to 2.0 g/cm^3. Error bars represent standard deviation across 3 experimental repeats.

could potentially be achieved in the future with a counterweight attached to the miniature 4-bar mechanism, similar to the setup shown in Figure 11b with the larger 4-bar mechanism.

5.4 Subsequent tests with larger wheels

In order to test the cohesion constraint without requiring significant hardware modifications, similar tests were then completed with the two larger wheels shown in Figure 63. In these tests, it is assumed that the 76.5 mm radius wheel is now the 1/6-scaled wheel relative to a theoretical 459 mm radius wheel in 1/6-g. Then, comparing the 76.5 mm radius wheel to the 153 mm radius wheel in 1-g allows estimation of the error introduced by ignoring the cohesion constraint. However, the wheel load needed to be 6$\times$ higher on the larger wheel, thus only low slip ratios could be tested due to motor limitations.

5.4.1 Experimental parameters

The lowest possible load that could be applied to the 76.5 mm radius wheel (without significant hardware modifications) was approximately 67 N. Thus, the load on the 153 mm radius wheel needed to be 402 N in order for the scaling laws to apply. As mentioned previously, this meant that only low slips could be tested (up to 20% in GRC-1 and up to 10% in LMS-1) or the motor would stall due to the high torque required to turn the wheel under this heavy load. The scaling parameters for these tests can be seen in Table 12, and the number of experiments completed at

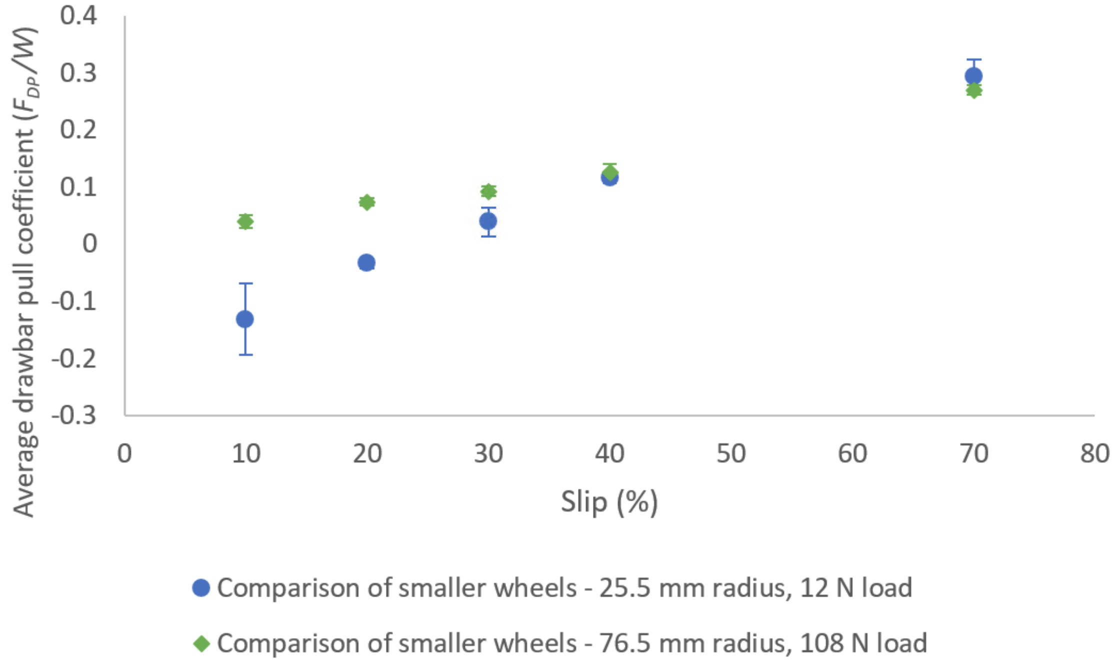

Figure 61: Average dimensionless drawbar pull vs. slip for tests with the 2 smaller wheels in GRC-1 (cohesionless) prepared to 1.62 g/cm^3. Error bars represent standard deviation across 3 experimental repeats.

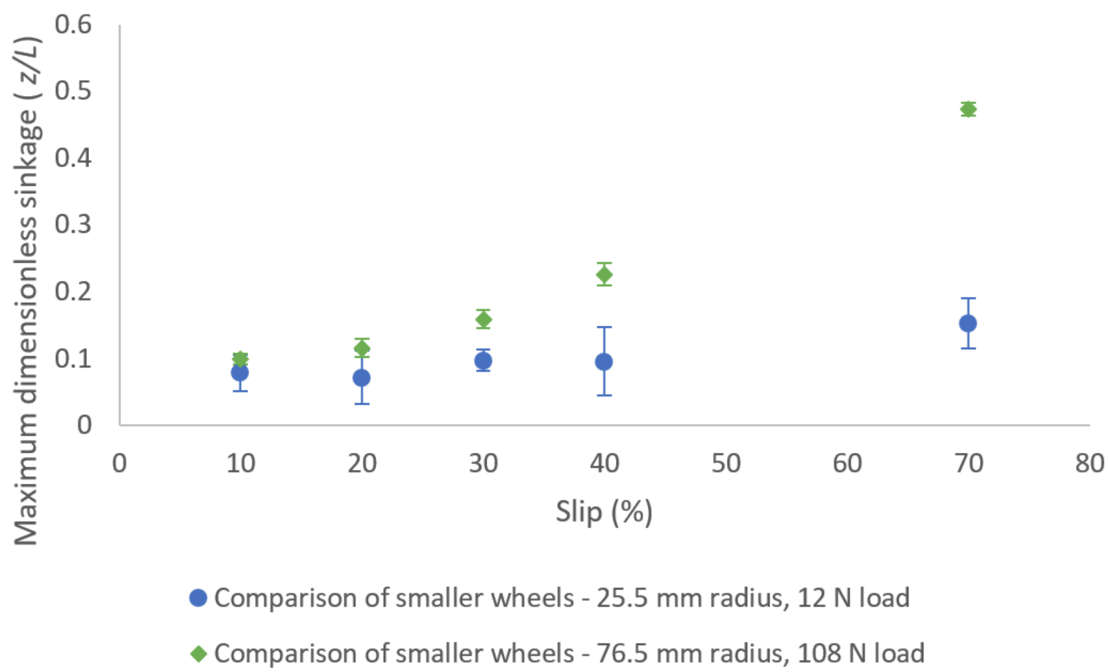

Figure 62: Average dimensionless drawbar pull vs. slip for tests with the 2 smaller wheels in GRC-1 (cohesionless) prepared to 1.62 g/cm^3. Error bars represent standard deviation across 3 experimental repeats.

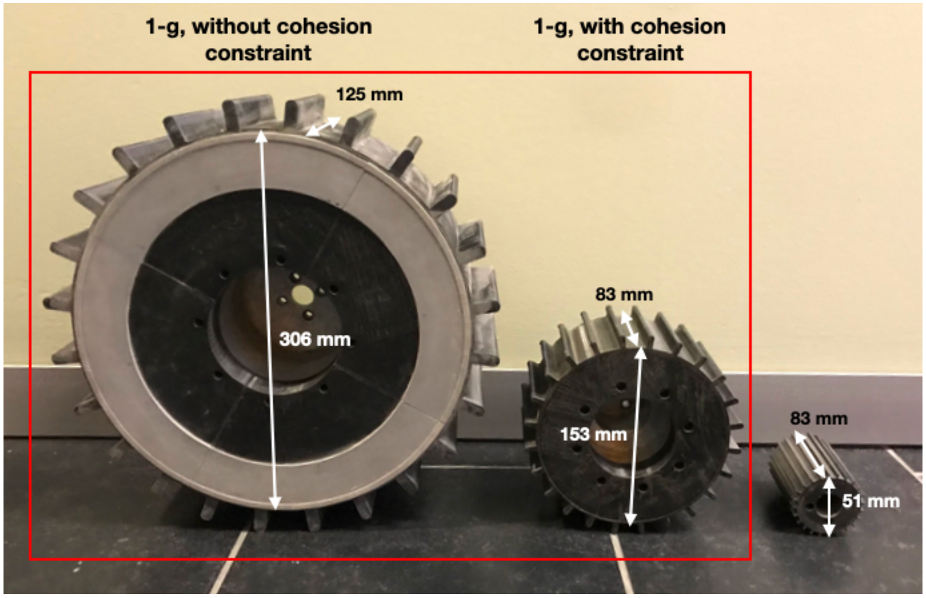

Figure 63: Larger wheels used in 1-g (left, middle) to predict performance of a theoretical huge wheel in lunar-g (not shown) in order to test a cohesion constraint proposed for GSL.

each combination of parameter settings can be seen in Table 13.

5.4.2 Results and discussion

First, tests were completed with the two larger wheels in GRC-1 to confirm that the scaled outputs matched as expected. Average F_{DP}/W vs. slip and maximum z/L vs. slip for tests with the two larger wheels in GRC-1 are shown in Figures 64 and 65, respectively, along with the previous results from the tests with the two smaller wheels for comparison. It can be seen that, although not perfect, the results are much closer when comparing the scaled outputs from the tests with the two larger wheels. In these tests, F_{DP}/W of the 76.5 mm radius wheel was 28% lower than that of the 153 mm radius wheel on average, and maximum z/L differed by 14%.

Next, the same tests were performed in LMS-1 to finally evaluate the cohesion constraint. Recall that tests with the 76.5 mm radius wheel now represent tests that follow the cohesion constraint relative to a theoretical 459 mm wheel in lunar-g, and that tests with the 153 mm radius wheel do not follow the cohesion constraint. Thus, any difference detected between these tests would be due to the error introduced by neglecting the cohesion constraint. Average F_{DP}/W vs. slip and maximum z/L vs. slip for tests with the two larger wheels driving in LMS-1 are shown in Figures 66 and 67, respectively, along with the prior results from the tests with the two smaller wheels for ease of comparison. Although only low slip ratios could be tested, it can be seen that the dimensionless outputs from the tests with the two larger wheels are much closer than they were with the two smaller wheels (average F_{DP}/W was 4% higher with the smaller wheel and maximum z/L was 30% lower with the smaller wheel), indicating that any error introduced by ignoring the cohesion constraint is dwarfed by errors arising from attempting to test very small wheels and/or wheels with vastly different aspect ratios. Thus, it appears that the cohesion constraint can be ignored for

Table 12: Scaling parameters for tests completed with the two larger (76.5 mm radius and 153 mm radius) wheels.

459 mm radius wheel in lunar-g	1/3-radius (153 mm) wheel in 1-g with q = 6, r = 1/3, s = 1/9 (ignoring cohesion constraint)	1/6-radius (76.5 mm) wheel in 1-g with q = 6, r = 1/6, s = 1/54 (considering cohesion constraint)
g_L	6 g_L	6 g_L
L_L	1/3 L_L	1/6 L_L
M_L	1/9 M_L	1/54 M_L
W_L	2/3 W_L	1/9 W_L
D_L	D_L	2/3 D_L
ω_L	$3\sqrt{2}\,\omega_L$	6 ω_L
V_L	$\sqrt{2}\,V_L$	V_L
$F_{DP,L}$	2/3 $F_{DP,L}$	1/9 $F_{DP,L}$
P_L	$\sqrt{8}/3\ P_L$	1/9 P_L
z_L	1/3 z_L	1/6 z_L
t_L	$1/(3\sqrt{2})\ t_L$	1/6 t_L

Table 13: Number of experiments performed at each combination of parameter settings with the two larger wheels. Wheel radii, angular velocities, and loads are scaled according to Table 12.

				Number of tests at each slip			
Wheel radius (mm)	Soil	Angular velocity (rad/s)	Load (N)	5%	10%	15%	20%
153	LMS-1	0.18	402	3	3	0	0
76.5	LMS-1	0.26	67	3	3	0	0
153	GRC-1	0.18	402	3	3	1	1
76.5	GRC-1	0.26	67	3	3	0	3

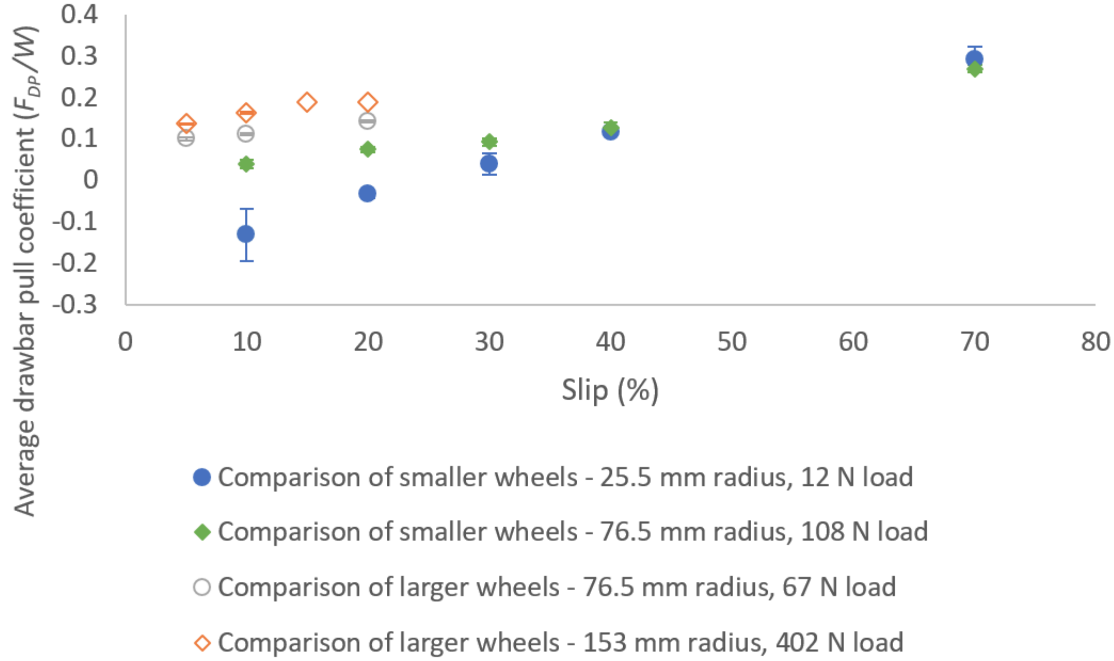

Figure 64: Average dimensionless drawbar pull vs. slip for tests comparing both the 2 larger wheels and the 2 smaller wheels in GRC-1 (cohesionless) prepared to 1.62 g/cm^3. Error bars represent standard deviation across 3 experimental repeats.

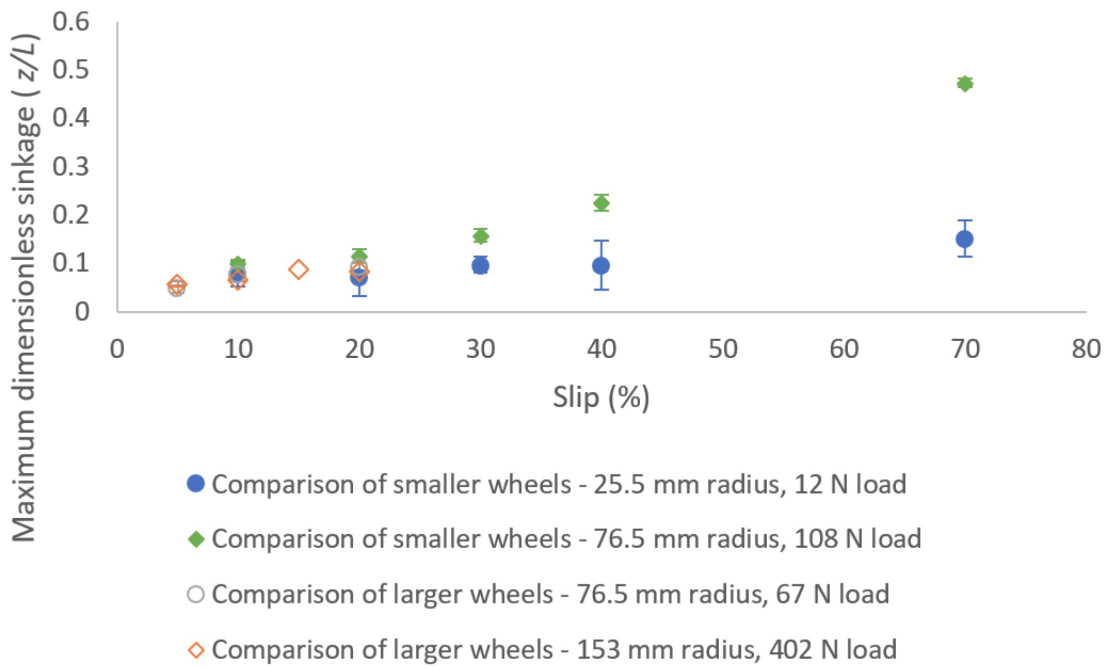

Figure 65: Maximum dimensionless sinkage vs. slip for tests comparing both the 2 larger wheels and the 2 smaller wheels in GRC-1 (mildly cohesive) prepared to 1.62 g/cm^3. Error bars represent standard deviation across 3 experimental repeats.

mildly cohesive soils such as lunar regolith, at least at low slip. Therefore, testing 1/6-scaled lunar rovers is likely unnecessary, and furthermore should probably not be attempted before further verification of the scaling laws for very small wheels.

Thoesen et al. [55] observed that if sinkage was not sufficient, GSL predictions were not accurate, and suggested that sinkage should be at least 10$\times$ the soil's average particle size. The average particle size of LMS-1 is 0.05 mm [174], so to follow Thoesen's rule of thumb, sinkage would need to be at least 0.5 mm for GSL to be applicable in LMS-1. The average particle size of GRC-1 is approximately 0.12 mm, so sinkage would need to be at least 1.2 mm in GRC-1. These conditions were met in most cases tested here, except for a few of the tests with the smallest wheel.

Previous research [63] has shown that similar scaling laws worked well to predict the slip ratio of four- and five-wheeled scaled rovers with even smaller wheels (12.5 mm radii) driving up a 15° slope. However, the soil characteristics (e.g. grain size) were not specified, and sinkage measurements were not reported. The wheel width in this case was scaled proportionally to the radius, so perhaps in our experiments the aspect ratio was the reason for the scaling discrepancy rather than the wheel radius.

Assumptions were made regarding the wheel's aspect ratio in the GSL derivations proposed by Slonaker et al. [8]. Recall, as described in Section 4.1.1, that Slonaker et al. derived GSL starting from both Resistive Force Theory (RFT) and Coulomb plasticity. Both derivations involved an assumption that wheel–soil interactions do not vary in the through-thickness direction (i.e. any "edge" effects at the sides of the wheel are neglected). In the Coulomb plasticity derivation, ignoring this assumption would result in the $\rho DL^2/M$ term becoming $\rho L^3/M$, and D would scale proportionally to L. This results in much less flexibility in the scaling laws, as the wheel width (i.e. along through-thickness) and therefore mass can no longer be changed independently of the radius.

However, Slonaker et al. did some validation tests with differing wheel aspect ratios. Let us define wheel aspect ratio as wheel width divided by wheel diameter, or D/δ. The maximum variation in D/δ tested by Slonaker et al. was in scaled tests with one wheel having $D/\delta = 0.60$ and a scaled wheel with $D/\delta = 0.93$. This represents a difference of approximately 55%. This resulted in reasonable agreement between scaled tests, although they did observe closer agreement when the aspect ratios of the scaled wheels were more similar. Thoesen at al. [55] also tested scaled wheels with different aspect ratios, with the maximum difference being about 37% ($D/\delta = 1.92$ and $D/\delta = 1.40$). For comparison, in our tests with the 25.5 mm and 76.5 mm wheels, the aspect ratio of the 25.5 mm radius wheel was 1.63 and the aspect ratio of the 76.5 mm radius wheel was 0.54, which is a difference of over 200%. The scaling laws had never previously been validated with such widely varying aspect ratios, and our results indicate that this large aspect ratio discrepancy may have led to invalidation of the scaling laws. Thus, to ensure scaling accuracy, it is recommended to keep the aspect ratio variation below $\sim$50%.

5.5 Chapter summary, conclusion and future work

Limitations of GSL were investigated including a recently proposed cohesion constraint, wheel size to soil particle size ratio, and aspect ratio variation between scaled wheels. First, experiments were performed in 1-g that were designed to predict lunar-g experiments with or without consideration of this cohesion constraint (that the wheel radius ratio must be the inverse of the gravity ratio).

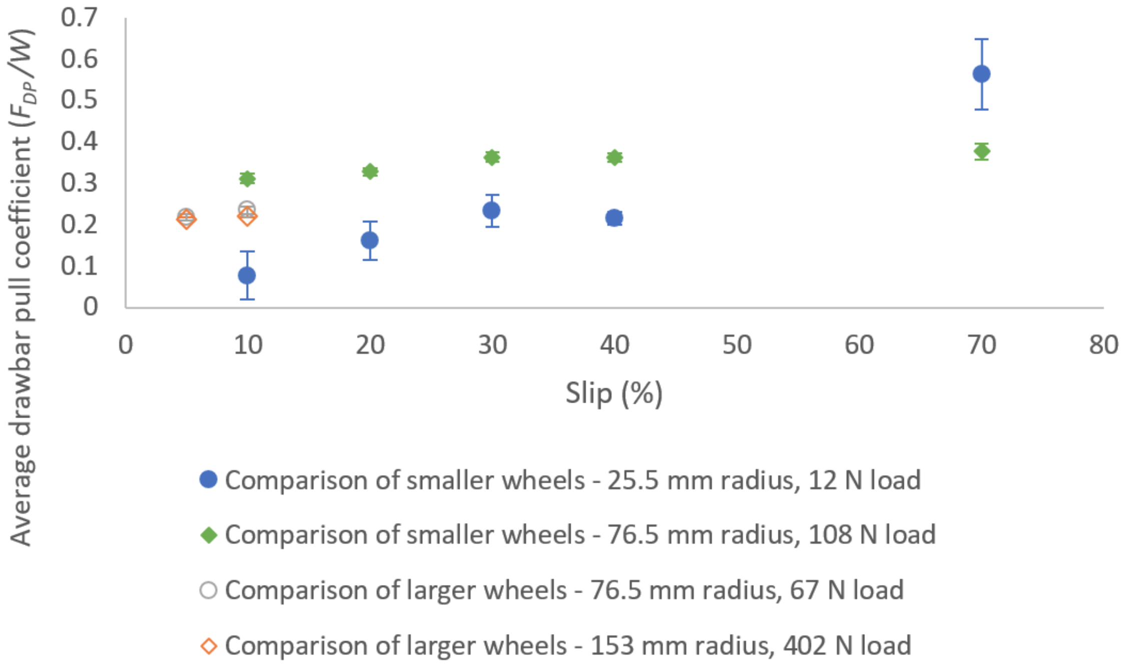

Figure 66: Average dimensionless drawbar pull vs. slip for tests comparing both the 2 larger wheels and the 2 smaller wheels in LMS-1 (mildly cohesive) prepared to 2.0 g/cm^3. Error bars represent standard deviation across 3 experimental repeats.

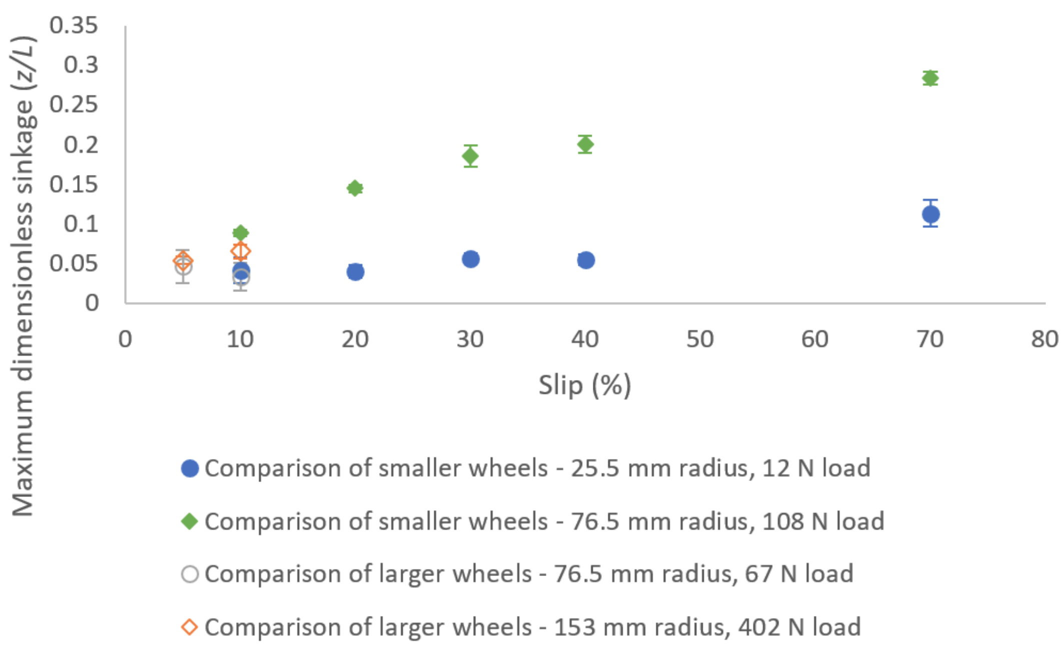

Figure 67: Maximum dimensionless sinkage vs. slip for tests comparing both the 2 larger wheels and the 2 smaller wheels in LMS-1 (mildly cohesive) prepared to 2.0 g/cm^3. Error bars represent standard deviation across 3 experimental repeats.

Experiments were completed with one wheel that has 1/6 of the radius of the wheel that will be tested in lunar-g (i.e. considering the cohesion constraint), and a second wheel that has 1/2 of the radius of the lunar-g wheel (i.e. ignoring the cohesion constraint). These experiments were designed to evaluate the error introduced by neglecting this constraint, and were performed in mildly cohesive soil simulant LMS-1, which has cohesion similar to that of lunar regolith. The dimensionless outputs from the 1/6- and 1/2-radius wheel tests did not match, which could suggest that the cohesion constraint cannot be ignored. However, since lunar-g data is not yet available for comparison, the same tests were performed in the soil simulant GRC-1 (which is cohesionless, so the cohesion constraint does not apply) to confirm the validity of the scaling laws for this wheel pair. It was observed that the dimensionless outputs did not match in GRC-1 either, indicating that some limitation of GSL was coming into effect. Either the radius of the 1/6 wheel was too small relative to the soil grain size, or the aspect ratio of the 1/6 wheel was too large relative to the aspect ratio of the 1/2 wheel (or both).

Thus, to test the cohesion constraint without lunar-g data for comparison, similar tests were performed at a larger scale (i.e. relative to a theoretical "huge" wheel driving in lunar-g), and with closer wheel aspect ratios. It was observed that the scaling laws could be successfully applied with these larger wheels in cohesionless GRC-1; thus, any further discrepancy observed between scaled tests in mildly cohesive LMS-1 would be due to error introduced by ignoring the cohesion constraint. Only low slip ratios could be tested due to testbed hardware limitations, however, minimal error was observed between the tests following the cohesion constraint and tests ignoring the cohesion constraint in LMS-1 with these larger wheels. This indicates that the cohesion constraint can likely be ignored for mildly cohesive soils such as lunar regolith, at least at low slip, although further validation is required to confirm this.

However, there are still unresolved questions regarding the wheel size and aspect ratio that could be answered by testing a 25.5 mm radius wheel with an aspect ratio closer to that of the wheel that will be tested in lunar-g. This could potentially be accomplished with a counterweight system similar to that used in the larger testbed (Figure 11b). For now, it is recommended that sinkage be at least 10$\times$ the average particle size (Thoesen's rule of thumb [55]), and that the variation in aspect ratio between scaled test pairs be less than approximately 50% (new rule of thumb based on tests reported here and investigation of previously published results).

Future work includes gathering lunar-g data with the 153 mm radius wheel in LMS-1 and comparing those dimensionless results to 1-g data collected with the 76.5 mm radius wheel (including tests at high slip). If those results match, it will be confirmed that the cohesion constraint can be ignored for mildly cohesive soils such as lunar regolith. However, one question would remain regarding the effects of wheel size: would tests that stray further from the cohesion constraint (i.e. tests with a full-sized wheel in 1-g, rather than a 1/2-scaled wheel) still be valid? To test this would require significant modifications to the experimental apparatus due to the large difference in wheel load that would be required, but this could be a potential avenue for future investigation. Finally, it would also be worthwhile to test a 25.5 mm radius wheel with an aspect ratio more similar to that of the larger wheels (which would also require some testbed hardware modifications) in order to isolate the effects of wheel size and aspect ratio.

Chapter 6

Applications of GSL

This chapter provides two examples illustrating the application of granular scaling laws (GSL) to tests with the aim of informing rover design. Both studies were conducted in collaboration with NASA's Jet Propulsion Laboratory (JPL) as part of the JPL Visiting Student Research Program (JVSRP). This work is listed as contribution 2 in Section 1.5.

The first example, discussed in Section 6.1, presents an investigation of wheel design changes for a potential future lunar rover, published by the author in [191].

The second example, presented in Section 6.2, describes the application of GSL to the design of two reconfigurable rover platforms to study the performance of different locomotion modes on steep terrain. This work will be published in a forthcoming conference article [7].

6.1 Single-wheel tests for a skid-steer lunar rover

As discussed in Section 1.4.6, skid steering is a popular choice for planetary rover missions due to its simplicity, low cost, and low mass compared to explicit steering systems. Skid steer rovers' wheels do not turn explicitly; vehicle turning is achieved by driving the left and right wheels at different velocities. To achieve a turn, the wheels must inherently experience a high amount of slip, which can lead to high sinkage. Furthermore, previous work presented in Chapters 3 and 4 has demonstrated that sinkage can increase in reduced gravity environments. Surveys of previous work regarding the applicability of single wheel tests to full rovers and wheel design for skid-steer rovers can be found in Sections 1.4.4 and 1.4.6, respectively.

During initial testing of a potential future lunar rover under development by NASA JPL, poor turning performance was observed in loose soil including high sinkage during point turns. This was concerning since wheel sinkage decreases ground clearance, increases entrapment risk, and increases power consumption [137]. Moreover, as mentioned above, mobility may be further hindered in reduced gravity—with even higher sinkage and lower traction—as previously observed in Chapters 3 and 4. Thus, an investigation of wheel design modifications to improve turning performance and reduce sinkage was initiated.

In this work, single-wheel tests were performed in the testbed described in Section 2.1.1 (and shown in Figure 11b) to evaluate skid-steer turning performance of seven different wheel designs (described in Section 2.2.4). The tests followed scaling laws described in Section 4.1 to represent lunar-g performance, and were performed in the soil simulant GRC-1 (see Section 2.3.2). Tests

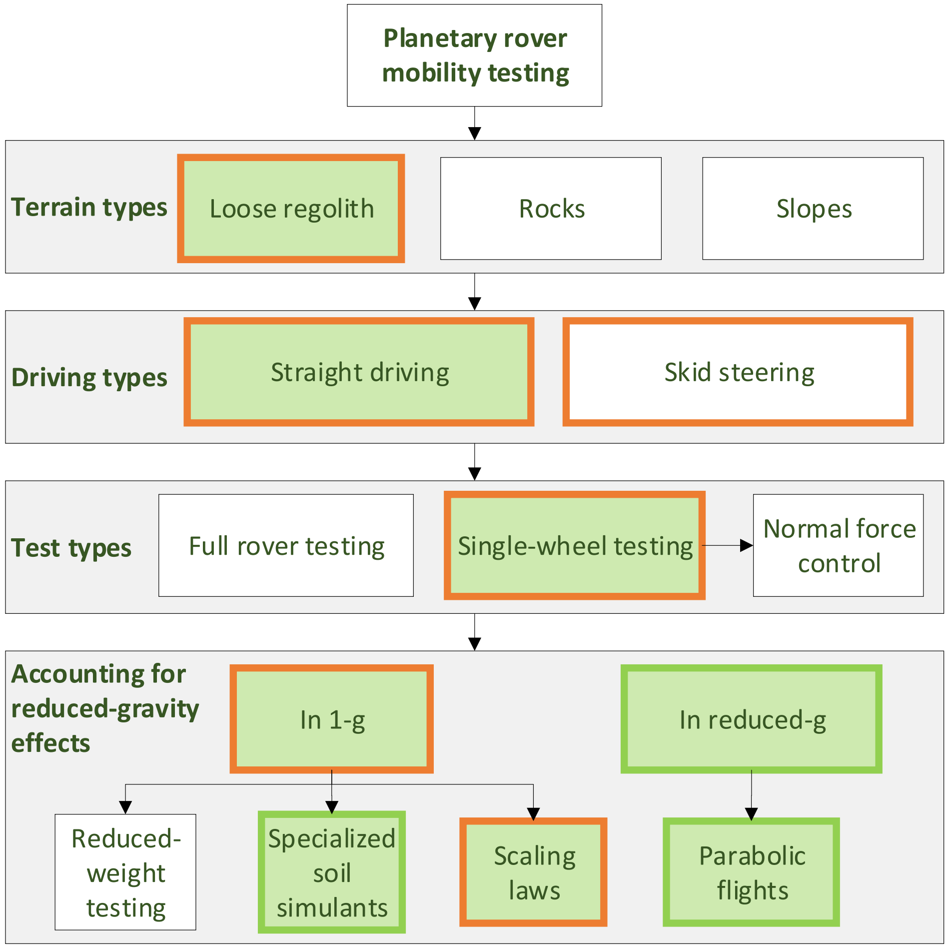

Figure 68: Diagram depicting the topics studied in this thesis, with major topics highlighted in green. The specific topics studied in this section are highlighted in orange.

were performed in GRC-1 since the initial rover mobility tests were performed in GRC-1 and the testbed was already filled with GRC-1. However, GSL (see Section 4.1) assumes driving in the same soil in different gravity levels. Tests following GSL in GRC-1 to represent driving performance on the Moon are thus most likely conservative, as it is expected that lunar soil would be easier than GRC-1 to drive on in 1-g; lunar soil's angular particles and cohesion result in higher shear strength, which can reduce sinkage and increase traction.

It was found that diagonal grousers improved skid-steer turning performance, as did wider and larger diameter wheels. Diagonal grousers are recommended for further testing for this rover since they do not add any mass or volume to the wheel. The work discussed in this section fits into the overall thesis as shown in Figure 68.

Table 14: Parameter settings.

Wheel load (N)	10
Angular velocity (rad/s)	1.3 (15 cm diameter wheels)
	0.98 (20 cm diameter wheel)
Traverse distance (m)	1.2
Bulk density (g/cm^3)	1.64 $\pm$ 0.06
Relative density (%)	16 $\pm$ 9

Table 15: Test matrix.

Wheel	Description	Tests
1	Baseline (15 cm dia., 3 cm wide)	60%, 70%, 80%, 90% slip, β = 44°
		3 × (5%, 30%, 60% slip), β = 0°
2	Closed sides	80% slip, β = 44°
3	Closed sides + side features	60%, 70%, 80%, 90% slip, β = 44°
4	20 cm dia	60%, 70%, 80%, 90% slip, β = 44°
5	6 cm wide	2 × 70%, 1 × 80% slip, β = 44°
6	Diagonal grousers	60%, 70%, 80%, 90% slip, β = 44°
		3 × (5%, 30%, 60% slip), β = 0°
7	Rounded profile	80% slip, β = 44°

6.1.1 Experimental parameters

These tests followed granular scaling laws (GSL, described and validated in Chapter 4) in order to predict wheel performance in lunar gravity. The scaling factor q was fixed by the relative gravity levels investigated ($q = 6$ since the gravity on Earth is 6× higher than lunar gravity). The scalars r and s were chosen to match the actual rover mass and dimensions (i.e. $r = s = 1$). Thus, in order for the 1-g tests to match the rover's performance in lunar gravity, only the speeds (ω and V) needed to be scaled by factors of $q^{1/2}r^{-1/2}$ and $q^{1/2}r^{1/2}$, respectively (or $\sqrt{6}$ for both, in this case). The nominal horizontal velocity of the rover is 0.04 m/s, thus the scaled speed for the GSL tests was 0.098 m/s.

Parameter settings applied to all tests are shown in Table 14 and the matrix of tests performed can be seen in Table 15. The wheel load for GSL tests was 10 N, which represents the full rover weight on Earth (since s = 1 was chosen as the mass scalar as described above). The rover mass was assumed to be 4 kg, and it has four wheels, resulting in 1 kg (and thus approximately 10 N in 1-g) of load on each wheel, assuming the load is equally distributed. Also, as mentioned previously, the nominal horizontal velocity of the rover is 0.04 m/s, thus the scaled nominal (0% slip) speed for the GSL tests was 0.098 m/s, resulting in a commanded angular velocity of 1.3 rad/s for the 15 cm diameter wheels, and 0.98 rad/s for the 20 cm diameter wheel. The wheel slip was controlled by reducing the horizontal velocity of the wheel to generate the desired slip ratio. GRC-1 was prepared to a relative density of approximately 16 $\pm$ 9% (average and standard deviation calculated from six cone penetrometer measurements). Finally, the traverse distance for each test was 1.2 m.

Recall from Section 2.1.1 that β is the angle between the wheel's forward/aft axis and its direction of motion, as illustrated in Figure 11. All wheels were initially tested at 80% slip and

β = 44°, chosen based on the geometry of the rover to represent a point turn. Note that some small (non-zero) radius turns may be worse than point turns in terms of sinkage [160], however for this mission, small non-zero radius turns will be avoided when operating the rovers, thus point turns represent the worst-case sinkage operationally. Only the best wheels were selected for further testing at additional slip values (due to time constraints for completion of the experiments). Straight-line driving tests were performed with the baseline wheel and the diagonal grouser wheel to determine if slope-climbing performance would be negatively affected by the diagonal grouser design. It was assumed that the two other designs that enhanced turning performance (the larger diameter and wider wheels) would not decrease straight-line driving performance or slope-climbing performance since the grouser pattern was not changed for those designs.

Outputs

The metrics used to evaluate wheel performance in these experiments include the drawbar pull coefficient (F_{DP}/W, used to characterize straight-driving performance) and sinkage (applicable to both straight-driving and turning), defined and described in Sections 1.2.2 and 2.4.4, as well as the tangent turning force coefficient to characterize turning performance.

Although the initial goal of the tests was to reduce sinkage during skid-steer turns, tangent turning force (F_{turn}) was also identified as an important metric for evaluating skid-steer performance. A positive value of F_{turn} represents the wheel being able to achieve a point turn via its own traction, therefore it is not desirable to reduce sinkage at the expense of reduced tangent turning force. F_{turn} is illustrated in Figure 69 and is calculated using the following equation:

$$F_{turn} = F_{DP} \cos \beta - F_{lateral} \sin \beta \tag{17}$$

where $F_{lateral}$ is the lateral force on the wheel due to soil resistance as the wheel pushes sideways into the soil. In this work, the tangent turning force coefficient, F_{turn}/W is computed by dividing the tangent turning force by the measured normal force at each time step. Averaging was performed following the procedure outlined in Section 3.1.2.

In this work, it is assumed that GSL can be applied to skid-steering, and that the tangent turning force coefficient, F_{turn}/W or F_{turn}/Mg, is an additional output of Equation 13. Also note that some of these wheels may not scale directly as their shape is not constant in the through-thickness direction, which violates the assumption in the RFT GSL derivation of Slonaker et al. [8] (see Section 5.4.2). This, and the effects of a 3D wheel trajectory (where the wheel is spinning along one axis and moving along a different axis at an angle β), could be investigated further, with a recent 3D implementation of RFT as a starting point [192]. However, these nuances are assumed to be negligible for the purposes of comparing the relative performance of different wheel designs.

6.1.2 Results and discussion

Average tangent turning force coefficient vs. slip can be seen in Figure 70. The 6 cm wide wheel (#5) exhibited the best performance, followed by the diagonal grouser wheel (#6) and the 20 cm diameter wheel (#4). Wheel #3 (closed sides + side grousers) performed similarly to the baseline wheel, and the worst wheels in terms of tangent turning force were the rounded profile wheel (#7) and the wheel with closed sides and no side features (#2). Wheels #2, #3, and #7 likely had

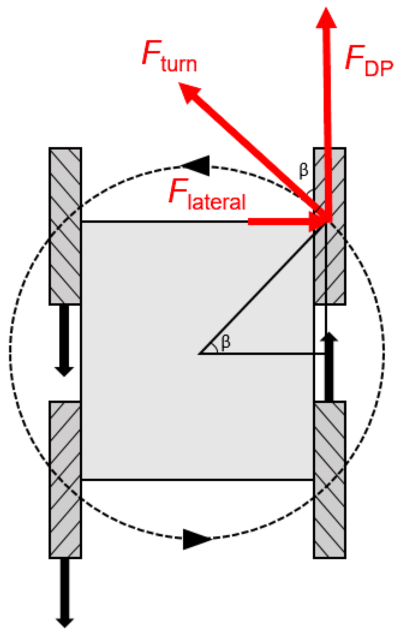

Figure 69: Diagram depicting tangent turning force (F_{turn}). Note that F_{turn} is not to scale based on F_{DP} and $F_{lateral}$ as drawn here.

the lowest tangent turning force due to high lateral forces on the closed sides of the wheel. This was slightly ameliorated by the side grousers in the case of wheel #3, since grousers are known to reduce bulldozing resistance by excavating soil in front of the wheel [123]. Average tangent turning force was negative for most tests because of relatively loose soil and a long traverse length (1.2 m), equivalent to about 360° of turning. Tangent turning force was usually positive near the beginning of the maneuver and then decreased throughout the test. Also, recall that these tests are conservative because GSL assumes the same soil in each gravity condition, whereas GRC-1 actually has lower shear strength than lunar soil would have in 1-g.

Figure 71 shows maximum sinkage vs. slip. It can be seen that all of the wheel designs reduced sinkage at 80% slip, but that trend is not seen at 60% or 70% slip. Unfortunately, these tests had a low signal-to-noise ratio for the sinkage measurements, and no repeats could be done due to time constraints. However, it is also worth noting that comparing sinkage at the same slip ratio may not be relevant—if the tangent turning force is higher for a certain wheel at a certain slip ratio, then a full rover equipped with those improved wheels would perform the turn at a lower slip value, and thus sinkage would likely be lower.

Additionally, since the goal was to evaluate wheels based on both sinkage reduction and tangent turning force, Figure 72 shows the average tangent turning force coefficient plotted against maximum sinkage at 80% slip (since that was the only slip ratio that all wheels were tested at). In this figure, data points lying further to the left and higher on the plot correspond to better wheel performance (lower sinkage and/or higher tangent turning force). From this plot, it is clear that the 6 cm wheel (#5) performed the best, followed by the diagonal grouser wheel (#6) and the 20 cm diameter wheel (#4). All other wheels reduced sinkage (at least at this slip ratio; see Figure 71), but also reduced the tangent turning force, which is undesirable.

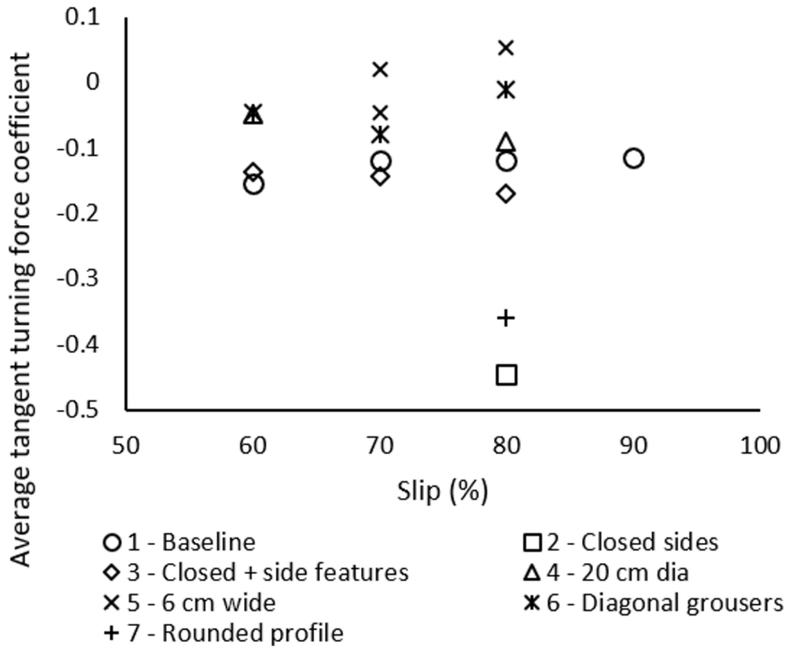

Figure 70: Average tangent turning force coefficient vs. slip for $\beta = 44°$ tests. All tests performed in GRC-1 prepared to approximately 1.64 g/cm^3.

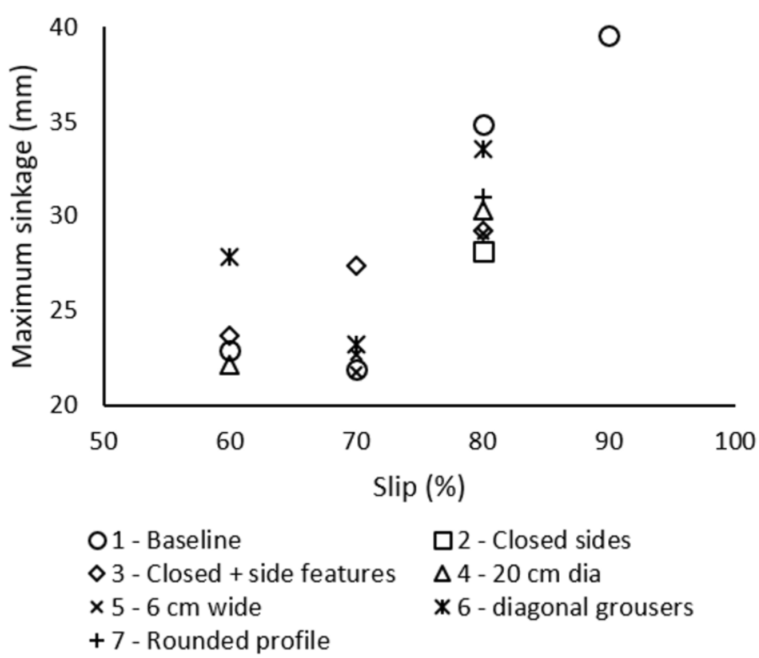

Figure 71: Maximum sinkage vs. slip for $\beta = 44°$ tests. All tests performed in GRC-1 prepared to approximately 1.64 g/cm^3.

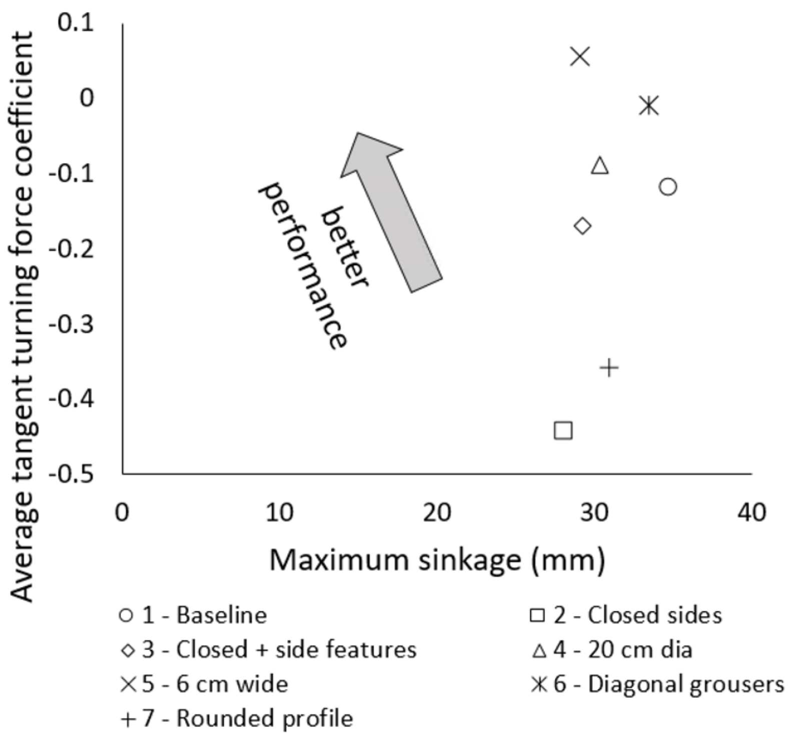

Figure 72: Average tangent turning force coefficient vs. maximum sinkage at 80% slip ($\beta = 44°$). All tests performed in GRC-1 prepared to approximately 1.64 g/cm^3.

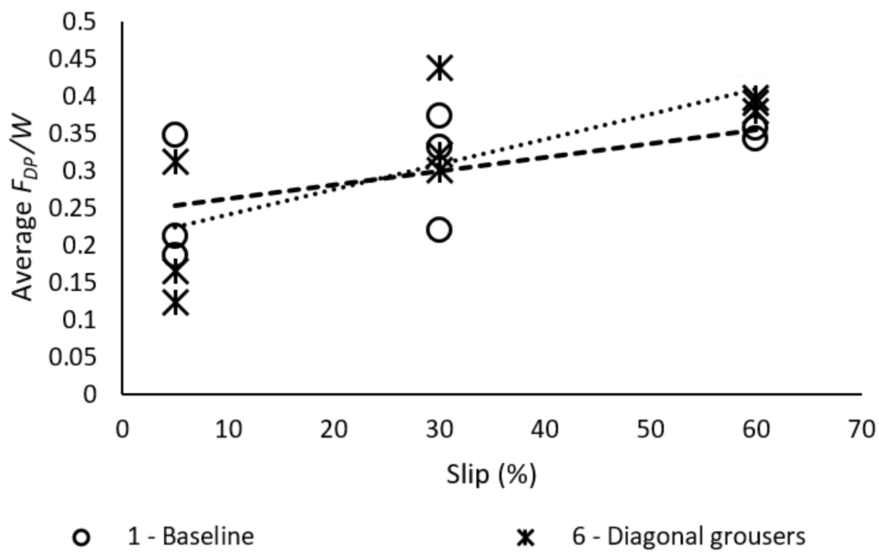

Figure 73: Average drawbar pull coefficient (F_{DP}/W) vs. slip for straight-driving tests. All tests performed in GRC-1 prepared to approximately 1.64 g/cm^3.

It is no surprise that the larger wheels performed better than the baseline, but planetary rover missions are invariably mass- and volume-constrained. The only wheel that did not require an increase in volume or mass and also improved performance was the diagonal grouser wheel. Thus, since this was the leading wheel in terms of the turning performance vs. mass trade, an investigation into straight-driving performance was done to determine if diagonal grousers caused any decrease in straight-driving or slope-climbing ability.

The diagonal wheel and baseline wheel were tested at controlled slip values of 5%, 30%, and 60% (3 repeats of each) to characterize straight-driving and estimate performance driving straight up a slope. Average F_{DP}/W vs. slip and maximum sinkage vs. slip can be seen in Figures 73 and 74, respectively. It can be seen that there was no statistically significant difference in F_{DP}/W (evaluated by a paired, two-tailed t-test, p = 0.86). However, sinkage was approximately 30% higher on average for the diagonal grouser wheel, and this was statistically significant (p = 0.05). This means that there may be a trade-off between turning performance and straight slope-climbing ability, which could potentially be optimized by reducing the angle of the grousers. However, cross-slope performance should also be considered; diagonal grousers have been found to perform better than straight grousers in cross-slope driving tests, since they have more grouser surface area to push against the soil in the down-slope direction which prevents the rover from sliding downwards when driving across a slope [1].

It is also worthwhile to note that drawbar pull tests on a flat surface do not perfectly approximate slope-climbing ability (the normal load distribution that would be present on a full rover is not represented, and the gravity vector on the soil is not in the correct direction to represent soil behaviour on a slope). Thus, to fully characterize slope-climbing performance of diagonal grouser wheels, full rover tests will be performed on a sloped testbed. Obstacle-climbing performance will be evaluated as well.

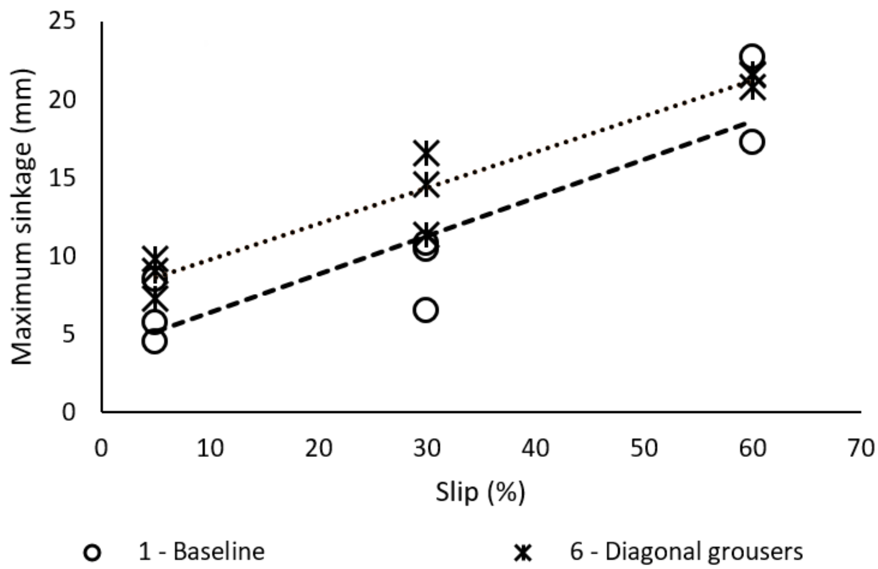

Figure 74: Maximum sinkage vs. slip for straight-driving tests. All tests performed in GRC-1 prepared to approximately 1.64 g/cm^3.

6.1.3 Section summary, conclusion and future work

Single-wheel tests were performed with seven wheel designs to evaluate skid-steer turning performance for a potential future lunar rover. It was observed that wider and/or larger diameter wheels improved skid-steer turning performance with lower sinkage and higher tangent turning forces. However, increasing the wheel size is not desirable in a highly mass- and volume-constrained planetary rover mission. The only wheel design that improved turning performance without requiring increased mass or volume was the wheel with diagonal grousers.

Straight-driving tests were also performed with the baseline wheel compared to the diagonal grouser wheel. No significant change was observed in terms of wheel traction, however, sinkage was 30% higher with diagonal grousers in straight-driving tests. This will be investigated further with full rover tests on sloped terrain, since drawbar pull tests on flat terrain do not fully represent slope-climbing performance. Obstacle-climbing ability will be evaluated as well. A trade-off may exist between turning performance and slope-/ obstacle-climbing performance with these wheels. This could potentially be optimized by decreasing the angle of the grousers (the wheel tested in this work had grousers angled at 45°). Diagonal grousers could be a good choice for an application where steep slopes are not expected to be encountered frequently, but many turns are required, such as a rocky area on flat terrain. Conversely, if straight slope-climbing ability is more important than turning ability, then angled grousers may not be worthwhile. Another factor that should be considered is cross-slope performance; diagonal grousers have previously been shown to perform better than straight grousers when driving across a slope. However, as mentioned previously, the effects of diagonal grousers on slope-climbing ability need to be investigated further.

Another source of error in this work that should be investigated further is the conservatism due to representation of lunar-gravity performance with granular scaling laws (GSL) in the soil simulant GRC-1. Since GSL assumes the same soil in each gravity level, tests should be performed in a different simulant that is more similar to lunar soil and compared to tests with GRC-1 to determine the amount of conservatism introduced by testing in GRC-1 using GSL (since it is expected that lunar soil may be easier to drive on because of angular particles and cohesion resulting in higher shear strength).

6.2 Sub-scale prototype testing for steep-terrain mobility on the Moon and Mars

As discussed in Section 1.4.5, much research has been conducted regarding techniques to improve mobility on steep terrain. Many different rover mobility configurations could be implemented to achieve this goal, but most of them are highly complex and therefore not desirable for rover missions because of prohibitive cost and risk. In the work summarized here, two sub-scale test platforms were designed that are capable of achieving a total of 11 different locomotion modes, and preliminary experiments were performed in the soil simulant GRC-1 (see Section 2.3.2) to systematically compare their performance. The design of these platforms followed GSL (see Section 4.1) in order to represent the performance of a full-sized rover operating on the Moon (i.e. in lunar gravity). The goal is to identify specific locomotion features that provide improved performance on steep terrain in order to obtain a solution that maximizes benefits with minimal complexity. This work was undertaken at JPL, with the main contribution from the author being the application of the scaling laws. The design of the test platforms and some preliminary results are also briefly presented here. This work fits into the overall thesis as shown in Figure 75.

6.2.1 Application of GSL

The version of GSL used in this work is shown in Equation 18 (i.e. including the terrain slope input and dimensionless sinkage output term, and neglecting cohesion since GRC-1 is essentially cohesionless and lunar and martian soils are estimated to have relatively low cohesion).

$$\left[\frac{P}{Mg\sqrt{Lg}}, \frac{V}{\sqrt{Lg}}, \frac{z}{L}\right] = \Omega\left(\sqrt{\frac{g}{L}}t, f, \frac{g}{L\omega^2}, \frac{\rho D L^2}{M}, \theta\right) \tag{18}$$

Using the framework outlined in Section 4.1.1, with q fixed by the relative gravity levels investigated, r and s were chosen to implement a 1/4-scale model of a 500 kg rover on the Moon. The chosen parameters are shown in Table 16. Note that the same scaling can also be applied to martian gravity solely by varying the speed of the rover.

6.2.2 Test platforms

Two reconfigurable platforms (named Asterix and Obelix, shown in Figures 76 and 77, respectively) capable of testing 11 different locomotion modes were designed and built. In addition to the different locomotion methods they can each achieve, their centres of mass can be changed manually using ballast weights, and the wheels can be inclined relative to the rover body such that the wheels remain upright during cross-slope driving (Figure 78). The platforms were designed according to the scaling analysis presented in Section 6.2.1, and both of them have the same geometry, specified in Table 16. The idea is to study the effects of different relative wheel motions,

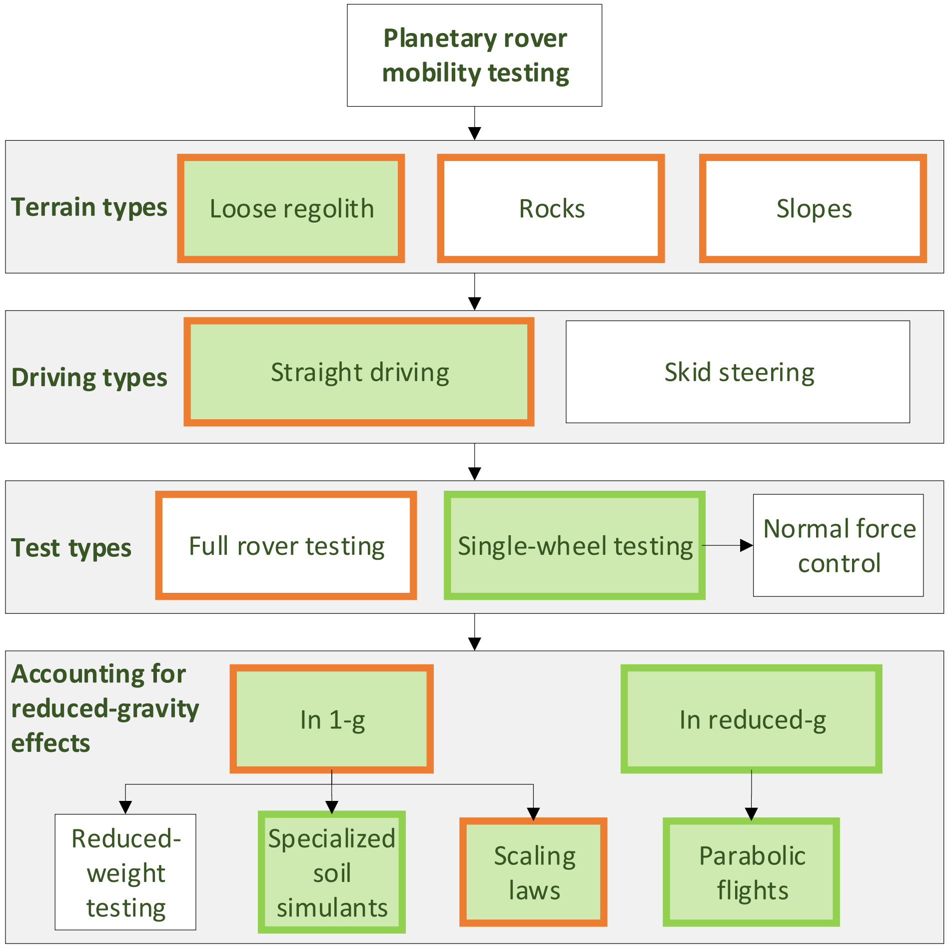

Figure 75: Diagram depicting the topics studied in this thesis, with major topics highlighted in green. The specific topics studied in this section are highlighted in orange.

Table 16: Parameters of the full-scale rover that are represented by the sub-scale models.

	Full-scale rover	Sub-scale model	Scaling calculation
Gravity (m/s^2)	1.62	9.81	$q = 6$
Mass (kg)	500	7.8	$s = 1/64$
Wheel diameter (m)	0.8	0.2	$r = 1/4$
Wheel width (m)	0.23	0.06	$sr^{-2} = 1/4$
Wheel track (m)	1.6	0.4	$r = 1/4$
Wheel base (m)	1.6	0.4	$r = 1/4$
Vehicle height (m)	0.8	0.2	$r = 1/4$
Horizontal velocity (m/s)	0.04	0.049	$q^{1/2}r^{1/2} = \sqrt{6}/2$
Wheel angular velocity (rad/s)	0.1	0.49	$q^{1/2}r^{-1/2} = 2\sqrt{6}$

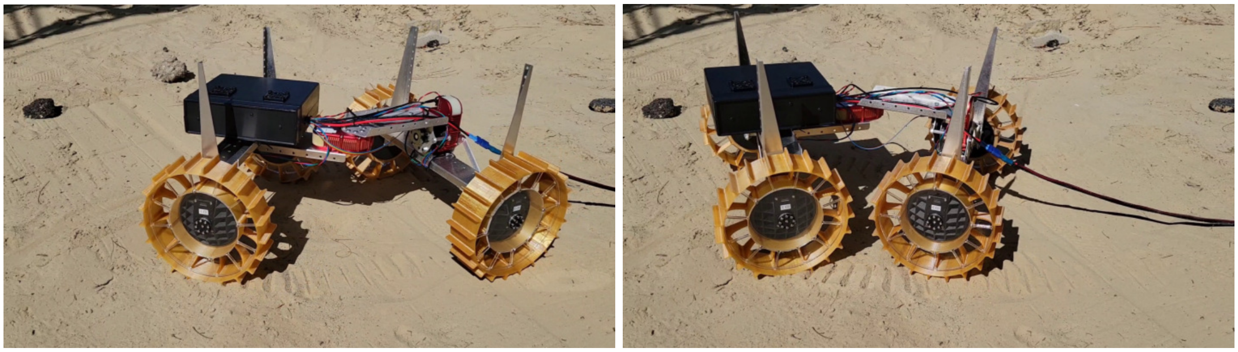

(a) (b)

Figure 76: “Asterix” platform [7].

centre of mass locations, and wheel load distributions on steep terrain mobility performance, not to dictate the specific mechanisms used to implement these capabilities.

Both platforms have a “bogie” suspension (i.e. a revolute joint between two pairs of wheels) which can be reconfigured to be either active or passive. On the Asterix platform, the axis of rotation of this bogie joint is along the rover’s longitudinal direction, and on Obelix, this joint’s axis of rotation is along the lateral direction.

Asterix also has a vertical revolute joint at the centre of its body such that the front part of the chassis can be rotated relative to the back, as shown in Figure 76. This allows the vehicle to turn without the need for dedicated steering actuators, yet also without the drawbacks seen with skid-steer systems [193]. This also allows the rover to achieve a “squirming” gait (and its derivatives), as illustrated in Figure 79, which is similar to previously studied “inchworming” or “push-pull” locomotion modes that have been shown to improve mobility performance on loose regolith and/or steep terrain [194, 195, 196]. The advantage of this type of configuration over similar previously studied implementations is the low number of actuators required to achieve the motion, which is always a plus for planetary rover missions which invariably aim to maximize vehicle capability while minimizing complexity and mass.

A common way to achieve inchworming locomotion that has previously been implemented [141, 142] is to use a “scissor” type of mechanism to change the distance between the front and back wheels. However, this couples the height of the rover body to the distance between the wheels such that the rover’s centre of mass moves up when the wheels move closer together, and down when the wheels spread apart. The Obelix platform was designed to mimic this behaviour but also to be capable of decoupling the height of the rover body from the distance between the wheels. This is shown in Figure 77 and Figure 80, which illustrates all of the locomotion modes that the Obelix platform can perform.

6.2.3 Preliminary results

Experiments with these two platforms are currently underway; tests will include driving over slopes and traversal of obstacles (e.g. rocks). Thus far, preliminary testing has been conducted on flat terrain as well as driving up a 20° slope.

Here, a brief summary of preliminary findings is outlined. Detailed preliminary results and

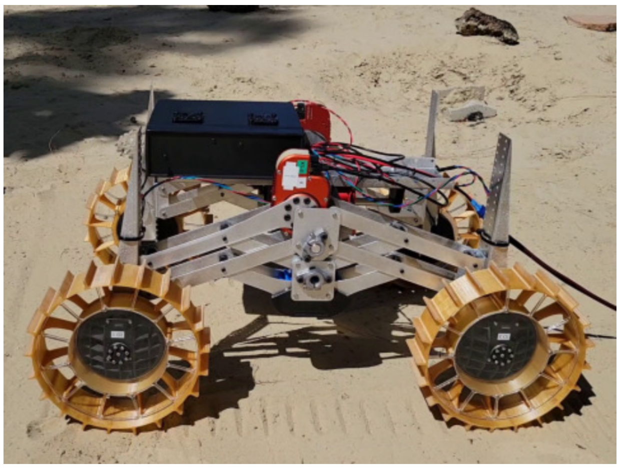

(a)

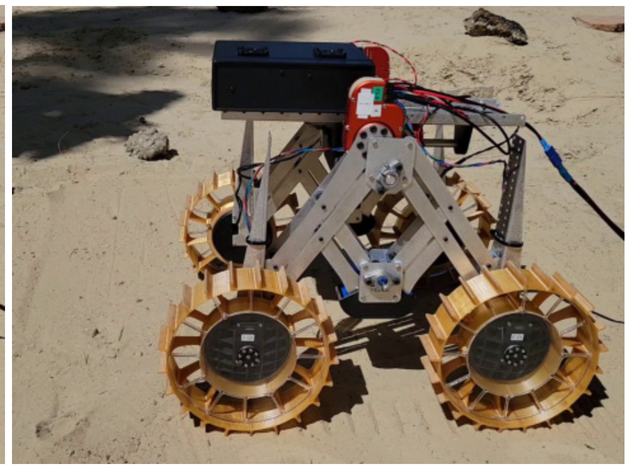

(b)

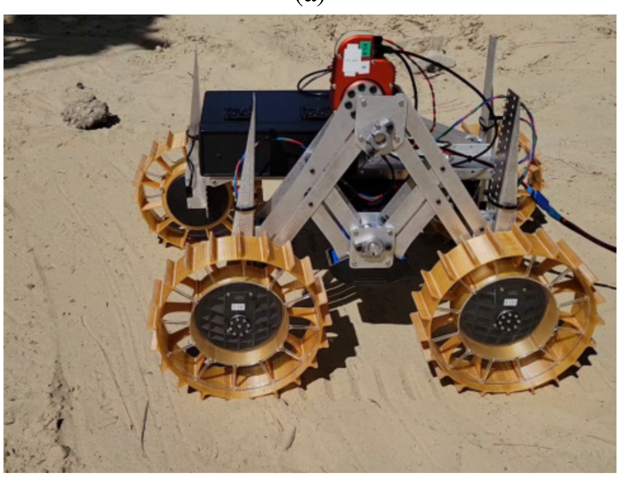

(c)

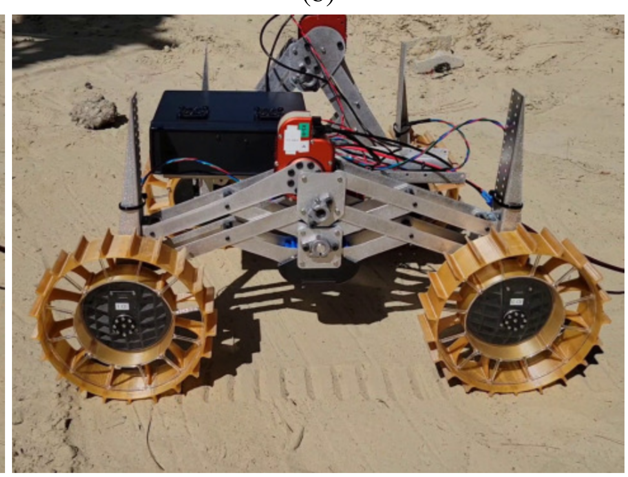

(d)

Figure 77: “Obelix” platform. (a) and (b) show the platform configured to represent inchworming, where the rover body moves upwards when the wheels move closer together. (c) and (d) show the push-rolling configuration, where the wheelbase can be changed independently of the rover body’s height [7].

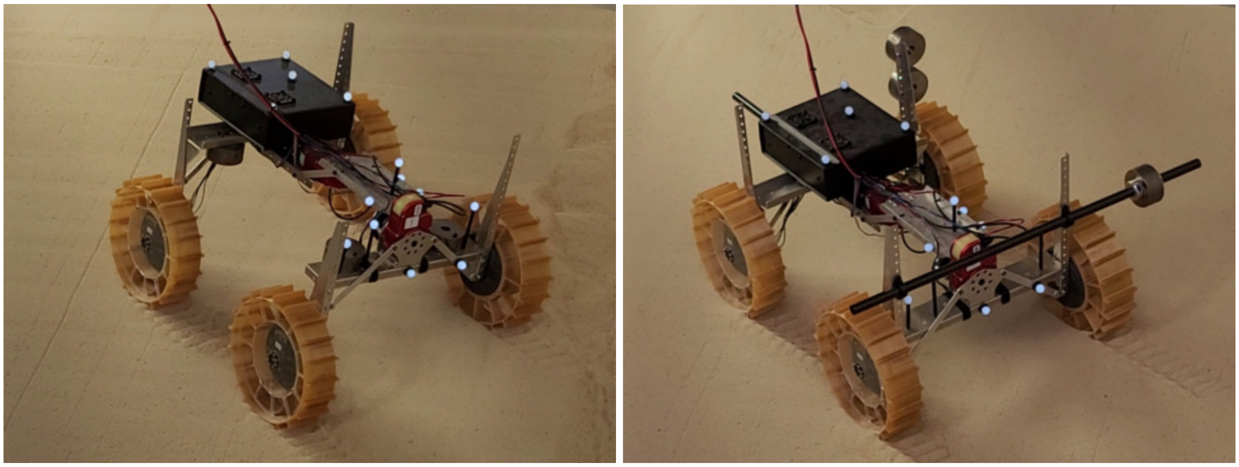

(a) (b)

Figure 78: Examples of manual reconfigurations of Asterix for climbing a 20° slope with a 45° angle of attack. (a) shows how the rover's body can be inclined to keep the wheels upright when crossing a slope, and (b) shows how ballast weights can be used to evenly distribute the wheel load without changing the inclination of the rover body [7].

further technical information will be reported in a forthcoming conference publication [7].

It was observed that the actively articulated locomotion modes mitigated travel reduction (the difference between expected and actual distance travelled) by up to 20%. This means that the active suspension systems achieved lower slip ratios, therefore leading to less sinkage and lower risk of entrapment. However, in terms of energy consumption, the passive suspension modes were still more efficient on slopes up to 20°. This might change on higher slopes, when embedding becomes more significant.

Another observation in the preliminary tests was that the inchworming locomotion mode (i.e. where the rover body moves up and down) required significantly more power than push-rolling (i.e. where the height of the rover body remains constant). It was additionally found that inclining the plane of the wheels to keep them upright when traversing a slope reduced lateral drift significantly.

6.2.4 Section summary, conclusion and future work

This section provided a second example of the successful application of GSL to rover testing. Two reconfigurable rover platforms were designed to represent lunar-g performance according to GSL. Preliminary tests have been conducted with these platforms to compare slope-climbing performance of different locomotion modes. Future work will include performing tests on steeper slopes, as well as traversing obstacles.

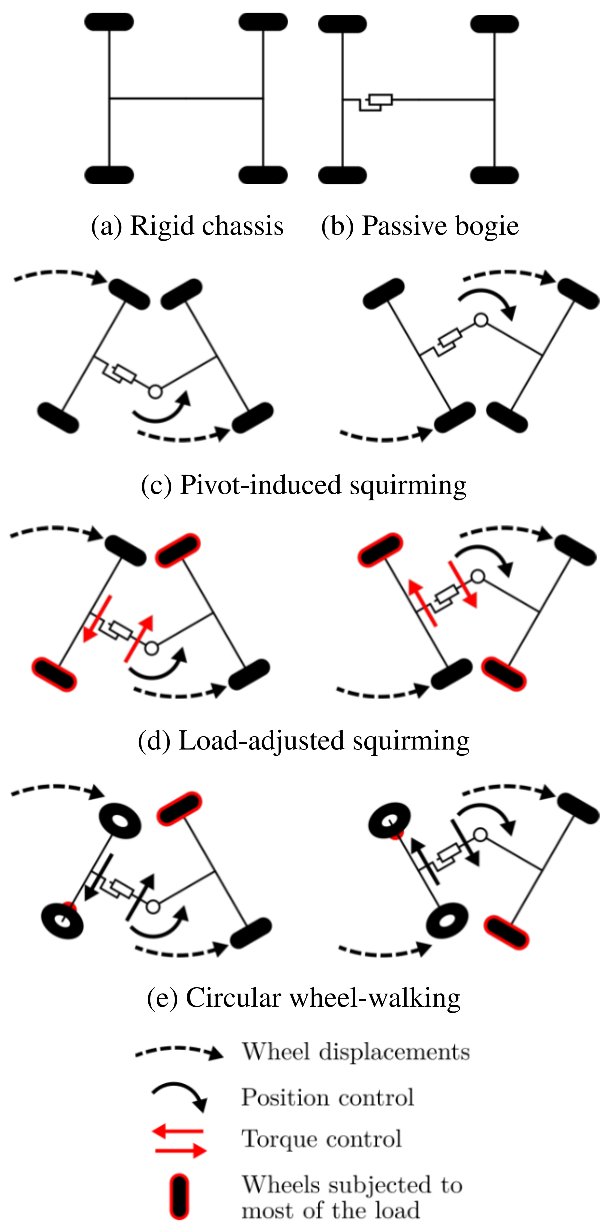

Figure 79: Diagrams of Asterix's locomotion modes (top view) [7].

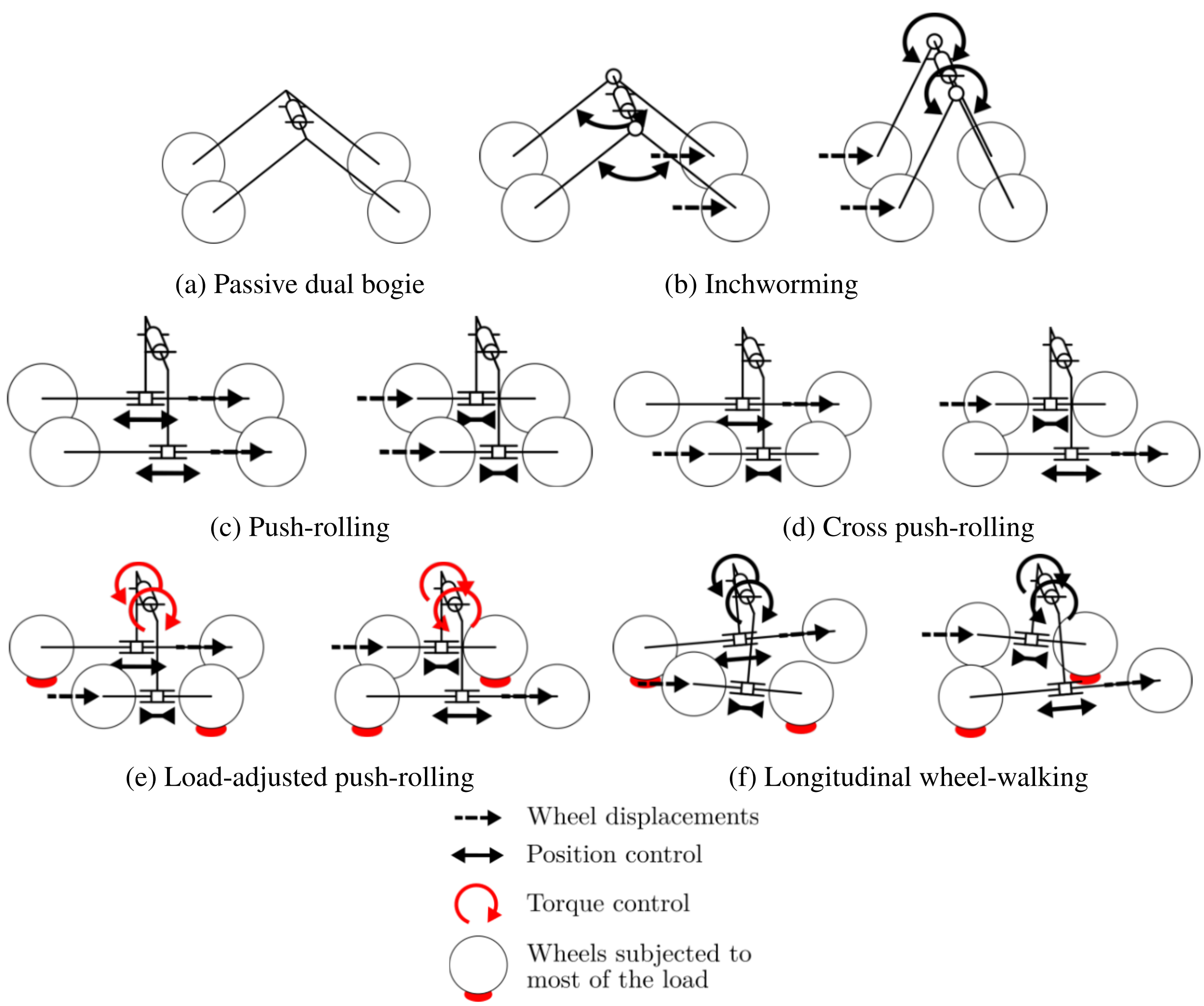

Figure 80: Diagrams of Obelix's locomotion modes (side view) [7].

Chapter 7

Conclusion and future work

Three methods for on-ground mobility testing of planetary rovers were evaluated experimentally by comparing reduced-gravity tests performed aboard parabolic flights to 1-g tests using each method. The first method, reduced-weight testing, which is usually performed using "skeleton" rovers or gravity offload systems, was evaluated in a first flight campaign, and was found to overestimate wheel performance with 25% higher traction in 1-g compared to lunar-g, and almost 30% lower sinkage in 1-g. Since the effect of gravity on the soil particles themselves was isolated in these tests, this result showed that gravity's effect on soil behaviour is an important factor to take into consideration in planetary rover mobility testing.

Next, two previously proposed methods that do attempt to account for reduced-gravity effects on soil behaviour were evaluated in a second parabolic flight campaign. The first of these methods involves matching soil test instrument response with specialized soil simulants. Specifically, in this work, the soil simulant GRC-1 was studied, which was designed to match the cone index gradient (G) measurements from the Apollo missions (which were performed in lunar gravity). This approach, called the "equal G" method in this work, involves the assumption that wheel performance correlates to cone penetrometer measurements regardless of the ambient gravity level. The next method evaluated as part of the second parabolic flight campaign was granular scaling laws (GSL). This method employs dimensionless numbers to scale experiments between gravity levels, similar to testing scale-model aircraft in wind tunnels. Comparing the measured wheel performance in lunar gravity to the predicted performance using each of these methods, the equal G method overestimated wheel performance with 14% lower sinkage and 44% higher traction in the 1-g tests, whereas the GSL method was more accurate with $<$10% error on each metric. Furthermore, GSL erred on the conservative side (i.e. it underestimated wheel performance, which is desirable from a testing standpoint). This is an important result since GRC-1 is very commonly used to test lunar rovers, and testing in this simulant may lead to overestimation of rover performance (note that limitations of these results are discussed in Section 7.2). GSL, on the other hand, has not been widely adopted, but in this work it has proven to be a useful tool for predicting rover mobility in reduced gravity.

Limitations of GSL were then explored experimentally, specifically with respect to its performance in mildly cohesive soils, in addition to restrictions on wheel sizes and relative aspect ratios required to produce accurate results. GRC-1 is essentially cohesionless, whereas lunar regolith is estimated to be mildly cohesive. A new cohesion constraint for GSL was recently proposed in the literature stating that the wheel radius ratio must be the inverse of the gravity ratio (i.e. tests in

1-g representing lunar-g performance must use 1/6-scaled wheels). Since testing 1/6-scaled lunar rovers may not be practical or desirable, experiments were performed to characterize the error introduced by ignoring this cohesion constraint. A series of 1-g experiments in GRC-1 and mildly cohesive simulant LMS-1 revealed that the cohesion constraint can likely be ignored for lunar regolith, at least at low slip values. Further, limitations of GSL regarding the wheel size and/or aspect ratio were observed. Specifically, a small (25.5 mm radius) wheel with a large aspect ratio (D/δ=1.63, over 200% higher than its scaled counterpart) did not follow the scaling laws. As of now, there is not enough data to confirm whether this was due to the ratio of the wheel size to the soil particle size, the aspect ratio difference between the pair of scaled wheels, or both.

Then, the application of GSL was demonstrated through two studies involving planetary rover prototypes under development at NASA's Jet Propulsion Laboratory as part of the JPL Visting Student Research Program (JVSRP). The first study compared different wheel designs for a skid-steer lunar rover in single-wheel tests scaled by GSL. It was found that diagonal grousers improved turning performance without requiring an increase in wheel size. This is an important result since mass is a limiting factor in planetary rover missions. The second study involved application of GSL to the design of two sub-scale test platforms that can be reconfigured to achieve a total of 11 different locomotion modes. Tests are currently underway to compare their performance on steep, regolith-covered slopes, with the ultimate goal of determining the configurations that improve steep-terrain mobility with minimal complexity. Preliminary results were presented demonstrating improved mobility with actively articulated suspension systems on slopes up to 20°, but this improved mobility comes at a cost—higher energy requirements. Further tests will study energy efficiency and mobility on slopes $> 20°$.

Finally, normal force oscillations in vertical-slider single-wheel testbeds (SWTBs) were also investigated, and their origin was shown to be slider friction. A 4-bar mechanism was developed that greatly reduced normal force oscillations and their negative transient dynamics impacts.

7.1 Guidelines for conducting and interpreting 1-g mobility tests for lunar rovers

Current recommendations based on available data are outlined here. These may require updates in the future based on the results of further investigations (such as those outlined in Section 7.2).

1. Granular scaling laws (GSL) are the recommended method to represent reduced-gravity wheel performance with 1-g tests. The cohesion constraint recently proposed in the literature (that the radius ratio must be the inverse of the gravity ratio) can most likely be ignored for mildly cohesive materials like lunar regolith. Thus, an easy way to apply GSL to rover testing is to use a full-size and full-mass rover prototype driven at a higher speed, similar to what was done for the single-wheel tests in Section 6.1. It is additionally recommended that the wheel be large enough such that its sinkage is at least $10\times$ the average particle size [55], and that the variation in aspect ratio between scaled test pairs be less than approximately 50%. Also, GSL tests should be performed in a soil simulant that is as similar as possible to the regolith at the rover's ultimate destination. Tests performed in a soil with different properties should be interpreted accordingly (e.g. tests following GSL in GRC-1 for a lunar rover most likely carry additional conservatism, as discussed in Section 6.1).

2. If performing gravity offload tests and/or using the equal G method (i.e. performing *non-GSL* tests in the soil simulant GRC-1), appropriate safety margins should be added to test results when designing planetary rover wheels to meet minimum traction and/or maximum sinkage requirements, since these tests are most likely non-conservative. The results presented in Chapters 3 and 4 offer starting points for such safety margins.

3. To predict the bounds of lunar-g rover performance, two sets of tests could be performed: one set following GSL, and one using the equal G method, with an assumption that lunar-g rover performance will fall somewhere between the two predictions.

4. Normal force oscillations in single-wheel testbeds should be characterized. If time-series data are to be analyzed, or if a constant normal force is desired for any other reason, a 4-bar mechanism or other normal force control method should be used.

7.2 Limitations and future work

The experiments that tested the equal G method (reported in Chapter 4) essentially showed that contrary to the assumption made during the creation of GRC-1, rover mobility does not correlate with cone index gradient (G) values regardless of ambient gravity level. Conducting the 1-g and 1/6-g tests in the same soil allowed for the elimination of any other soil-specific variables, however, it was observed that the effect of gravity on shear strength played a major role in determining wheel performance in terms of traction, sinkage, and the behaviour of soil beneath the wheel, and that this effect could not be replicated by simply reducing the soil's compaction. The in-situ cone index gradient values measured during the Apollo missions were higher (approximately G = 3 to 10 kPa/mm [2]) than those seen in 1/6-g in the present research (approximately G = 1 to 2 kPa/mm). This is due to the high strength of lunar soil—owing to its angularity and wide particle size distribution [163]—in comparison to GRC-1. Thus, to further evaluate the efficacy of GRC-1 as a lunar terramechanics simulant, planned future work includes experiments comparing wheel performance in lunar-g in a stronger simulant, LMS-1, which more accurately represents the cohesion and angularity of lunar regolith, to wheel performance in GRC-1 in 1-g at densities producing equivalent G values.

These future lunar-g tests in LMS-1 will also be used to further characterize the performance of GSL. Lunar-g tests will be compared to 1-g GSL tests that do not follow the cohesion constraint to confirm if this constraint can be ignored for mildly cohesive soils at both high and low slip values. Potential further avenues for investigation include (i) tests with a 1/6-scaled wheel (i.e. one that does follow the cohesion constraint) with an aspect ratio that is more similar to the full-size wheel tested in lunar-g in order to isolate the effects of wheel size and aspect ratio, and (ii) tests with a full-sized wheel in 1-g to determine if any additional error is introduced when straying further from the cohesion constraint. Both of these sets of experiments would require modifications to the experimental apparatus to increase the range of achievable wheel loads (a much lower load than presently achievable would be required for the former, and a much higher load would be required for the latter).

Regarding the applications of GSL demonstrated in Chapter 6, one source of error that should be investigated further is the conservatism due to representation of lunar-gravity performance with GSL in GRC-1. Since GSL assumes the same soil in each gravity level, tests should be performed in a different simulant that is more similar to lunar soil and compared to tests with GRC-1 to determine the amount of conservatism introduced by testing in GRC-1 using GSL (since it is expected that lunar soil may be easier to drive on because of angular particles and cohesion resulting in higher shear strength). Additionally, future work stemming from the wheel design investigation in Section 6.1 includes further investigation of the effects of diagonal grousers on slope-climbing ability, and full-rover mobility tests comparing diagonal and straight grouser performance on slopes, traversing obstacles, and in turns. Future work related to the steep-terrain mobility tests detailed in Section 6.2 will include testing on steeper slopes as well as traversing obstacles.

Additionally, the optical flow technique used in this work may smooth over discontinuities (e.g. at the soil shear plane beneath the wheel), as mentioned in Sections 3.2.4 and 4.4.2. The original validation was done without discontinuities [157]; thus, investigating optical flow techniques that are able to accurately capture discontinuities would be a worthwhile topic for future research.

Other avenues for potential future work include the following:

1. The extension of GSL from quasi-2D to 3D could be investigated, with 3D Resistive Force Theory as a starting point [192].

2. Efforts to accurately model wheel–soil interactions in reduced gravity are currently underway (e.g. [197]). Potential future work includes improving existing models and validating models against reduced-gravity experimental data.

3. Low-density soil simulants are also an interesting avenue of study (e.g. Fillite [35]) for predicting reduced-gravity wheel performance.

4. Other proposed techniques such as testing with magnetic particles subject to magnetic fields to produce effectively reduced gravity [44] could be investigated further and validated against experimental data from reduced-gravity parabolic flights.

5. The Froude number (Fr) increases as g decreases and/or as V increases. As Fr approaches 1, the quasi-static/rate-independent assumption no longer applies.

    - Testing methods for mobility in extremely low-gravity environments (i.e. decreasing g) should be explored (e.g. Saturn's moon Enceladus, which has a gravity level of about 1/100-g, or Mars' moon Phobos, which has a gravity level of about 1/2000-g, for which an upcoming rover mission is planned [19]). At the wheel speeds and wheel radii studied in our work, for Fr $= 1$, g would be 0.001 m/s^2 or 1/10000-g. However, the rate-independent assumption may break down much before this point. For example, in Phobos gravity, Fr ≈ 0.5 for the wheel sizes and speeds studied here, which may be high enough for GSL to be invalidated.
    - High speed mobility (i.e. increasing V) is of interest for future rover missions [198]. Thus, an interesting area for future research would be expanding GSL from quasi-static to dynamic applications. A starting point for this might be dynamic Resistive Force Theory [199]. Another option for future investigation would be adding the inertial number I to GSL. The inertial number is defined as $I = \dot{\gamma} d_p/(P/\rho_s)^{0.5}$, where $\dot{\gamma}$ is the strain rate, d_p is the particle diameter, P is the applied normal stress, and ρ_s is the particle density. Small values of I indicate quasi-static behaviour, and large values

correspond to inertial or dynamic states. In the $\mu(I)$ rheology it is assumed that the coefficient of friction of a granular material, μ, is a function only of the inertial number for fast and dense granular flows [200].

References

[1] K. Nagaoka, K. Sawada, and K. Yoshida, "Shape effects of wheel grousers on traction performance on sandy terrain," *Journal of Terramechanics*, vol. 90, pp. 23–30, 2020.

[2] H. Oravec, X. Zeng, and V. Asnani, "Design and characterization of GRC-1: A soil for lunar terramechanics testing in Earth-ambient conditions," *Journal of Terramechanics*, vol. 47, no. 6, pp. 361–377, 2010.

[3] E. Robens, A. Dąbrowski, E. Mendyk, J. Goworek, K. Skrzypiec, M. Drewniak, M. Dumańska-Słowik, W. Gac, R. Dobrowolski, S. Pasieczna-Patkowska, *et al.*, "Investigation of surface properties of lunar regolith-Part IV," *Annales Universitatis Mariae Curie-Skłodowska Lublin, Polonia, Sectio AA Chemia*, vol. 63, pp. 144–168, 2008.

[4] Exolith Lab, "LMS-1 Lunar Mare Simulant." `https://exolithsimulants.com/collections/regolith-simulants/products/lms-1-lunar-mare-simulant`. Accessed: 2022-09-21.

[5] P. Niksirat, A. Daca, and K. Skonieczny, "The effects of reduced-gravity on planetary rover mobility," *The International Journal of Robotics Research*, vol. 39, no. 7, pp. 797–811, 2020.

[6] A. Biguri, "Perceptually uniform colormaps," 2019.

[7] A. Bouton, W. Reid, T. Brown, A. Daca, M. Sabzehi, and H. Nayar, "A comparative study of alternative rover configurations and mobility modes for planetary exploration," in *2023 IEEE Aerospace Conference*, IEEE, 2023.

[8] J. Slonaker, D. C. Motley, Q. Zhang, S. Townsend, C. Senatore, K. Iagnemma, and K. Kamrin, "General scaling relations for locomotion in granular media," *Physical Review E*, vol. 95, no. 5, p. 052901, 2017.

[9] A. Daca and K. Skonieczny, "Evaluating 1-g testing methods for predicting planetary rover mobility in reduced gravity," in *16th Symposium on Advanced Space Technologies in Robotics and Automation (ASTRA)*, 2022.

[10] N. V. Bondarenko and M. A. Kreslavsky, "Surface properties and surficial deposits on Venus: New results from Magellan radar altimeter data analysis," *Icarus*, vol. 309, pp. 162–176, 2018.

[11] International Space Exploration Coordination Group, "Global exploration roadmap," tech. rep., National Aeronautics and Space Administration Headquarters, Washington, DC, 2018.

[12] A. Fujiwara, J. Kawaguchi, D. Yeomans, M. Abe, T. Mukai, T. Okada, J. Saito, H. Yano, M. Yoshikawa, and D. Scheeres, "The rubble-pile asteroid Itokawa as observed by Hayabusa," *Science*, vol. 312, pp. 1330–1334, Jun 2006.

[13] B. Rozitis, E. MacLennan, and J. P. Emery, "Cohesive forces prevent the rotational breakup of rubble-pile asteroid (29075) 1950 DA," *Nature*, vol. 512, no. 7513, pp. 174–176, 2014.

[14] R. Arvidson, J. Bell, P. Bellutta, N. Cabrol, J. Catalano, J. Cohen, L. Crumpler, D. Des Marais, T. Estlin, W. Farrand, R. Gellert, J. Grant, R. Greenberger, E. Guinness, K. Herkenhoff, J. Herman, K. Iagnemma, J. Johnson, G. Klingelhöfer, R. Li, K. Lichtenberg, S. Maxwell, D. Ming, R. Morriss, M. Rice, S. Ruff, A. Shaw, K. Siebach, P. de Souza, A. Stroupe, S. Squyres, R. Sullivan, K. Talley, J. Townsend, A. Wang, J. Wright, and A. Yen, "Spirit mars rover mission: Overview and selected results from the northern home plate winter haven to the side of scamander crater," *Journal of Geophysical Research: Planets*, vol. 115, no. E7, 2010.

[15] D. Brown and G. Webster, "Now a stationary research platform, NASA's Mars rover Spirit starts a new chapter in red planet scientific studies," *NASA Press Release*, 2010.

[16] R. E. Arvidson, J. W. Ashley, J. Bell, M. Chojnacki, J. Cohen, T. Economou, W. H. Farrand, R. Fergason, I. Fleischer, P. Geissler, R. Gellert, M. Golombeck, J. Grotzinger, E. Guinness, R. Haberle, K. Kerkenhoff, J. Herman, D. Iagnemma, B. Jolliff, J. Johnson, G. Klingelhöfer, A. Knoll, A. Knudson, R. Li, S. McLennan, D. Mittlefehldt, R. Morriss, T. Parker, M. Rice, C. Schröder, L. Soderblom, S. Squyres, R. Sullivan, and M. Wolff, "Opportunity mars rover mission: Overview and selected results from purgatory ripple to traverses to endeavour crater," *Journal of Geophysical Research: Planets*, vol. 116, no. E7, 2011.

[17] R. E. Arvidson, K. D. Iagnemma, M. Maimone, A. A. Fraeman, F. Zhou, M. C. Heverly, P. Bellutta, D. Rubin, N. T. Stein, J. P. Grotzinger, and A. R. Vasavada, "Mars science laboratory curiosity rover megaripple crossings up to sol 710 in gale crater," *Journal of Field Robotics*, vol. 34, no. 3, pp. 495–518, 2017.

[18] N. C. Costes, J. E. Farmer, and E. B. George, *Mobility Performance of the Lunar Roving Vehicle: Terrestrial Studies, Apollo 15 Results*, vol. 401. NASA, 1972.

[19] S. Ulamec, P. Michel, M. Grott, U. Böttger, H.-W. Hübers, N. Murdoch, P. Vernazza, K. Özgür, J. Knollenberg, K. Willner, *et al.*, "A rover for the jaxa mmx mission to phobos," in *70th InternationalAstronautical Congress*, pp. IAC–19, International Astronautical Federation, 2019.

[20] J. Carsten, A. Rankin, D. Ferguson, and A. Stentz, "Global planning on the Mars Exploration Rovers: Software integration and surface testing," *Journal of Field Robotics*, vol. 26, no. 4, pp. 337–357, 2009.

[21] M. Heverly, J. Matthews, J. Lin, D. Fuller, M. Maimone, J. Biesiadecki, and J. Leichty, "Traverse performance characterization for the Mars Science Laboratory rover," *Journal of Field Robotics*, vol. 30, no. 6, pp. 835–846, 2013.

[22] K. Skonieczny, D. S. Wettergreen, and W. L. Whittaker, "Advantages of continuous excavation in lightweight planetary robotic operations," *The International Journal of Robotics Research*, vol. 35, no. 9, pp. 1121–1139, 2016.

[23] J. L. Callas, "Mars exploration rover spirit end of mission report," Tech. Rep. JPL D-92756, 2015.

[24] M. G. Bekker, *Theory of land locomotion*. Ann Arbor: University of Michigan Press, 1956.

[25] D. Freitag, A. Green, and K. Melzer, "Performance evaluation of wheel for lunar vehicles," *Marshall Space Flight Center. National Aeronautics and Space Administration*, pp. 1–53, May 1970.

[26] B. Das, "Principles of geotechnical engineering, PWS-Kent," *Inc., Boston*, 1985.

[27] J. Y. Wong and A. Reece, "Prediction of rigid wheel performance based on the analysis of soil-wheel stresses part i. performance of driven rigid wheels," *Journal of Terramechanics*, vol. 4, pp. 81–98, 1967.

[28] J. Wong, "Behaviour of soil beneath rigid wheels," *Journal of Agricultural Engineering Research*, vol. 12, pp. 257–269, 1967.

[29] T. Kobayashi, Y. Fujiwara, J. Yamakawa, N. Yasufuku, and K. Omine, "Mobility performance of a rigid wheel in low gravity environments," *Journal of Terramechanics*, vol. 47, pp. 261–274, 2010.

[30] H. H. Bui, T. Kobayashi, R. Fukagawa, and J. C. Wells, "Numerical and experimental studies of gravity effect on the mechanism of lunar excavations," *Journal of Terramechanics*, vol. 46, pp. 115–124, 2009.

[31] G. Meirion-Griffith and M. Spenko, "A modified pressure–sinkage model for small, rigid wheels on deformable terrains," *Journal of Terramechanics*, vol. 48, pp. 149–155, 2011.

[32] L. Ding, Z. Deng, H. Gao, J. Tao, K. D. Iagnemma, and G. Liu, "Interaction mechanics model for rigid driving wheels of planetary rovers moving on sandy terrain with consideration of multiple physical effects," *Journal of Field Robotics*, vol. 32, pp. 827–859, 2015.

[33] R. Irani, R. Bauer, and A. Warkentin, "A dynamic terramechanic model for small lightweight vehicles with rigid wheels and grousers operating in sandy soil," *Journal of Terramechanics*, vol. 48, no. 4, pp. 307–318, 2011.

[34] C. Senatore and K. Iagnemma, "Analysis of stress distributions under lightweight wheeled vehicles," *Journal of Terramechanics*, vol. 51, pp. 1–17, 2014.

[35] M. B. Edwards, M. M. Dewoolkar, D. R. Huston, and C. Creager, "Bevameter testing on simulant fillite for planetary rover mobility applications," *Journal of Terramechanics*, vol. 70, pp. 13–26, 2017.

[36] M. Jiang, F. Liu, H. Wang, and X. Wang, "Investigation of the effect of different gravity conditions on penetration mechanisms by the distinct element method," *Engineering Computations*, vol. 32, no. 7, pp. 2067–2099, 2015.

[37] L. L. Kovács, B. Ghotbi, F. González, P. Niksirat, K. Skonieczny, and J. Kövecses, "Effect of gravity in wheel/terrain interaction models," *Journal of Field Robotics*, vol. 37, no. 5, pp. 754–767, 2020.

[38] L. Newton, "NASA, Blue Origin Partner to Bring Lunar Gravity Conditions Closer to Earth," *NASA Press Release*, 2021.

[39] N. Costes, G. Cohron, and D. Moss, "Cone penetration resistance test-an approach to evaluating in-place strength and packing characteristics of lunar soils," in *Lunar and Planetary Science Conference Proceedings*, vol. 2, p. 1973, 1971.

[40] K. A. Alshibli, S. N. Batiste, and S. Sture, "Strain localization in sand: plane strain versus triaxial compression," *Journal of Geotechnical and Geoenvironmental Engineering*, vol. 129, no. 6, pp. 483–494, 2003.

[41] M. Kleinhans, H. Markies, S. De Vet, and F. Postema, "Static and dynamic angles of repose in loose granular materials under reduced gravity," *Journal of Geophysical Research: Planets*, vol. 116, no. E11, 2011.

[42] J. P. Marshall, R. C. Hurley, D. Arthur, I. Vlahinic, C. Senatore, K. Iagnemma, B. Trease, and J. E. Andrade, "Failures in sand in reduced gravity environments," *Journal of the Mechanics and Physics of Solids*, vol. 113, pp. 1–12, 2018.

[43] W. Boles, W. D. Scott, and J. F. Connolly, "Excavation forces in reduced gravity environment," *Journal of Aerospace Engineering*, vol. 10, pp. 99–103, 1997.

[44] P.-Q. Mo, F. Gao, G. Zhou, R. Li, K. Yan, and J. Chen, "An experimental study on triaxial compression tests and cone penetration tests in planetary regolith simulant under low gravity fields," *Journal of Testing and Evaluation*, vol. 47, no. 3, pp. 1677–1700, 2018.

[45] R. Sullivan, "Earthmoving in minature," *Journal of Terramechanics*, vol. 1, no. 4, pp. 85–106, 1964.

[46] D. R. Freitag *et al.*, *A dimensional analysis of the performance of pneumatic tires on soft soils*, vol. 3. Auburn University., 1965.

[47] R. L. Schafer, *Model-prototype studies of tillage implements*. PhD thesis, Iowa State University, 1965.

[48] A. Soltynski, "Physical similarity and scale effects in soil-machine systems," *Journal of Terramechanics*, vol. 5, no. 2, pp. 31–43, 1968.

[49] D. R. Freitag, R. L. Schafer, and R. D. Wismer, “Similitude studies of soil-machine systems,” *Journal of Terramechanics*, vol. 7, no. 2, pp. 25–58, 1970.

[50] R. Wismer, D. Freitag, and R. Schafer, “Application of similitude to soil-machine systems,” *Journal of Terramechanics*, vol. 13, no. 3, pp. 153–182, 1976.

[51] J. Hetherington and I. Littleton, “The rolling resistance of towed, rigid wheels in sand,” *Journal of terramechanics*, vol. 15, no. 2, pp. 95–105, 1978.

[52] J. Hetherington, “The use of scale model tests to verify earth anchor design predictions,” *Journal of terramechanics*, vol. 29, no. 2, pp. 257–263, 1992.

[53] J. G. Hetherington, “Scale-model testing of soil-vehicle systems,” *Journal of Battlefield Technology*, vol. 7, no. 2, pp. 7–10, 2004.

[54] J. Hetherington, “Tracked vehicle operations on sand–investigations at model scale,” *Journal of terramechanics*, vol. 42, no. 1, pp. 65–70, 2005.

[55] A. Thoesen, T. McBryan, D. Mick, M. Green, J. Martia, and H. Marvi, “Comparative performance of granular scaling laws for lightweight grouser wheels in sand and lunar simulant,” *Powder Technology*, vol. 373, pp. 336–346, 2020.

[56] A. Thoesen, T. McBryan, M. Green, D. Mick, J. Martia, and H. Marvi, “Revisiting scaling laws for robotic mobility in granular media,” *IEEE Robotics and Automation Letters*, vol. 5, no. 2, pp. 1319–1325, 2020.

[57] A. Thoesen, T. McBryan, and H. Marvi, “Helically-driven granular mobility and gravity-variant scaling relations,” *RSC advances*, vol. 9, no. 22, pp. 12572–12579, 2019.

[58] A. Thoesen, T. McBryan, D. Mick, M. Green, J. Martia, and H. Marvi, “Granular scaling laws for helically driven dynamics,” *Physical Review E*, vol. 102, no. 3, p. 032902, 2020.

[59] Q. Zhang, S. Townsend, and K. Kamrin, “Expanded scaling relations for locomotion in sloped or cohesive granular beds,” *Physical Review Fluids*, vol. 5, no. 11, p. 114301, 2020.

[60] A. L. Kemurdjian, V. V. Gromov, I. F. Kashukalo, and V. N. Petriga, “Methods for determining traction characteristics of planet rover movers and conducting running tests,” *Planetokhodyi*, 1993.

[61] H. Kanamori, “Terramechanics in lunar and planetary exploration,” *Journal of the Robotics Society of Japan*, vol. 21, no. 5, pp. 480–483, 2003 (In Japanese).

[62] Y. Kuroda, T. Teshima, Y. Sato, and T. Kubota, “Mobility performance evaluation of planetary rover with similarity model experiment,” in *IEEE International Conference on Robotics and Automation, 2004. Proceedings. ICRA’04. 2004*, vol. 2, pp. 2098–2103, IEEE, 2004.

[63] Y. Kuroda, T. Teshima, Y. Sato, and T. Kubota, “Mobility performance evaluation of planetary rovers in consideration of different gravitational acceleration,” in *2005 IEEE/RSJ International Conference on Intelligent Robots and Systems*, pp. 2991–2996, IEEE, 2005.

[64] M. Li, F. Gao, and P. Sun, "Prediction method of lunar rover's tractive performance based on similitude methodology," in *Fifth International Conference on Intelligent Computation Technology and Automation*, pp. 686–689, IEEE, 2012.

[65] E. Markow, "Predicted behavior of lunar vehicles with metalastic wheels," *SAE Transactions*, vol. 72, pp. 388–396, 1964.

[66] A. S. Lessem, "Operations and maintenance manual for a scale-model lunar roving vehicle.," tech. rep., U.S. Army Engineer Waterways Experiment Station, 1972.

[67] K. Johnson, V. Asnani, J. Polack, and M. Plant, "Experimental evaluation of the scale model method to simulate lunar vehicle dynamics," in *International Society for Terrain-Vehicle Systems (ISTVS) Americas Regional Conference*, 2016.

[68] M. A. Knuth, J. Johnson, M. Hopkins, R. Sullivan, and J. Moore, "Discrete element modeling of a mars exploration rover wheel in granular material," *Journal of Terramechanics*, vol. 49, no. 1, pp. 27–36, 2012.

[69] A. Haeri and K. Skonieczny, "Accurate and real-time simulation of rover wheel traction," in *2021 IEEE Aerospace Conference (50100)*, pp. 1–9, IEEE, 2021.

[70] A. Azimi, J. Kövecses, and J. Angeles, "Wheel–soil interaction model for rover simulation and analysis using elastoplasticity theory," *IEEE Transactions on robotics*, vol. 29, no. 5, pp. 1271–1288, 2013.

[71] B. Ghotbi, L. Kovács, F. González, P. Niksirat, K. Skonieczny, and J. Kövecses, "Including the effect of gravity in wheel/terrain interaction models," in *Proceedings of the in Proceedings of the 14th International Symposium on Artificial Intelligence, Robotics and Automation in Space (i-SAIRAS 2018*, 2018.

[72] C. H. Mullis, "A study and analysis of the MSFC lunar roving vehicle dust profile test program," Tech. Rep. NASA CR-121075, NASA, 1971.

[73] G. H. Peters, W. Abbey, G. H. Bearman, G. S. Mungas, J. A. Smith, R. C. Anderson, S. Douglas, and L. W. Beegle, "Mojave mars simulant—characterization of a new geologic mars analog," *Icarus*, vol. 197, no. 2, pp. 470–479, 2008.

[74] M. Sutoh, "Traveling performance analysis of planetary rovers using a repeatable test system in vacuum," *Journal of Terramechanics*, vol. 95, pp. 15–24, 2021.

[75] K. Iizuka, Y. Sato, Y. Kuroda, and T. Kubota, "Experimental study for rover mobility on lunar simulant terrain in vacuum condition," *Journal of Asian Electric Vehicles*, vol. 4, no. 1, pp. 857–860, 2006.

[76] H. Kanamori, S. Aoki, and H. Nakashima, "Terramechanics of a micro lunar rover," in *Engineering, Construction, and Operations in Challenging Environments: Earth and Space 2004*, pp. 123–130, 2004.

[77] M. Sutoh, S. Wakabayashi, and T. Hoshino, “Traveling and abrasion characteristics of wheels for lunar exploration rover in vacuum,” *Journal of Terramechanics*, vol. 68, pp. 37–49, 2016.

[78] M. Sutoh, S. Wakabayashi, and T. Hoshino, “Influence of atmosphere on lunar rover performance analysis based on soil parameter identification,” *Journal of Terramechanics*, vol. 74, pp. 13–24, 2017.

[79] K. Iagnemma, H. Shibly, and S. Dubowsky, “On-line terrain parameter estimation for planetary rovers,” in *Proceedings of the 2002 IEEE international conference on robotics and automation (Cat. No. 02CH37292)*, vol. 3, pp. 3142–3147, IEEE, 2002.

[80] H. Shibly, K. Iagnemma, and S. Dubowsky, “An equivalent soil mechanics formulation for rigid wheels in deformable terrain, with application to planetary exploration rovers,” *Journal of terramechanics*, vol. 42, no. 1, pp. 1–13, 2005.

[81] R. Bauer, W. Leung, and T. Barfoot, “Development of a dynamic simulation tool for the exomars rover,” in *Proceedings of the 8th International Symposium on Artificial Intelligence, Robotics and Automation in Space*, pp. 1–8, 2005.

[82] R. Bauer, W. Leung, and T. Barfoot, “Experimental and simulation results of wheel-soil interaction for planetary rovers,” in *2005 IEEE/RSJ international conference on intelligent robots and systems*, pp. 586–591, IEEE, 2005.

[83] C. Senatore and K. Iagnemma, “Analysis of stress distributions under lightweight wheeled vehicles,” *Journal of Terramechanics*, vol. 51, pp. 1–17, 2014.

[84] G. D. Puszko, “Terramechanical analysis of rover wheel mobility over simulated martian terrain at various slip conditions and vertical loads,” 2013.

[85] C. Senatore, N. Stein, F. Zhou, K. Bennett, R. Arvidson, B. Trease, R. Lindemann, P. Bellutta, M. Heverly, and K. Iagnemma, “Modeling and validation of mobility characteristics of the mars science laboratory curiosity rover,” in *12th International Symposium on Artificial Intelligence, Robotics and Automation in Space (i-SAIRAS), Montreal, QC, Canada, June*, pp. 17–19, 2014.

[86] M.-R. Bouguelia, R. Gonzalez, K. Iagnemma, and S. Byttner, “Unsupervised classification of slip events for planetary exploration rovers,” *Journal of Terramechanics*, vol. 73, pp. 95–106, 2017.

[87] K. Yoshida, T. Watanabe, N. Mizuno, and G. Ishigami, “Terramechanics-based analysis and traction control of a lunar/planetary rover,” in *Field and Service Robotics*, pp. 225–234, Springer, 2003.

[88] K. Yoshida and G. Ishigami, “Steering characteristics of a rigid wheel for exploration on loose soil,” in *2004 IEEE/RSJ International Conference on Intelligent Robots and Systems (IROS)(IEEE Cat. No. 04CH37566)*, vol. 4, pp. 3995–4000, IEEE, 2004.

[89] G. Ishigami, A. Miwa, K. Nagatani, and K. Yoshida, "Terramechanics-based model for steering maneuver of planetary exploration rovers on loose soil," *Journal of Field robotics*, vol. 24, no. 3, pp. 233–250, 2007.

[90] S. Higa, K. Nagaoka, and K. Yoshida, "Stress distributions of a grouser wheel on loose soil," *Journal of Terramechanics*, vol. 85, pp. 15–26, 2019.

[91] K. Nakagoshi, D. Rodríguez-Martínez, and K. Yoshida, "A new single-wheel testbed for fast-moving planetary robots," in *Aerospace Europe Conference*, Association Aéronautique et Astronautique de France, 2020.

[92] S. Michaud, L. Richter, N. Patel, T. Thüer, T. Huelsing, L. Joudrier, R. Siegwart, and A. Ellery, "RCET: rover chassis evaluation tools," in *Proceedings of the 8th ESA Workshop on Advanced Space Technologies for Robotics and Automation*, pp. 2–4, 2004.

[93] S. Michaud, L. Richter, T. Thüer, A. Gibbesch, T. Huelsing, N. Schmitz, S. Weiss, A. Krebs, N. Patel, L. Joudrier, *et al.*, "Rover chassis evaluation and design optimisation using the RCET," in *9th ESA Workshop on Advanced Space Technologies for Robotics and Automation (ASTRA 2006)*, Swiss Federal Institute of Technology (ETHZ), Autonomous Systems Lab, 2006.

[94] N. Patel, R. Slade, and J. Clemmet, "The exomars rover locomotion subsystem," *Journal of Terramechanics*, vol. 47, no. 4, pp. 227–242, 2010.

[95] S. Michaud, G. Kruse, M. Karaoulis, D. de Lange, and M. van Winnendael, "Sensing techniques to characterize locomotion on soils to be traversed by a rover," *ASTRA*, vol. 2017, no. 21th, 2017.

[96] K. Iizuka, Y. Sato, Y. Kuroda, and T. Kubota, "Experimental study of wheeled forms for lunar rover on slope terrain," in *9th IEEE International Workshop on Advanced Motion Control, 2006.*, pp. 266–271, IEEE, 2006.

[97] K. Iizuka, Y. Sato, Y. Kuroda, and T. Kubota, "Study on wheel of exploration robot on sandy terrain," in *2006 IEEE/RSJ International Conference on Intelligent Robots and Systems*, pp. 4272–4277, IEEE, 2006.

[98] C. Sandu, B. Taylor, J. Biggans, and M. Ahmadian, "Building an infrastructure for indoor terramechanics studies: the development of a terramechanics rig at Virginia Tech," in *Proceedings of 16th ISTVS international conference, Turin, Italy*, pp. 177–85, 2008.

[99] B. Taylor, C. Sandu, V. Asnani, and C. Creager, "Effect of individual wheel parameters on the tractive performance on lunar soil simulant," in *Proceedings of 11th European Regional Conf. of ISTVS, Bremen, Germany*, 2009.

[100] S. D. Naranjo, *Experimental Investigation of the Tractive Performance of an Instrumented Off Road Tire in a Soft Soil Terrain*. PhD thesis, Virginia Tech, 2013.

[101] S. D. Naranjo, C. Sandu, S. Taheri, and S. Taheri, "Experimental testing of an off-road instrumented tire on soft soil," *Journal of Terramechanics*, vol. 56, pp. 119–137, 2014.

[102] R. He, C. Sandu, and J. E. Osorio, "Systematic tests for study of tire tractive performance on soft soil: Part i–experimental data collection," *Journal of Terramechanics*, vol. 85, pp. 59–76, 2019.

[103] L. Ding, H.-b. Gao, Z.-q. Deng, and J.-g. Tao, "Wheel slip-sinkage and its prediction model of lunar rover," *Journal of Central South University of Technology*, vol. 17, no. 1, pp. 129–135, 2010.

[104] J. Liu, H. Gao, Z. Deng, and J. Tao, "Effect of slip on tractive performance of small rigid wheel on loose sand," in *International Conference on Intelligent Robotics and Applications*, pp. 1109–1116, Springer, 2008.

[105] J. Liu, H. Gao, and Z. Deng, "Effect of straight grousers parameters on motion performance of small rigid wheel on loose sand," *Information Technology Journal*, vol. 7, no. 8, pp. 1125–1132, 2008.

[106] L. Ding, H. Gao, Z. Deng, K. Nagatani, and K. Yoshida, "Experimental study and analysis on driving wheels' performance for planetary exploration rovers moving in deformable soil," *Journal of Terramechanics*, vol. 48, no. 1, pp. 27–45, 2011.

[107] J. Guo, H. Gao, L. Ding, T. Guo, and Z. Deng, "Linear normal stress under a wheel in skid for wheeled mobile robots running on sandy terrain," *Journal of Terramechanics*, vol. 70, pp. 49–57, 2017.

[108] K. Skonieczny, S. J. Moreland, and D. S. Wettergreen, "A grouser spacing equation for determining appropriate geometry of planetary rover wheels," in *2012 IEEE/RSJ International Conference on Intelligent Robots and Systems*, pp. 5065–5070, IEEE, 2012.

[109] S. Moreland, K. Skonieczny, H. Inotsume, and D. Wettergreen, "Soil behavior of wheels with grousers for planetary rovers," in *2012 IEEE Aerospace Conference*, pp. 1–8, IEEE, 2012.

[110] D. Apostolopoulos, M. D. Wagner, S. Heys, and J. Teza, "Results of the inflatable robotic rover testbed," tech. rep., Carnegie Mellon University, 2003.

[111] Y. Yang, Y. Sun, and S. Ma, "Drawbar pull of a wheel with an actively actuated lug on sandy terrain," *Journal of Terramechanics*, vol. 56, pp. 17–24, 2014.

[112] G. Genta and C. Pizzamiglio, "Testing of planetary rover wheels: Design and setup of a testing machine," in *2016 IEEE Metrology for Aerospace (MetroAeroSpace)*, pp. 43–48, IEEE, 2016.

[113] R. A. Irani, R. J. Bauer, and A. Warkentin, "Modelling a single-wheel testbed for planetary rover applications," in *ASME 2010 Dynamic Systems and Control Conference*, pp. 181–188, American Society of Mechanical Engineers Digital Collection, 2010.

[114] R. Irani, *Dynamic terramechanic model for lightweight wheeled mobile robots*. PhD thesis, Dalhousie University, 2011.

[115] A. Männel, "Modeling of the wheel-soil contact for planetary exploration rovers," Master's thesis, Technische Universität München, 2016.

[116] D. Flippo, R. Heller, and D. P. Miller, "Turning efficiency prediction for skid steer robots using single wheel testing," in *Field and Service Robotics*, pp. 479–488, Springer, 2010.

[117] G. Sharma, S. Tiwary, A. Kumar, H. S. Kumar, and K. K. Murthy, "Systematic design and development of a flexible wheel for low mass lunar rover," *Journal of Terramechanics*, vol. 76, pp. 39–52, 2018.

[118] C. Padmanabhan, S. Gupta, A. Mylswamy, *et al.*, "Estimation of terramechanics parameters of wheel-soil interaction model using particle filtering," *Journal of Terramechanics*, vol. 79, pp. 79–95, 2018.

[119] W. Li, Y. Huang, Y. Cui, S. Dong, and J. Wang, "Trafficability analysis of lunar mare terrain by means of the discrete element method for wheeled rover locomotion," *Journal of Terramechanics*, vol. 47, no. 3, pp. 161–172, 2010.

[120] B. Chen, J. Li, M. Zou, W. Ma, Y. Li, and L. Ren, "Research on tractive force characteristics of the rigid wheel on the loose sand by orthogonal experiment.," in *International Agricultural Engineering Conference, Bangkok, Thailand*, Asian Association for Agricultural Engineering, 2007.

[121] B. Chen, "Research on traction characteristics of the rigid wheel with grousers on sandy soil," Master's thesis, Jilin University, Changchun, China (in Chinese), 2007.

[122] A. M. Sedara, "Development of a single wheel test rig for measuring motion resistance," *Journal of Engineering Research and Reports*, vol. 4, pp. 1–13, 2019.

[123] A. A. F. Nassiraei and K. Skonieczny, "Grousers improve drawbar pull by reducing resistance and generating thrust at the front of a wheel," *Journal of Terramechanics*, vol. 91, pp. 73–84, 2020.

[124] K. Skonieczny, P. Niksirat, and A. Nassiraei, "Rapid automated soil preparation for testing planetary rover-soil interactions aboard reduced-gravity aircraft," *Journal of Terramechanics*, vol. 83, pp. 35–44, 2019.

[125] M. Jiang, Y. Dai, L. Cui, and B. Xi, "Soil mechanics–based testbed setup for lunar rover wheel and corresponding experimental investigations," *Journal of Aerospace Engineering*, vol. 30, no. 6, p. 06017005, 2017.

[126] B. Shamah, D. Apostolopoulos, E. Rollins, and W. L. Whittaker, "Field validation of nomad's robotic locomotion," in *Mobile Robots XIII and Intelligent Transportation Systems*, vol. 3525, pp. 214–222, International Society for Optics and Photonics, 1999.

[127] C. Mungas, D. Fisher, G. S. Mungas, D. Apostolopoulos, and M. Wagner, "SILVRCLAW III-Advanced Wheel Design and Testing," in *2007 IEEE Aerospace Conference*, pp. 1–10, IEEE, 2007.

[128] A. Daca, A. A. F. Nassiraei, D. Tremblay, and K. Skonieczny, "Comparison of wheel load application methods in single-wheel testbeds," *Journal of Terramechanics*, vol. 99, pp. 35–55, 2022.

[129] A. Yahya, M. Zohadie, D. Ahmad, A. Elwaleed, and A. Kheiralla, "UPM indoor tyre traction testing facility," *Journal of Terramechanics*, vol. 44, no. 4, pp. 293–301, 2007.

[130] Y. Kawase, H. Nakashima, and A. Oida, "An indoor traction measurement system for agricultural tires," *Journal of Terramechanics*, vol. 43, no. 3, pp. 317–327, 2006.

[131] H. Shinone, H. Nakashima, Y. Takatsu, T. Kasetani, H. Matsukawa, H. Shimizu, J. Miyasaka, and K. Ohdoi, "Experimental analysis of tread pattern effects on tire tractive performance on sand using an indoor traction measurement system with forced-slip mechanism," *Engineering in Agriculture, Environment and Food*, vol. 3, no. 2, pp. 61–66, 2010.

[132] A. Tola, A. Sedara, O. Olatunde, and A. Babalola, "Effect of soil moisture content, dynamic load and wheel slippage in measuring traction in an indoor traction bed," *Poljoprivredna tehnika*, vol. 46, no. 1, pp. 22–30, 2021.

[133] A. Hendy, S. Hegazy, M. Emam, and Y. Hendawy, "Development of an in-door tire soil bin testing facility experimental setup," in *International Conference on Aerospace Sciences and Aviation Technology*, vol. 15, pp. 1–11, The Military Technical College, 2013.

[134] O. A. Ani, B. Uzoejinwa, A. Ezeama, A. Onwualu, S. Ugwu, and C. Ohagwu, "Overview of soil-machine interaction studies in soil bins," *Soil and Tillage Research*, vol. 175, pp. 13–27, 2018.

[135] G. W. Turnage and D. C. Banks, "Lunar surface mobility studies past and future," 1989.

[136] D. Flippo, *Design and analysis of Rover wheel testbed.* The University of Oklahoma, 2009.

[137] J.-S. Fiset, M. Effati, and K. Skonieczny, "Effects of turning radius on skid-steered wheeled robot power consumption on loose soil," in *Field and Service Robotics, Springer Proceedings in Advanced Robotics, vol 16*, pp. 115–129, Springer Singapore, 2021.

[138] B. Ghotbi, F. González, J. Kövecses, and J. Angeles, "Mobility evaluation of wheeled robots on soft terrain: Effect of internal force distribution," *Mechanism and Machine Theory*, vol. 100, pp. 259–282, 2016.

[139] D. B. Bickler, "The new family of jpl planetary surface vehicles," *Missions, Technologies, and Design of Planetary Mobile Vehicles*, pp. 301–306, 1993.

[140] National Academies of Sciences, Engineering, and Medicine and others, "Origins, worlds, and life: A decadal strategy for planetary science and astrobiology 2023-2032," 2022.

[141] D. Wettergreen, S. Moreland, K. Skonieczny, D. Jonak, D. Kohanbash, and J. Teza, "Design and field experimentation of a prototype lunar prospector," *The International journal of robotics research*, vol. 29, no. 12, pp. 1550–1564, 2010.

[142] P. S. Schenker, E. T. Baumgartner, R. A. Lindemann, H. Aghazarian, D. Q. Zhu, A. Ganino, L. F. Sword, M. S. Garrett, B. A. Kennedy, G. S. Hickey, *et al.*, "New planetary rovers for long-range mars science and sample return," in *Intelligent Robots and Computer Vision XVII: Algorithms, Techniques, and Active Vision*, vol. 3522, pp. 2–15, SPIE, 1998.

[143] B. H. Wilcox, T. Litwin, J. Biesiadecki, J. Matthews, M. Heverly, J. Morrison, J. Townsend, N. Ahmad, A. Sirota, and B. Cooper, "ATHLETE: A cargo handling and manipulation robot for the moon," *Journal of Field Robotics*, vol. 24, no. 5, pp. 421–434, 2007.

[144] S. Karumanchi, K. Edelberg, I. Baldwin, J. Nash, J. Reid, C. Bergh, J. Leichty, K. Carpenter, M. Shekels, M. Gildner, *et al.*, "Team RoboSimian: semi-autonomous mobile manipulation at the 2015 DARPA robotics challenge finals," *Journal of Field Robotics*, vol. 34, no. 2, pp. 305–332, 2017.

[145] W. Reid, G. Meirion-Griffith, S. Karumanchi, B. Emanuel, B. Chamberlain-Simon, J. Bowkett, and M. Garrett, "Actively articulated wheel-on-limb mobility for traversing Europa analogue terrain," in *Field and Service Robotics*, pp. 337–351, Springer, 2021.

[146] A. Colaprete, D. Andrews, W. Bluethmann, R. C. Elphic, B. Bussey, J. Trimble, K. Zacny, and J. E. Captain, "An overview of the volatiles investigating polar exploration rover (viper) mission," in *AGU Fall Meeting Abstracts*, vol. 2019, pp. P34B–03, 2019.

[147] M. Azkarate, M. Zwick, J. Hidalgo-Carrio, R. Nelen, T. Wiese, P. Poulakis, L. Joudrier, and G. Visentin, "First experimental investigations on wheel-walking for improving triple-bogie rover locomotion performances," *Proceedings Advanced Space Technologies for Robotics and Automation (ASTRA). Noordwijk, The Netherlands: European Space Agency*, 2015.

[148] I. A. Nesnas, J. B. Matthews, P. Abad-Manterola, J. W. Burdick, J. A. Edlund, J. C. Morrison, R. D. Peters, M. M. Tanner, R. N. Miyake, B. S. Solish, *et al.*, "Axel and duaxel rovers for the sustainable exploration of extreme terrains," *Journal of Field Robotics*, vol. 29, no. 4, pp. 663–685, 2012.

[149] S. F. Morea, "The lunar roving vehicle: Historical perspective," in *NASA. Johnson Space Center, The Second Conference on Lunar Bases and Space Activities of the 21st Century, Volume 2*, 1992.

[150] European Space Agency, "Moving on mars."

[151] NASA Technology Transfer Program, "Mechanical and fluid systems superelastic tire (LEW-TOPS-99) a viable alternative to the pneumatic tire."

[152] M. Sutoh, J. Yusa, T. Ito, K. Nagatani, and K. Yoshida, "Traveling performance evaluation of planetary rovers on loose soil," *Journal of Field Robotics*, vol. 29, no. 4, pp. 648–662, 2012.

[153] H. Nakashima, H. Fujii, A. Oida, M. Momozu, H. Kanamori, S. Aoki, T. Yokoyama, H. Shimizu, J. Miyasaka, and K. Ohdoi, "Discrete element method analysis of single wheel performance for a small lunar rover on sloped terrain," *Journal of Terramechanics*, vol. 47, no. 5, pp. 307–321, 2010.

[154] T. Watanabe and K. Iizuka, "Study on wheel typed rovers with soil hardening function by vibration to travel on loose soil," in *International Society for Terrain-Vehicle Systems (ISTVS) Americas Regional Conference*, 2021.

[155] K. Skonieczny, P. Niksirat, and A. A. F. Nassiraei, "Rapid automated soil preparation for testing planetary rover-soil interactions aboard reduced-gravity aircraft," *Journal of Terramechanics*, vol. 83, pp. 35–44, 2019.

[156] A. Daca, D. Tremblay, and K. Skonieczny, "The relationship between cone penetration resistance and wheel-soil interactions in lunar gravity," in *IEEE Aerospace Conference Proceedings*, March 2021.

[157] K. Skonieczny, S. Moreland, H. Inotsume, D. S. Wettergreen, V. Asnani, and C. Creager, "Visualizing and Analyzing Machine-soil Interactions using Computer Vision," *Journal of Field Robotics*, vol. 31, pp. 753–769, January 2014.

[158] J. McRae, C. Powell, and R. Wismer, "Performance of soils under tire loads, report 1: test facilities and techniques," *U.S. Army Engineer Waterways Experiment Station*, 1965.

[159] H. A. Oravec, *Understanding mechanical behavior of lunar soils for the study of vehicle mobility*. Case Western Reserve University, 2009.

[160] J.-S. Fiset, "Effects of turning radius on skid-steered wheeled robot power consumption on loose soil," Master's thesis, Concordia University, 2019.

[161] B. H. Wilcox and R. M. Jones, "The muses-cn nanorover mission and related technology," in *2000 IEEE Aerospace Conference. Proceedings (Cat. No. 00TH8484)*, vol. 7, pp. 287–295, IEEE, 2000.

[162] H. Inotsume, S. Moreland, K. Skonieczny, and D. Wettergreen, "Parametric study and design guidelines for rigid wheels for planetary rovers," *Journal of Terramechanics*, vol. 85, pp. 39–57, 2019.

[163] W. D. Carrier, G. R. Olhoeft, and W. Mendell, "Physical properties of the lunar surface," *Lunar sourcebook*, pp. 475–594, 1991.

[164] Y. Wang, X. Feng, W. Liang, H. Zhou, Z. Dong, X. Li, and C. Xue, "Numerical simulation of subsurface penetrating radar in isidis planitia on mars for china's first mission to mars," in *IOP Conference Series: Earth and Environmental Science*, vol. 660, p. 012024, IOP Publishing, 2021.

[165] C. Li, Y. Zheng, X. Wang, J. Zhang, Y. Wang, L. Chen, L. Zhang, P. Zhao, Y. Liu, W. Lv, *et al.*, "Layered subsurface in utopia basin of mars revealed by zhurong rover radar," *Nature*, vol. 610, no. 7931, pp. 308–312, 2022.

[166] C. Brunskill, N. Patel, T. P. Gouache, C. M. Scott, G. P. Saaj, M. Matthews, and L. Cui, "Characterisation of martian soil simulants for the Exomars rover testbed," *Journal of Terramechanics*, vol. 48, no. 6, pp. 419–438, 2011.

[167] Y. Li, X. Zeng, and A. Wilkinson, "Measurement of small cohesion of JSC-1A lunar simulant," *Journal of Aerospace Engineering*, vol. 26, no. 4, pp. 882–886, 2013.

[168] A. Green, J. Smith, and N. Murphy, "Measuring soil properties in vehicle mobility, research; strength-density relations of an air-dry sand," tech. rep., 1964.

[169] J. L. Smith, "Strength-moisture-density relations of fine-grained soils in vehicle mobility research," 1964.

[170] M. Bekker, "Land locomotion on the surface of planets," *ARS journal*, vol. 32, no. 11, pp. 1651–1659, 1962.

[171] M. G. Bekker, "Mechanics of locomotion and lunar surface vehicle concepts," *Sae Transactions*, pp. 549–569, 1964.

[172] K. Melzer, "Performance of the boeing LRV wheels in a lunar soil simulant. report 2: Effects of speed, wheel load, and soil," 1971.

[173] J. M. Long-Fox, Z. A. Landsman, D. T. Britt, J. Morales Gonzales, and C. D. Schultz, "Quantifying the Shear Strength Properties of Lunar Regolith Simulants LHS-1 and LMS-1," in *Luxembourg Space Resources Week*, 2021.

[174] Exolith Lab, "LMS-1 Lunar Mare Simulant Fact Sheet." `https://cdn.shopify.com/s/files/1/0398/9268/0862/files/lms-1-spec-sheet-2021.pdf?v=1616795572`, 2021. Accessed: 2022-09-21.

[175] C. Creager, V. Asnani, H. Oravec, and A. Woodward, "Drawbar pull (DP) procedures for off-road vehicle testing," tech. rep., NASA, 2017.

[176] A. C. Woodward, "Experimental analysis of the effects of the variation of drawbar pull test parameters for exploration vehicles on GRC-1 lunar soil simulant," Master's thesis, Virginia Tech, 2011.

[177] P. Niksirat, "Characterizing the effect of reduced gravity on rover wheel-soil interactions," Master's thesis, Concordia University, 2018.

[178] F. Qian, K. Daffon, T. Zhang, and D. I. Goldman, "An automated system for systematic testing of locomotion on heterogeneous granular media," in *Nature-Inspired Mobile Robotics*, pp. 547–554, World Scientific, 2013.

[179] R. Lichtenheldt, J.-Y. Burlet, F. Buse, and B. Rebele, "Towards automated soil preparation for planetary rovers–methods for reproducible measurements in regolith simulants," in *Symposium on Advanced Space Technologies in Robotics and Automation, ASTRA*, pp. 1–12, 2017.

[180] R. Irani, R. Bauer, and A. Warkentin, "Application of a dynamic pressure-sinkage relationship for lightweight mobile robots," *International Journal of Vehicle Autonomous Systems*, vol. 12, pp. 1–23, 2014.

[181] A. Daca, D. Tremblay, and K. Skonieczny, "Experimental evaluation of cone index gradient as a metric for the prediction of wheel performance in reduced gravity," *Journal of Terramechanics*, vol. 99, pp. 1–16, 2022.

[182] C. Li, T. Zhang, and D. I. Goldman, "A terradynamics of legged locomotion on granular media," *Science*, vol. 339, no. 6126, pp. 1408–1412, 2013.

[183] R. M. Nedderman *et al.*, *Statics and kinematics of granular materials*, vol. 352. Cambridge University Press Cambridge, 1992.

[184] D. Schuring, "Scale model testing of land vehicles in a simulated low gravity field," *SAE Transactions*, vol. 75, pp. 699–705, 1967.

[185] D. L. Henann and K. Kamrin, "A finite element implementation of the nonlocal granular rheology," *International Journal for Numerical Methods in Engineering*, vol. 108, no. 4, pp. 273–302, 2016.

[186] N. Murphy and A. Green, "Effects of test techniques on wheel performance," *Journal of Terramechanics*, vol. 6, no. 1, pp. 37 – 52, 1969.

[187] T. Fong, "Volatiles investigating polar exploration rover," in *Australasian Conference on Robotics and Automation*, 2020.

[188] Z. Tang, J. Liu, X. Wang, X. Ren, W. Chen, W. Yan, X. Zhang, X. Tan, X. Zeng, D. Liu, *et al.*, "Physical and mechanical characteristics of lunar soil at the chang'e-4 landing site," *Geophysical Research Letters*, vol. 47, no. 22, p. e2020GL089499, 2020.

[189] A. Gans, O. Pouliquen, and M. Nicolas, "Cohesion-controlled granular material," *Physical Review E*, vol. 101, no. 3, p. 032904, 2020.

[190] L. Grill, P. Ostermeier, M. Würth, and P. Reiss, "Behaviour of lunar regolith simulants in fluidised bed reactors for in-situ resource utilisation," *Planetary and Space Science*, vol. 180, p. 104757, 2020.

[191] A. Daca, K. Skonieczny, and S. Moreland, "Diagonal grousers improve turning performance in skid-steer rovers," in *2022 International Society for Terrain-Vehicle System (ISTVS) Americas Symposium*, October 2022.

[192] L. K. Treers, C. Cao, and H. S. Stuart, "Granular resistive force theory implementation for three-dimensional trajectories," *IEEE Robotics and Automation Letters*, vol. 6, no. 2, pp. 1887–1894, 2021.

[193] A. Bouton and Y. Gao, "Crawling locomotion enabled by a novel actuated rover chassis," in *2022 International Conference on Robotics and Automation (ICRA)*, pp. 8164–8170, IEEE, 2022.

[194] A. Halme, I. Leppänen, S. Salmi, and S. Ylönen, "Hybrid locomotion of a wheel-legged machine," in *3rd Int. Conference on Climbing and Walking Robots (CLAWAR'00)*, 2000.

[195] F. B. Amar, C. Grand, G. Besseron, and F. Plumet, “Performance evaluation of locomotion modes of an hybrid wheel-legged robot for self-adaptation to ground conditions,” in *ASTRA’04, 8th ESA Workshop on Advanced Space Technologies for Robotics and Automation*, 2004.

[196] C. Creager, K. Johnson, M. Plant, S. Moreland, and K. Skonieczny, “Push–pull locomotion for vehicle extrication,” *Journal of Terramechanics*, vol. 57, pp. 71–80, 2015.

[197] A. Haeri and K. Skonieczny, “Three-dimensionsal granular flow continuum modeling via material point method with hyperelastic nonlocal granular fluidity,” *Computer Methods in Applied Mechanics and Engineering*, vol. 394, p. 114904, 2022.

[198] D. Rodríguez-Martínez, M. Van Winnendael, and K. Yoshida, “High-speed mobility on planetary surfaces: A technical review,” *Journal of Field Robotics*, vol. 36, no. 8, pp. 1436–1455, 2019.

[199] L. Huang, J. Zhu, Y. Yuan, and Y. Yin, “A dynamic resistive force model for designing mobile robot in granular media,” *IEEE Robotics and Automation Letters*, vol. 7, no. 2, pp. 5357–5364, 2022.

[200] P. Jop, Y. Forterre, and O. Pouliquen, “A constitutive law for dense granular flows,” *Nature*, vol. 441, no. 7094, pp. 727–730, 2006.

Appendix A

Soil slope correction

Despite attempts to maintain the aircraft's X acceleration at 0 m/s^2 and its pitch attitude at 0° during soil preparation, the soil level became sloped after vibration in the second parabolic flight campaign (Chapter 4). Level soil was observed after it was loosened with compressed air; it was during the vibration step that the slope appeared. The soil was higher on the left side of the sandbox such that the wheel was rolling down a slight slope throughout the experiments. This may have been caused by nonzero X acceleration, or by the position of the apparatus inside the aircraft—the apparatus was positioned over the wing, and the aircraft structure on either side of the sandbox may have responded differently to the vibration, with one side absorbing more energy than the other. A soil leveling system is currently under development to mitigate this if it occurs in future flights.

The slope angle was estimated from each video (an average slope of 6° was observed) and a correction was applied to the F_{DP} data according to Equation 19, the derivation of which is illustrated in Figure A.1. A correction was also applied to the sinkage data; the change in soil height was estimated from the video and subtracted from the sinkage measurements. To verify the accuracy of this correction approach, experiments were conducted in the lab with similarly sloped soil and then corrected results were compared to reference lab experiments performed on a flat soil surface. To create the soil slope in the lab, approximately 5.5° on average, one side of the testbed was jacked up for soil preparation using a car jack. These experiments were completed at both

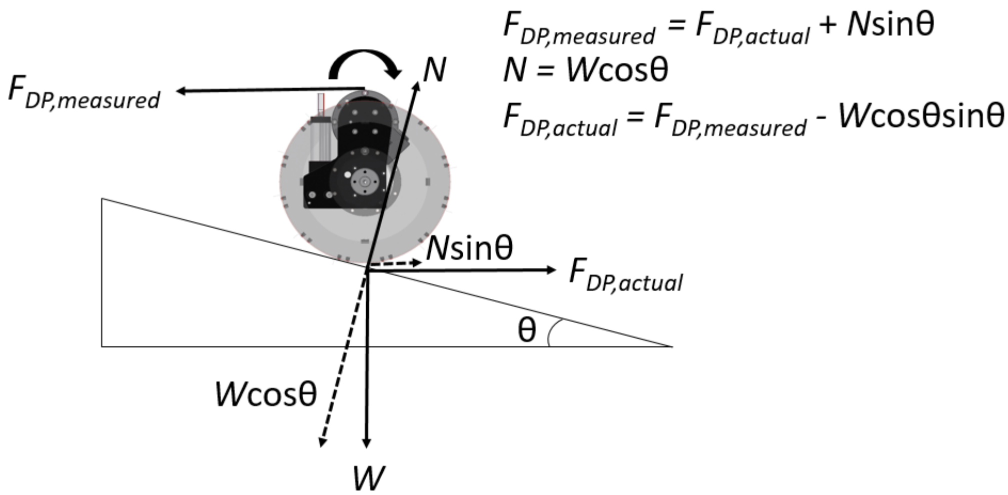

Figure A.1: Derivation of the slope correction applied to the F_{DP} data. θ is the angle of the slope, $F_{DP,measured}$ is the measured drawbar pull force, N is the normal force, W is the wheel load, and $F_{DP,actual}$ is the actual drawbar pull force.

20% slip and 70% slip (3 repeats of each).

$$F_{DP,actual} = F_{DP,measured} - W\cos\theta\sin\theta \tag{19}$$

Figures A.2 and A.3 compare the F_{DP} and sinkage results, respectively, from the flat experiments and the sloped experiments, along with the results after performing the same corrections that were applied to the parabolic flight data. These figures show that the corrections were effective in bringing the results into the expected ranges for corresponding experiments on flat terrain. The mean squared percentage error (MSPE) of uncorrected and corrected sloped terrain results compared to flat terrain results can be found in Table A.1. Since GSL development is based on a steady-state assumption [8], the MSPE was calculated from 5–20 s, when the experiments were in a quasi-steady state. Uncorrected F_{DP}/W results were 23% higher than flat terrain results, on average, whereas the corrected F_{DP}/W results had an MSPE of 2.1% on average. Uncorrected sinkage results were 674% higher than sinkage observed on flat terrain; the error was very high because the potentiometer measurements included the slope of the terrain, rather than only the sinkage of the wheel into the soil. After applying the slope correction, the sinkage MSPE was

Table A.1: Mean squared percentage error (MSPE) of uncorrected and corrected sloped ($5.5°$) terrain results compared to flat terrain results, calculated from 5–20 s.

	Uncorrected			Corrected		
	20% slip	70% slip	Average	20% slip	70% slip	Average
F_{DP}/W	40%	6%	23%	4%	0.2%	2.1%
Sinkage	1310%	37%	674%	10%	0.4%	5%
Power	0.8%	0.5%	0.7%	-	-	-

reduced to 5% on average. The wheel's power requirements were very similar between the flat and sloped experiments ($<$ 1% MSPE), so no correction was performed for power. Also note that the difference between the sloped and flat results is much smaller at 70% slip. This is most likely due to the fact that at 70% slip, the soil slope is not dominating the sinkage measurement and soil resistance, since slip-sinkage also has a significant effect. In contrast, at 20% slip, a more nominal case with less slip-sinkage, the soil slope has a more prominent effect on the sinkage measurement and soil resistance. This large difference in the uncorrected results amplifies error in the correction calculation, resulting in worse correction performance at 20% slip. Thus, bounds can be placed on the error introduced by the lightly sloped terrain during reduced-g flights and the subsequent data correction: approximately 2%–4% error in F_{DP}/W, and 5%–10% in sinkage.

A comparison of the processed images is shown in Figure A.4. This figure shows visualizations of the magnitude of soil flow velocity for the tests on sloped and flat terrain at 20% and 70% slip. The velocities are normalized with respect to the commanded rim speed such that the colormap indicates black as static and light yellow as maximum motion (i.e. commanded rim speed or higher). Note that the wheel is traveling from right to left in these images. Slightly more soil motion is seen beneath the wheel when driving on flat terrain at 20% slip. Output images from the parabolic flight campaign were not corrected in any way; this should be kept in mind when looking at the results from the flights in Chapter 4. However, the shapes of the soil motion regions are similar between tests on sloped and flat terrain, verifying that meaningful comparisons can still be made between the 1/6-g and 1-g experiments. Furthermore, the soil flow directions, shown in Figure A.5, confirm that the soil behaviour beneath the wheel is similar for corresponding experiments

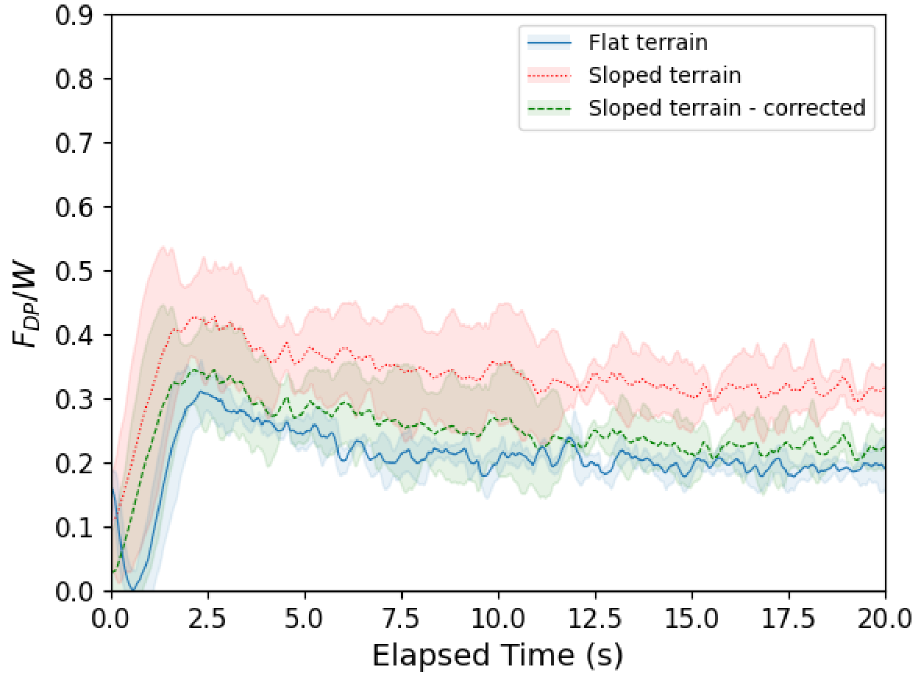

(a) 20% slip

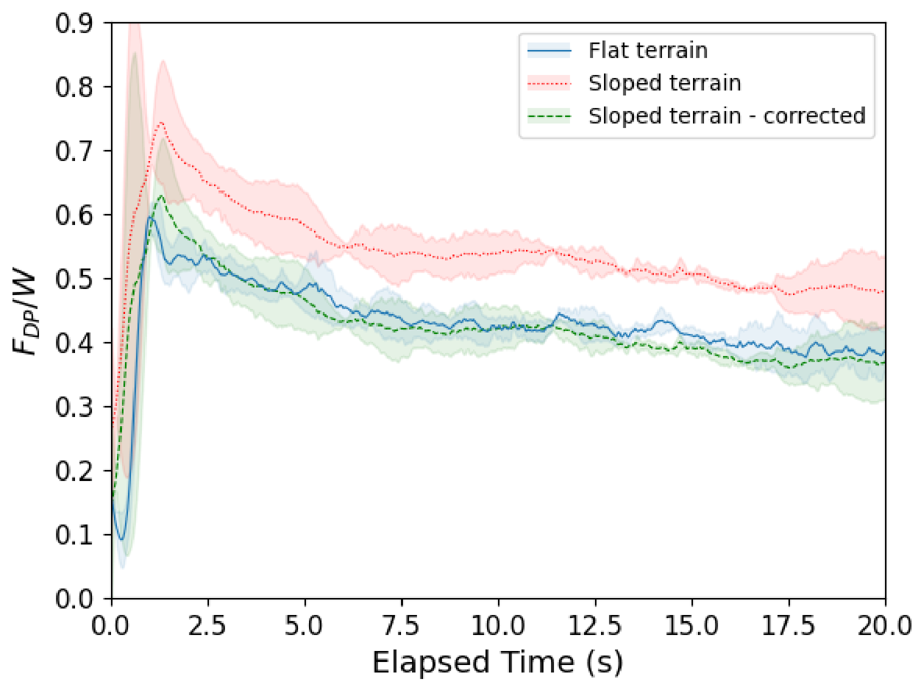

(b) 70% slip

Figure A.2: Drawbar pull–weight ratio (F_{DP}/W) measured on flat terrain and sloped ($5.5°$) terrain, compared to corrected F_{DP}/W from sloped terrain experiments. Each line consists of an average of three experimental repeats, and light-colored regions represent the 95% confidence intervals.

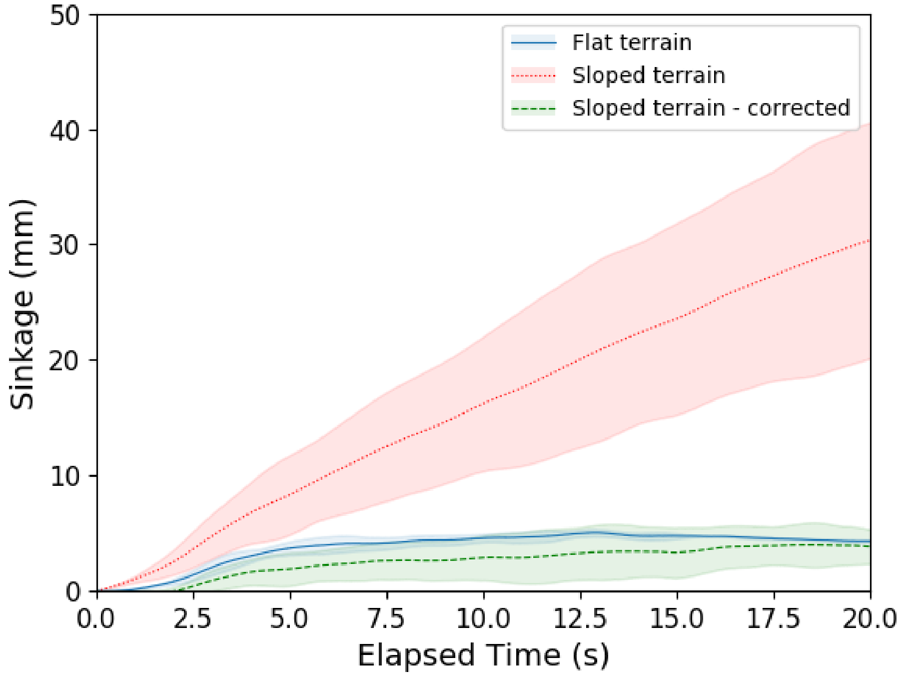

(a) 20% slip

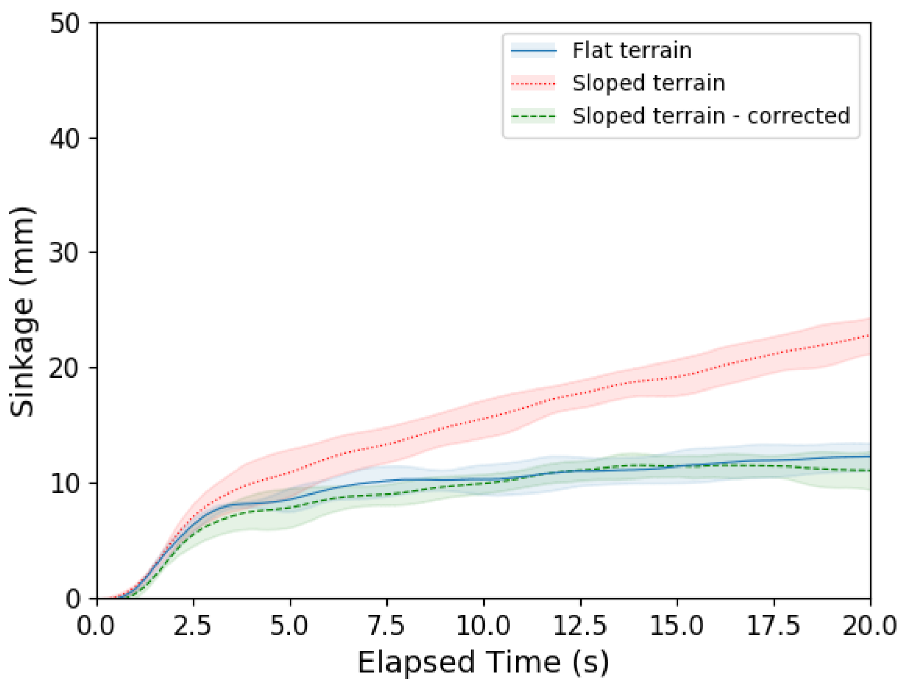

(b) 70% slip

Figure A.3: Sinkage measured on flat terrain and sloped (5.5°) terrain, compared to corrected sinkage from sloped terrain experiments. Each line consists of an average of three experimental repeats, and light-colored regions represent the 95% confidence intervals.

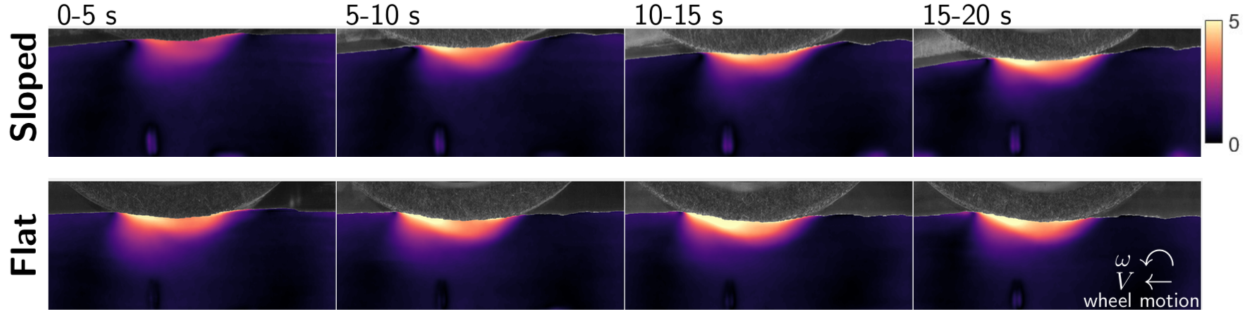

(a) Experiments conducted on sloped terrain (top) and flat terrain (bottom) at 20% slip.

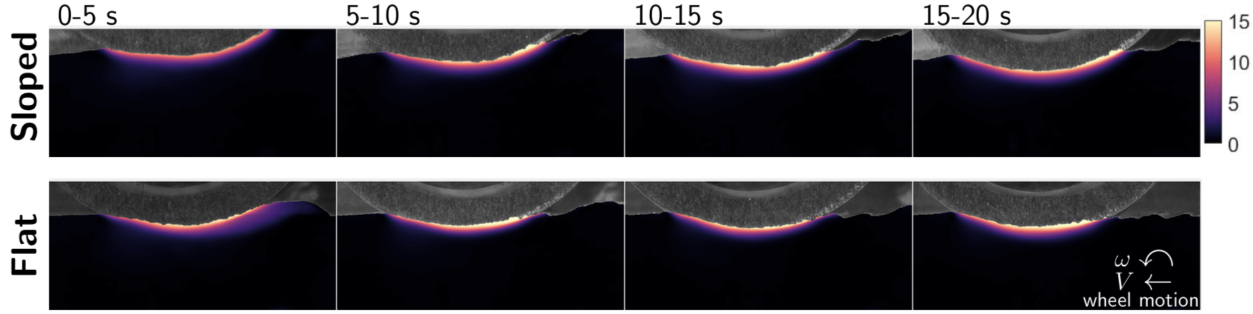

(b) Experiments conducted on sloped ($5.5°$) terrain (top) and flat terrain (bottom) at 70% slip.

Figure A.4: Visualizations of magnitude of soil flow velocity for experiments conducted on sloped ($5.5°$) and flat terrain, averaged over 5-second periods. The colorbars indicate velocity in mm/s with the maximum being commanded rim speed.

on lightly sloped and flat terrain. This figure shows the soil flow directions for the 15–20 second period (corresponding to the 4$^{\text{th}}$ columns in Figures A.4) at 20% slip.

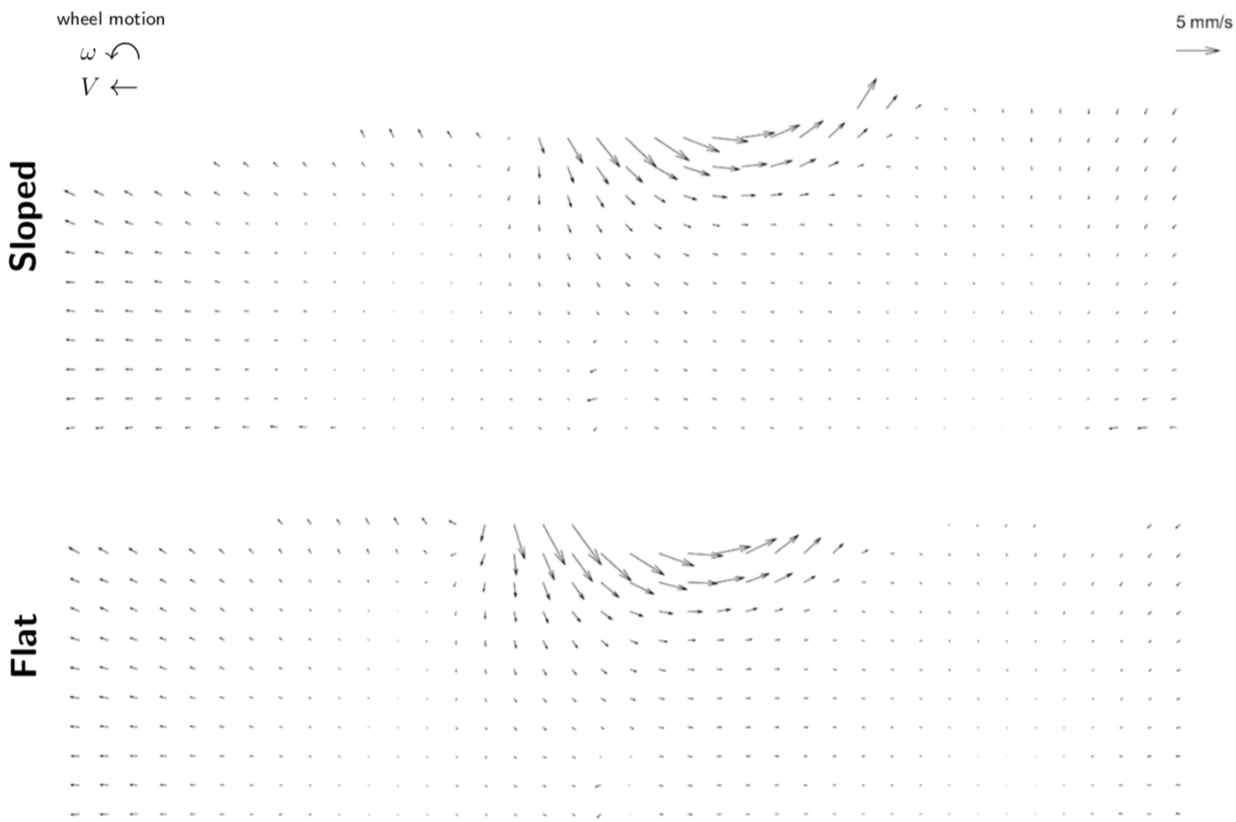

Figure A.5: Visualizations of the direction of soil motion on sloped ($5.5°$) terrain (top) and flat terrain (bottom) at 20% slip, averaged over 5 second period (from 15–20 s). The arrows represent velocity in mm/s.